THREE-DIMENSIONAL MODELS OF MANTLE CONVECTION : INFLUENCE OF PHASE TRANSITIONS AND TEMPERATURE-DEPENDENT VISCOSITY

Thesis by

Paul James Tackley

In Partial Fulfillment of the Requirements

for the Degree of

Doctor of Philosophy

California Institute of Technology

Pasadena, California

1994

(Submitted May 17, 1994)

Acknowledgments

I am grateful to the faculty at the Seismological Laboratory for providing the environment and freedom which enabled me choose this line of research, including a thesis advisor who is not in the Seismological Laboratory. Dave Stevenson has been the ideal thesis advisor, giving me great freedom to pursue this research in the directions and manner I choose, but always being ready to provide stimulating ideas and thoughtful guidance. My time here has been very fruitful: Caltech was surely the best place I could have chosen, and I thank Ron Girdler for encouraging me to make this choice! Discussions with other researchers at Caltech, notably Don Anderson and Slava Solomatov, have been useful.

Interaction and collaboration with researchers outside Caltech has been an essential component in much of this work. In particular I thank Gary Glatzmaier, whose spherical-shell mantle convection code has formed the basis for a large fraction of this work, and Gerald Schubert, who has been a valuable source of advice and enthusiasm. My thinking about links with seismic tomography has been helped by collaborations with Thomas Jordan, Peter Puster, Guy Masters and Stuart Johnson, and discussions with Adam Dziewonski. I thank David Yuen for useful discussions and his constant interest in my research, and for inviting me to his meetings! I also thank Geoff Davies for alerting me to the potential of multigrid methods during his 1990 visit to Caltech, W.R. Peltier for useful discussions on phase transition modulated convection, and W.M. Kaula for providing us with planetary gravity coefficients used in Chapter 3. Parts of this thesis have benefited from reviews by U.R. Christensen (Chapter 2), S.D. King and W.S. Kiefer (Chapter 3) and M. Gurnis (most Chapters).

The annual IGPP mantle convection workshop at Los Alamos National Laboratory has always provided a stimulating and inspiring exchange of ideas and results, which has

been very helpful in this work. In particular, talks at the 1992 workshop inspired me to develop the multigrid code used in the latter part of this thesis.

The majority of the computer simulations reported in this thesis were performed on the Intel Touchstone Delta System, operated by Caltech on behalf of the Concurrent Supercomputing Consortium, and I am grateful to the Caltech Concurrent Supercomputer Facility (CCSF) for providing me with the necessary access to this facility. The Delta has substantially enhanced the progress that has been possible. In addition, the CCSF staff have always been helpful and fast in responding to questions and problems. Many of the more recent simulations reported in Chapter 6 were performed on the Intel Paragon at San Diego Supercomputer Center (SDSC), and I thank SDSC and NSF for access to this resource. Rob Clayton, Doug Neuhauser and Gary Barber provided the local computing environment and advice. This work was supported by NSF grant EAR9017893.

My time at Caltech has been made more enjoyable by many friends and fellow students, including Doug Dreger, Brad Woods, Linda Rowan, Craig Scrivner, Dave Wald, Sharon Kedar, Shingo Watada, and long-term officemates Weishi Huang and Xiaodong Song. I thank Helen Qian for her love and support through much of my time at Caltech. Finally, I thank my parents for their support and encouragement over the years. I dedicate this thesis to them.

Abstract

Two of the most important questions in mantle dynamics are investigated in three separate studies: the influence of phase transitions (studies 1 and 2), and the influence of temperature-dependent viscosity (study 3).

(1) Numerical modeling of mantle convection in a three-dimensional spherical shell incorporating the two major mantle phase transitions reveals an inherently three-dimensional flow pattern characterized by accumulation of cold downwellings above the 670 km discontinuity, and cylindrical 'avalanches' of upper mantle material into the lower mantle. The exothermic phase transition at 400 km depth reduces the degree of layering. A region of strongly-depressed temperature occurs at the base of the mantle. The temperature field is strongly modulated by this partial layering, both locally and in globally-averaged diagnostics. Flow penetration is strongly wavelength-dependent, with easy penetration at long wavelengths but strong inhibition at short wavelengths. The amplitude of the geoid is not significantly affected.

(2) Using a simple criterion for the deflection of an upwelling or downwelling by an endothermic phase transition, the scaling of the critical phase buoyancy parameter with the important lengthscales is obtained. The derived trends match those observed in numerical simulations, i.e., deflection is enhanced by (a) shorter wavelengths, (b) narrower up/downwellings (c) internal heating and (d) narrower phase loops.

(3) A systematic investigation into the effects of temperature-dependent viscosity on mantle convection has been performed in three-dimensional Cartesian geometry, with a factor of 1000-2500 viscosity variation, and Rayleigh numbers of 10^5-10^7. Enormous differences in model behavior are found, depending on the details of rheology, heating mode, compressibility and boundary conditions. Stress-free boundaries, compressibility, and temperature-dependent viscosity all favor long-wavelength flows, even in internally-

heated cases. However, small cells are obtained with some parameter combinations. Downwelling plumes and upwelling sheets are possible when viscosity is dependent solely on temperature. Viscous dissipation becomes important with temperature-dependent viscosity.

The sensitivity of mantle flow and structure to these various complexities illustrates the importance of performing mantle convection calculations with rheological and thermodynamic properties matching as closely as possible those of the Earth.

Table of Contents

List of Figures

List of Tables

Chapter 1

General introduction

The aim of this chapter is to set this thesis in a broad context, describing the developments in various fields of geophysics that have motivated this present work, the important constraints, and a historical overview of previous work. More specific introductory material is given in each chapter; the aim here is to provide a broader perspective, rather than simply repeating that material.

Paradigm

Convection of the solid mantle of the Earth by slow viscous creep is now accepted as the driving mechanism of plate tectonics, and the unifying concept in solid Earth geophysics. Mantle convection provides a framework which links together the major disciplines, such as seismology, mineral physics, geochemistry, tectonics, and geology, and thus, a thorough understanding of this process is essential to understand the dynamics, structure and evolution of the Earth, and other terrestrial planets. Much progress has been

made using laboratory experiments and numerical simulations; however, due to the complexity of material properties and the interactions between various effects, some of the most fundamental, first-order questions are not satisfactorily resolved, and remain the subject of intense debate. The most important such question is whether the mantle convects as two or more layers, or whether the flow extends throughout the entire mantle. Another is the influence of variations in viscosity, a property which is known to vary enormously over the range of conditions experienced in the mantle, and is thus expected to exert a huge influence on the flow. Recent advances in supercomputer technology, and in particular the appearance of massively-parallel supercomputers, have allowed the mantle convective process to be simulated in three dimensions with unprecedented realism and complexity. This thesis reports such simulations which address the fundamental questions of whether the phase transition at 660 km depth can enforce layered convection, and the influence of temperature-dependent viscosity.

Conception

Although mantle convection was proposed over a century ago [*Fisher*, 1881] and again over six decades ago as a mechanism for transporting heat from the Earth [*Holmes*, 1931; *Pekeris*, 1935] or for causing continental drift [*Wegener*, 1929], it was not until a number of advances in the 1960s, leading to the theory of plate tectonics, that these ideas became widely accepted. The chief lines of evidence for plate tectonics were (1) symmetric paleomagnetic lineations on the ocean floor [*Vine and Mathews*, 1963; *Hertzler et al.*, 1966], supporting the idea of sea floor spreading [*Hess*, 1962; *Dietz*, 1961], (2) paleomagnetic evidence for continental drift and the good 'fit' of continents [*Runcorn*, 1956; *Irving*, 1956; *Bullard et al.*, 1965], (3) seismic 'Benioff zones' mapping the position of subducted oceanic plates [*Benioff*, 1954; *Plafker*, 1965; *Stauder and Bollinger*, 1966; *Isaaks and Molnar*, 1971], with the associated gravity profiles [*Talwani*, 1961]

suggesting deep extension of the dipping lithosphere [*McKenzie*, 1969a; *Minear and Toksoz*, 1970], (4) the discovery of transform faults [*Wilson*, 1965], the final component of plate boundaries, and (5) the global distribution of seismicity clearly marking plate boundaries [*Isaacs et al.*, 1968] with earthquake mechanisms along mid-ocean ridge transform faults indicating seafloor spreading [*Sykes*, 1967].

These lines of evidence led to a theory of 'plate tectonics' [*McKenzie and Parker*, 1967; *Morgan*, 1968; *Le Pichon*, 1968] with the oceanic plates forming the upper boundary layer [*Turcotte and Oxburgh*, 1967] of a convective system by which the Earth loses its heat [*Holmes*, 1931; *Tozer*, 1967; *Schubert et al.*, 1969]. Continents were envisioned as compositionally more buoyant material which do not subduct [*Isaaks et al.*, 1968; *McKenzie*, 1969b]. Further discussions and references may be found in various review papers [*Turcotte and Oxburgh*, 1972; *Richter*, 1978a; *Schubert*, 1979; *Hager and Gurnis*, 1987].

Observation

A successful theory of mantle convection must satisfy a large variety of observational and physical constraints, arising from fields such as seismology, geochemistry, mineral physics, plate tectonic models and reconstructions, and gravitational measurements. These constraints are now outlined.

Basic pattern

A successful model must reproduce the basic surface pattern of mantle convection, with linear subduction zones and spreading centers, continents, and relatively fixed 'hot spots'. Some of the observations demand a quantitative explanation, for example, the heat flow, bathymetry and gravity signal of cooling oceanic plates, observations which can be

fit fairly well with a simple half-space cooling model [e.g., *Turcotte and Oxburgh*, 1967; *McKenzie and Sclater,* 1968; *McKenzie et al.*, 1974; *Parsons and Sclater*, 1977; *Jarvis and Peltier,* 1982].

Seismology

Seismology is the most important tool for probing the Earth's interior and provides an invaluable role in constraining the structure and dynamics of the Earth's mantle. For the purposes of this present work, there are three main types of constraint.

(1) Information about radial structure, which often takes the form of spherically-averaged models. It was this type of observation that allowed the first order structure of the Earth to be mapped out. *Birch* [1952] used seismic velocity profiles to obtain his conclusion that there are large changes in structure through the transition zone. Indeed, seismic techniques are still being used to refine our understanding of the major discontinuities in this region [e.g., *Benz and Vidale*, 1993], as discussed later on. From seismically-derived models of spherically-averaged properties, for example PREM [*Dziewonski and Anderson*, 1981], combined with mineral physics data, the composition of different regions in the mantle can be inferred [e.g., *Anderson*, 1967, 1970; *Burdick and Anderson*, 1975; *Anderson and Bass,* 1984; *Bina and Wood*, 1987; *Weidner*, 1987; *Duffy and Anderson*, 1989; *Ita and Stixrude*, 1992], although the uncertainties in such inferences are currently quite large.

(2) Global information about lateral heterogeneity in seismic velocity, giving long-wavelength (typically longer than about 4000 km) constraints on mantle structure, in particular, three-dimensional seismic tomographic models [*Dziewonski*, 1984; *Nataf et al.*, 1986; *Woodhouse and Dziewonski*, 1987, 1989; *Hager and Clayton*, 1989; *Tanimoto*, 1990b; *Inoue et al.*, 1990; *Zhang and Tanimoto*, 1991, 1992, 1993; *Su et al.*, 1992b; *Masters et al.*, 1992; *Pulliam et al.*, 1993; *Vasco et al.*, 1993; *Li and Romanowicz,* 1994].

Although individual convective features cannot be imaged at these wavelengths, these models provide important information. One of the chief findings of these is that the heterogeneity in the mantle is strongly dominated by very long wavelengths [*Nakanishi and Anderson*, 1983; *Tanimoto*, 1990a,b; *Su and Dziewonski,* 1991, 1992], unlike simple numerical convection models, which display a broader spectrum [*Jarvis and Peltier*, 1986, 1989]. Obtaining this long-wavelength heterogeneity is an important challenge for the numerical community. The higher resolution of these models give information about the depth to which structures extend beneath hotspots and mid-ocean ridges [*Zhang and Tanimoto*, 1991, 1992, 1993] although there is some debate over these issues [*Su et al.*, 1992a]. Global tomographic datasets can also be used in a statistical manner, for example, in correlation with past subduction histories [e.g., *Richards and Engebretson*, 1992; *Scrivner and Anderson,* 1992], or other surface observables [*Ray and Anderson*, 1993]; and in conjunction with mineral physics, for calculation of mantle temperature anomalies [*Hager et al.*, 1985; *Cadek et al.*, 1994], or for comparison with datasets from numerical convection models [e.g., *Jordan et al.*, 1993]. Other global information includes mapping of topography on the 660 km discontinuity [*Shearer and Masters,* 1992].

(3) Information about local or regional structure, which gives direct information about the individual small features that are dynamically important in convection at the high Rayleigh number thought to be appropriate for the Earth's mantle. This class of study includes local one-dimensional models, which, for example, can give information about structures in D" [e.g., *Lay and Helmberger*, 1983a,b; *Young and Lay*, 1990; *Garnero et al.*, 1993; *Nataf and Houard*, 1993], as well as regional [e.g., *Grand*, 1987] and local tomographic images. Particularly important for this thesis are the local tomographic studies of slabs [*Zhou and Anderson*, 1989; *Zhou and Clayton*, 1990; *van der Hilst et al.*, 1991; *Fukao et al.*, 1992], which indicate that in many areas, slabs are deflected at the 660 km discontinuity and stagnate in the transition zone, whereas in other areas, apparent extensions of the slabs are observed in the lower mantle. These and other seismic

constraints on slab penetration are reviewed in *Lay* [1994]. Recently, an attempt has been made to detect mantle plumes [*Nataf and VanDecar*, 1993].

Plate motions and history

Motions of tectonic plates provide important constraints on the convection process. There are two ways of approaching these constraints: (1) trying to reproduce certain general characteristics of plate motions with theoretical experiments; (2) using the specific details of current or historical plate motions for various geodynamical calculations.

(1) There are several general characteristics of plate motions that can be investigated. One of these is the motion of continents, which may periodically assemble into supercontinents and break up again [e.g., *Gurnis*, 1988; *Lowman and Jarvis*, 1993]. Continents may also generate long-wavelength heterogeneity [*Gurnis and Zhong*, 1991; *Zhong and Gurnis*, 1993]. In addition to the horizontal motion of continents, vertical motions, possibly resulting in flooding, provide additional constraints [*Gurnis*, 1990a&b, 1992, 1993].

Another important feature of plate motions is that they exhibit a significant component of toroidal flow [*Lithgow-Bertelloni et al.*, 1993], a mode of flow that is not obtained in constant-viscosity convection with homogeneous boundary conditions, and some analyses have been made of this problem [*Forte and Peltier*, 1987; *Olson and Bercovici*, 1991; *Gable et al.*, 1991; *Cadek and Ricard*, 1992].

The mechanisms by which plate boundaries form are poorly understood, and in particular, the initiation of subduction [*Mueller and Phillips*, 1991]. In laboratory experiments with a dense paraffin skin floating on liquid paraffin, the skin must be forcibly pushed into the interior in order to initiate subduction-like behavior [*Jacoby*, 1976]. Plates in numerical models are usually imposed by the modeler, and do not arise self-consistently. Strongly non-linear rheology produces concentrated deformation in the upper boundary

layer which may result in plate-like behavior [*Cserepes*, 1982; *Christensen*, 1984b; *Christensen and Harder,* 1991; *Weinstein and Olson*, 1992; *Bercovici*, 1993]; however, more work is needed to establish whether this behavior is realistic for the Earth. Obtaining self-consistent plates remains a major technical and theoretical challenge for the geodynamical community.

(2) There are several ways in which current or historical plate motions can be used to establish constraints. Some researchers have focused past locations of subduction, attempting to establish the location of subducted slab material by correlating integrated subduction locations with global seismic tomographic models [*Richards and Engebretsen,* 1992; *Scrivner and Anderson*, 1992] or by using a simple, semi-dynamical model to advect slabs vertically into the mantle and relate the results to various geophysical observables [*Ricard et al.*, 1993]. Another research area is to combine current plate motions with buoyancy distributions inferred from seismic tomography to derive information about the viscosity structure and/or scaling of density/velocity with depth [e.g., *Forte et al.*, 1991; *Ricard and Wuming*, 1991]. Spherical convection models can be used to simulate and study episodes in the Earth's history such as the breakup of Pangea [*Baumgardner*, 1993].

Geoid and topography

The surface gravitational field, in the form of the equipotential surface or geoid, provides important geodynamic information about processes and structure in planetary interiors. Dynamic surface topography is a related clue, although it can be obscured by crustal and lithospheric effects, particularly on the Earth. The observed geoid is related to internal mass anomalies and is highly sensitive to the viscosity structure. Thus, by combining information about internal mass anomalies derived from seismic tomographic models with the geoid, the spherically-averaged viscosity profile of the Earth can be constrained, a principle which has been employed in many studies [*Ricard et al.*, 1984;

Richards and Hager, 1984; *Hager and Richards*, 1989; *Hager and Clayton*, 1989; *Kaula*, 1989; *Rapp and Pavlis*, 1990; *King et al.*, 1992; *Forte et al.*, 1993]. Further clues are provided by admittance ratios, i.e., the ratio of geoid to surface topography, which are an important constraint on Venus (where seismic tomographic models are not yet possible) and have been used to argue against the presence of an asthenosphere on Venus [*Kiefer et al.*, 1986]. Unfortunately, a fundamental difficulty with geoid modeling is the non-uniqueness of the results.

Geochemistry, mineral physics and layered mantle models

Important constraints on mantle structure and dynamics arise from geochemical observations, and results from mineral physics and seismology. Useful reviews are presented by *Carlson* [1987] and *Wyllie* [1988].

It is well established that large increases in seismic velocity occur through the transition zone, and although these were initially thought to be diffuse [*Birch*, 1952], later studies indicated sharp seismic discontinuities at depths of around 400 and 660 km [e.g., *Anderson and Toksöz*, 1963; *Lees et al.*, 1983; *Benz and Vidale*, 1993], depths at which major phase transitions in the olivine system are expected to occur [e.g., *Birch*, 1952; *Anderson*, 1967; *Akimoto and Fujisawa*, 1968; *Ringwood and Major,* 1970; *Ringwood*, 1972; *Kumazawa et al.*, 1972] (Further historical background and references can be found in *Anderson* [1991]). However, results from mineral physics suggest that it may not be possible to obtain the seismically observed seismic velocity and density jumps with a homogeneous mantle composition, suggesting a change in bulk composition at the same depths in addition to the phase transition [*Anderson*, 1967, 1979; *Burdick and Anderson,* 1975; *Liu*, 1979; *Jackson*, 1983; *Jeanloz and Thompson*, 1983; *Lees et al.*, 1983; *Anderson and Bass*, 1986; *Jeanloz and Knittle*, 1989; *Stixrude et al.*, 1992]. It is possible that a chemical boundary could coincide on average, but not exactly, with the phase

boundary, an effect which may not be detectable seismically [*Jeanloz and Thompson*, 1983; *Jeanloz,* 1991]. *Weinstein* [1993] has demonstrated how chemical layering at 670 km may arise dynamically, by a 'filter effect' of the endothermic phase transition on chemical heterogeneity.

Additional support for chemical layering or heterogeneity comes from geochemical observations, i.e., isotopic analyses of mantle derived rocks, which indicate distinct reservoirs of magma source material that have retained their separate identities for a billion years or more, an inference which is commonly explained in terms of different convecting regions within the mantle. The idea of layered mantle convection was first proposed by P.P. Bijlaard, as reported in *Gutenberg et al.* [1951], which at that time was motivated by Birch's seismically-derived observations of large structural changes though the mantle transition zone [*Birch*, 1952]. Many layered models based on geochemical constraints have been proposed, with the chemical boundaries coinciding with seismically observed discontinuities. These include the two-layered model of *DePaolo and Wasserburg* [1976, 1979] and *Jacobsen and Wasserburg* [1981] (although the inversion of *Allegre and Lewin* [1989] questions the validity of this model); the three-layered model of *Anderson* [1982a; 1989], the two-layered 'megalith' model of [*Ringwood*, 1982, 1991], and the 'marble cake' upper mantle model of *Allegre and Turcotte* [1986]. Whole-mantle models have also been proposed, such as the model of *Hofmann and White* [1982] in which chemically different slab material accumulates above the Core-Mantle Boundary (CMB).

The idea of layered mantle convection has also been proposed in various geophysical studies, e.g., *Turcotte and Oxburgh* [1967, 1972]; *Richter*, [1973]; *Richter and McKenzie*, [1978].

Modeling

Philosophy

There are a number of approaches to studying mantle convection. The approach which has been most useful in developing a systematic understanding of the important processes is to conduct theoretical studies using idealized models, in which the parameters and results may not be Earth-like, but some particular aspect of the dynamics can be examined and understood in detail. The other approach is to tune the parameters to make the resulting model look as similar as possible to that of the Earth (clearly it can only reproduce the general character of the Earth, not the exact details). It is also possible to use mantle convection models to specifically model specific events in Earth history [*Baumgardner*, 1993].

Historical overview

Systematic laboratory investigations of convection in a viscous fluid heated from below date back to *Bénard* [1901], and a mathematical formulation to *Rayleigh* [1916]. Thus, not surprisingly, this type of convection is generally referred to as Rayleigh-Bénard convection. Rayleigh made a number of simplifying assumptions which he attributed to *Boussinesq* [1903], and this set of assumptions, known as the Boussinesq approximation, has been commonly used in mantle convection modeling. The Boussinesq approximation assumes that (1) density is constant except for weak variations with temperature, so that density variations appear only in the buoyancy term of the momentum equation and (2) all material properties are constant. This second restriction is not good for the mantle and is commonly relaxed in numerical studies. The first approximation is marginally applicable to the mantle, and studies in which the density is allowed to vary with depth are now

common. Mantle convection models are now reaching a state of realism where compressible effects are important.

To study mantle convection, both laboratory experiments and numerical simulations have been performed. Laboratory experiments have been a useful tool, particularly during the 1970s and early 1980s, when numerical simulations were mostly limited to two dimensions, but are fundamentally limited in their applicability to the Earth due to the relatively simple material properties of laboratory materials, the common use of rigid boundaries (the mobility of plates on the Earth suggests that free-slip boundaries are more appropriate), and low Prandtl numbers (that for the Earth is $\sim 10^{23}$), limiting the Rayleigh number that can be reached before inertial effects become important. By contrast, the scope of numerical simulations has followed the development of computing technology, and the sophistication and realism now achievable in numerical simulations exceeds that which can be accomplished in the laboratory.

A brief historical chronology of mantle convection studies follows. It is beyond the scope of this to detail the exact findings of each study - the aim is simply to give an idea of the important research areas and trends. Detailed reviews of work relevant to this thesis are found in the various chapters, and more general reviews in *Schubert* [1979,1992], *Peltier* [1985], *Hager and Gurnis* [1987], *Christensen* [1989d], and *Jarvis and Peltier* [1989].

Most of the work performed in the 1970s, which is reviewed by *Schubert* [1979], concentrated on two-dimensional solutions at fairly low Rayleigh numbers [e.g., *Torrance and Turcotte*, 1971, *Richter*, 1973a, *Turcotte et al.*, 1973; *McKenzie et al.*, 1974; *Parmentier et al.*, 1976], or axisymmetric spherical finite-amplitude convection [*Hsui et al.*, 1972; *Turcotte et al.*, 1972; *Young and Schubert,* 1974; *Cassen and Young*, 1975; *Schubert and Young*, 1976; *Schubert et al.,* 1977], with fully three-dimensional spherical solutions reported by *Young* [1974]. Laboratory experiments were also performed [e.g., *Richter and Parsons*, 1975; *Booker*, 1976; *Whitehead*, 1976, 1978; *Richter*, 1978a, *Nataf et al.*, 1981, 1988].

The 1980s saw development of more sophisticated two-dimensional models, with systematic studies of compressibility [*Jarvis and McKenzie*, 1980; *Steinbach et al.*, 1989; *Schmeling*, 1989; *Machetel and Yuen*, 1989], variable-viscosity convection [*Daly*, 1980; *Cserepes*, 1982; *Parmentier and Morgan*, 1982; *Jacoby and Schmeling,* 1982; *Christensen*, 1983, 1984a&b, 1985a&b, 1987a&b; *Christensen and Yuen*, 1989], phase transitions [*Christensen and Yuen,* 1984, 1985] and chemical layering [*Richter and McKenzie*, 1981; *Christensen and Yuen*, 1984, 1985]. In the second half of the decade, advances in vector supercomputers allowed time-dependent three-dimensional simulations, both in Cartesian geometry [*Cserepes et al.*, 1988; *Houseman*, 1988; *Travis et al.*, 1990b&c; *Cserepes and Christensen,* 1990; *Balachandar and Yuen*, 1992] and spherical geometry [*Baumgardner*, 1985, 1988; *Machetel et al.*, 1986; *Glatzmaier*, 1988; *Bercovici et al.*, 1989abc; *Glatzmaier et al.*, 1990; *Schubert et al.*, 1990]. There was a general trend towards more realistic parameters, which is continuing today, such as higher Rayleigh number [*Schubert and Anderson*, 1985; *Gurnis and Davies,* 1986a; *Machetel and Yuen,* 1987; *Christensen*, 1989a; *Solheim and Peltier*, 1990; *Malevsky and Yuen*, 1993; *Yuen et al.*, 1993], large aspect-ratio [*Christensen*, 1987a; *Christensen and Yuen*, 1988; *Hansen and Ebel*, 1988; *Weinstein et al.*, 1989; *Hansen et al.*, 1992], depth-dependent parameters associated with compressibility [*Leitch and Yuen*, 1989; *Leitch et al.*, 1991; *Hansen et al.*, 1993; *Moser et al.*, 1993] and viscosity variations [*Malevsky and Yuen*, 1992; *van Keken et al.*, 1992; *Larsen et al.*, 1993a&b]. At this time, detailed studies of plate [*Gurnis*, 1988, 1989; *Davies*, 1986, 1988a&b, 1989a&b; *Weinstein and Olson*, 1992; *Zhong and Gurnis*, 1993], slab [*Christensen and Yuen*, 1984; *Kincaid and Olson*, 1987; *Gurnis and Hager,* 1988; *Davies*, 1989a; *Zhong and Gurnis*, 1992; *King and Hager,* 1994] and plume [*Olson et al.*, 1987, 1988, 1993; *Kellogg*, 1991] dynamics and chemical mixing [*Olson et al.*, 1984; *Hoffman and McKenzie*, 1985; *Gurnis and Davies*, 1986b,c,d; *Davies and Gurnis*, 1986; *Kellogg and Turcotte*, 1987,1990; *Christensen*, 1989b; *Kellogg and Stewart,* 1991; *Olson and Kincaid*, 1991; *Todesco and Spera*, 1992; *Kellogg*, 1992; *Hansen et al.*, 1992] also

started appearing. Another area of study has been small-scale convection [*Richter*, 1982; *Schmeling and Marquart*, 1991] or complete mantle layering [*Ellsworth and Schubert,* 1988].

Two major exciting new developments occurred in the 1990s. The first was a resurgence of interest in the question of layering induced by phase transitions, and the second was the appearance of the first systematic (though limited) three-dimensional numerical studies of variable-viscosity convection [*Christensen and Harder,* 1991; *Ogawa et al.*, 1991]. These two topics form the focus of this thesis and are discussed in the next two sections.

Mantle layering and phase transitions

From the earlier discussion on geochemical constraints, it is clear that mantle layering is an important hypothesis to investigate. The debate was recently enlivened by various seismological lines of evidence discussed earlier, notably (1) tomographic studies of subducted slabs which show some slabs being deflected at the 660 km discontinuity (2) global mapping of topography on the 660 km discontinuity favoring models in which the slabs are deflected horizontally [*Shearer and Masters*, 1992] and (3) good correlations between integrated subduction history and transition zone structure [e.g., *Scrivner and Anderson*, 1992].

How would layering occur dynamically? One mechanism is that the inherent density change associated with the chemical differences could prevent mantle mixing. However, numerical [*Richter and McKenzie,* 1981; *Christensen and Yuen*, 1984; *Kellogg*, 1991; *Todesco and Spera*, 1992 and laboratory [*Richter and Johnson*, 1974; *Richter and McKenzie*, 1981; *Olson*, 1984; *Nataf et al.*, 1988] experiments suggest that the likely density jump in the Earth would be too small to prevent whole-mantle convection by itself.

The second mechanism is related to the deflection of the phase boundary at 660 km depth. Due to the negative Clapeyron slope of this transition [*Navrotsky*, 1980; *Ito and Yamada*, 1982; *Ito and Takahashi*, 1989], this deflection results in anomalous buoyancy forces which act to inhibit the flow of material across the 660 km discontinuity [*Schubert and Turcotte*, 1971; *Schubert et al.*, 1975; *Yuen and Olson*, 1982], possibly causing layering, even in an isochemical mantle. Although this basic result was established a decade ago [*Christensen and Yuen*, 1984, 1985], it is only recently that strong interest in its application to the Earth has occurred, with a series of two-dimensional isochemical models [*Machetel and Weber*, 1991; *Liu et al.*, 1991; *Peltier and Solheim*, 1992; *Zhao et al.*, 1992; *Steinbach and Yuen*, 1992, 1993; *Machetel*, 1993; *Steinbach et al.*, 1993; *Weinstein*, 1993; *Solheim and Peltier*, 1994a&b; *Ita and King*, 1994; *Zhong and Gurnis*, 1994]. The consensus emerging from these calculations is that of a partially or intermittently layered mantle characterized by accumulation of slabs in the transition zone, followed by vigorous catastrophic avalanches of cold material into the lower mantle. Given this consensus, the challenge now is twofold: (1) to improve the realism of the numerical models, including such effects as three dimensionality, spherical geometry, temperature-dependent viscosity, plates, chemical variations, etc., (2) to establish more ways in which the theoretical models can be related to and constrained by observational constraints such as those from seismic tomographic models, the geoid and historical plate motions.

Both of these challenges are addressed in this thesis.

Variable viscosity

The most important material property influencing the convection of mantle rocks is viscosity, which is strongly temperature-dependent, varying by many orders of magnitude over the range of conditions experienced in the mantle [*Weertman*, 1970; *Stocker and Ashby*, 1973; *Weertman and Weertman*, 1975; *Ashby and Verrall*, 1977; *Durham et al.*,

1979; *Yuen et al.*, 1983]. However, the majority of numerical studies, particularly in three-dimensions, have not included this effect, due to computational difficulty and expense. Many two-dimensional studies of variable-viscosity convection have been performed, and were listed earlier. These can be roughly divided into idealized studies of individual features such as plumes or slabs, and general studies of whole-mantle convection with variable viscosity, which may not reproduce individual local features very well, but are important for establishing the first-order flow pattern.

Three-dimensional work consists of laboratory experiments [e.g., *Booker*, 1976; *Richter et al.*, 1983; *White*, 1988] which are limited in their applicability to the Earth, as discussed earlier, and numerical simulations [*Busse and Frick*, 1985; *Christensen and Harder,* 1991; *Weinstein and Christensen*, 1991; *Ogawa et al.*, 1992]. The numerical work has generally been limited to low Rayleigh-number, steady-state, Boussinesq, heated-from-below solutions in limited domains. While these have been useful for establishing some basic results, to understand the Earth it is necessary to simulate compressible convection in wide domains, at high Rayleigh number, and with most of the heating from within. This thesis presents a systematic study of these additional effects, in Chapters 5 and 6. Chapter 6 begins with a review of studies of variable viscosity convection. A longer review of rheology and convection experiments can be found in *Christensen* [1989d].

Computation

The sophistication and scale of numerical mantle convection simulations has been controlled mainly by the growth of computing power, with numerical methods being another, less important factor. Throughout the period in question, available computing power has risen steadily [*Buzbee*, 1993; *Baskett and Hennessy*, 1993; *Dongarra*, 1993], with vector supercomputers by vendors such as Cray playing a major role since the mid 1980s. Recently, however, a step-up in computing power has occurred in the form of

massively-parallel supercomputers, with vendors such as Thinking Machines Corporation and Intel offering machines with several times the power of contemporary vector computers (for a review see *Hills and Boghosian* [1993]). The California Institute of Technology has been strongly involved with the development of such computers since the 1980s, and since 1992, has housed and operated the 512-node Intel Touchstone Delta system, owned by the Concurrent Supercomputer Consortium. It is on this computer, which has a theoretical peak speed to 32 billion floating point operations per second, that the majority of the simulations reported in this thesis were performed, with many of the cases in Chapter 6 being performed on the 400-node Intel Paragon at San Diego Supercomputer Center. To run on these computers, codes must be explicitly parallelized using a MIMD (Multiple Instruction Multiple Data) message-passing paradigm, and a description of this and the implementation of the codes used in this thesis are included in the appendices.

Thesis

From the above discussion, it is clear that two of the major issues in mantle dynamics are (1) the ability of phase transitions to induce layered or partially layered mantle convection, and (2) the influence of variations in viscosity on the convective flow. The increase in computer power described in the previous section makes this a timely moment in which to make progress on these issues in three-dimensional geometry. This forms the focus of the work reported in this thesis.

Phase transitions

Chapters 2 and 3, which consist largely of *Tackley et al.* [1993b] and *Tackley et al.* [1994] respectively, present the results of three-dimensional compressible simulations of phase-change modulated mantle convection in a spherical shell, and how the results may be

compared to geophysical observables, particularly the results from global seismic tomographic inversions. This work was performed in collaboration with David Stevenson and Gerald Schubert, who both acted in an advisory role, and Gary Glatzmaier, who provided the original computer code, which I subsequently parallelized and modified. Chapter 2 focuses on the effect of the endothermic phase transition at 670 km depth, providing a basic characterization of the flow characteristics and relationship to observables. The analysis is extended in Chapter 3 by additional calculations including the exothermic phase transition at 400 km depth, and a broader and more detailed analysis of how the results may be compared to geophysical observables. Further analysis and comparisons with seismic tomographic models were performed in two collaborative efforts which are reported elsewhere, in *Jordan et al.* [1993] and *Johnson et al.* [1993].

It is important to understand the effects observed in numerical experiments, and a theoretical analysis of constant-viscosity upwellings and downwellings encountering an endothermic phase transitions is reported in Chapter 4. The phase change strength required to deflect idealized convective features is found as a function of the important lengthscales in the system, explaining most of the trends observed in numerical simulations. A collaborative analysis of the interaction of high viscosity downwellings with an endothermic phase transition was reported in *Bercovici et al.* [1993].

Variable viscosity

Chapters 5 and 6 present a systematic suite of simulations of three-dimensional convection with strongly variable viscosity, performed in a wide Cartesian box. Four simulations are presented in Chapter 5, which consists largely of *Tackley* [1993]; these illustrate some important basic results pertaining to the effect of boundary conditions and aspect ratio. The effects of other complexities, namely compressibility, heating mode,

depth-dependency of the rheology, and Rayleigh number, are systematically investigated in Chapter 6.

Technical aspects

Appendices A and B describe the two computer codes used to perform most of this research, detailing how they were implemented on parallel computers, and giving some performance and benchmarking results. Appendix C describes the solution method used in Chapter 4.

Other work

There are a number of related studies I have performed or been involved with at Caltech, which are not reported in this thesis, but which have been published or will be published in the future. These include the three collaborative ventures already mentioned [*Jordan et al.*, 1993; *Johnson et al.*, 1993; *Bercovici et al.*, 1993].

Two aspects of phase transition modulated mantle convection have been studied using the Cartesian multigrid code. The first aspect is the effect of dimensionality, i.e., 2-D versus 3-D. The results from that study indicate that although the behavior is qualitatively similar, the time variability of the system is intrinsically weaker in 3-D than in 2-D, illustrating the importance of performing three-dimensional simulations if any quantitative conclusions are desired. The second aspect is the effect of temperature-dependent viscosity. The results indicate that when viscosity is dependent solely on temperature, the degree of layering is greatly enhanced compared to a constant viscosity case with similar heat flux. However, realistic subduction zones are not obtained. When a yield stress is added to the rheology, allowing the upper boundary layer to enter the interior easily, the degree of layering is greatly reduced.

A focus of attention with the spherical code has been the amount of true polar wander that it is possible to induce by mantle convection. Convection induces mass anomalies in the mantle which result in non-uniform moment of inertia. The Earth will realign itself so that the maximum principle moment of inertia axis corresponds to the rotation axis. The rate of true polar wander calculated for whole mantle and phase change convection simulations [*Tackley et al.*, 1993b] is high, compatible with the theoretical prediction of *Goldreich and Toomre* [1969].

Venus has been another focus of attention. Recently, I have started to study the influence of phase transitions in three-dimensional spherical Venusian mantle convection, focusing particularly on the effect of boundary conditions. Earlier studies looked at the possibility of generating Coronae by melt-driven instabilities in the shallow mantle [e.g., *Tackley and Stevenson*, 1993b], a mechanism that is described in *Tackley and Stevenson* [1993a].

Chapter 2

Effects of an endothermic phase transition at 670 km depth in a spherical model of convection in the Earth's mantle

Numerical modeling of mantle convection in a spherical shell with an endothermic phase change at 670 km depth reveals an inherently three-dimensional flow pattern, containing cylindrical plumes and linear sheets which behave differently in their ability to penetrate the phase change. The dynamics are dominated by accumulation of downwelling cold material above 670 km depth, resulting in frequent avalanches of upper mantle material into the lower mantle. This process generates long-wavelength lateral heterogeneity, helping to resolve the contradiction between seismic tomographic observations and expectations from mantle convection simulations.

Introduction

The question of whether an endothermic phase transition associated with the seismic discontinuity at 670 km depth could enforce layered convection in the Earth's mantle has received much attention [*Christensen and Yuen*, 1985; *Liu et al.*, 1991; *Zhao et al.*, 1992;

Machetel and Weber, 1991; *Peltier and Solheim*, 1992], and has profound implications for the Earth's thermal and chemical structure and evolution [*Wyllie*, 1988]. Early two-dimensional numerical modeling [*Christensen and Yuen*, 1985] seemed to show that an unrealistically large Clapeyron slope of -6 MPa K^{-1} would be required for layering to occur. Recent work in two-dimensional Cartesian [*Liu et al.*, 1991; *Zhao et al.*, 1992; *Weinstein*, 1993] and spherical axisymmetric [*Machetel and Weber*, 1991; *Peltier and Solheim*, 1992] geometries with realistic phase-change parameters has, however, indicated significant layering, as well as complex new phenomena and modes of time-dependence in the flow.

To understand the Earth it is essential to determine how the effects observed in these two-dimensional studies are modified in three-dimensional geometry. Here we present results from a numerical simulation of fully three-dimensional compressible mantle convection in a spherical shell with an endothermic phase change at 670 km depth. The spatial resolution and Rayleigh number are much higher than in previous spherical models with no phase change [*Bercovici et al.*, 1989a,b,c; *Glatzmaier et al.*, 1990; *Schubert et al.*, 1990]. Although there are some similarities with the two-dimensional results, the simulated flow pattern is inherently three-dimensional, with features that penetrate the phase change being exclusively cylindrical in form. The upper mantle is characterized by interconnected linear downwellings which do not penetrate. At the intersections of these downwelling sheets, cold material accumulates above 670 km depth, building up until huge catastrophic breakthroughs [*Christensen and Yuen*, 1985; *Machetel and Weber*, 1991; *Peltier and Solheim*, 1992] into the lower mantle are precipitated, flushing the local upper mantle contents through broad cylindrical downwellings to the core-mantle boundary (CMB). These events occur in a globally asynchronous manner, with typically three to four in progress at any particular time. This process generates large amplitude long-wavelength lateral heterogeneity, which may go some way towards reconciling observations of long-wavelength dominance from seismic tomography [*Nakanishi and Anderson*, 1983;

Tanimoto, 1990a&b; *Su and Dziewonski*, 1991, 1992; *Su et al.*, 1992b] with the much broader spectrum predicted by high Rayleigh number convection simulations [*Jarvis and Peltier*, 1989; *Glatzmaier*, 1988].

The behavior of downwellings is similar to that observed in a completely basally heated three-dimensional Cartesian layer with two phase changes [*Honda et al.*, 1993]. However, we find that the use of spherical geometry and realistic internal heating greatly modifies the heat flow characteristics, geometry of lower-mantle flow, upwelling plume structure, and global time-dependence as well as facilitating direct comparison with seismic tomography.

Model Characteristics

Our model incorporates the effect of the endothermic spinel to perovskite plus magnesiowüstite transition occurring at ~670 km depth, consistent with a peridotitic mantle composition [*Ito and Takahashi*, 1989]. Some authors have included additional phase changes in their models [*Liu et al.*, 1991; *Zhao et al.*, 1992; *Peltier and Solheim*, 1992; *Honda et al.*, 1993; *Weinstein*, 1993]. These slightly alter the propensity toward layering and cause some other second-order effects, but considering the other approximations and uncertainties in current mantle modeling we choose to restrict these calculations to an examination of the first-order effect due to the endothermic phase change at 670 km depth. Our preliminary modeling results with the 400 km phase change added display little qualitative difference in behavior.

The equations of compressible self-gravitating flow are solved and integrated in time using a spectral-transform method [*Glatzmaier*, 1988], implemented on the Intel Touchstone Delta parallel supercomputer system at the California Institute of Technology. As the mantle is characterized by very high Prandtl number, inertial terms are ignored. The anelastic approximation is used, eliminating acoustic waves which propagate many orders

of magnitude faster than convective velocities. Entropy, pressure, gravitational potential and poloidal mass flux potential are expanded laterally in spherical harmonics, up to degree and order 127, and the nonlinear products associated with advection and viscous dissipation are evaluated in grid space using 384 longitudinal points by 192 latitudinal points. Variables are expanded vertically in separate Chebyshev series for the upper and lower mantles, with 33 radial levels in the lower mantle and 17 radial levels in the upper mantle. Use of two Chebyshev expansions matched at 670 km depth gives excellent vertical resolution at the core-mantle boundary (CMB), 670 km depth and the surface, where it is most needed. The fields are adequately resolved since the horizontal and vertical variances of variables fall by many orders of magnitude between maximum values and truncation [*Glatzmaier*, 1988; *Bercovici et al.*, 1989a; *Glatzmaier et al.*, 1990; *Schubert et al.*, 1990].

As the phase boundary deflection observed in the Earth [*Shearer and Masters*, 1992] is at least an order of magnitude smaller than the characteristic size of convective features in our model, it is not necessary (to a good approximation) to resolve the exact details of the phase change. Thus, deflection of the phase change resulting from lateral temperature variations at 670 km depth is represented as a sheet mass anomaly at this depth, resulting in discontinuous normal stress between the two Chebyshev regimes. This approach has the advantage of a phase loop (the pressure or depth interval over which the multivariant phase change occurs) of zero-width, important because the phase loop width significantly affects the inhibition of flow across the boundary [*Peltier and Solheim*, 1992], and recent experiments [*Ito and Takahashi*, 1989] constrain this width to be a few kilometers at most. For numerical reasons, the latent heat release (absorption) that accompanies upward (downward) motion through the phase change must be spread out 25 km on either side of the interface. This treatment of the phase change has been validated by computing two-dimensional Cartesian and spherical axisymmetric results and comparing to previously published results [*Christensen and Yuen*, 1985; *Machetel and Weber*, 1991].

Parameters

Entropy, pressure and gravitational potential are expanded as perturbations relative to a self-gravitating adiabatic reference state. The Murnaghan equation is assumed, leading to a polytrope [*Glatzmaier*, 1988] (i.e., $P \propto [\rho^{1+1/n} - \rho_0^{1+1/n}]$, where n is the polytropic index). A constant Gruneisen parameter of 1.0 and polytropic index of 0.5 gives a reasonable fit to the Earth model PREM [*Dziewonski and Anderson*, 1981]. Implicit in this treatment is the depth-dependence of material properties such as density, bulk modulus and thermal expansivity, with the latter varying from 3.0×10^{-5} at the surface to 2.2×10^{-5} at 670 km depth and 1.2×10^{-5} at the CMB. Heat capacity is assumed constant at 1250 J $kg^{-1}K^{-1}$. Thermal conductivity and viscosity are specified as functions of depth only, with dynamic viscosity increasing roughly exponentially from 1.7×10^{22} Pa s at the surface to 1.9×10^{22} Pa s at 670 km depth and 2.1×10^{23} Pa s at the CMB. Thermal conductivity is 2.3 $Wm^{-1}K^{-1}$ at the surface, increasing with depth as the fourth power of density, giving a lower mantle increase consistent with experiments [*Osako and Ito*, 1991] and theory [*Anderson*, 1987]. The boundary conditions at the surface and CMB are stress-free and isothermal, with the temperatures at the CMB and surface fixed at 3450 K and 1060 K respectively. Of the total temperature drop across the mantle, 1250 K is superadiabatic and 1140 K is due to adiabatic compression. The unrealistically high surface temperature is a consequence of treating the viscosity as a function of depth only rather than a function of temperature, so rheologically stiff plates are not produced. However, absolute temperatures in such a calculation are not meaningful except to the extent that they are adjusted to be realistic at some level (for example, the upper mantle); only temperature differences are relevant to the convective style and vigor.

Because the ratio of internal heating to basal heating strongly affects the degree of layering in two-dimensional models [*Solheim and Peltier*, 1994], it is important to match

the internal heating rate and core heat flux of the Earth as closely as possible. We therefore use an internal heating rate of 2.75×10^{-12} W kg^{-1}, compatible with chondritic values. The volume-averaged Rayleigh numbers resulting from internal heating and superadiabaticity [*Schubert et al.*, 1990] are 1.8×10^{7} and 1.2×10^{6} respectively, an order of magnitude higher than in previous studies [*Glatzmaier et al.*, 1990], but almost an order of magnitude less than those characterizing the Earth. Realistic Rayleigh numbers are obtainable in two-dimensional calculations [*Liu et al.*, 1991; *Zhao et al.*, 1992; *Peltier and Solheim*, 1992], which are useful for predicting how the effects observed here might scale to the Earth-like regime.

We take the value of the Clapeyron slope to be -4 MPa K^{-1}, the preferred value from recent experimental results [*Ito et al.*, 1990], though at the high end of the range from previous experiments [*Ito and Takahashi*, 1989]. We choose a high value in order to determine and characterize the maximum effect that the phase change could have on the flow. Although this value has been observed to cause very strong layering in one axisymmetric result [*Machetel and Weber*, 1991], the inhibiting effect of the phase change in that simulation was greatly enhanced by the use of a much lower thermal expansivity at 670 km depth than is consistent with experimental and theoretical estimates [*Anderson et al.*, 1992], and the imposed two-dimensionality.

The simulation was started from a case with no phase change and run for about 15,000 timesteps, corresponding to about 3 billion years; the results we present here are characteristic of the last 9000 timesteps, after the system has overcome the initial transient adjustment to the presence of the phase change.

Observables

We obtain a mean surface heat flow of 2×10^{13} W, of which ~40% comes from the core. The total is similar to that of the Earth, but the basal heatflow is considerably larger

than most estimates for the Earth [*Schubert*, 1979; *Schubert et al.*, 1980; *Davies and Richards*, 1992]. Even so, it drives very little plume activity, as discussed below. It is possible that the mantle heating rate should be substantially augmented by the effect of secular cooling [*Sharpe and Peltier*, 1978; *Schubert*, 1979; *Schubert et al.*, 1980] which is missing from the model because the heating is treated as time-independent, but this is an issue for the future.

Maximum convective velocities are around 40 mm yr^{-1} and average surface velocities typically 6 mm yr^{-1}, an order of magnitude lower than plate velocities, although a direct comparison may be flawed because our simulation lacks rigid plates. The principal difference between our parameters and the Earth probably lies in the use of higher than realistic viscosities, which is necessitated by computing limitations. At the higher Rayleigh number which would result from lower viscosities, the phase change has a stronger inhibitive effect on the flow [*Christensen and Yuen*, 1985; *Zhao et al.*, 1992]; thus our calculation may underpredict the degree of layering which would occur in the Earth-like regime.

Flow pattern

In Fig. 2.1, which illustrates cold features for the final frame of the calculation, a network of interconnected cold downwelling sheets, which do not penetrate the phase change, is observed in the upper mantle. The distance between sheets that are roughly parallel is typically 3000-8000 km, a scale which is consistent with present subduction zones in some regions of the Earth. They have some small-scale complexity due to local boundary-layer instabilities, which would probably be suppressed by the high-viscosity lithospheric plates on the Earth. At the intersections of these sheets, large pools of cold material form above the 670 km phase change. This cold material is gravitationally unstable and after building up sufficiently triggers a sudden avalanche into the lower mantle, in the

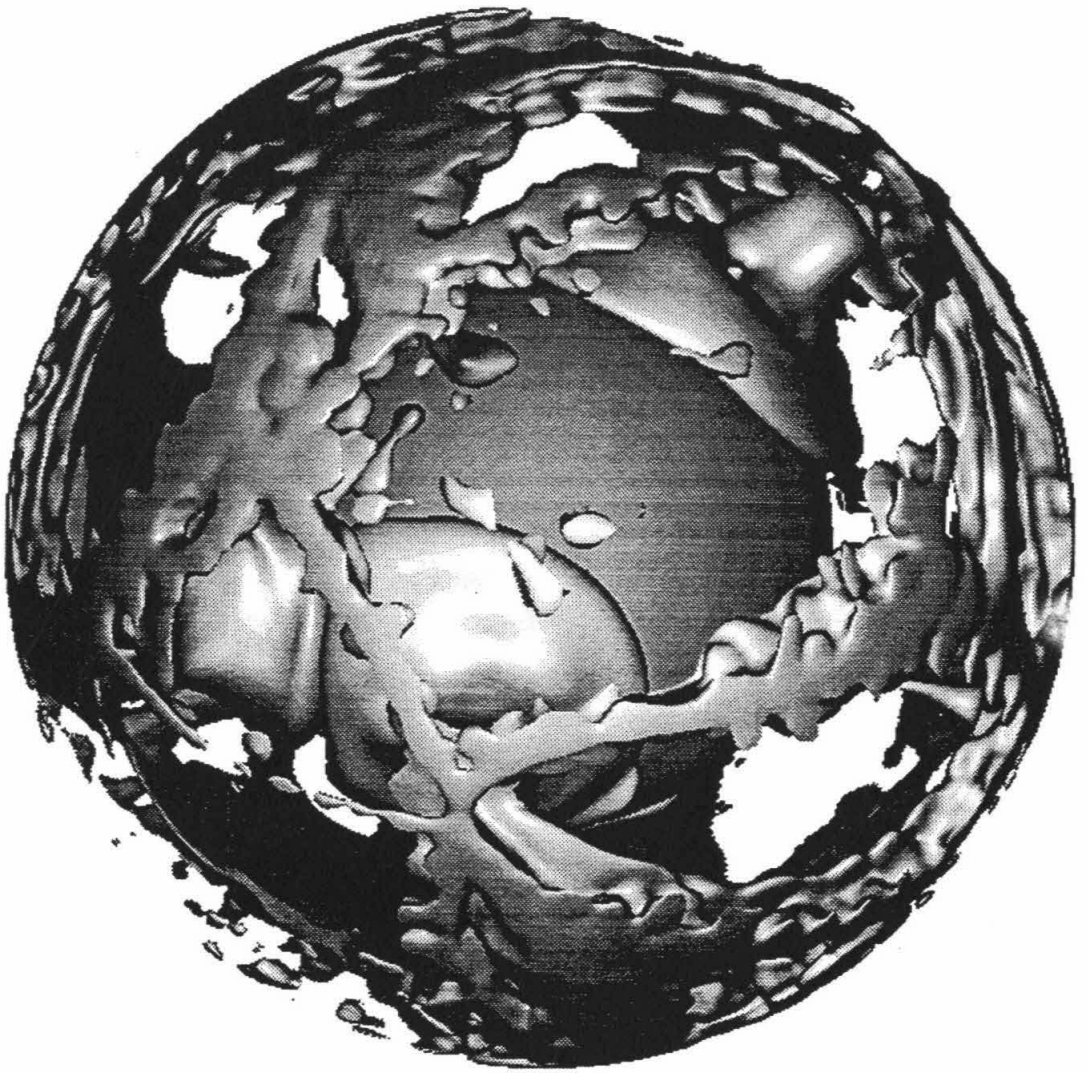

FIG.2.1 Cold downwellings for final frame of simulation. Blue surface is an isocontour showing where the temperature is 110 K lower than the horizontally averaged value. Green surface is the core. A network of interconnected linear downwellings is visible in the upper mantle, with three huge cylindrical downwellings in the lower mantle, spreading out into pools of cold material above the core-mantle boundary.

FIG.2.2 Hot upwellings for final frame of simulation. Red surface is an isocontour of superadiabatic temperature, showing where the temperature is 110 K higher than the reference state adiabat. A single plume from the core-mantle boundary feeds a hot region in the upper mantle. However, most broad hot regions in the upper mantle are not directly linked to lower mantle structures.

form of a very large diameter (~1000km) cylindrical downwelling plume. This downwelling acts as a conduit to the CMB, effectively emptying the cold material from the local upper mantle to a large pool at the base of the mantle, despite the increase in viscosity with depth. The downwelling then shuts off completely and is not observed to recur in exactly the same place during the course of the simulation, though many such events may occur in the same general area, and a total of about 15 events are observed during this part of the simulation. Thus, these events cool all areas of the lower mantle and core. At any one time, several of these flushing events are in progress at different places around the sphere, triggering in a globally asynchronous manner. Owing to the spherical geometry, the surface area of the CMB is about 35% of the surface area of the 670 km interface, and thus the combined effect of flushing events occurring in different places around the sphere is to surround the core with cold material, resulting in a heat flow (40% of surface heat flow) considerably higher than most estimates for the Earth [*Sharpe and Peltier*, 1978; *Schubert*, 1979; *Schubert et al.*, 1980; *Davies and Richards*, 1992], but with very little upwelling plume activity.

Figure 2.2 shows the corresponding hot, upwelling regions for the final frame. The most prominent features are the broad hot regions in the upper mantle, which are generally not associated with any deep features in the lower mantle. The lateral heterogeneity is much greater in the upper mantle than in the lower mantle, as shown quantitatively later on. At the CMB, ridges of hot material are observed. These are swept around by the enormous injections of cold upper mantle material caused by flushing events, and occasionally a short-lived, transient plume is formed at the intersection of these ridges, rising to the 670 km interface and injecting hot material into the upper mantle. One of these can be observed in Fig. 2.2. Thus, in both directions, cylindrical forms (plumes) are seen to penetrate the 670 km phase change, whereas linear forms (sheets) do not. The upward flow in the upper mantle and in the top of the lower mantle is generally the weak, distributed return flow

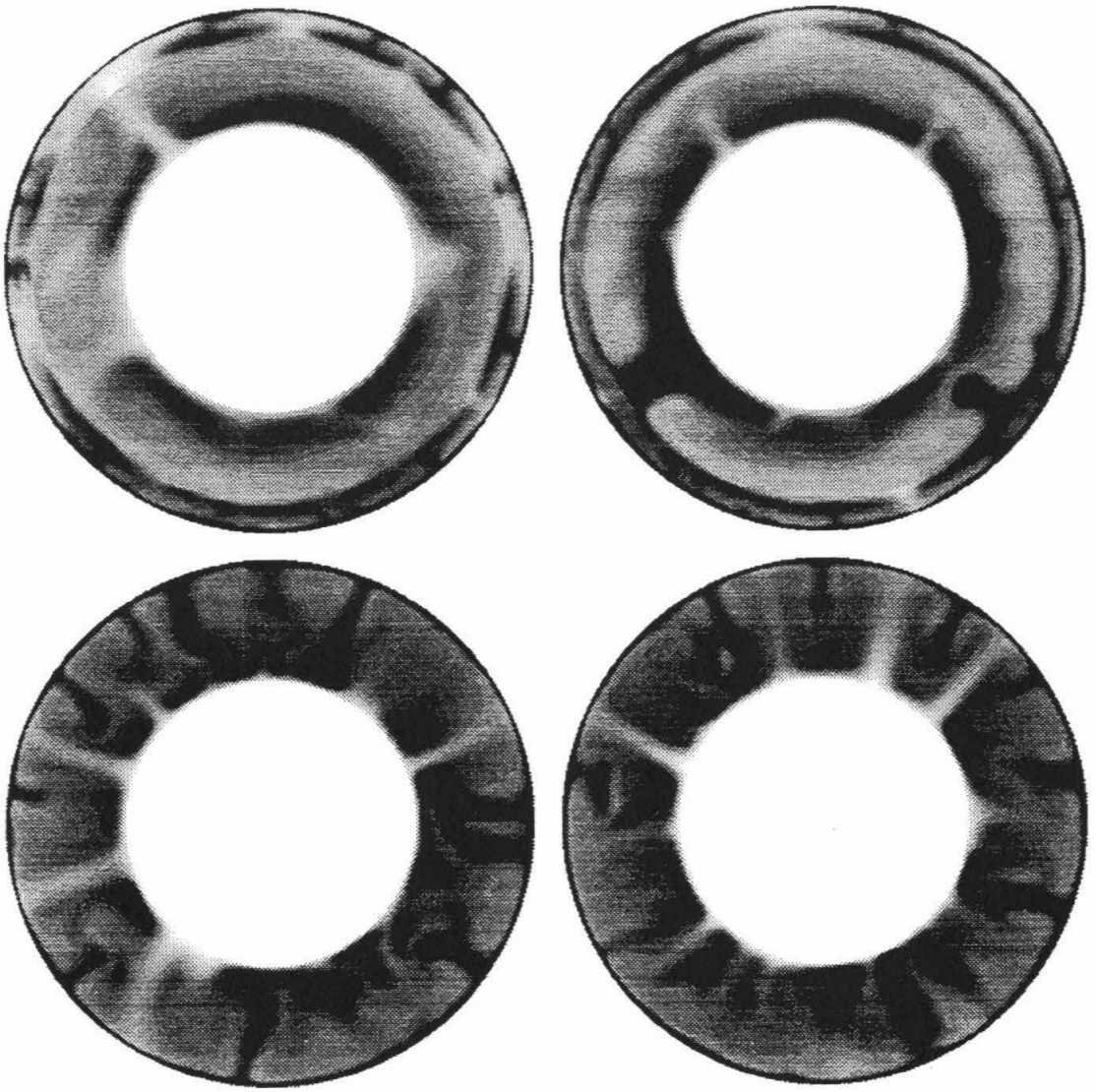

FIG.2.3 Superadiabatic temperature field on different cross-sectional slices. a&b (top row), The final frame of the phase change simulation. Scale ranges from -1050K to +350K. c&d (bottom row) , A typical case with no phase change. This case is representative of mainly internally-heated whole-mantle models [*Houseman*, 1988; *Bercovici et al.*, 1989b; *Glatzmaier et al.*, 1990; *Schubert et al.*, 1990; *Travis et al.*, 1990c], and has Rayleigh numbers for internal and basal heating of 1.4×10^7 and 5.5×10^5 respectively, a factor ten viscosity increase with depth, and a basal heat flow of ~16% of the surface heat flow. Scale ranges from -780K to +220K.

characterizing mainly internally heated convection [*Houseman*, 1988; *Bercovici et al.*, 1989b; *Glatzmaier et al.*, 1990; *Schubert et al.*, 1990; *Travis et al.*, 1990c].

The radial dependence of the flow structure is clearly visible in Fig. 2.3a and b, which shows the superadiabatic temperature field in two cross-sectional slices for the final frame of the simulation. The upper mantle is extremely heterogeneous on long wavelengths, containing some broad (up to ~10,000 km) regions of anomalously cold or hot material, as well as regions with the classical small aspect-ratio convection cells [*Christensen and Yuen*, 1988; *Busse*, 1989]. In the lower mantle two large cylindrical downwellings are visible (Fig. 2.3b), and a thick layer of cold material surrounds the core. One broad upwelling plume from the CMB (Fig. 2.3a) penetrates the 670 km phase change and injects hot material into the upper mantle, but this is the only such feature in the whole lower mantle. The inclusion of realistic temperature-dependent viscosity would result in a low viscosity layer immediately above the CMB because of the thermal boundary layer, which may result in more upwelling plumes. The lack of strong plume activity in our model is not, however, of concern since on the Earth plumes are merely secondary features, carrying only 10-15% of the total heat flux [*Davies and Richards*, 1992].

The ability of the cold downwelling lower mantle plumes to reach the CMB, despite the increasing viscosity and decreasing thermal expansivity with depth, is in marked contrast to a similar case with no phase change illustrated in Fig. 2.3c and d, in which the somewhat smaller downwellings slow down and broaden in the lower half of the mantle, allowing the formation of many upwelling plumes, despite the low basal heat flux. It is possible that a larger viscosity increase with depth, as favored by some researchers [*Davies and Richards*, 1992], may slow down the giant drips observed in the phase-change case. However, they are such large features, with a large reservoir of feeding material, that it seems unlikely they will be prevented from reaching the CMB.

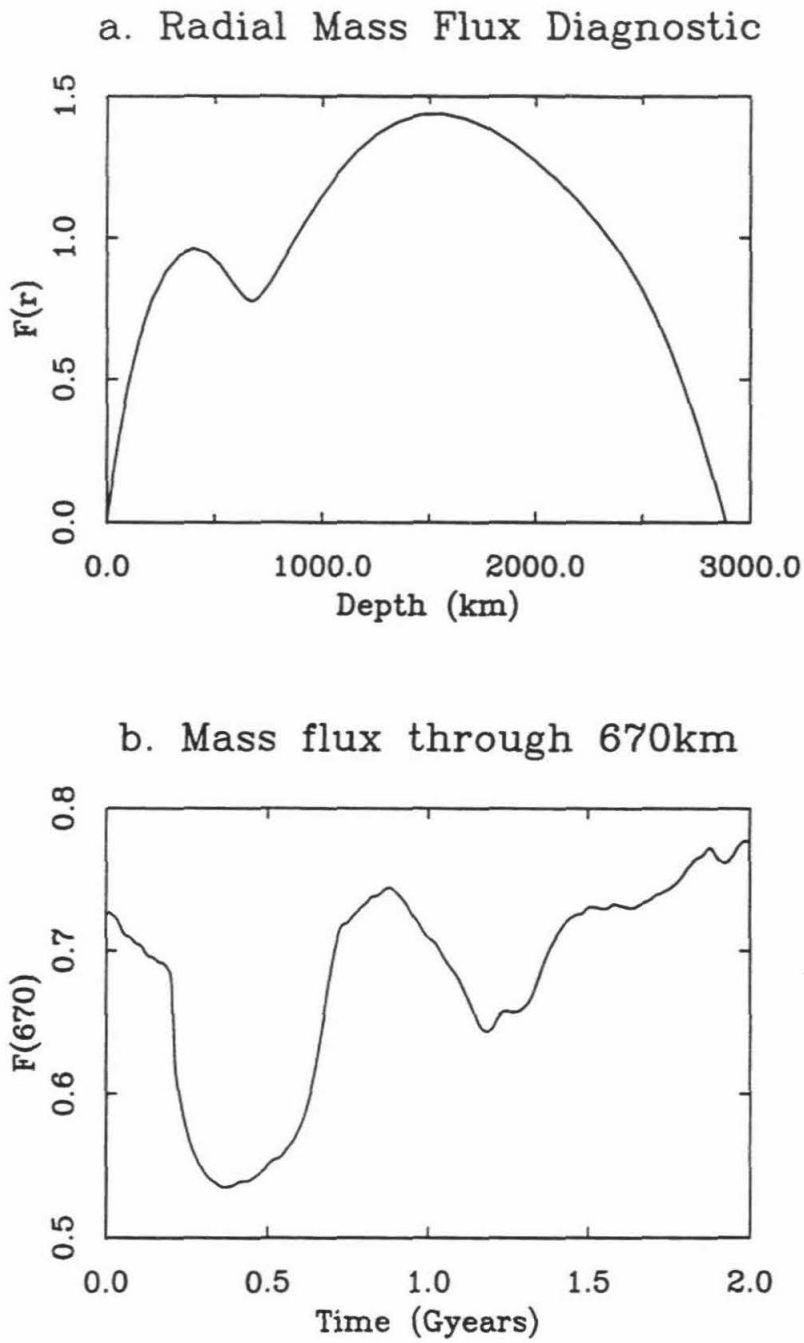

FIG. 2.4 a, Radial mass flux diagnostic F(r) for the final frame of simulation. b, Time series of F(670) for the last 9000 timesteps (2 Gyr). F(r), defined in *Peltier and Solheim*, [1992], is the spherically-averaged modulus of radial mass flux, normalized so that the integral over nondimensional depth is unity.

Radial mass flux

A useful indicator is the radial mass flux diagnostic [*Peltier and Solheim*, 1992], defined as the spherically-averaged absolute radial mass flux, normalized so that the integral over nondimensional depth is unity. This diagnostic for the final frame is shown in Fig. 2.4, together with the time-series of mass flux through the 670 km discontinuity for the last 9000 timesteps (~2 Gyr) of the simulation. The phase change is observed to have a marked inhibitive effect on the flow, indicated by the minimum in the radial mass flux at 670 km. Examination of this diagnostic for individual spherical harmonic degrees indicates that long wavelengths of flow are virtually unaffected by the phase change, whereas short wavelengths are increasingly inhibited; for spherical harmonic degrees above ~40, flow is effectively confined to the upper mantle.

From the radial mass flux across the interface at 670 km depth it is possible to calculate a 'mixing time', defined as the time required for a mass equal to the mass of the mantle to pass through 670 km. For this case the time is 4.5 Gyr. To scale to the Earth's Rayleigh number (Ra), it is likely that the mass flux (of downwelling cold material) scales roughly as the heat flux, suggesting a $Ra^{1/3}$ scaling [*Turcotte and Schubert,* 1982] which would reduce the mixing time to ~2.1 Gyr for an order of magnitude increase in Ra. This is less than half the age of the Earth, but the increased effect of the phase change at higher Ra [*Christensen and Yuen*, 1985; *Zhao et al.*, 1992] may increase this time.

There is some time-dependence of the flow through the phase change at 670 km depth, with the mass flux diagnostic at 670 km depth (F(670)) varying between 0.5 and 0.8 during this simulation. However, this time-dependence is much weaker than that observed in two-dimensional axisymmetric [*Machetel and Weber*, 1991; *Peltier and Solheim,* 1992] or Cartesian [*Weinstein*, 1993] geometries, because due to the large effective aspect ratio in our 3-D spherical simulation, several flushing events are typically occurring at any given time, so the convection is never strongly layered on a global scale.

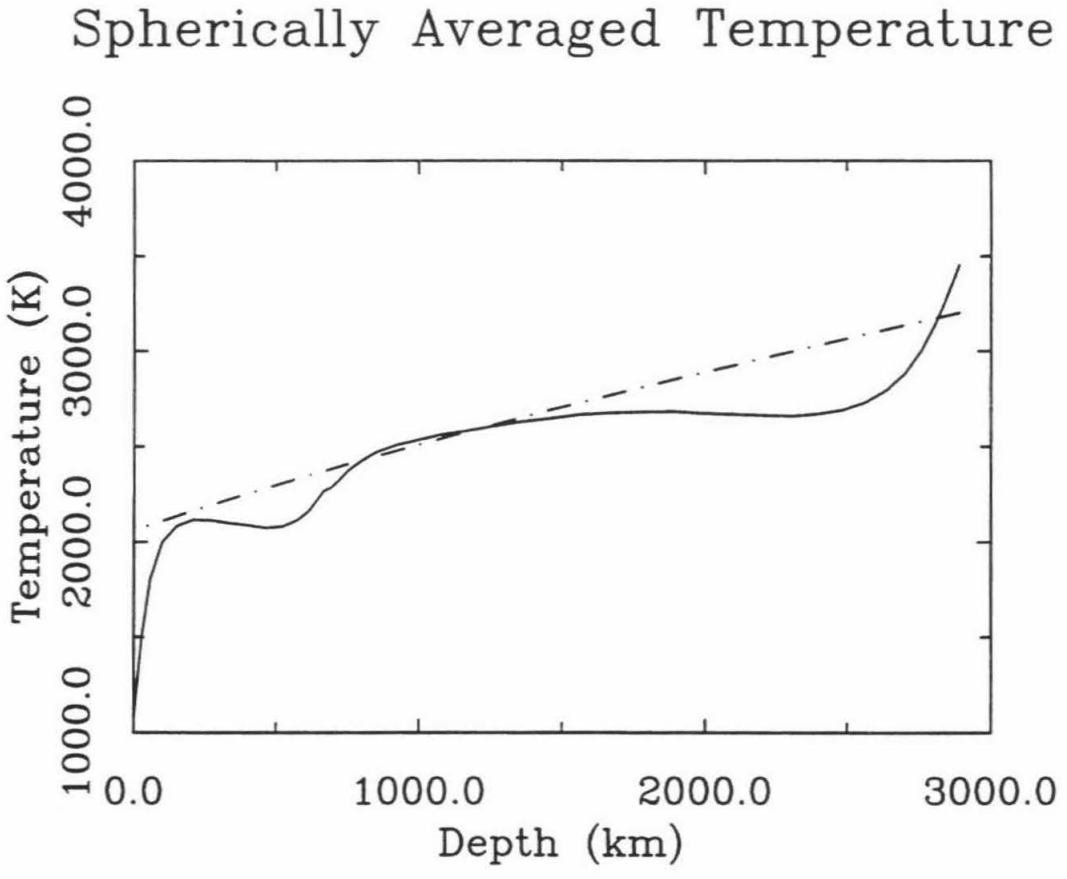

FIG.2.5. Radial profile of spherically-averaged temperature for final frame (solid line). Reference state adiabat is shown as dashed line.

As a result, globally averaged diagnostics such as F(670), mean temperature, and so on are not greatly affected by an individual flushing event. Given the observed preference for penetration in cylindrical rather than linear forms, it is also possible that in two-dimensional geometry, where up/downwellings are restricted to being linear, cold material builds up to a greater extent before it can be flushed into the lower mantle, and thus these events are more violent. It is possible that our flushing events would be more abrupt and violent if we could decrease the viscosity to Earth-like values, as observed in two-dimensional models [*Weinstein*, 1993; *Solheim and Peltier*, 1994]. However, we believe that with an Earth-like viscosity, flushing events would still overlap in time, and the global time-dependence would be intrinsically weaker in full three-dimensional spherical geometry than in spherical axisymmetric or two-dimensional Cartesian geometries.

Spherically-averaged temperature

The horizontally-averaged (l=0) temperature field is shown in Fig. 2.5. A temperature drop of several hundred degrees occurs around 670 km depth. In addition a small kink is observed at 670 km, due to the release or absorption of latent heat by material advected across the phase change. The net thermal gradient at 670 km depth is low, and thus the conductive heat flow across the 670 km interface is only ~10% of the surface heat flow, with most of the heat flux across 670 km depth being advected. On local scales, much steeper temperature gradients are observed in regions far from cylindrical downwellings and most of the radial heat flux may be conductive.

Lateral heterogeneity and seismic tomography

The effects of the phase change on the horizontal spectrum of density anomalies and

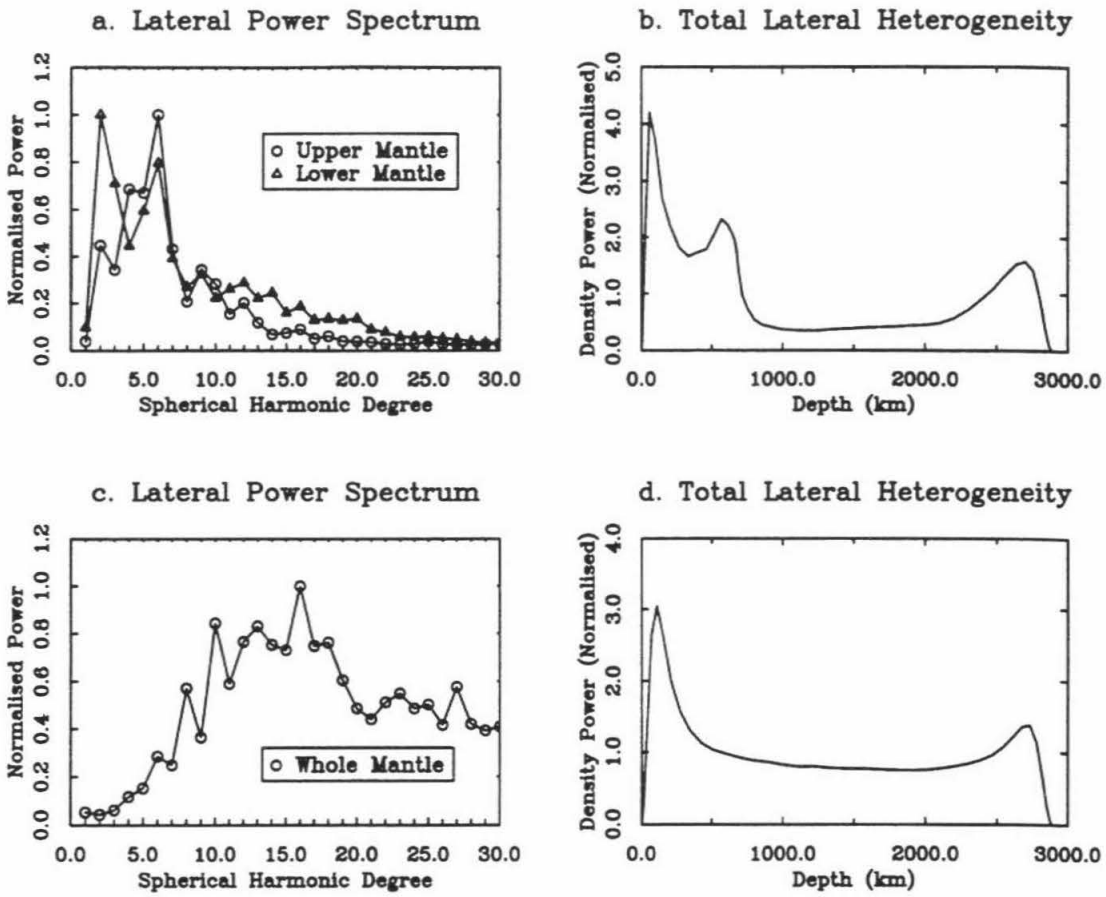

FIG.2.6 a, Power in each spherical harmonic degree, vertically averaged through upper and lower mantles, for the final frame. The lateral power spectrum has similarities with that observed by *Inoue et al.* [1990] using seismic tomography (plotted in *Su and Dziewonski*, [1991] Fig.2.5) b, Radial profile of total lateral heterogeneity (in density). A peak is observed at 670 km depth, as with two-dimensional results [*Peltier and Solheim,* 1992]. c, Power in each spherical harmonic degree, vertically averaged through the whole mantle, for the case with no phase change (illustrated in Fig. 2.3c&d). d, as b for the case with no phase change.

the depth-dependence of total power [*Peltier and Solheim*, 1992] is pronounced, resulting in a dominance of long-wavelength power in the upper mantle and base of the lower mantle, and a concentration of total power in the same areas (Fig. 2.6a and b), compatible with seismic tomography [*Su and Dziewonski*, 1991, 1992]. In the upper mantle the dominant frequencies are spherical harmonic degrees ℓ=2-7, with a peak at ℓ=6, while in the deepest ~400km of the lower mantle, ℓ=2 and 3 dominate, with a secondary peak at ℓ=5-6. This is very different from the illustrated result with no phase change (Fig. 2.6c and d), in which a broad peak is observed in the range ℓ=8-20; and also with a published basally-heated model at $Ra=10^6$ [Fig. 1 in *Glatzmaier*, 1988] which peaks at ℓ=10. Indeed, the lateral spectrum is fairly consistent with the observations of long-wavelength dominance from seismic tomography [*Nakanishi and Anderson*, 1983; *Tanimoto*, 1990a&b; *Su and Dziewonski*, 1991, 1992; *Inoue et al.*, 1990], particularly that of *Inoue et al.* (plotted in *Su and Dziewonski* [1991, 1992]). The flow lacks the dominant ℓ=2 component found in some seismic models [*Nakanishi and Anderson*, 1983; *Tanimoto*, 1990a&b]; this is probably due to the absence of tectonic plates and continents, as discussed later. The asymptotic fall off in power with spherical harmonic degree varies with depth, but is roughly proportional to ℓ^{-2}.

Even when filtered to seismic tomographic resolution (e.g., ℓ=10, Chebyshev degree n=13), the effect of the phase change is still clearly discernible, both in the entropy field and in radial correlations between layers [*Jordan et al.*, 1993]. However, all plume-like upwellings on the lower mantle disappear completely. The strongest of the broad cylindrical downwellings are visible as smeared out cold anomalies, and thus may be discernible in tomographic models. The peak in the radial heterogeneity profile (Fig. 2.6b) is still visible at n=13, but disappears at n=6. Although the lateral heterogeneity spectrum exhibits a dominance at long wavelengths, it is necessary to expand to at least ℓ~31 in order to see all the main features.

Slab penetration

The issue of whether subducting lithospheric slabs penetrate the lower mantle, or are deflected by the 670 km discontinuity, has received much attention [*Christensen and Yuen*, 1984; *Creager and Jordan*, 1986; *Vidale and Garcia-Gonzales*, 1988; *Zhou and Anderson*, 1989; *Zhou and Clayton*, 1990; *van der Hilst et al.*, 1991; *Fukao et al.*, 1992] and is central to the question of mantle layering. The closest analogues to slabs in our model are the linear downwellings in the upper mantle, and thus our model results suggest that slabs do not immediately penetrate, but instead build up in the transition zone until sufficient cold mass has accumulated to precipitate an avalanche into the lower mantle [*Solheim and Peltier*, 1994]. This picture would be consistent with (1) strong correlations between past locations of subduction and seismically fast ('cold') regions at the base of the upper mantle and top of the lower mantle [*Scrivner and Anderson*, 1992], (2) recent tomography of slabs [*Zhou and Clayton*, 1990; *van der Hilst et al.*, 1991; *Fukao et al.*, 1992] showing that at least in some areas slabs flatten out along the 670 km discontinuity and appear to stagnate in the transition zone, (3) recent global tomography [*Su et al.*, 1992b] showing broad seismically fast areas at 600 km depth in places where subducted slabs would be expected to accumulate, and (4) global mapping of topography on the 670 km discontinuity [*Shearer and Masters*, 1992] favoring models in which subducting slabs are deflected horizontally at the discontinuity.

Differences from the Earth?

Although our model does not include the effects of variable viscosity, tectonic plates or continents, many of the major characteristics of the Earth are reproduced, such as the predominance of linear downwellings in the upper mantle (analagous to slabs except for their symmetric nature), wavelength of upper mantle features (compatible with typical plate

sizes), the secondary nature of upwelling plumes, and the similarity of lateral heterogeneity spectra at different depths with seismic tomographic models [*Su and Dziewonski*, 1991, 1992].

One difference is that junctions of linear downwellings, at which the large pools of cold material build up in our model, are not observed in the Earth except at the intersection of the Pacific, Philippine and Eurasia plates. This may make catastrophic breakthrough more difficult and more violent, as in two-dimensional models [*Christensen and Yuen*, 1985; *Machetel and Weber*, 1991; *Peltier and Solheim*, 1992; *Weinstein*, 1993; *Solheim and Peltier*, 1994]. In addition, the cold slab material is highly viscous and if deflected by the phase change, may have a greater tendency to stagnate in the transition zone.

The addition of rigid plates would probably reinforce the long wavelength nature of the flow [*Davies*, 1988b; *Gurnis and Zhong*, 1991]. The plate tectonic cycle, including subduction zone locations, may be controlled by the assembly and breakup of supercontinents [*Gurnis*, 1988], which would pump power into the very lowest spherical harmonic degrees [*Scrivner and Anderson*, 1992].

Chapter 3

Effects of multiple phase transitions in a 3-D spherical model of convection in the Earth's mantle

Numerical models of mantle convection that incorporate the major mantle phase changes of the transition zone reveal an inherently three-dimensional flow pattern, with cylindrical features and linear features that behave differently in their ability to penetrate the 670 km discontinuity. The dynamics are dominated by accumulation of cold linear downwellings into rounded pools above the endothermic phase change at 670 km depth, resulting in frequent 'avalanches' of upper mantle material into the lower mantle. The effect of the exothermic phase transition at 400 km depth is to reduce the overall degree of layering by pushing material through the 670 km phase change, resulting in smaller and more frequent avalanches, and a wider range of morphologies. Large quantities of avalanched cold material accumulate above the core-mantle-boundary (CMB), resulting in a region of strongly-depressed mean temperature at the base of the mantle. The 670 km phase change has a strong effect on the temperature field, with three distinct regions being visible: the upper mantle,

containing linear downwellings and pools of cold material in the transition zone, and characterized by a high-amplitude long-wavelength spectrum; the mid-mantle, containing quasi-cylindrical avalanche conduits and characterized by a low-amplitude, broad spectrum; and the deep mantle, containing large pools of cold, avalanched material and characterized by a high amplitude, ultra-red (i.e., long wavelength) spectrum. The effect on the velocity field is very different. Flow penetration across the 670 km phase change is strongly wavelength-dependent, with easy penetration at long wavelengths but strong inhibition at short wavelengths. Thus, when comparing numerical models with long-wavelength seismic tomography, diagnostics based on the density field, such as the radial correlation function, are much more sensitive to the effects of phase transitions than those based on the velocity field. The amplitude of the geoid is not significantly affected by the partial layering, because the contribution from the strong heterogeneity in the transition zone is almost perfectly balanced by the contribution from deflection of the 670 km discontinuity. Avalanches are associated with geoid lows. However, a more complex viscosity structure is required to correctly match the sign of the geoid over slabs in the Earth .

Introduction

The major seismic discontinuities at depths variously described as 400-440 km and 650-700 km bound the transition zone, and are now widely accepted as primarily representing mineralogical phase transformations [*Birch*, 1952; *Anderson*, 1967; *Ringwood*, 1982, 1991], although associated and perhaps induced chemical changes at around the same depths remain an intriguing possibility [*Anderson*, 1989; *Jeanloz*, 1991; *Ringwood*, 1991; *Weinstein*, 1992].

The lower of these transitions, associated with the phase change from γ-spinel to perovskite + magnesiowüstite at around 670 km depth, is endothermic and therefore resists

the flow of material across it [*Schubert et al.*, 1975]. The question of whether this phase transition could enforce layered convection in the Earth's mantle has received much attention, and has profound implications for the Earth's thermal and chemical structure and evolution [e.g., *Wyllie,* 1988]. Early two-dimensional (2-D) numerical modeling [*Christensen and Yuen,* 1985] indicated that an unrealistically large Clapeyron slope of -6 MPa K^{-1} would be required for layering to occur. However, recent work in two-dimensional Cartesian [*Liu et al.,* 1991; *Zhao et al.,* 1992; *Weinstein,* 1993] and spherical axisymmetric [*Machetel and Weber,* 1991; *Peltier and Solheim,* 1992] geometries with realistic phase-change parameters has indicated significant layering, as well as complex phenomena and modes of time-dependence in the flow. In particular, *Peltier and Solheim* [1992] and *Weinstein* [1993] find periods of strong layering punctuated by brief, vigorous episodes of whole-mantle flow associated with catastrophic 'avalanches', which were first noted by *Christensen and Yuen* [1985].

The additional influence exerted by the other major phase transition at around 400 km depth, associated with the phase change from olivine to ß-spinel, which is exothermic and therefore enhances the flow of material across it [*Schubert et al.*, 1975], has been included in many of these studies. *Zhao et al.* [1992] and *Steinbach and Yuen* [1992] demonstrate its effect on introducing another dynamical timescale to the system. However, the question of whether its influence increases or decreases the overall propensity to layering is unclear, since different studies show conflicting results on this issue [*Steinbach and Yuen*, 1992; *Zhao et al.*, 1992; *Solheim and Peltier*, 1994].

In order to understand the Earth, it is essential to determine how the effects observed in these two-dimensional studies are modified in three-dimensional (3-D) geometry. *Tackley et al.* [1993b] presented a simulation performed in three-dimensional spherical geometry with the endothermic phase change at 670 km depth and heat flow approximately a factor of two lower than that characteristic of the Earth, suggesting a Rayleigh number too low by almost an order of magnitude (assuming $Nu \propto Ra_T^{1/3}$ [*Turcotte and Schubert,*

1982]), and found that the avalanches, or 'flushing events' occurred exclusively in cylindrical forms, and that the time-dependence of global quantities was weak. These results were corroborated by the calculation of *Honda et al.* [1993] in a completely basally-heated Cartesian box with two phase changes present, and at a similar Rayleigh number. More recent results by *Yuen et al.* [1994] in the same geometry demonstrate the effect of higher Rayleigh number in reducing the mass flux across the 670 km discontinuity, which was previously demonstrated in 2-D by *Christensen and Yuen* [1985].

Although such 3-D calculations still lack many of the features of the real Earth, such as plates, they are progressively becoming more 'realistic', and thus it is desirable to fully understand and analyze their implications for mantle dynamics, and to devise ways of comparing them to actual observations of the Earth, such as seismic tomographic models and the geoid. By understanding and quantifying the strengths and weaknesses of current convection models in these comparisons, we can establish a reference point for future, perhaps more realistic, studies. For this purpose, the use of spherical geometry is clearly an important ingredient, as it facilitates direct comparison with Earth observations, and has previously been found to significantly modify the heat flow characteristics, geometry of lower-mantle flow, and upwelling plume structure [*Bercovici et al.,* 1989c; *Tackley et al.*, 1993b]. Thus, in this paper we extend the analysis of the result reported in *Tackley et al.* [1993b], and compare this with new simulations which contain the 400 km phase change, as well as with observations of the Earth, including seismic tomographic models. The geoid has not been considered in any of the numerical results referenced above, yet is one of the most important constraints on the internal structure and dynamics [*Kaula*, 1989]. Thus, we calculate the geoid for these cases, and characterize its amplitude spectrum and relationship to internal processes in our model. The spatial resolution and Rayleigh number of these convection models are much higher than in previous spherical models with no phase change [*Baumgardner,* 1985, 1988; *Bercovici et al.*, 1989a,b,c; *Glatzmaier et al.*, 1990; *Schubert et al.*, 1990].

Model, method and parameters

Overview

Our physical model and numerical method are modified versions of those described in *Glatzmaier* [1988]. The equations of compressible self-gravitating flow are solved and integrated in time using a spectral-transform method, implemented on the Intel Touchstone Delta parallel supercomputer system at the California Institute of Technology. Since the mantle is characterized by very high Prandtl number, inertial terms are ignored. The anelastic approximation is used, eliminating acoustic waves which propagate many orders of magnitude faster than convective velocities. The state of the system is expressed as the combination of a time-independent, radially-dependent adiabatic reference state (discussed later), and the time-dependent three-dimensional variables of poloidal mass flux potential, and perturbations to entropy, pressure, and gravitational potential fields. The time-dependent variables are expanded laterally in spherical harmonics, up to degree and order 127, and the nonlinear products associated with advection and viscous dissipation are evaluated in grid space using 384 longitudinal points by 192 latitudinal points. Variables are expanded vertically in Chebyshev series. For the cases with two phase changes, three separate expansions are used, corresponding to the lower mantle (33 radial levels), transition zone (13 radial levels), and shallow mantle (13 radial levels). For the case with a single phase change, two expansions are used with 33 lower mantle and 17 upper mantle levels, and for whole-mantle cases, a single expansion of 41 radial levels is used. Use of multiple Chebyshev expansions matched at the phase change depths gives excellent vertical resolution (~5 km) at the core-mantle boundary (CMB), phase change depths and the surface, where it is most needed. Adjacent Chebyshev expansions are matched at the internal interfaces by continuity of temperature, conductive heat flux, mass flux, tangential

velocity and tangential stress, with a discontinuity in normal stress and gravitational acceleration, as explained in the next section. External boundaries (surface and CMB) are stress-free and isothermal. The fields are adequately resolved since the horizontal and vertical variances of variables fall by many orders of magnitude between maximum values and truncation [*Glatzmaier*, 1988; *Bercovici et al.*, 1989b; *Schubert et al.*, 1990].

Phase change parameterization

Our model incorporates the effects of the exothermic olivine to ß-spinel transition occurring at around 400 km depth (hereafter referred to as the '400'), and endothermic γ-spinel to perovskite plus magnesiowüstite transition occurring at around 670 km depth (hereafter referred to as the '670'), consistent with a peridotitic mantle composition [*Ito and Takahashi*, 1989].

Since the phase boundary deflection observed in the Earth [*Shearer and Masters*, 1992] is at least an order of magnitude smaller than the characteristic size of convective features in our model, it is not necessary (to a good approximation) to resolve the exact details of the phase change. *A posteriori* justification of this assumption is provided by the actual calculated phase boundary deflections. Thus, deflection of the phase change resulting from lateral temperature variations at 400 or 670 km depth is represented as a sheet mass anomaly at that depth, resulting in discontinuous normal stress and gravitational acceleration between two adjacent Chebyshev regimes. This approach has the advantage of a zero-width phase loop (the pressure or depth interval over which the multivariant phase change occurs), important since the phase loop width significantly affects the inhibition of flow across the boundary [*Peltier and Solheim*, 1992], and recent laboratory experiments [*Ito and Takahashi*, 1989] and seismological observations [*Benz and Vidale*, 1993] constrain this width at 670 km to be a few kilometers at most. This method is equivalent to the 'effective thermal expansivity' approach [*Christensen and Yuen,* 1985], collapsed into a

discontinuity. For numerical reasons, the latent heat release (absorption) that accompanies upward (downward) motion through the phase change must be spread out 25 km on either side of the interface. Latent heat release has a very small effect on the propensity to layering, as shown by *Christensen and Yuen* [1985], thus the details of its implementation are probably not critical to the model results. This treatment of the phase change has been validated by computing two-dimensional Cartesian and spherical axisymmetric results and comparing to previously published results in which the phase boundary deflection is fully resolved [*Christensen and Yuen,* 1985; *Machetel and Weber*, 1991]. These tests confirm that this approximation is reasonable, giving the right magnitude of the effect, at the Rayleigh numbers presented here. Additional tests suggest that at higher Rayleigh numbers, where peak-to-peak phase boundary deflection is comparable to the width of convective features, both this technique and the 'effective thermal expansivity' technique may overestimate the effect of the phase changes.

Gravitational field

Although perturbations in the gravitational field have a negligible effect on the time evolution of the flow [*Glatzmaier*, 1988], we include them in order to study the geoid, which is one of the most important geophysical observables, providing clues as to processes in the interior [*Kaula*, 1989]. The net geoid is a balance between two opposite and nearly equal contributions: internal mass anomalies, and dynamic surface and CMB topography [*Ricard et al.,* 1984; *Richards and Hager*, 1984]. Since the resulting gravitational perturbation acts in such a way as to produce further surface deformation, a self-gravitational effect which is very important at long wavelengths, it is essential to calculate gravitational perturbation simultaneously with the flow field. We do this, using a first-order treatment of surface and CMB dynamic topography [*Richards and Hager*, 1984], in which the deformation is treated as a sheet mass anomaly causing a discontinuity

in vertical gradient of gravitational potential over the boundary in question. Deflection of the phase changes due to temperature perturbations are treated in a similar manner. The external and internal fields are constrained to be bounded solutions [*Glatzmaier*, 1988]. This implementation was checked by computing geoid kernels for sheet mass anomalies at various depths, and comparing to published kernels calculated using a propagator matrix technique [*Hager and Clayton*, 1989].

Reference state

Entropy, pressure, and gravitational potential are expanded as perturbations relative to a self-gravitating adiabatic reference state. The Murnaghan equation is assumed, leading to a polytrope [*Glatzmaier,* 1988] (i.e., $P \propto [\rho^{1+1/n} - \rho_0^{1+1/n}]$, where n is the polytropic index, ρ is the density and ρ_0 is the zero-pressure density). Implicit in this treatment is the depth-dependence of material properties such as density, bulk modulus and thermal expansivity, but with the Gruneisen parameter and heat capacity kept constant. Thermal conductivity and viscosity are specified as functions of depth only. Parameter values are given in Table 3.1. The parameters were chosen to give a reasonable fit to Earth model PREM [*Dziewonski and Anderson*, 1981], and were improved when the 400 km phase change was added, resulting in two different, though fairly similar, sets of parameters.

The fractional decrease of thermal expansivity over the lower mantle (about 2.1) is reasonably close to the factor of 2.5 found in recent thermodynamic analyses [*Chopelas and Boehler*, 1992; *Anderson et al.*, 1992; *Duffy and Ahrens*, 1993]. Thermal conductivity increases with depth as the fourth power of density, giving a lower mantle increase consistent with experiments [*Osako and Ito*, 1991] and theory [*Anderson*, 1987].

However, much more significant than uncertainties in the exact depth-dependencies of such thermodynamic parameters, are the uncertainties in the radial profile of viscosity, and perhaps most importantly, the assumption that the viscosity is constant horizontally.

Parameter	2-layer cases	3-layer cases	units
Gruneisen	1.0	1.0	
Poly. index n	0.5	0.4	
Heat capacity	1250	1250	$J\ kg^{-1}K^{-1}$
ρ: surface	3610	3610	$kg\ m^{-3}$
ρ: CMB	5600	5600	$kg\ m^{-3}$
α: surface	$3.0x10^{-5}$	$3.3x10^{-5}$	K^{-1}
α: 670km	$2.2x10^{-5}$	$2.3x10^{-5}$	K^{-1}
α: CMB	$1.2x10^{-5}$	$1.1x10^{-5}$	K^{-1}
η: surface	$1.7x10^{22}$	$1.8x10^{22}$*	Pa s
η: 670 km	$1.9x10^{22}$	$2.1x10^{22}$*	Pa s
η: CMB	$2.1x10^{23}$	$2.1x10^{23}$*	Pa s
k: surface	2.4	2.4	$W\ m^{-1}K^{-1}$
k: CMB	14.0	14.0	$W\ m^{-1}\ K^{-1}$
Tsurface	1060	940	K
Tcmb	3450	3150	K
ΔTsa	1250	1250	K
Qint	$2.0x10^{-12}$	$2.0x10^{-12}$	$W\ kg^{-1}$
Ra_T	$1.2x10^{6}$	$1.2x10^{6}$	
Ra_H	$1.8x10^{7}$	$1.8x10^{7}$	
$Ra_{T,surf}$	$3.5x10^{6}$	$3.7x10^{6}$	

*Case 5 has a constant kinematic viscosity of $4.7x10^{16}\ m^2\ s^{-1}$, giving a dynamic viscosity of $1.7x10^{22}$(surface) to $2.6x10^{22}$ (CMB) Pa s

TABLE 3.1: Reference State Parameters

We make the latter assumption to keep the computational task reasonable, since time-dependent 3-D simulations with strongly temperature-dependent viscosity require considerable computational resources, and are only recently becoming feasible [*Tackley*, 1993]. There is general agreement in the literature for a viscosity increase with depth across the mantle [*Hager and Richards*, 1989; *Ricard and Wuming*, 1991; *King and Masters,* 1992; *Forte et al.,* 1993; *Mitrovica and Peltier*, 1993]. However, the magnitude and exact form of this increase are highly uncertain, since there is a considerable null space associated with current datasets and inversion techniques [*King*, 1994]. For this study we arbitrarily specify a smooth, power-law dependence of viscous diffusivity on density (giving a depth profile similar to an exponential dependence on depth) with an index of zero in the upper mantle (constant viscous diffusivity) and 7 in the lower mantle, resulting in an increase of dynamic viscosity by a factor of approximately 12 over the depth of the mantle. Values of dynamic viscosity at the surface, 670 km depth and CMB are given in Table 3.1.

Thermal parameters

Surface and CMB temperatures, and internal heating rates, are also listed in Table 3.1. Since our formulation lacks rigid plates, the surface temperature is chosen to represent of the base of the lithosphere [as in *Bercovici et al.*, 1989b&c; *Glatzmaier et al.*, 1990; *Machetel and Weber*, 1991]. However, absolute temperatures in such a calculation are not meaningful except to the extent that they are adjusted to be realistic at some level (e.g., the upper mantle); only temperature differences are relevant to the convective style and vigor. Since the ratio of internal heating to basal heating strongly affects the degree of layering in two-dimensional models [*Solheim and Peltier*, 1994], it is important to obtain a ratio similar to that in the Earth. Thus, because our superadiabatic temperature drop is lower than that of the Earth, as explained above, we reduce the chondritic heating rate [*Stacey*, 1992]

proportionally in order to maintain a ratio of internal to basal heating similar to that commonly believed, although this ratio is not well known [*Leitch and Yuen*, 1989].

The volume-averaged Rayleigh numbers resulting from internal heating (Ra_H) and superadiabaticity (Ra_T), as defined below, are given in Table 3.1.

$$Ra_T = \left\langle \frac{\overline{g}(r)\overline{\alpha}(r)}{\overline{\nu}(r)\overline{\kappa}(r)} \right\rangle \Delta T_{sa} d^3$$
$$Ra_H = \left\langle \frac{\overline{g}(r)\overline{\alpha}(r)}{\overline{\nu}(r)\overline{\kappa}(r)\overline{k}(r)} \right\rangle Q d^5 \qquad (3.1)$$

where barred quantities denote radially-dependent reference state quantities thermal expansivity (α), gravitational acceleration (g), viscous diffusivity (ν), thermal diffusivity (κ) and thermal conductivity ($k=\rho c_p \kappa$). ΔT_{sa} is the superadiabatic temperature drop, Q is the internal heating rate per unit mass and d is the depth of the mantle. Table 3.1 also lists Ra_{surf}, the surface Rayleigh number used by some authors [e.g., *Honda et al.*, 1993], which is defined as Ra_T above but with the volume average being replaced by values at the surface. These Rayleigh numbers are about an order of magnitude higher than in previous spherical studies [*Glatzmaier et al.*, 1990], but almost an order of magnitude less than those characterizing the Earth. This is due to computational limitations: higher Rayleigh numbers would result in narrower features which could not be adequately resolved at the highest numerical resolution currently practical. Realistic Rayleigh numbers are obtainable in 2-D calculations [*Liu et al.*, 1991; *Zhao et al.*, 1992; *Peltier and Solheim*, 1992], and in 3-D Cartesian calculations [*Yuen et al.*, 1994], which might be useful for predicting how the effects observed here might scale to the Earth-like regime.

Phase change parameters

There has been a tendency in studies of convection with phase transitions to focus on the Clapeyron slope as the only important parameter; however, this is misleading since the effectiveness of a phase transition in inhibiting or assisting flow, due to the anomalous buoyancy associated with its vertical deflection, is given by a nondimensional combination of parameters known as the phase buoyancy parameter P [*Schubert and Turcotte*, 1971; *Christensen and Yuen*, 1985].

$$P = (\gamma\Delta\rho) / (\alpha\rho^2 gh) \qquad (3.2)$$

where γ is the Clapeyron slope, $\Delta\rho$ is the density change associated with the phase transition, α is the thermal expansivity, ρ is the background density, g is the gravitational acceleration and h is a depth scale for the convection, here taken to be the depth of the mantle. Thus, the magnitude of the density jump across the phase change and the local thermal expansivity at the phase change depth are as important as the Clapeyron slope, and all three parameters are subject to some uncertainty.

The 670 km phase transition has a density jump of 10-11% and a Clapeyron slope which is given by laboratory experiments as -2.8 MPa K^{-1} [*Ito and Takahashi*, 1989], -4±2 MPa K^{-1} [*Ito et al.*, 1990] or -3±1 MPa K^{-1} [*Akaogi and Ito*, 1993], compatible with the value of -1.7 to -4.4 MPa K^{-1} calculated by *Wicks and Richards* [1993] by combining seismic observations of '670' deflection beneath the Izu-Bonin subduction zone with a thermal model of the subducted slab. The 400 km transition has a lower density jump given as 5% in PREM [*Dziewonski and Anderson*, 1981] or 8% in recent mineralogical studies [*Akaogi et al.*, 1989; *Katsura and Ito*, 1989], and a Clapeyron slope in the range 1.5 MPa K^{-1} [*Akaogi et al.*, 1989] to 2.5 MPa K^{-1} [*Katsura and Ito*, 1989]. Thus, the magnitude of P_{400} is much smaller than the magnitude of P_{670}, since both the density jump and

Clapeyron slope are of lower magnitude, and the thermal expansivity is larger at 400 km depth than at 670 km depth [*Chopelas and Boehler*, 1992; *Anderson et al.*, 1992]. However, there is some uncertainty about the relative importance of the '400' and '670' since the phase transitions are not equidistant from all boundaries, which may affect the best choice of lengthscale 'h' in equation (2).

The latent heat release or absorption Q_L associated with a phase transition is related to the other parameters by:

$$Q_L = \gamma T \Delta\rho / \rho^2 \qquad (3.3)$$

where T is the temperature and the other symbols are defined above.

Simulation details

Five simulations are presented here, using four different sets of phase change parameters, as listed in Table 3.2, which lists the phase buoyancy parameters P_{400} and P_{670} as well as the dimensional Clapeyron slopes and density jumps. For the '670', we take the preferred values of density change and Clapeyron slope from *Ito et al.* [1990], except for Case 4, in which we test the sensitivity of the system to γ_{670} by reducing it to -3 MPa K^{-1}. In cases 1 to 3, the strength of the '400' is increased from zero to a value much larger than that likely for the mantle, in order to assess its influence on the convective system. Case 5 is as case 2 except with a constant viscous diffusivity throughout the mantle, instead of a smooth viscosity increase with depth.

Although a value of -4 MPa K^{-1} for γ_{670} has been observed to cause very strong layering in one axisymmetric result [*Machetel and Weber*, 1991], the inhibiting effect of the phase change in that simulation was greatly enhanced by the use of a very much lower thermal expansivity at 670 km depth (1.4×10^{-5} K^{-1}) than is consistent with experimental

and theoretical estimates [*Chopelas and Boehler*, 1992; *Anderson et al.*, 1992; *Duffy and Ahrens*, 1993] resulting in a very low P_{670} of around -0.22.

Case:	1	2,5	3	4	Units
γ_{400}	0	3.0	4.0	3.0	MPa K^{-1}
$\delta\rho_{400}$	0	200.0	400.0	200.0	kg m^{-3}
γ_{670}	-4.0	-4.0	-4.0	-3.0	MPa K^{-1}
$\delta\rho_{670}$	400.0	400.0	400.0	400.0	kg m^{-3}
P_{400}	0.0	0.055	0.135	0.055	
P_{670}	-0.147	-0.147	-0.147	-0.110	

TABLE 3.2: Phase Change Parameters

Case 1 was started from a case with no phase change and run for about 15,000 timesteps, corresponding to about 3 billion years; the results we present here are characteristic of the last 9000 timesteps, after the system has overcome the initial transient adjustment to the presence of the phase change. Cases 2-5 were started from final states of other runs with similar parameters, and run until the system overcame its transient adjustment to the new parameters, which typically took 5-10,000 timesteps.

Results

Heat flow and velocities

We obtain mean surface heat flows of around 1.8×10^{13} W, of which ~40% comes from the core in cases 1-4, and ~60% comes from the core in case 5. The total is about a

factor of two smaller than that of the Earth, but the fraction of basal heating is considerably larger than most estimates for the Earth [*Schubert,* 1979; *Schubert et al.*, 1980; *Davies and Richards,* 1992]. It is possible that the mantle heating rate should be substantially augmented by the effect of secular cooling [*Sharpe and Peltier*, 1978; *Schubert et al.*, 1980] which may account for 30% of the surface heat flow [*Breuer and Spohn*, 1993]. This is missing from the model because the heating is treated as time-independent; the effect is only recently receiving attention from the numerical modeling community [*Steinbach et al.,* 1993].

Maximum convective velocities are in the range 25-45 mm yr^{-1}, depending on the size and vigor of avalanches, and average surface velocities are typically 5-6 mm yr^{-1}, an order of magnitude lower than plate velocities, though a direct comparison may be flawed because our simulations lack rigid plates. The principal difference between our parameters and the Earth probably lies in the use of higher than realistic viscosities, which is necessitated by computing limitations. At the higher Rayleigh numbers which would result from lower viscosities, the phase change has a stronger inhibitive effect on both two-dimensional [*Christensen and Yuen*, 1985; *Zhao et al.,* 1992] and three-dimensional [*Yuen et al.*, 1994] flow; thus our calculation may underpredict the degree of layering which would occur in the Earth-like regime.

Flow pattern

Effect of the '670'. Figure 3.1 illustrates cold and hot features for case 1 (with only the '670' included), at three times at intervals of approximately 500 million years. The basic structure of the flow was described in *Tackley et al.* [1993b]. A network of interconnected cold downwelling sheets, which do not penetrate the phase change, is observed in the upper mantle (UM). The distance between sheets that are roughly parallel is typically 3000-8000 km, a scale which is consistent with present subduction zones on the

Earth. They have some small-scale complexity due to local boundary-layer instabilities, which would likely be suppressed by the high-viscosity lithospheric plates on the Earth. At the intersections of these sheets, large pools of cold material form above the 670 km phase change. This cold material is gravitationally unstable and after building up sufficiently triggers a vigorous avalanche into the lower mantle, in the form of a very large diameter (~1000 km) cylindrical downwelling plume, which reaches the CMB on a timescale of several 10s Ma. This downwelling acts as a conduit to the CMB, effectively emptying the cold material from the local upper mantle to a large pool at the base of the mantle, despite the increase in viscosity with depth. The increase in viscosity with depth slows these downflows and results in the region of spreading being of greater vertical extent. The downwelling then shuts off completely and is not observed to recur in exactly the same place during the course of the simulation, though many such events may occur in the same general area (such as the lower left region of these plots) and about 15 events are observed in total during the final 2 billion years of the simulation. Thus, these events cool all areas of the lower mantle and core. At any one time, several of these avalanches are in progress at different places around the sphere, triggering in a globally asynchronous manner. Because of the spherical geometry, the surface area of the CMB is about 35% of the surface area of the 670 km interface, and thus the combined effect of avalanches occurring in different places around the sphere is to surround the core with cold material, resulting in a CMB heat flow (~40% of surface heat flow) considerably higher than most estimates for the Earth, as discussed above, but with very little upwelling plume activity. Thus, most of the core heat flux is taken up in heating up these "dead slabs" rather than feeding active upwelling plumes. This may be in accord with the Earth, since *Olson et al.* [1993] conclude on the basis of numerical simulations of plumes with realistic rheology that the entire mantle plume population draws material from less than 20% of the core-mantle boundary.

In some areas, where elongated or larger pools of cold material accumulate above the '670', multiple cylindrical avalanches, closely spaced in time, may occur. This is happening in the region at the lower left of Figure 3.1.

The most prominent features in the pattern of hot upwellings are the broad hot regions in the upper mantle, which are often not directly associated with any deep features in the lower mantle. It is apparent that the lateral heterogeneity is much greater in the upper mantle than at mid-mantle depths, as shown quantitatively later on. At the CMB, interconnected ridges of hot material are observed, which extend radially upward several hundred kilometers. These are swept around by enormous injections of cold upper mantle material caused by avalanches, and occasionally a larger accumulation of hot material is formed at the intersection of these ridges, causing a short-lived, transient plume to rise through the mid-mantle to the 670 km interface and inject hot material into the upper mantle. One of these can be observed in the upper part of Figure 3.1 (lower right plot). Thus, in both directions, cylindrical forms (plumes) are seen to penetrate the 670 km phase change, whereas linear forms (sheets) do not. The upward flow in the upper mantle and in the top of the lower mantle is generally the weak, distributed return flow characterizing mainly internally heated convection [*Houseman*, 1988; *Glatzmaier et al.*, 1990; *Travis et al.*, 1990c]. It is interesting that the large hot structures in the deep mantle, which should be quite buoyant, have difficulty ascending through the mid-mantle. The reason is that although they are hot relative to the spherically-averaged temperature in the deep mantle, they are not particularly hot relative to the spherically-averaged mid-mantle temperature, because the temperature in the deep mantle is strongly depressed by the large pools of cold avalanched material.

Effect of adding the '400'. Figure 3.2 shows similar views for case 3 (with a '400' of approximately equal strength to the '670'), at three times at intervals of 500 million years. Here, the flow is more complex. Avalanches display a wider range of morphologies, including quasi-linear, and are generally smaller and more frequent. This is because the

Fig. 3.1. Cold downwellings (left) and hot upwellings (right) for Case 1 (single phase change) at three times during the simulation, at intervals of ~500 million years. Cold and hot isosurfaces show where the temperature is 110 K lower and higher respectively than the horizontal average. The core-mantle boundary is shown in green. Time increases down the page, with the lowermost figures depicting the final state of the simulation.

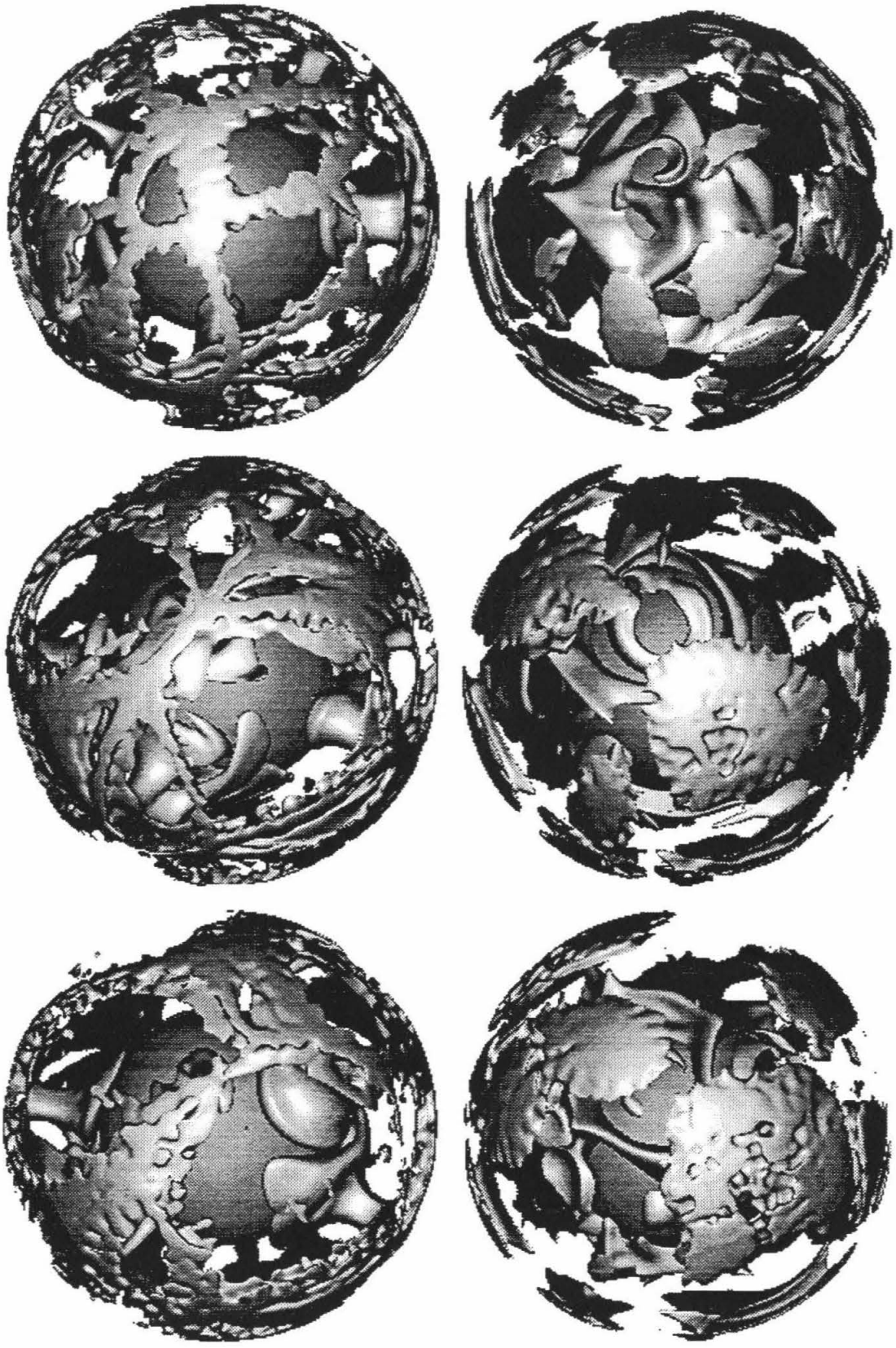

Fig. 3.2. As figure 3.1, but for case 3 (both phase changes), again at intervals of around 500 million years.

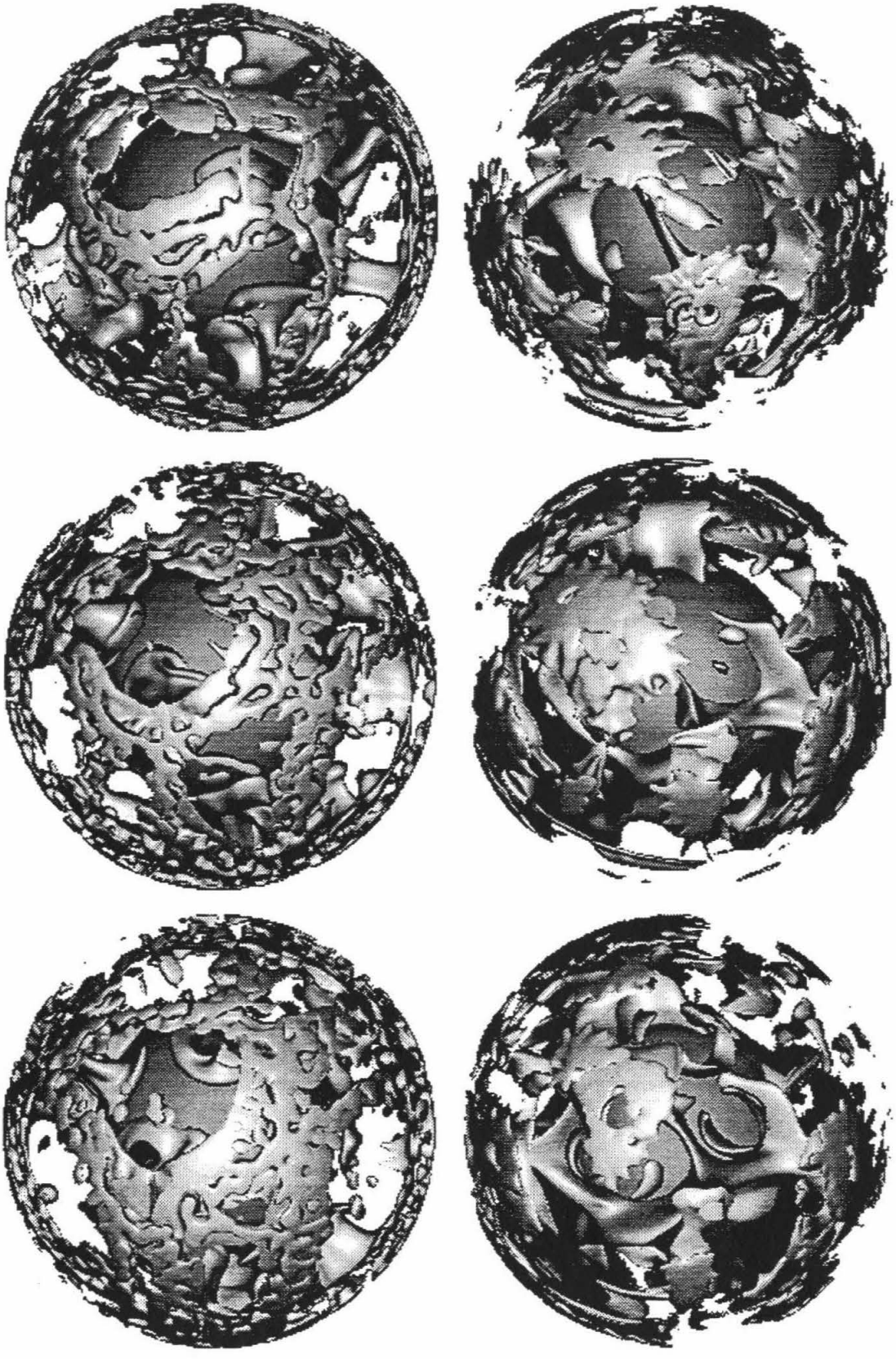

'400' limits the extent to which cold material can accumulate above the '670': when accumulations become thick enough to straddle the '400', the additional negative buoyancy caused by the upward deflection of the 400 km phase change pushes the cold material through the '670', resulting in more frequent and smaller avalanches. Thus, it appears that the effectiveness of the '670' on inhibiting mass flux between the upper and lower mantles is reduced by the '400', a point which is shown quantitatively later. A range of downflow morphologies occurs because such break-throughs may be forced before cold material is able to flow to triple junctions and accumulate into broad pools.

Several strong, stable plume-like upwellings, which penetrate the '670' with ease, are visible. These form in this case partly because the smaller avalanches are less effective in surrounding the CMB with cold material, and thus a larger fraction of the core flux is taken up in driving active upwellings, and partly because the mid-mantle region is less hot than in case 1, due to the smaller thermal boundary layer at 670 km depth, thus allowing hot plumes from the deep mantle to rise easily through this region.

There has been a tendency to regard plumes, which are postulated to cause hotspots such as Hawaii [e.g., *Sleep*, 1990; *Davies and Richards*, 1992], as a distinct, secondary mode of convection, somehow decoupled from the main, plate-scale flow [*Loper and Stacey*, 1983; *Davies and Richards*, 1992]. However, such a mode of flow has never been observed in any self-consistent numerical or laboratory experiment. Upwelling plumes always occur as part of the main, and only, convective system, as we observe in these results. However, there is a problem with obtaining hotspot-like plumes, which must simultaneously satisfy the requirements of being relatively stationary in position, and fairly weak, since hotspots are estimated to carry only 6% of the surface heat flux (excluding the plume head contribution) [*Davies and Richards*, 1992]. For example, in case 1 the plumes are weak, but short-lived and transient, whereas in case 3 the plumes are quite stationary, but much stronger than those thought to drive hotspots like Hawaii. It may be that the

solution to this problem lies in the use of realistic temperature-dependent viscosity, which we plan to incorporate in future phase change experiments [*Tackley*, 1993].

On the basis of these observations, three distinct regions of the mantle can be identified: the upper mantle (UM), characterized by linear downwellings and pools of cold material building up above '670', the mid-mantle (MM), characterized by large cylindrical downwelling plumes and weaker upwelling plumes, and the deep mantle (DM), characterized by pools of avalanched material surrounding the core and a network of interconnected hot ridges which sometimes break through the MM in the form of plumes to the UM. The UM can be further subdivided into the transition zone (TZ), in which the pools of cold material accumulate, and the shallow mantle (SM), containing narrow linear downwellings and the upper thermal boundary layer. The next section examines these distinct regions in more detail, and discusses their relationship to the surface observables, geoid and dynamic topography.

Surface observables and radial structure

Figure 3.3 shows the geoid, dynamic topography, and superadiabatic temperature field for case 1 (with only the '670'). The superadiabatic temperature field is shown on four surfaces of constant radius, corresponding to the four distinct regions discussed above: SM, TZ, MM and DM. This frame corresponds to the last frame in Figure 3.1. In the SM, the downwelling sheets are clearly visible, separated by broad hot regions. In the TZ, broad regions of cold material are visible, caused by pooling of cold material above the '670'. At MM depth, the picture is completely different, with a few broad cylindrical downwellings in a generally warm background, and a few faint upwelling plumes visible. At DM depth, broad circular cold pools corresponding to the downwellings in MM are seen, with an interconnected system of hot ridges separating them.

Fig. 3.3. Surface observables, and sections of constant radius for the final frame of Case 1. a. (top left) Geoid, with scale ±120 m. b.(top right) dynamic surface topography, scale ±5.0 km. c.(mid left), d.(mid right), e.(bottom left) and f.(bottom right) show the superadiabatic temperature field at depths 200, 550, 1200 and 2600 km respectively, representing regions SM, TZ, MM and DM. Scale ranges from -1050 to +350 K. Plots are scaled according to the radius; lines of longitude and latitude indicate the position of the surface.

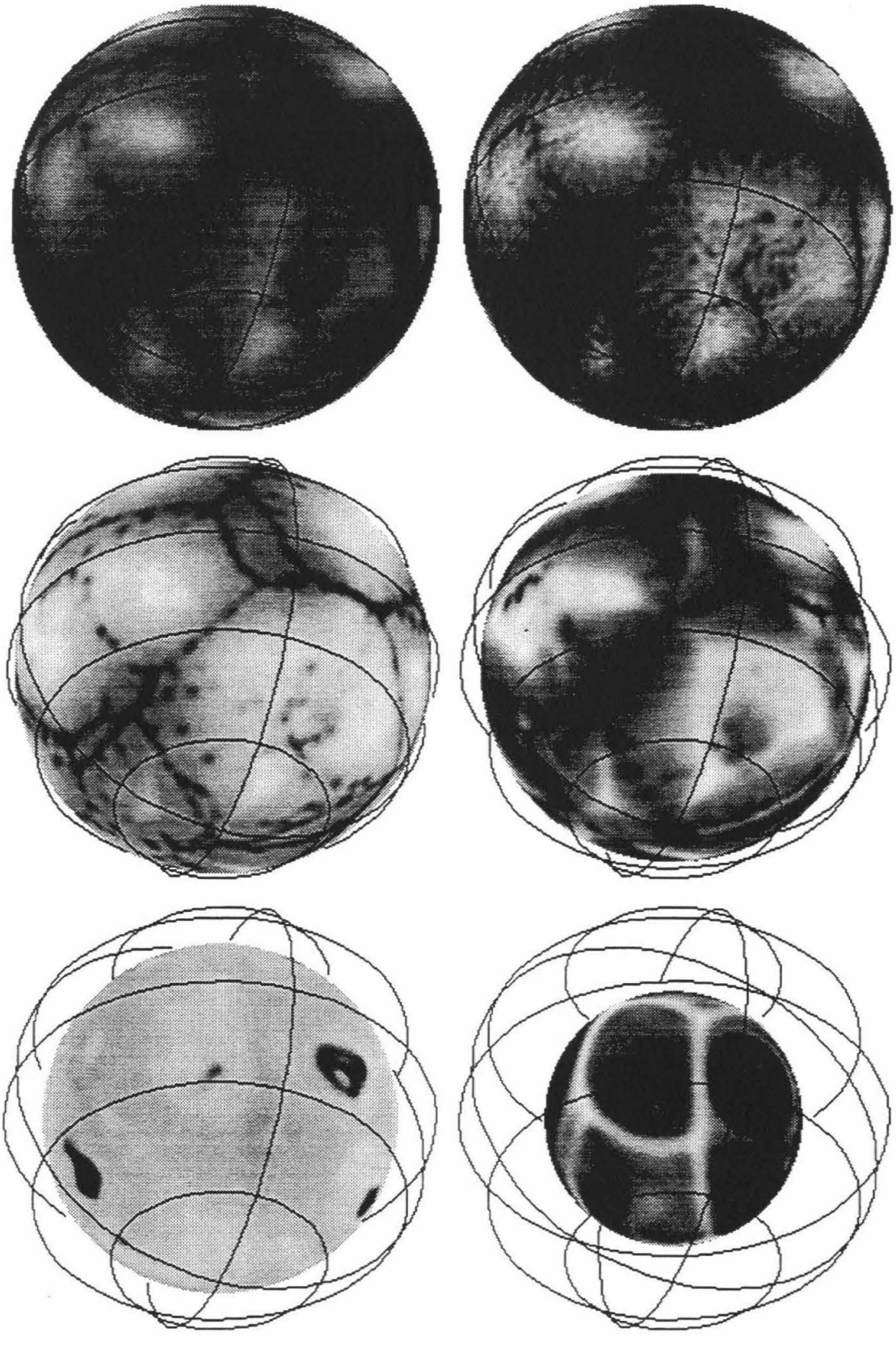

Fig. 3.4. As Figure 3.3, but for Case 3. Geoid ranges ±110 m, topography ±5.0 km, and superadiabatic temperature from -950 to +300 K.

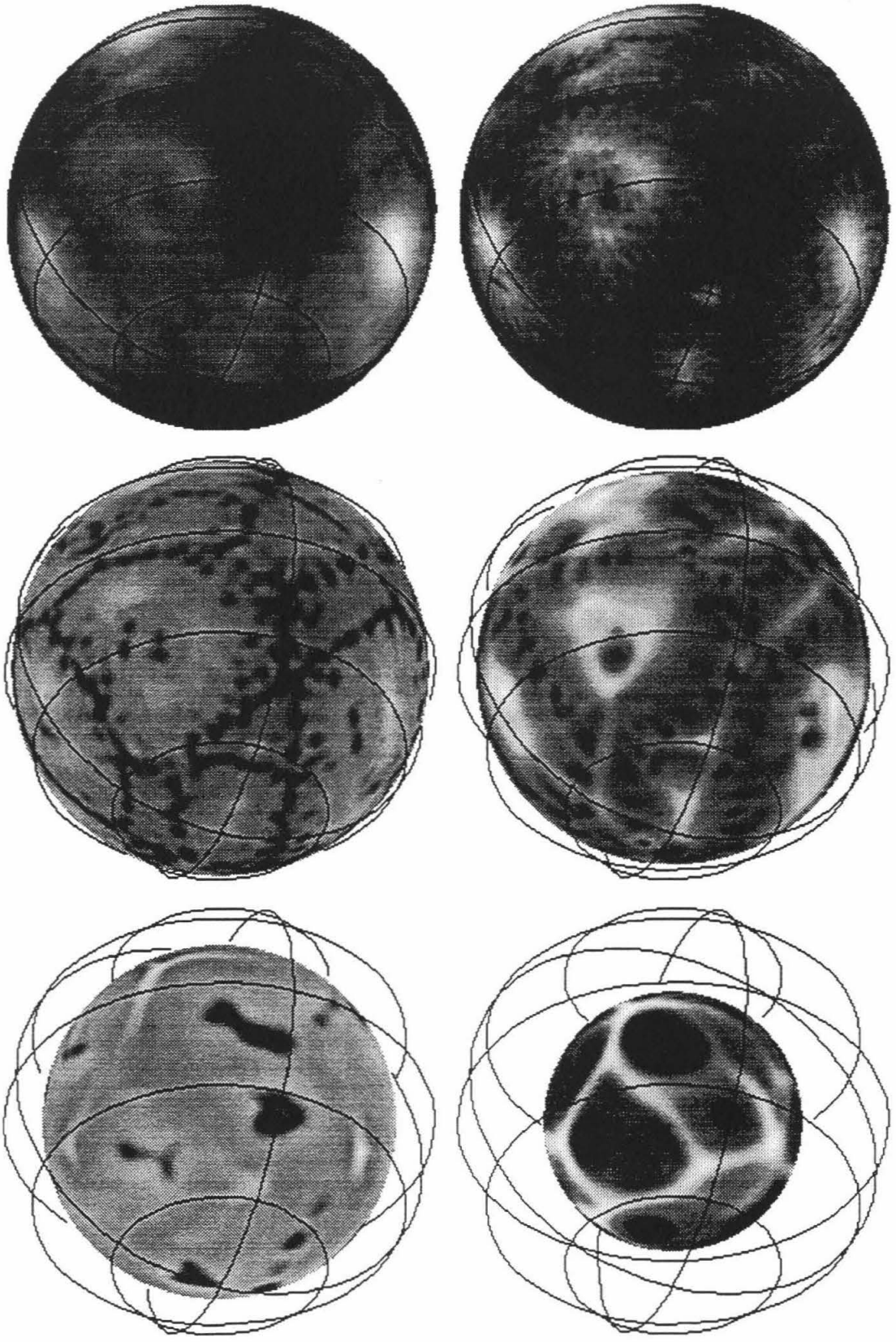

The dynamic surface topography is closely related to shallow upper-mantle (UM) structure, with the narrow downwelling sheets having a clear surface expression. The geoid, however, resembles a combination of filtered UM and MM structure, with the pattern of upper-mantle downwellings visible, but negative peaks over the mid-mantle avalanches. Cold regions are associated with geoid lows, and hot regions with geoid highs.

Figure 3.4 shows the same plots for case 3 (with a strong '400' added). In this case, there is less pooling of material in the TZ at the intersections of downwellings; rather, a general thickening of the downwellings is observed in this region. At MM depth, there are more avalanches visible, typically smaller than in case 1, and including at least one which is elongated. The surface topography and geoid display the same characteristics as in case 1, with the geoid even more strongly reflecting upper mantle structure, and the position of MM avalanches barely visible.

As shown in various studies [*Ricard et al.*, 1984; *Richards and Hager,* 1984; *Hager and Clayton*, 1989], the net geoid resulting from, for example, a cold temperature anomaly (i.e., a positive mass anomaly) is the small difference of two large terms, the geoid high associated with the anomaly itself, and the geoid low associated with the dynamically-induced negative topography at the surface and CMB. The sign and amplitude of the observed geoid are highly sensitive to the exact details of the radial viscosity profile and any chemical stratification. For a simple constant viscosity profile and chemically-homogeneous mantle, the contribution from surface topography is always dominant, and thus the net geoid associated with a cold temperature anomaly is a geoid low, as observed in our model.

These different contributions can be combined to obtain kernels giving the observed geoid for sheet mass anomalies of different spherical harmonic degrees at different depths. These kernels go to zero at the boundaries due to perfect isostatic compensation of mass anomalies at chemical boundaries. For a homogeneous, constant-viscosity mantle, the long wavelength kernels peak deep in the interior, with ℓ=2 peaking at around mid-mantle

depth, ℓ=8 peaking in the transition zone, and shorter wavelengths peaking at progressively shallower depths [*Hager and Richards*, 1989; *Hager and Clayton*, 1989]. This explains why the geoid signal observed in our models, which is dominated by long wavelengths, is closely related to structure in the TZ and MM.

The downward deflection of the phase boundary at 670 km depth caused by a cold temperature anomaly (resulting in a positive mass anomaly) at that depth results in a negative mass anomaly. Thus, the geoid contributions of these opposite anomalies partially cancel, reducing the geoid contribution from transition zone heterogeneity. In contrast, deflection of the '400' results in a geoid contribution of the same sense to temperature anomalies in that region, enhancing the geoid contribution from the mid upper-mantle. This partly accounts for the differences between case 1, in which geoid resembles a combination of UM and MM structure, and case 3, in which the UM completely dominates the geoid signal.

The major downwellings (slabs) of the Earth are associated with geoid highs rather than geoid lows, as in our model. This discrepancy could be corrected by a large viscosity jump at 670 km depth [*Hager and Clayton*, 1989] which is a common feature of mantle viscosity models derived using geoid data [e.g., *Davies and Richards*, 1992; *King et al.*, 1992; *Forte et al.*, 1993].

Time-dependence

Figure 3.5 shows the geoid, TZ and MM structure, and cross-sections for case 1 at three times corresponding to the same times and viewing angle as in Figure 3.1. The radial dependence of the flow structure is clearly visible in the right plots (d,h,l), which show the superadiabatic temperature field in constant-longitude cross-sections. The upper mantle is clearly heterogeneous on long wavelengths, containing some broad (up to ~10,000 km) regions of anomalously cold or hot material, as well as regions with the classical small

Fig. 3.5. Time evolution of case 1, showing three times during the simulation, at intervals of ~500 million years (as figure 3.1). Left column (parts a,e,i) shows geoid, with scale ±120 m, other columns show superadiabatic temperature in the transition zone (second column, parts b,f,j), mid-mantle (third column, parts c,g,k) and in vertical cross section (i.e., at constant longitude, parts d,h,l), with the right-hand side of the cross sections corresponding to a vertical line running down the center of the constant-radius sections. Superadiabatic temperature scale ranges from -1050 to 350 K.

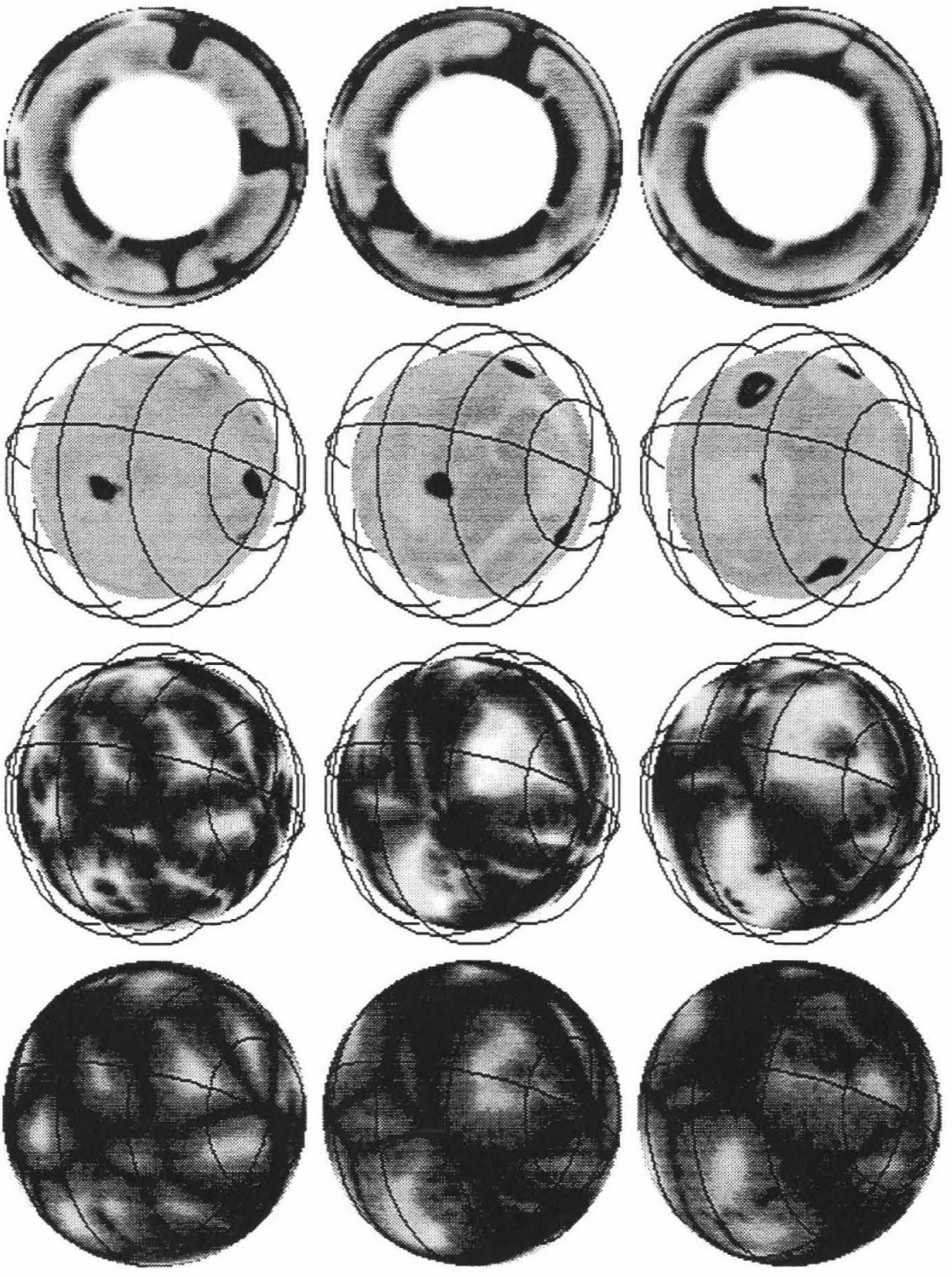

Fig. 3.6. As Figure 3.3, for case 3. Geoid ranges ±110 m, and superadiabatic temperature from -950 to +300 K.

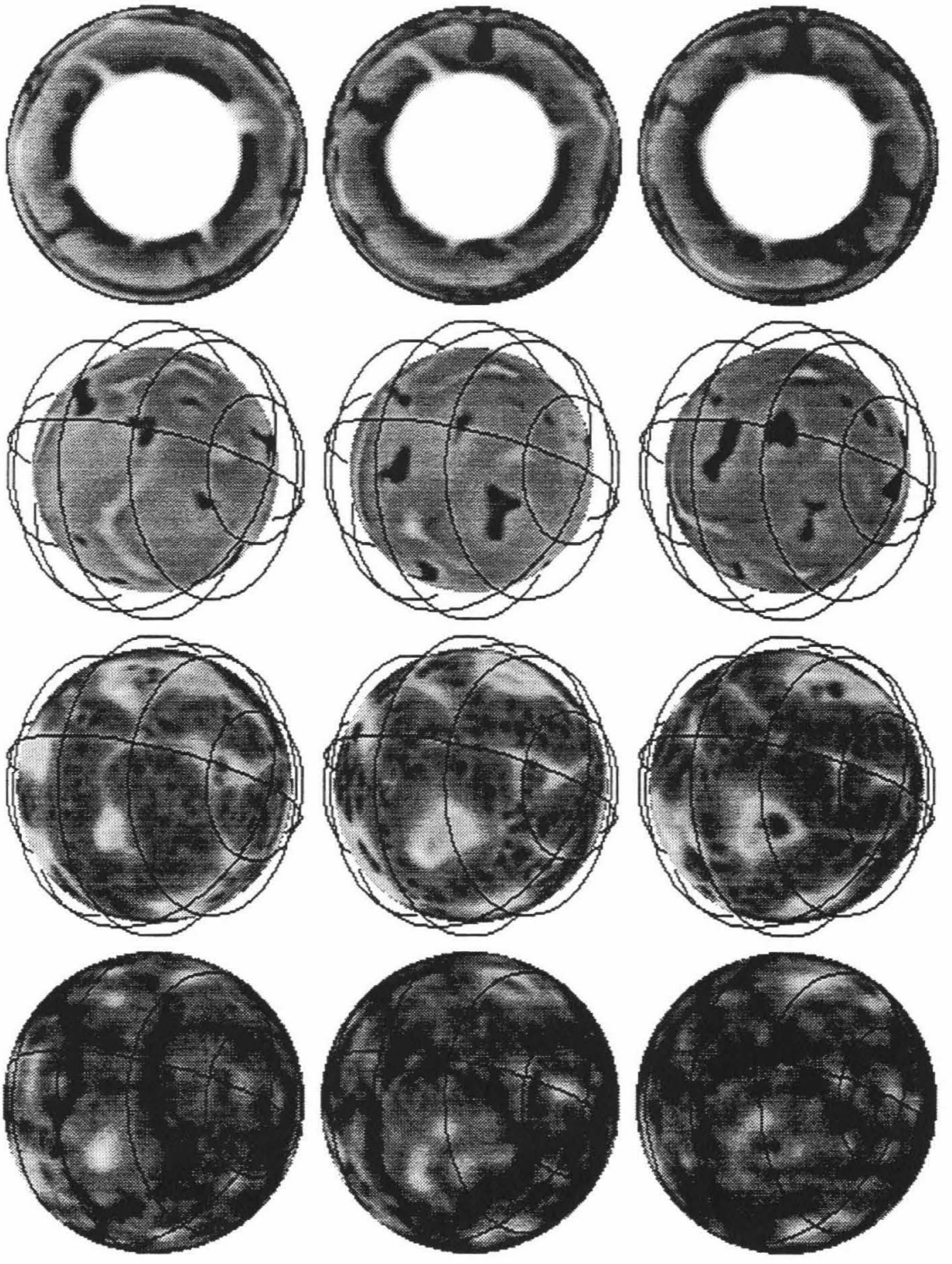

aspect-ratio convection cells [*Christensen and Yuen*, 1988; *Busse*, 1989]. Pooling of cold material can be seen in the TZ. The MM and DM can be clearly distinguished, with DM occupying the lowermost ~800 km of the mantle.

Comparing the geoid with the TZ and MM for the three times, it appears that the geoid closely resembles upper-mantle structure. Avalanche conduits in the MM are associated with distinct geoid lows that are of only slightly higher amplitude than the signature of the upper-mantle structure.

The same plots for Case 3 (Figure 3.6) reveal a similar behavior. In the MM region, distinct hot upwelling structures can be identified more clearly than in Case 1. However, in this case, avalanche conduits have a weaker surface expression, which is partly because the mid-mantle is colder, thus reducing the temperature anomaly associated with avalanche conduits, and partly because the contribution from '400' deflection reinforces the upper-mantle signature, as discussed earlier.

Spherically-averaged temperature

The horizontally-averaged (ℓ=0) superadiabatic temperature fields for all cases are shown in Figure 3.7. Due to slightly different reference adiabats in different cases, these have been aligned at the surface and CMB. In general, both the upper and lower mantles are strongly subadiabatic. There is a strong boundary layer at 670 km, having a temperature change of several hundred degrees over a vertical extent of ~250 km, in addition to the usual boundary layers at the surface and CMB. Small kinks, of vertical extent ~30 km, are observed at 670 km and 400 km, due to the release or absorption of latent heat by material advected across the phase change. This effect was previously noted by *Christensen and Yuen* [1985]. In regions of high vertical mass flux (i.e., high local Peclet number) at 670 km depth, the release or absorption of latent heat is dominant and local conductive heat flux is negative (i.e., downwards). However, in regions where cold material is pooling above

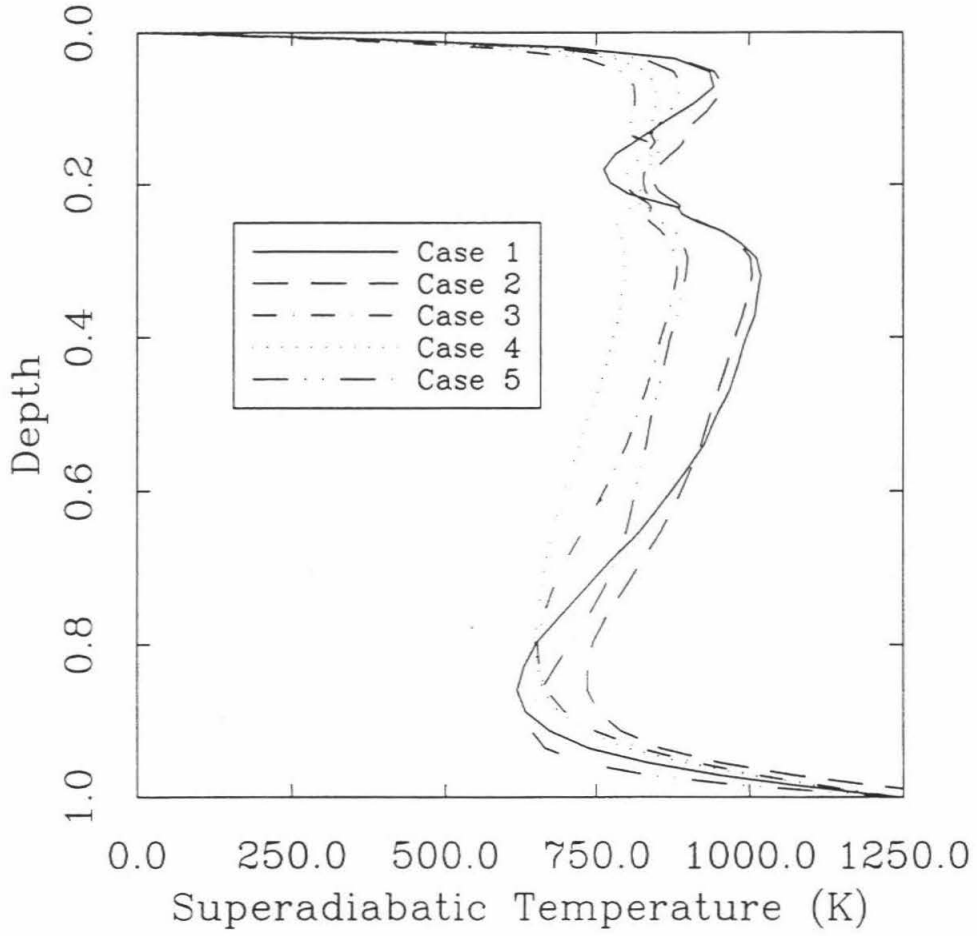

Fig. 3.7. Radial profile of spherically-averaged (l=0) superadiabatic temperature for Cases 1-5. Profiles are aligned by boundary conditions.

the '670' and thus the radial velocity through the '670' is very low, the resulting thermal boundary layer results in strong upward conduction of heat. When spherically averaged, these effects nearly cancel in a very localized region around the '670', so that the net thermal gradient at 670 km depth is low, and thus the net thermal conduction across the '670' is close to zero, and most of the heat flux across 670 km is advected. The subadiabatic upper mantle and the thermal boundary layer across the '670' result in a local temperature minimum in the transition zone [*Weinstein*, 1993], which, if temperature-dependent viscosity were included, would result in higher viscosity in this region.

Comparing cases 1, 2 and 3, it is clear that the magnitude of the thermal boundary layer across the '670' diminishes as P_{400} increases, due to an increase in either Clapeyron slope or density change. Thus, it seems reasonable to conclude that the amount of layering decreases due to the presence of the '400'. This decrease in the temperature change across the '670' is associated mainly with a reduction of the temperature in the MM, resulting in easier penetration of upwelling hot plumes from the DM. Case 4, which has a weaker '670' Clapeyron slope of -3 MPa K^{-1}, but otherwise the same parameters as case 2, displays virtually no boundary layer at 670 km depth, suggesting that the strength of the '670' exerts a much greater influence on stratification than the strength of the '400'.

In the DM, where avalanches spread out into pools of cold material surrounding the core, the temperature is strongly depressed from an adiabat extrapolated from the upper mantle. This effect is greatly enhanced by the spherical geometry, because the surface area of the core is ~35% of the surface area of the 670 km interface. The departure of the geotherm from an adiabat is of similar magnitude to the r.m.s. temperature variations in the interior, but a factor of ~5 lower than the peak-to-peak temperature variations at a particular depth. A subadiabatic interior temperature gradient is expected in a mantle heated substantially from within [*Schubert*, 1992; *Parmentier et al.*, 1994]. However, the avalanches strongly increase this subadiabaticity. This region of depressed temperature in the deep mantle is important in the interpretation of seismic tomography, as discussed later.

In case 5, in which the viscosity is constant with depth, the DM region has a smaller vertical extent, as can be seen by examination of the temperature profiles in Figure 3.7. The thermal gradient at the CMB is steeper, resulting in a higher core heat flux. These effects arise because cold avalanched material is not slowed down by a viscosity increase in the deep mantle, as it is in the other cases.

Radial mass flux

A useful indicator of the degree of flow stratification is the radial mass flux diagnostic [*Peltier and Solheim*, 1992], defined as the spherically-averaged absolute radial mass flux, normalized so that the integral over nondimensional depth is unity.

$$f(r) = \frac{<\rho|u_r|>}{\frac{1}{\Delta r}\int <\rho|u_r|> dr} \tag{3.4}$$

where $<\rho|u_r|>$ is the absolute value of the mass flux averaged over a surface of constant radius, the integral in the denominator is performed from the CMB to surface, and Δr is $r_{surface}$-r_{cmb}.

The radial mass flux diagnostic for the various cases, averaged over several thousand timesteps, is shown in Figure 3.8. The phase change is observed to have a marked inhibitive effect on the flow, as indicated by the minimum in the radial mass flux at 670 km. Comparison of cases 1-3 indicates the effect of the '400' on the propensity to layering. The most pronounced minimum at 670 km is shown by case 1, which has no phase change at 400 km. Cases 2 and 3, with increasingly stronger phase changes at 400 km (P_{400} is 0.055 and 0.135, respectively), display progressively less pronounced minima, indicating that increasing the strength of the '400' decreases the degree of layering. This was also indicated by examination of the spherically-averaged temperature profile (previous section). *Solheim and Peltier* [1994] reach the same conclusion based on 2-D spherical axisymmetric

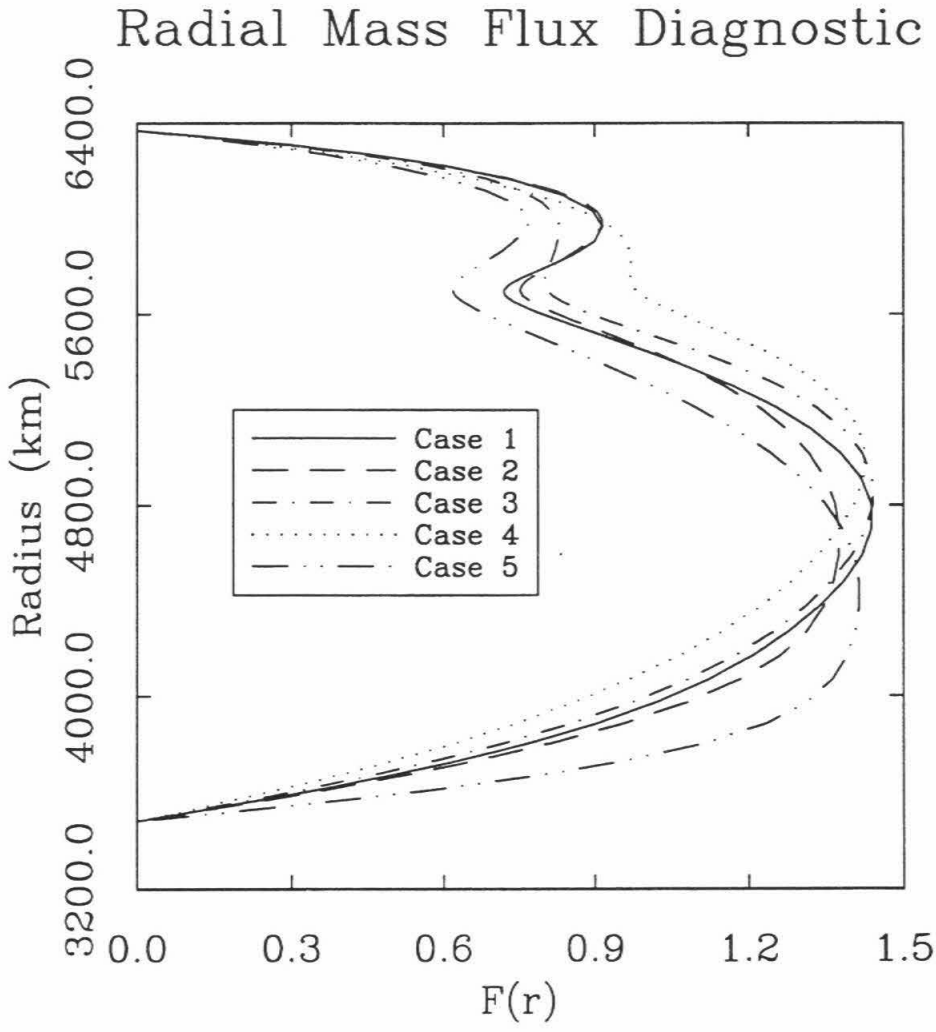

Fig. 3.8. Radial mass flux diagnostic for cases 1-5. See text for definition.

modeling, but *Steinbach and Yuen* [1992] and *Zhao et al.* [1992] find that adding the '400' decreases the mass flux across 670 km in their 2-D Cartesian experiments. This difference could be related to the depths at which the phase changes are placed, or the difference between Cartesian and spherical geometries. It does not seem to be related to Rayleigh number or dimensionality since our experiments are almost an order of magnitude lower in Rayleigh number, and have an additional dimension, compared with those of *Solheim and Peltier* [1994], but we reach the same conclusion.

For case 4, which has a weaker '670' Clapeyron slope of -3 MPa K^{-1} and the same '400' strength as case 2, the radial mass flux diagnostic displays no minimum, but just a change in slope at 670 km depth. Thus, the degree of layering is highly sensitive to the strength of the '670'. From a comparison of cases 1 to 4, it is evident that the degree of layering is much more sensitive to the strength of the phase change at 670 km depth than the strength of the phase change at 400 km depth. The constant viscosity case (case 5) displays a similar amount of layering as case 2, but has greater mass flux towards the base of the mantle, presumably due to the lower viscosity there.

Examination of the radial mass flux for individual spherical harmonic degrees (i.e., the spherical harmonic coefficients of ρu_r on surfaces of constant radius) for the most stratified case (case 1, Figure 3.9) indicates that long wavelengths of flow, such as ℓ=2 and ℓ=5, are virtually unaffected by the phase change, whereas short wavelengths are increasingly inhibited, with a noticeable effect at ℓ=10; and flow for spherical harmonic degrees above around 40, is effectively confined to the upper mantle. At the wavelengths employed in the current generation of global seismic tomographic models, the flow appears essentially unlayered, compatible with the long-wavelength flow pattern in the Earth calculated by *Phipps Morgan and Shearer* [1993], which takes into account density anomalies derived both from global seismic tomography and from the observed deflection of the '670' [*Shearer and Masters,* 1992]. A qualitative explanation of this phenomenon is as follows: At a particular point, flow with a given horizontal wavelength is sensitive to

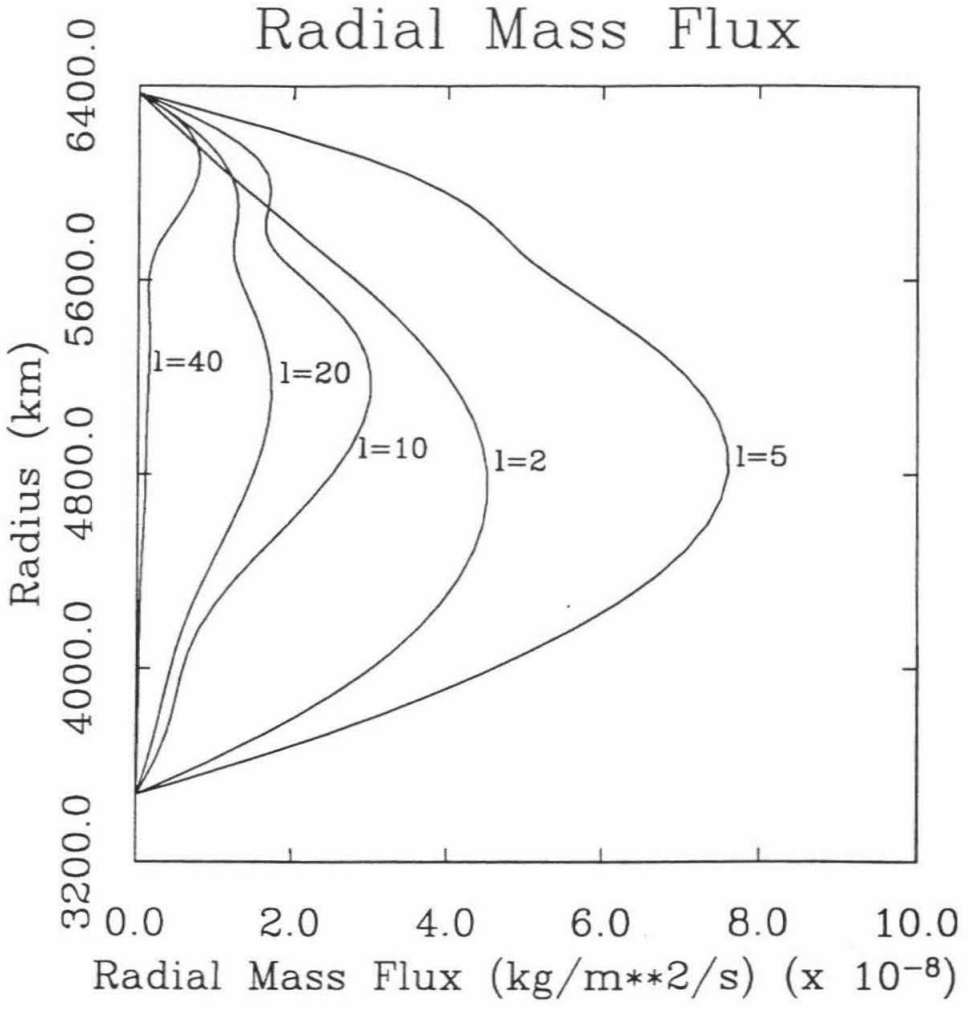

Fig. 3.9. Radial mass flux for case 1, at individual spherical harmonic degrees (ℓ) of 2,5,10,20 and 40, as indicated.

density anomalies vertically-averaged over a lengthscale similar to this horizontal wavelength. For short wavelengths, flow through '670' is sensitive only to density anomalies in the immediate vicinity of the '670', and thus is strongly influenced by deflection of this interface. At the longest wavelengths, however, flow across 670 is influenced by density anomalies vertically-averaged through the entire mantle, and thus a much larger deflection of the 670 would be needed to balance this integrated buoyancy and thereby prevent flow penetration. Deflection of a downwelling by the '670' is associated with short wavelengths of flow; avalanches are associated with long wavelengths of flow. The calculation that the long-wavelength flow field in the Earth penetrates the '670' is still compatible with slabs being deflected when they first encounter the phase transition.

From the radial mass flux across the interface at 670 km depth it is possible to calculate a 'mixing time', defined as the time required for a mass equal to the mass of the mantle to pass through 670 km. For cases 1-5 this time is 4.5, 4.3, 4.1, 2.3 and 3.7 Gyr, respectively. This further quantifies the conclusions discussed above: the effect of the '400' is to moderately decrease the propensity to layering, while the effect of slightly weakening the '670' is to greatly decrease the degree of layering. To scale these mixing times to the Earth's Rayleigh number (Ra), it is likely that the mass flux (of downwelling cold material) scales roughly as the heat flux, suggesting a $Ra^{1/3}$ scaling [*Turcotte and Schubert*, 1982] which would reduce the mixing time to ~2.1, 2.0, 1.9, 1.1 and 1.7 Gyr, respectively, for an order of magnitude increase in Ra. This is less than half the age of the Earth, but the increased effect of the phase change at higher Ra [*Christensen and Yuen*, 1985; *Yuen et al.*, 1994] may increase this time.

Globally-averaged time-dependence

The time-dependence of radial mass flux through the phase changes, and total heat flow through the CMB and surface are shown for the last billion years of Case 3 in Figure

3.10. There is some time-dependence of the flow through the phase changes at 400 and 670 km depth, with the mass flux diagnostic at 670 km depth (F_{670}) varying between 0.75 and 0.85 during this period. F_{400} and F_{670} display similar variations, with F_{400} generally higher than F_{670}, except during one brief period towards the end of the simulation. The surface and CMB heat flux displays very weak time-dependence, in contrast to the two-dimensional calculation of *Weinstein* [1993], in which they show a sharp peak for each individual avalanche.

These plots show that the time-dependence of globally-averaged quantities is much weaker than that observed in spherical axisymmetric [*Machetel and Weber,* 1991; *Peltier and Solheim*, 1992] or 2-D Cartesian [*Weinstein*, 1993] geometries, because due to the large effective aspect ratio of the sphere, several avalanches are occurring at any given time, and thus the convection is never strongly layered on a global scale. As a result, globally averaged diagnostics such as F_{670}, surface heat flux, mean temperature, etc., are not greatly affected by an individual avalanche.

It is possible that our avalanches would be more abrupt and violent if we could decrease the viscosity (thus increasing the Rayleigh number) to Earth-like values, as observed in two-dimensional models [*Weinstein*, 1993; *Solheim and Peltier*, 1994]. However, we believe that with an Earth-like viscosity, avalanches would still overlap in time, and the global time-dependence would be intrinsically weaker in full three-dimensional spherical geometry than in spherical axisymmetric or two-dimensional Cartesian geometries. Four arguments support this view: (1) Cylindrical downflows penetrate the endothermic phase change more easily than linear downflows, and thus result in smaller, less vigorous and more frequent avalanches. This is indicated by our numerical results, and by the analytical model of *Bercovici et al.* [1993]. (2) Cylindrical avalanches last for longer, thus increasing the probability of temporal overlap with other avalanches. This is because they take longer to exhaust their pool of feeding material than linear avalanches, due to the radially-convergent influx of material towards the conduit. (3) The

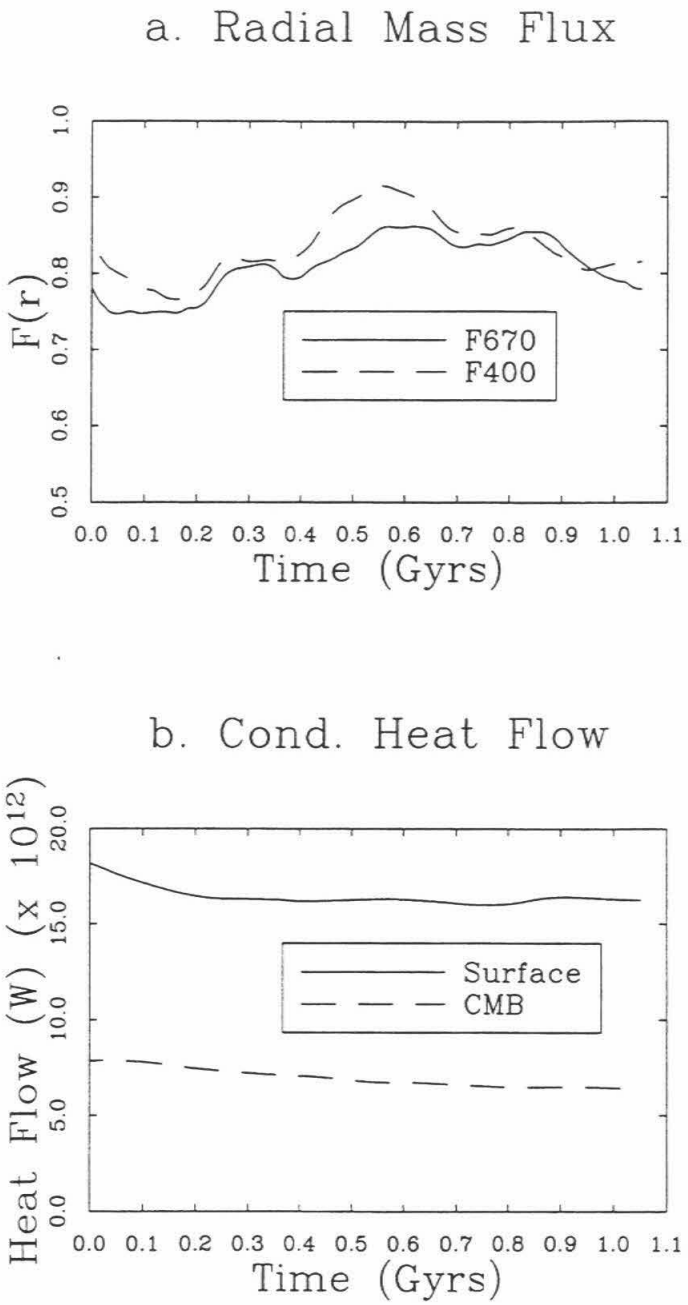

Fig. 3.10. Time-dependence of mass and heat fluxes for the last billion years of case 3. a) Radial mass flux diagnosic at 400 and 670 km depth. b) Conductive heat flux at surface, 400 km depth, 670 km depth and CMB.

synchronicity observed in 2-D, whereby an avalanche in one place induces a simultaneous avalanche in another place, is less likely to occur in 3-D. This is because the velocity field associated with 3-D cylindrical downflows decreases with distance much more rapidly than that for a linear downflow (1/distance rather than 1/log(distance)), and thus cylindrical avalanches will have a much smaller influence on their distant surroundings. (4) If avalanches are essentially unsynchronized, there is a much higher probability of temporal overlap in a 3-D sphere than in an axisymmetric sphere, because, due to simple geometry, it is possible to fit many simultaneous cylindrical avalanches into a 3-D sphere, but only about 3 linear avalanches in a 2-D axisymmetric sphere.

Comparisons with the Earth

Lateral heterogeneity

The effect of the phase changes, particularly the endothermic transition at 670 km depth, on the spectrum of density anomalies at different radii is pronounced. Previous work has focused on the depth-dependence of total power, which shows a peak at 670 km [*Peltier and Solheim*, 1992; *Tackley et al.*, 1993b], and the vertically-averaged lateral spectrum, which for case 1, shows some similarity with the global seismic tomographic model of *Inoue et al.* [1990] [*Tackley et al.*, 1993b]. Here we investigate the spectral characteristics further by considering spectral heterogeneity maps (i.e., the long-wavelength spherical harmonic spectrum as a function of radius) for cases 1 and 4, which are the most stratified and least stratified cases respectively, and the seismic model SH12/WM13 of *Su et al.* [1992b]. Such comparisons between convection models and seismic models are made complicated by the problem of an uncertain radially-dependent coefficient to scale between entropy or temperature and seismic velocity. In particular, this coefficient may be much higher in the transition zone than in the surrounding layers

(suggested by the inversion of *Forte et al.* [1993] and supported by the thermodynamic analysis of *Karato* [1993]), which would suppress transition zone heterogeneity in the seismic models. The problem of this uncertain radially-dependent coefficient can be eliminated by normalizing the spectrum at each radius by the total r.m.s. amplitude at that radius. Thus, we present normalized spectra in addition to unnormalized spectra which still retain information about radial variation of total r.m.s. amplitude.

In the spectral heterogeneity map (SHM) for case 1 (Figure 3.11a,b), the three distinct regions, previously identified from the spatial images of the temperature field, are clearly visible from their spectral characteristics. The upper mantle (UM) is characterized by a high amplitude 'red' (i.e., long-wavelength, peaking at ℓ<8) spectrum, although since it also contains narrow features, there is still significant amplitude at much higher degrees, as may be true in the Earth [*Gudmundsson et al.*, 1990; *Davies et al.*, 1992]. The mid-mantle (MM), comprising the upper ~1000 km of the lower mantle, is characterized by a low-amplitude, broad spectrum, with a wide peak at ℓ=5-20, and the deep mantle (DM) is again characterized by a high-amplitude red spectrum (peak ℓ<6). These can be understood qualitatively by the following argument: *Jarvis and Peltier* [1986] showed that for simple convection cells, boundary layers are characterized by a high-amplitude, long-wavelength spectrum, with the interior of the convective region having a low amplitude, broad spectrum. Thus, the UM and DM display the boundary layer signature, while the MM corresponds to the interior of the convective region. The entire UM has a boundary layer signature due to the pooling of cold material above the '670', which also creates an additional boundary layer at 670 km depth, identified by a peak in the total power [*Tackley et al.*, 1993b; *Peltier and Solheim*, 1992]. Avalanched cold material pooling above the CMB gives the DM its long-wavelength signature. The height of this region is influenced by the magnitude of the viscosity increase with depth, as shown earlier by consideration of spherically-averaged temperature profiles.

Fig. 3.11. Spectral heterogeneity maps (SHM) for cases 1 and 4 and the seismic model SH12/WM13 of *Su et al.* [1992b]. Plotted are contours of r.m.s. spherical harmonic amplitude as a function of (normalized) depth. In the left column (a,c,e) are the entropy perturbations (for simulations) and seismic velocity anomalies (for seismic model). The plots in the right column have been normalized by the total r.m.s. amplitude at each radius. Thickness of contour line proportional to amplitude, with ten contour levels scaled to maximum value in each plot.

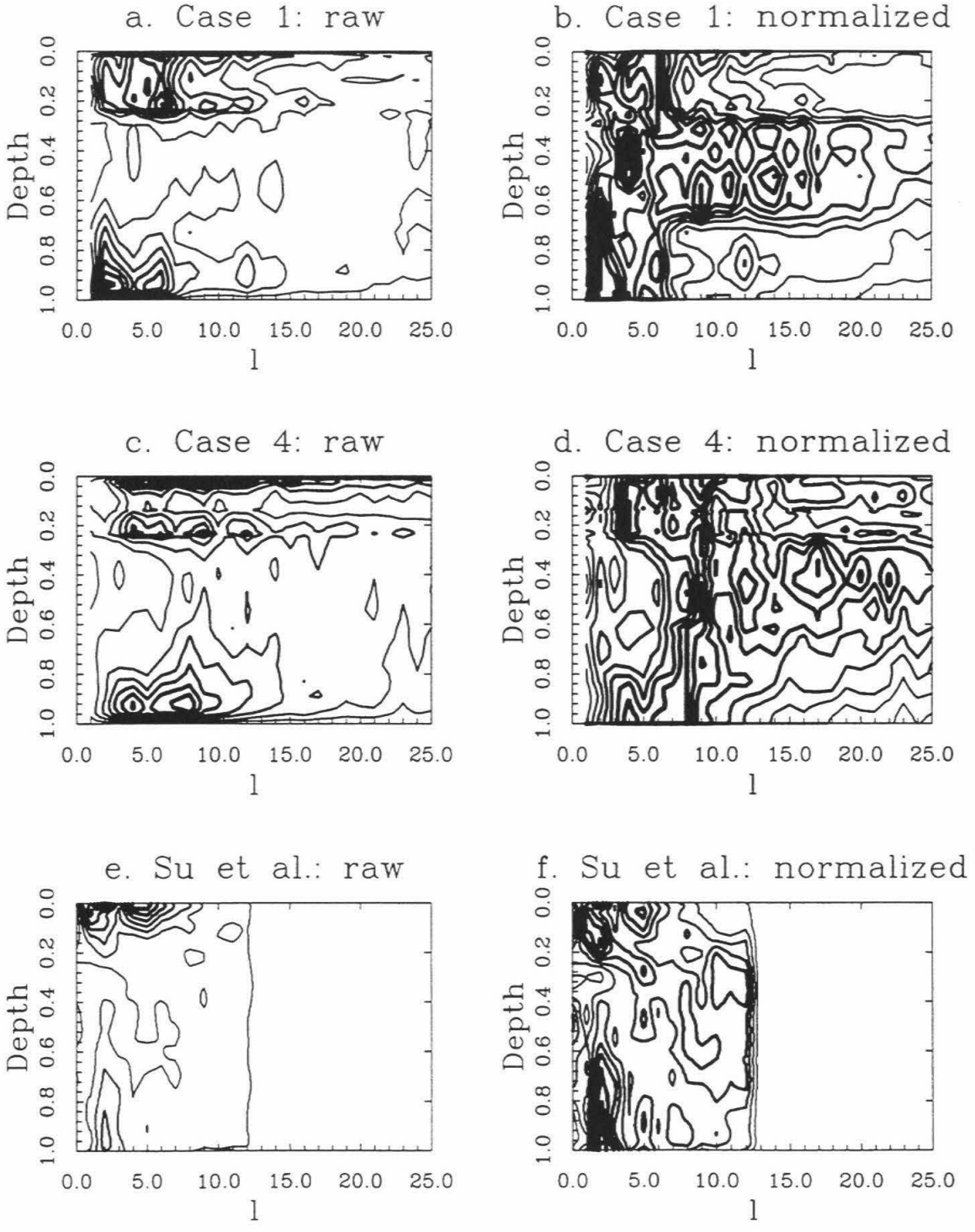
a. Case 1: raw
b. Case 1: normalized
c. Case 4: raw
d. Case 4: normalized
e. Su et al.: raw
f. Su et al.: normalized
Depth
1.0 0.8 0.6 0.4 0.2 0.0
0.0 5.0 10.0 15.0 20.0 25.0
l

Figure 3.11 c,d show the SHM for case 4, the case with the least stratification, as discussed earlier. Even with the very small degree of layering, the three main regions are again visible, though less clearly, indicating that long-wavelength averaged characteristics of the thermal field are very sensitive to even small degrees of flow stratification. The upper boundary layer is much stronger than the 670 km boundary layer (Figure 3.11 c), whereas they are of comparable amplitude in case 1 (Figure 3.11 a). In addition, the spectral peak has shifted to shorter wavelengths and broadened in this case.

The raw seismic model (Figure 3.11 e) does not display much r.m.s. heterogeneity in the transition zone, or a peak in total amplitude at 670 km depth. This is also true of other seismic models we have examined [*Tanimoto*, 1990b; *Inoue et al.*, 1990; *Masters et al.*, 1992]. However, when normalized, a more coherent upper mantle signature emerges, with a change in the spectral characteristics at around 670 km depth, marking the start of the MM. The DM is visible in both raw and normalized spectra, and extends over a somewhat greater depth range than in the convection models.

Thermal fields from the convection models lack the dominant ℓ=2 component found in some seismic models [*Nakanishi and Anderson*, 1983; *Tanimoto*, 1990a,b; *Su and Dziewonski*, 1991, 1992]; possible reasons for this are discussed later. The asymptotic behavior of power with spherical harmonic degree varies with depth, but goes approximately as ℓ^{-2}.

Geoid spectra

Figure 3.12 shows the amplitude spectra of the geoid (i.e., the total geoid amplitude at each spherical harmonic degree, summed over order) for four convection models, compared to observations of Earth [*Rapp and Pavlis*, 1990] and Venus [*Konopliv, personal communication,* 1993]. The geoid is normalized to the radius of the planet, which is equivalent to normalizing gravitational potential to GM/R, where G is the gravitational

constant, M is the planetary mass and R is the planetary radius. The convection models are case 1 (Figure 3.12 a), case 2 (Figure 3.12 b), an 85% internally-heated case with no phase change, reported in *Tackley et al.* [1993b] (Figure 3.12 c), and an unpublished case with no internal heating, no phase change, constant viscosity and a Rayleigh number of $3x10^6$ (Figure 3.12 d).

There are two main characteristics to compare: the slope ($\partial \ln A/\partial \ln \ell$) and the absolute amplitude. All simulations and data display roughly the same slope ($\partial \ln A/\partial \ln \ell \cong -1.5$) and absolute amplitudes, except for the internally-heated, no phase-change case (Figure 3.12 c) which has a plateau for low degrees up to about 20-30. The absolute amplitudes of geoid coefficients for the simulations with phase changes are broadly comparable to those of Earth and Venus and to the basally-heated case with no phase change, although there are differences in detailed degree-by-degree comparisons.

This is somewhat surprising, since (1) the geoid kernels (discussed earlier) for low degrees peak at mid-mantle (ℓ=2) to transition zone (ℓ=8) depths, falling to zero at the surface and CMB [*Hager and Clayton*, 1989]. (2) The phase change introduces high-amplitude, long-wavelength heterogeneity in the transition zone, where these geoid kernels are most sensitive. Thus, one would expect a much larger geoid, an argument that has been used in the past to argue against any significant layering [*Davies and Richards*, 1992, and references therein]. The lack of any significant signal from the strong transition zone heterogeneity is due to the near canceling of its contribution by an opposite and nearly equal contribution from density anomalies associated with deflection of the 670 km interface. In this dynamically self-consistent system, cold material accumulates in the transition zone while its negative buoyancy is balanced by positive buoyancy from downward deflection of the phase boundary. A balancing of mass anomalies close together results in a near canceling of geoid contributions. The cases with no phase changes have their long-wavelength power concentrated in the surface and CMB thermal boundary layers [*Jarvis and Peltier*, 1986], where the long-wavelength geoid kernels are close to zero.

Fig. 3.12. Geoid amplitude spectra, normalized to planetary radius, for four convection models, compared to the Earth and Venus. a) Case 1. b) Case 3. c) Whole-mantle model with 85% internal heating. d) Whole-mantle model with completely basal heating. e) Earth. f) Venus.

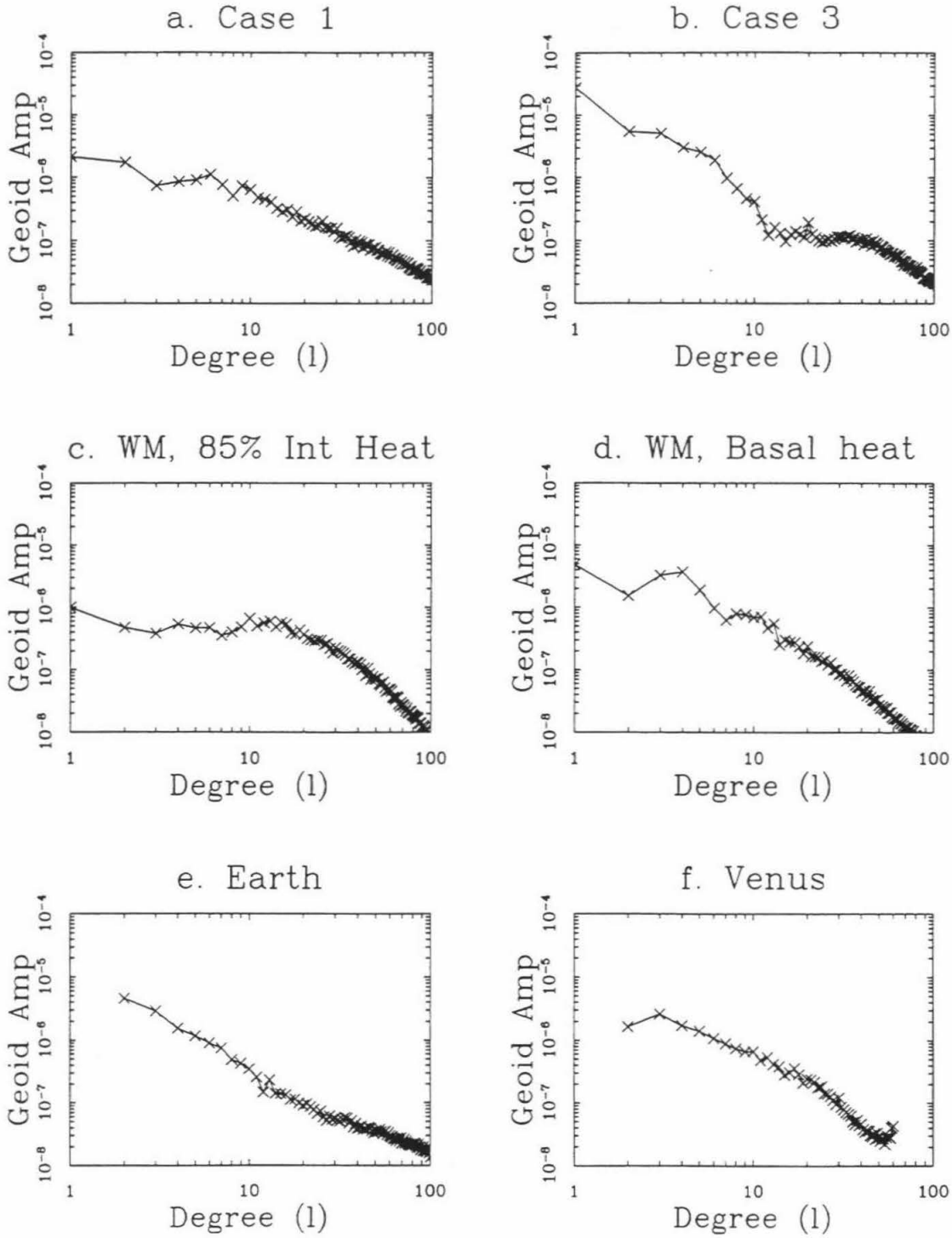
a. Case 1
b. Case 3
c. WM, 85% Int Heat
d. WM, Basal heat
e. Earth
f. Venus
Geoid Amp
Degree (l)
1
10
100
10^-4
10^-5
10^-6
10^-7
10^-8

The ℓ=1 geoid is usually set to zero by taking the origin of coordinates to be the center of mass. However, in these simulations the coordinate origin is fixed, and it is interesting to note that in case 1 and the two whole-mantle cases, the ℓ=1 coefficient was the largest, indicating offsets (up to ~24 m) of the fixed coordinate origin (the center of figure) from the instantaneous center of mass. This is much smaller than the observed offsets of 280m for Venus [*Bindschadler et al.*, 1994] and 2.1 km for the Earth [*Balmino et al.*, 1973]; this could be because crustal thickness variations plays a large role in determining the center of figure for these planets, and the crust is not included in our model.

Visual comparison with tomography: effect of filtering

In order to make any comparisons between convection simulations and seismic models, it is necessary to consider the effects of limited seismic resolution on the convective features. Although the filtering that seismic tomographic datasets and inversions perform on the actual Earth structure is complex, for the moment we approximate it by a simple truncation of the convection results at the nominal resolution of typical current tomographic models, i.e., ℓ=10, Chebyshev degree n=13, and removal of the spherically-symmetric (ℓ=0) component, although in the near future, more realistically-filtered datasets may be possible [*Johnson et al.*, 1993].

We show in other sections that even when filtered to seismic tomographic resolution, the effect of the phase change on globally-averaged diagnostics of the thermal field is still clearly discernible, both in spectral heterogeneity maps (SHM) and in radial correlations between layers [*Jordan et al.*, 1993]. The strong heterogeneity around the '670' (Figure 3.11a) which is associated with a peak in the radial profile of horizontally-averaged heterogeneity [*Peltier and Solheim*, 1992; *Tackley et al.*, 1993b] is still visible at Chebyshev degree n=13, but disappears at n=6.

In the filtered temperature field for Case 1 (Figure 3.13), all plume-like upwellings in the mid-mantle disappear completely. The strongest of the broad cylindrical downwellings are visible in the MM as smeared out cold anomalies, and thus may be discernible in tomographic models. Although the lateral heterogeneity spectrum in the upper mantle is dominated by long wavelengths, the most important convective features (the linear downwellings) are very narrow and it is necessary to expand to at least ℓ~31 in order to see these features clearly, indicating the importance of obtaining seismic Earth models out to high spherical harmonic degree, even though most of the power has been demonstrated to be at long wavelengths [*Tanimoto*, 1990a; *Su and Dziewonski,* 1991].

There are some significant differences in deep mantle morphology between seismic Earth models and the convection simulations presented here. Seismic models indicate the existence of two major quasi-circular slow ("hot") regions at the base of the mantle underneath the Pacific and Africa, which are frequently interpreted as sources of hot upwelling plumes. These are surrounded by linear fast ("cold") regions situated approximately underneath past subduction zone locations [*Fukao*, 1992; *Scrivner and Anderson*, 1992; *Richards and Engebretson*, 1992]. In contrast, our models contain circular pools of cold material surrounded by hot ridges. Some convection simulations seem to demonstrate broad hot upwellings compatible with those seen in seismic tomography [e.g., *Balachandar and Yuen*, 1992]; however, a large fraction of basal heating is required for these broad plumes, which is not compatible with various geophysical constraints, as summarized in *Stacey* [1992].

If avalanches occur in the Earth, these calculations indicate that the deep mantle would have a strongly depressed mean temperature, due to the efficient deposition of large volumes of cold material above the CMB. Calculation of actual temperature anomalies in the deep mantle from seismic tomography supports the hypothesis [*Yuen et al.*, 1993b]. When compared to this depressed mean temperature, hot anomalies in the DM appear much hotter than they actually are in absolute terms. This was shown in Figure 3.1, where large

Fig. 3.13. Effect of filtering on the temperature field for case 1. Field has been truncated to spherical harmonic degrees 1-10, and whole-mantle Chebyshev degree 13. View is from same angle as figure 3.3. a) shallow mantle: 200 km depth. b) mid-mantle: 1200 km depth. c) deep-mantle: 2600 km depth. d) cross-section.

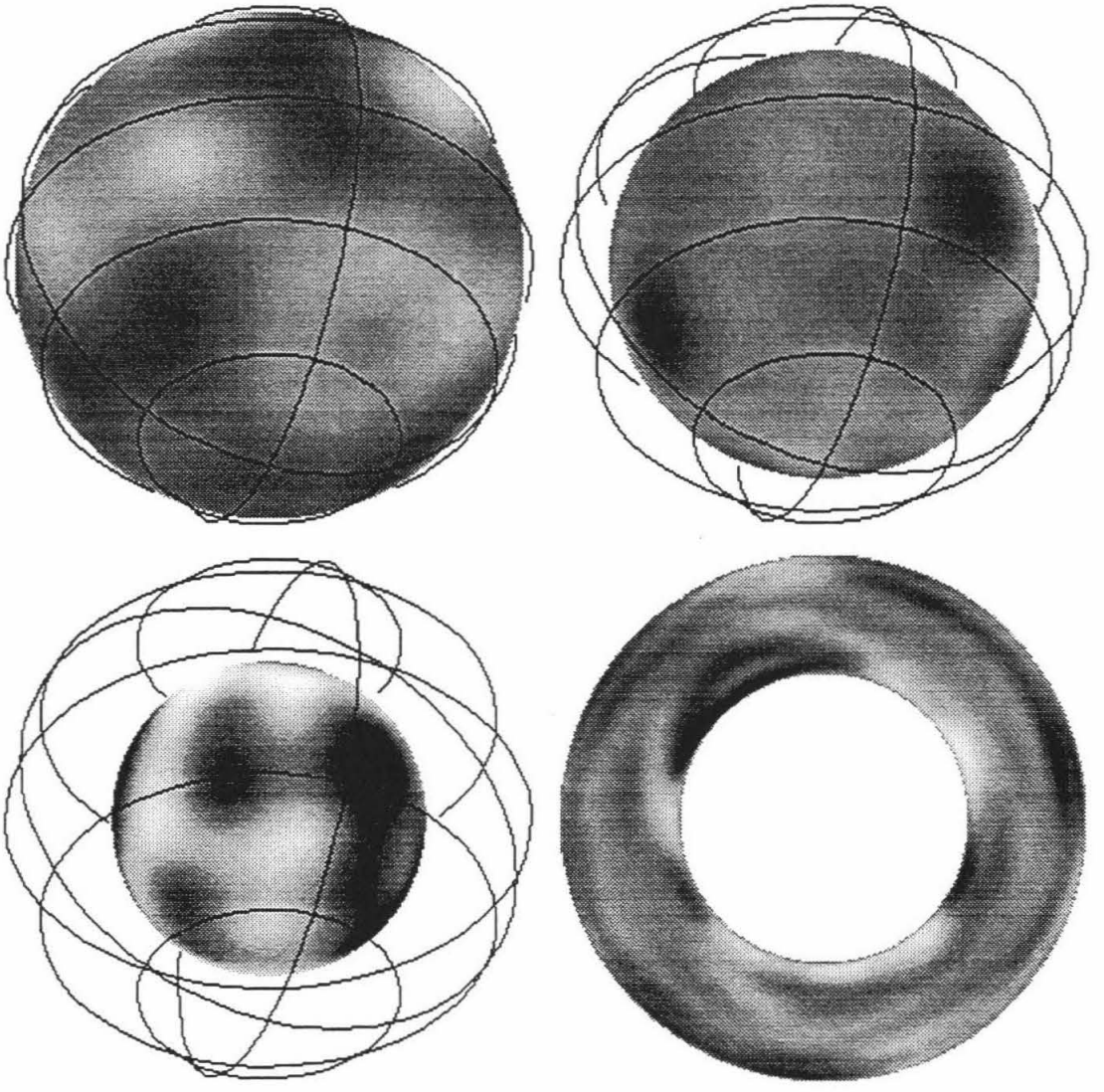

hot ridges are seen in the deep mantle. It can also be seen clearly by comparing the cross-section in Figure 3.13, which has the ℓ=0 term removed, with the unfiltered cross-sections in Figure 3.5. This effect may be important in the interpretation of seismic tomography, which is insensitive to the spherically-symmetric temperature. The large, hot plumes which appear in the DM region of tomographic models may not be as hot in absolute terms as they appear relative to their surroundings. In the mid-mantle region, where our model predicts that the spherically-averaged superadiabatic temperature is higher, their buoyancy relative to the immediate surroundings is lower, and they may not be able to rise to the upper mantle, as was seen in case 1. This may explain why only tenuous structure is visible in the mid-mantle above these seemingly giant plumes. As discussed earlier, the departure of the geotherm from an adiabat is of similar magnitude to the r.m.s. temperature variations in the interior.

Two-point correlation functions

It is desirable to develop ways of quantitatively comparing mantle flow models with seismic tomographic models, since visual comparisons can be somewhat subjective. *Puster and Jordan* [1993] proposed and tested a class of two-point auto-correlation functions to extract globally-averaged characteristics from simulated or seismic datasets. Of these, *Jordan et al.* [1993] compare radial correlation functions (RCFs) for global seismic tomographic models, with those for frames from the phase change simulation of *Tackley et al.* [1993b and case 1 in this paper], finding the RCF to be a very sensitive detector of any flow stratification at 670 km depth, even at the nominal resolution of seismic tomography. Any stratification results in a decorrelation of structures across 670 km depth. *Glatzmaier and Schubert* [1993] show that a completely impermeable boundary at 670 km causes an extreme decorrelation in the RCF at this depth. Here, in Figure 3.14, we compare the RCF for the most strongly layered case (case 1) with the RCF for the most weakly layered case

(case 4), both for the full temperature fields and for those which are truncated to the nominal resolution of typical global tomographic models.

In the unfiltered plots, the characteristic narrowing of the central correlation peak (running along the diagonal of the plots) at 670 km depth (nondimensional depth 0.23), is still clearly visible even for case 4, although the strong decorrelation between upper and lower mantles is less pronounced for that case. In the filtered plots, this narrowing is still clear in case 1, but less pronounced in case 4. In case 1, an additional constriction is visible in the lower mantle, indicating the boundary between regions MM and DM.

RCFs for the current generation of seismic tomographic models do not, however, display any characteristics of flow stratification at 670 km, even though such characteristics should still be visible at the nominal resolution of these seismic models [*Jordan et al.*, 1993]. Reasons for this are discussed in the conclusions section.

Slab penetration

The issue of whether subducting lithospheric slabs penetrate the lower mantle, or are deflected by the 670 km discontinuity is central to the question of mantle layering. The closest analogues to slabs in our model are the linear downwellings in the upper mantle, and thus our model results suggest that slabs do not immediately penetrate, but instead build up in the transition zone until sufficient cold mass has accumulated to precipitate an avalanche into the lower mantle [*Christensen and Yuen*, 1985; *Solheim and Peltier*, 1994]. This picture would be consistent with (1) strong correlations between past locations of subduction and seismically fast ('cold') regions at the base of the upper mantle and top of the lower mantle [*Scrivner and Anderson*, 1992; *Ray and Anderson*, 1993], (2) recent tomography of slabs [*Zhou and Clayton*, 1990; *van der Hilst et al.*, 1991; *Fukao et al.*, 1992] showing that at least in some areas slabs flatten out along the 670 km discontinuity and appear to stagnate in the transition zone, (3) recent global tomography [*Su et al.*, 1992]

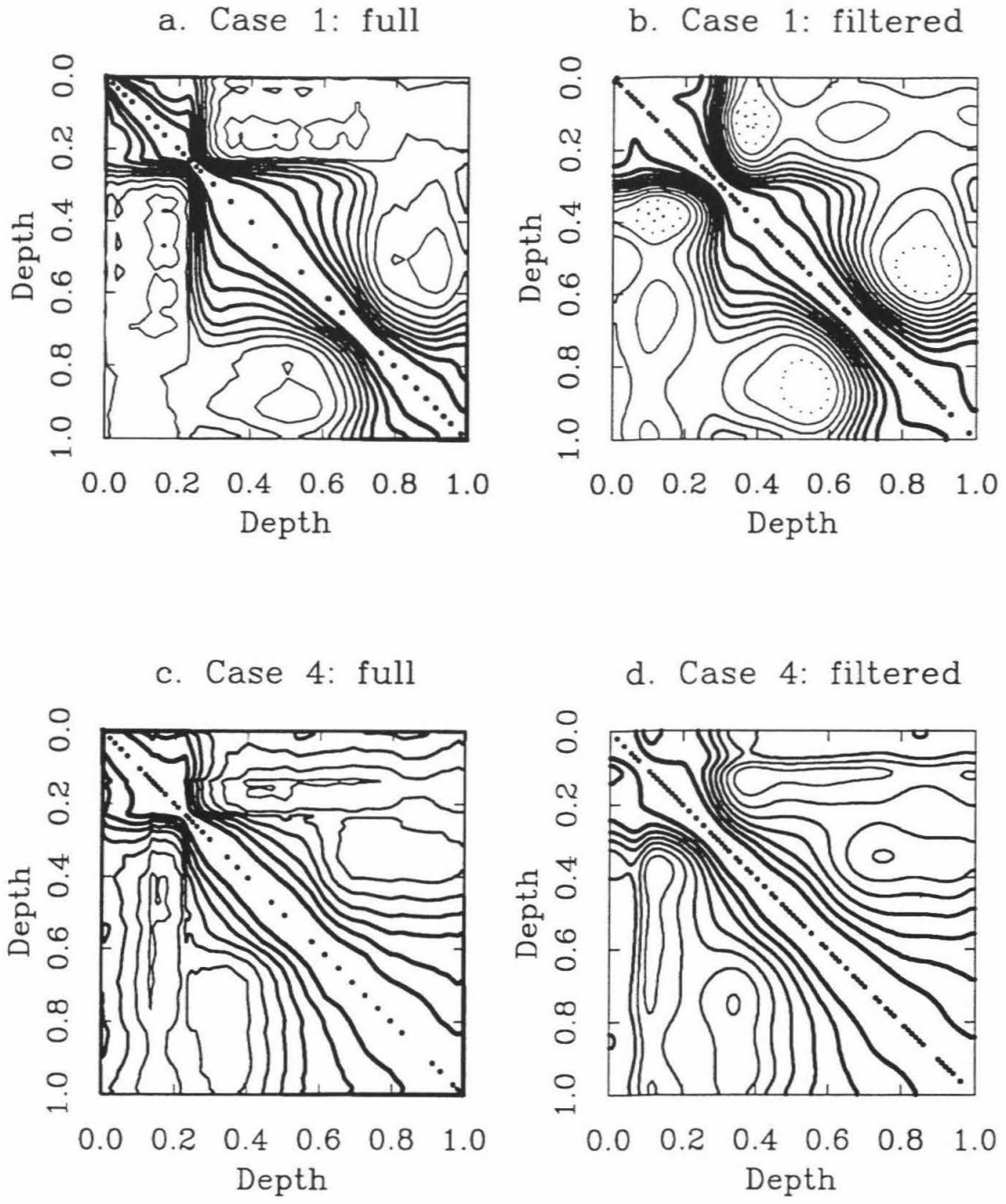

Fig. 3.14. Radial correlation functions (RCF) for cases 1 and 4. a) and c) are for the full entropy field, b) and d) are for fields that have been truncated to the nominal resolution of typical seismic tomography (spherical harmonic degree 10, Chebyshev degree 13 using a whole-mantle expansion).

showing broad seismically fast areas at 600 km depth in places where subducted slabs would be expected to accumulate, and (4) global mapping of topography on the 660 km discontinuity [*Shearer and Masters*, 1992] favoring models in which subducting slabs are deflected horizontally at the discontinuity.

However, the seismic evidence, reviewed by *Lay* [1994], does not paint a uniform picture, as slabs do appear to penetrate into the lower mantle in some regions [*Creager and Jordan*, 1984; *Vidale and Garcia-Gonzalez*, 1988; *Fukao et al.*, 1992] and thus the true situation is probably complex, with some slabs penetrating and others being deflected at 670 km depth. Our model lacks temperature-dependent viscosity, and hence the high viscosity of slabs (although slabs have warmed slightly by the time they reach 670 km depth), which may alter the results in two ways: (1) the overall planform and morphology of downwellings and avalanches and (2) the ability of a slab-like downwelling to penetrate the '670' [*Zhong and Gurnis*, 1994].

On the first point, we note that during a cylindrical avalanche in our models, cold material flows laterally along the "slabs" towards the avalanche, a mode of flow that is not possible when the slab is of much higher viscosity than its surroundings. Thus, in the Earth, the supply of new cold material to an ongoing cylindrical avalanche is much more restricted, and the avalanche may therefore be shorter in duration. Indeed, junctions of linear downwellings, at which the large pools of cold material build up in our model, are not observed in the Earth except at the intersection of the Pacific, Philippine and Eurasia plates. If most of the build-ups and avalanches are linear, this may make catastrophic breakthrough more difficult and more violent, as in two-dimensional models.

On the second point, simulations by *Christensen and Yuen* [1984] indicate that a viscous slab acts as a stress guide, penetrating the 670 km phase boundary more easily. However, their model is strongly constrained in a manner that is likely to be most favorable to penetration: the slab is forced to be vertical, an angle of subduction not seen in the Earth, and must bend back upon itself in order to deflect, a mode of deflection apparently not seen

in the Earth. In addition, no overall lateral movement of the slab or migration of the subduction zone was allowed. In contrast, laboratory experiments [*Kincaid and Olson*, 1987; *Buttles et al.*, 1993] indicate that in the presence of retrograde trench migration [*Garfunkel et al.*, 1986] and a viscosity jump at 670 km, a highly viscous slab can flatten out along the 670 km discontinuity without a phase change being necessary at all, provided there is a large enough viscosity contrast across '670'. In addition, the cold slab material is highly viscous and when deflected by the phase change, has a greater tendency to stagnate in the transition zone [*Kincaid and Olson*, 1987; *Gurnis and Hager*, 1988; *Buttles et al.*, 1993].

Any jumps in viscosity at 670 km depth, which could be a viscosity increase [*Davies and Richards*, 1992; *Mitrovica and Peltier*, 1993], viscosity decrease [*Karato and Li*, 1992], or narrow zone of low viscosity [*Forte et al.*, 1993] may serve to decouple flow in the upper and lower mantles [*Ellsworth and Schubert*, 1988], altering the likelihood of slab penetration.

Other possible influences of variable viscosity

Clearly, high priority must be given to incorporating temperature-dependent viscosity in convection models with phase changes. However, a viscosity which is dependent solely on temperature arguably makes such models less Earth-like than constant viscosity models. This is because the downwellings in models with purely temperature-dependent viscosity are broad and symmetric (i.e., two-sided) [*Tackley*, 1993; *Steinbach and Yuen*, 1993], with considerable stress occurring where they leave the upper boundary layer. Thus, they do not resemble slabs in the Earth, which are narrow, asymmetric (single-sided), and enter the interior easily due to subduction zone faults, thereby allowing them to transmit more stress onto any obstacle. The dynamics of a slab encountering the '670' may be significantly different from the dynamics of one of the former downwellings encountering

the '670'. Realistic Earth-like slabs are obtainable by imposing subduction zone 'faults' [*Zhong and Gurnis*, 1992] or 'weak zones' [*Gurnis and Hager*, 1988; *Davies*, 1989a; *King and Hager*, 1994] at prescribed locations and much has been learned from such models. However, none of the above studies included phase changes; those that did [*Christensen and Yuen*, 1984; *Zhong and Gurnis*, 1994] have vertical, two-sided downwellings. In the long term it is desirable to generate a self-consistent (i.e., with no imposed features) model of variable-viscosity flow with phase changes, which must include some way of self-consistently generating plates and slabs, in itself a theoretical and numerical challenge that has so far eluded the geodynamical community.

The inclusion of temperature-dependent viscosity would result in a low viscosity layer immediately above the CMB due to the thermal boundary layer, which would strongly affect the formation and dynamics of upwelling plumes [*Olson et al.*, 1987, 1993], making them narrower, more concentrated, more vigorous, possibly resulting in more of them, and allowing the formation of plume heads [*Duncan and Richards*, 1991]. However, the possible lack of realism in plume activity in our model is not of concern since on the Earth plumes are minor features, carrying only 10-15% of the total heat flux [*Davies and Richards,* 1992; *Sleep*, 1990].

The addition of rigid plates and continents would probably reinforce the long wavelength nature of the flow [*Davies*, 1988b; *Gurnis and Zhong*, 1991; *Zhong and Gurnis,* 1993]. The plate tectonic cycle, including subduction zone locations, may be controlled by the assembly and breakup of supercontinents [*Gurnis*, 1988], which would pump power into the very lowest spherical harmonic degrees [*Anderson*, 1982; *Scrivner and Anderson*, 1992].

Conclusions

We have provided a detailed analysis of numerical simulations of mantle convection which incorporate the major phase changes of the transition zone, and investigated many ways in which the results can be compared to observations, such as seismic tomographic Earth models and the geoid. Although our model does not include the effects of variable viscosity, tectonic plates or continents, many of the major characteristics of the Earth are reproduced, such as the predominance of linear downwellings in the upper mantle (analagous to slabs), and the dominance of long-wavelength heterogeneity in the upper mantle and base of the mantle.

Our results indicate unambiguously that the effect of adding the exothermic phase change at 400 km depth is to diminish the propensity to layering by making avalanches smaller and more frequent. The system is much more sensitive to the strength of the 670 km phase change than to the strength of the 400 km phase change. Indeed, the current range of uncertainty in the Clapeyron slope at 670 km (-2 to -6 MPa K^{-1} [*Ito et al.*, 1990]) is likely to encompass a huge difference in model behavior.

Three distinct regions are evident, on the basis of both visual, and globally-averaged (e.g., spectral) characteristics. These are the upper mantle (UM), the mid-mantle (MM), and the deep mantle (DM). The upper mantle may be further subdivided into the transition zone, where the pooling of material occurs, and the shallow mantle. The UM and DM have large-amplitude long-wavelength signals, due to the pooling of cold downwellings at these depths, whereas the MM has the low-amplitude, broad spectrum typically associated with the interior of convecting regions. In the DM region, the pooling of cold avalanched material results in a zone of strongly depressed temperature, which may partially explain the appearance of large, seemingly very hot regions at this depth in seismic Earth models.

The geoid amplitude and spectrum are not significantly affected by the phase-change induced layering, and are similar to those of the Earth, Venus and simulations with no

phase change. This is because the contribution from the heterogeneity introduced into the transition zone is balanced by an opposite and nearly equal contribution from deflection of the 670 km discontinuity. The geoid is strongly influenced by structure of the upper mantle and weakly influenced by mid-mantle structure. Avalanches may be visible as geoid lows. However, the sign of the geoid anomaly over downwellings is opposite to that of the Earth. The most likely explanation for Earth's behavior is a large viscosity increase at around 670 km depth. Further models including an appropriate viscosity increase will be needed to examine the nature of the circulation and layering for models with realistic geoids.

In order to make comparisons with seismic Earth observations, we have looked at diagnostics based on the thermal field (spectral heterogeneity maps and radial correlation functions) and shown that these indicators are very sensitive, even at seismic tomographic resolution, to quite small amounts of stratification. Diagnostics based on the long-wavelength velocity field (such as radial mass flux), however, are rather insensitive to the degree of layering occurring in our model, due to the wavelength-dependence of flow stratification: At long wavelengths, whole-mantle flow is observed, whereas short wavelengths display flow stratification due to the modulation of downwellings in the transition zone.

This observation that the long-wavelength thermal field is strongly affected by the phase transition whereas long-wavelength flow field is not, may appear contradictory, since the thermal and flow fields are coupled in a convecting system, and most of the heat transport across the phase boundaries is by advection. It is not surprising that long-wavelengths of flow penetrate the '670', since these long wavelengths are sensitive only to structure that is vertically-averaged over a large lengthscale similar to the horizontal wavelength. The question then is: how can long-wavelength thermal structure build up about '670' if the flow field goes through? There are two points to make here. One is that the long wavelengths in the TZ thermal field arise not through direct inhibition of long-wavelength thermal structures but rather through a cascade of power from short

wavelengths (a narrow downwelling encountering the phase transition) to longer wavelengths (as the downwelling pools). The second is that the spectral content of velocity field will be a highly filtered (both radially and azimuthally) version of the thermal field, with a 1/wavelength^2 relationship expected from simple scaling analysis of the momentum equation. Thus, even if the long-wavelength thermal field changes abruptly at 670, the long-wavelength velocity field would not. Combining these two points one can understand the sequence of events at a particular azimuthal location: (1) a downwelling encounters the '670' and pools. Long-wavelength flow is inhibited at all radii, as a broad pool accumulates in the TZ until (2) the point of criticality is passed and an avalanche occurs.

Actual comparisons with Earth observations appear contradictory. The characteristics of the lateral spectrum at different depths (shown by spectral heterogeneity maps), and in particular the identification of three distinct regions in the mantle, are compatible with seismic tomographic models, particularly that of *Su et al.* [1992b]. However, there is no evidence of the peak in the globally-averaged lateral heterogeneity amplitude at 670 km depth which would be expected, even for weak layering [*Peltier and Solheim*, 1992; *Tackley et al.*, 1993b]. In addition, there is no evidence in the radial correlation functions (RCFs) of current generation seismic models, for any flow stratification at 670 km [*Jordan et al.*, 1993].

Since we have demonstrated that such diagnostics based on the thermal field are very sensitive to small degrees of stratification, even when filtered to the nominal resolution of seismic tomography, it would be tempting to conclude that the Earth does not currently exhibit any significant amount of flow stratification. However, such a conclusion would be contradicted by other forms of more localized evidence, such as tomographic images of slabs being deflected along the 670 km discontinuity [*van der Hilst et al.*, 1991; *Fukao et al.*, 1992]. It could be that there are inherent limitations in the data, parameterization or inversion techniques used in current seismic models which would mask characteristics such as a decorrelation in the RCF. Alternatively, it could be that future, more realistic

convection models will display a mode of stratification that is not detected in these diagnostics. It has been suggested that the Earth may flip in a globally-synchronous manner between layered and whole-mantle modes of flow, with it currently exhibiting a whole-mantle state [*Peltier and Solheim*, 1993]. However, we have argued that such global synchronicity is unlikely in three-dimensions. In addition, there is no evidence in the geological data for a recent massive acceleration in surface plate velocities as large as that expected to accompany such a global transition [*Weinstein*, 1993; *Solheim and Peltier*, 1994].

In any case, reconciling both globally-averaged and local characteristics of mantle convection simulations with observations of the Earth and Venus is an important challenge for the future.

Chapter 4

On the penetration of an endothermic phase transition by upwellings and downwellings

Using a simple criterion for the deflection of a constant-viscosity upwelling or downwelling by an endothermic phase transition, the scaling of the critical phase buoyancy parameter P_{crit} with the important lengthscales is obtained. The derived trends match those previously observed in time-dependent numerical simulations, implying that geometry is the dominant factor in determining the propensity to layering. For a sinusoidal temperature anomaly, P_{crit} is found to be proportional to wavelength, so that a stronger phase change is required to stop longer wavelengths, in accord with observations from three-dimensional numerical simulations. For more realistic Gaussian up- and downwelling features, the dependence of P_{crit} on width of feature, spacing of features, depth of phase transition and thickness of phase transition are determined for idealized internally-heated and basally-heated systems. Narrow up/downwellings are deflected more easily than broad ones, providing a first-order explanation for the increased propensity to layering as Rayleigh number is increased. Internal heating is found to strongly favor deflection, particularly when the phase

change is at shallow depth. For basally heated systems, the depth of the phase transition is found to be relatively unimportant, in contrast to internally-heated systems, where shallower phase transition strongly favors layering. Only weak dependence of P_{crit} on the spacing of up/downwellings is found. A narrower phase loop enhances deflection.

Introduction

The ability of the endothermic phase transition at 660 km depth to enforce layered convection in planetary mantles has been the focus of much recent numerical modeling [*Christensen and Yuen*, 1985; *Liu et al.*, 1991; *Machetel and Weber*, 1991; *Zhao et al.*, 1992; *Peltier and Solheim*, 1992; *Weinstein*, 1993; *Honda et al.*, 1993; *Tackley et al.*, 1993b, 1994], and the consensus emerging from these results is that of a partially or intermittently layered mantle characterized by accumulation of cold downwellings above the 660 km discontinuity followed by vigorous, catastrophic 'avalanches' of pooled material into the lower mantle. However, despite these recent modeling advances, a theoretical understanding of the important processes is not well developed.

From the numerical experiments, a number of trends are apparent: (1) Flow penetration through the phase transition is strongly wavelength-dependent, with whole-mantle convection observed at long-wavelengths, compatible with calculated flow for the Earth [*Phipps Morgan and Shearer*, 1993], but stratification at short wavelengths [*Tackley et al.*, 1994]. The propensity to layering is increased by (2) increasing the Rayleigh number [*Christensen and Yuen*, 1985; *Solheim and Peltier*, 1994; *Yuen et al.*, 1993]. (3) greater internal heating and (4) narrower phase loops [*Peltier and Solheim*, 1992].

There are two dynamical effects associated with phase transitions: the anomalous buoyancy resulting from vertical deflection of the phase boundary, and the latent heat release or absorption [*Schubert and Turcotte*, 1971; *Schubert et al.*, 1975]. At low

Rayleigh numbers, latent heat effects are dominant, and an endothermic phase transition is destabilizing, enhancing whole-mantle convection, as demonstrated in early theoretical work involving linear stability analysis [*Schubert and Turcotte*, 1971; *Schubert et al.*, 1975]. At higher, more realistic Rayleigh numbers, however, the buoyancy effect is dominant, and an endothermic phase transition favors layered convection. Indeed, *Christensen and Yuen* [1985] demonstrated that latent heat can be ignored to first order at higher Rayleigh numbers. An explanation for this is that in the linear stability analyses, an initially conductive temperature profile is assumed, so that latent heat release or absorption due to movement across the phase boundary results in horizontal temperature differences which drive further flow. This flow enhances convection for an endothermic transition and inhibits convection for an exothermic transition. However, at high Rayleigh numbers, a convective system tends to adopt an adiabatic temperature stratification, so that the temperature offset due to latent heat occurs everywhere, and movement through the phase transition does not result in additional horizontal temperature gradients. Thus, it is reasonable to focus exclusively on buoyancy effects due to deflection, when analyzing the effects due to phase transitions at high Rayleigh numbers.

In order to analyze the interaction of convective upwelling or downwellings with an endothermic phase transition, three distinct stages or regimes can be identified, which are sketched in Fig. 4.1. (1) (Fig. 4.1a) An upwelling or downwelling reaches the phase transition: does it penetrate or get deflected ? (2) (Fig. 4.1b) If deflected, deflected material pools above (for a downwelling) or below (upwelling) the phase transition, until the pool reaches a sufficient size to break through. This regime has been analyzed for the case of highly viscous downwellings by *Bercovici et al.* [1993] who find that cylindrical and linear downwellings are fundamentally different in their penetrative behavior. (3) (Fig. 4.1c) If pooling of material is pervasive, an internal boundary layer builds up: when does breakdown of layering occur ? This regime has been studied by applying a local boundary-layer analysis to the internal boundary layer to predict when it will become unstable and

Figure 4.1. The three stages/regimes of behavior, in the interaction of convective features with an endothermic phase boundary. Black features are cold downwellings, white features hot upwellings. a) Up/downwellings first meet the phase transition. b) Pooling of a downwelling above the phase transition. c) Pervasive layering.

a.

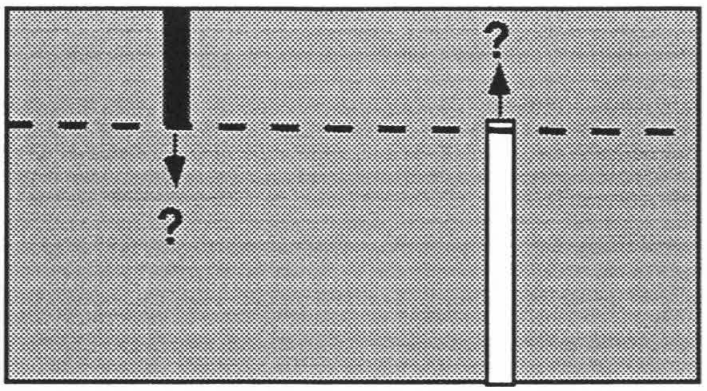

b.

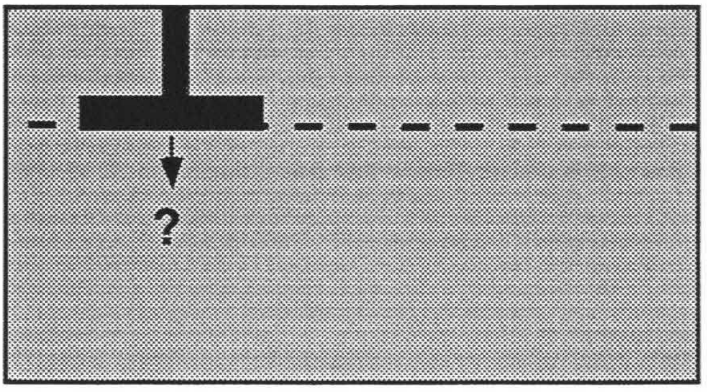

c.

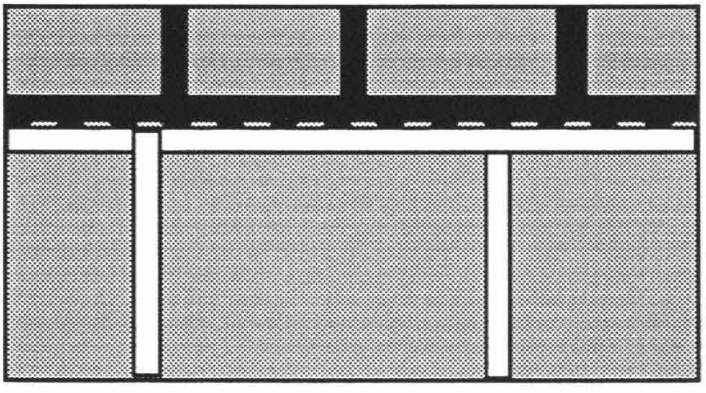

hence breakthrough will occur [*Solheim and Peltier*, 1994], which results in a periodicity with a distinct timescale.

Although the second and third regimes have received recent attention, the first regime, shown in Fig. 4.1a, has not. *Yuen and Olson* [1982] present some analytical calculations for a plume encountering phase transitions and conclude that the Clapeyron slope of the transition must exceed -30 MPa K^{-1} to prevent penetration. Later numerical simulations, however, indicated that a much lower value of -6 MPa K^{-1} could enforce total layering [*Christensen and Yuen*, 1985], with strongly intermittent layering occurring at lower values such as -2 MPa K^{-1} [*Machetel and Weber*, 1991], or -2.8 MPa K^{-1} [*Peltier and Solheim*, 1992]. The purpose of this present study is to examine this regime in detail, by means of analytic models in which the interaction of idealized up/downwellings with the endothermic phase change is examined and the effect of the important lengthscales is determined.

Model

The Boussinesq approximation is assumed in two-dimensional Cartesian geometry, allowing a simple streamfunction formulation of the governing equations [e.g., *Turcotte and Schubert*, 1982].

$$\nabla^4 \psi = \rho_x \tag{4.1}$$

$$u = \psi_z \quad ; \quad v = -\psi_x \tag{4.2}$$

where Ψ=stream function, ρ=density, and u and v are horizontal and vertical velocities, respectively.

Two-dimensional Cartesian geometry is assumed for this present study. The use of three-dimensional and/or spherical geometry will probably change the quantitative nature of the results, but not the observed trends, which are the main focus of this study.

The anomalous buoyancy resulting from phase boundary deflection is represented as a mass anomaly at a prescribed depth (discontinuous phase transition) or depth range (finite-width phase transition). This is equivalent to the sheet mass anomaly approach of *Tackley et al.* [1993b,1994] (discontinuous phase transition) or the effective thermal expansivity approach of *Christensen and Yuen* [1985] (finite-width phase transition), both of which have been found in numerical simulations to give a reasonable approximation to a full treatment when phase boundary deflection is small compared to the width of convective features. When phase boundary deflection becomes comparable to width of convective features, this approximation become inaccurate. However, since the aim of this study is to establish trends and to derive simple scaling relationships, this seems a reasonable approximation at this stage.

The effect of the phase transition is represented by a single parameter, the phase buoyancy parameter, which can be interpreted as the ratio of buoyancy due to phase change deflection to the buoyancy due to thermal effects, integrated over a column:

$$\sigma_{phase} = \delta_{ph}\Delta\rho_{ph} = \frac{\gamma\Delta T}{\rho g}\Delta\rho_{ph} \tag{4.3}$$

$$\sigma_{thermal} = \rho g \alpha \Delta T h \tag{4.4}$$

$$P = \frac{\sigma_{phase}}{\sigma_{thermal}} = \frac{\gamma\Delta\rho}{g\alpha\rho^2 h} \tag{4.5}$$

Where σ_{phase} and $\sigma_{thermal}$ are the anomalous surface densities (i.e., mass per unit area) due to phase change deflection and thermal expansion respectively, δ_{ph}=phase change

deflection, γ=Clapeyron slope, $\Delta\rho_{ph}$=density jump across phase change, g=gravitational acceleration, α=thermal expansivity, ΔT=temperature scale (usually taken to be the superadiabatic temperature drop across the layer), and h=a lengthscale (usually taken to be the depth of the layer). It is important to note that the influence of the phase transition is independent of temperature scale, since both phase change deflection and thermal buoyancy are proportional to this parameter.

Representative values of the relevant parameters are listed in Table 4.1. The phase buoyancy parameter resulting from these is of order -0.1.

Symbol	Parameter	Value	Units
γ_{660}	Clapeyron Slope at 660 km	-3	MPa K^{-1}
$\Delta\rho_{660}$	Density jump at 660 km	400	kg m^{-3}
g_{660}	gravitational acceleration	9.8	m s^{-2}
α_{660}	thermal expansivity	$2.5x10^{-5}$	K^{-1}
ρ_{660}	mean density	4200	kg m^{-3}
h	mantle depth	2890	km
P_{660}	phase buoyancy parameter	-0.096	-

Table 4.1. Representative values of parameters at the 660 km discontinuity

The analysis starts with the simplest possible case and progresses through models of increasing realism as follows:

(1) The interaction of sinusoidal temperature anomaly in an infinite domain with an endothermic phase change is examined analytically. This regime is relevant to a local analysis around the phase change region, when the effects of upper and lower boundary conditions are not significant. Information about the wavelength-dependence of flow

penetration, and the scaling of critical phase buoyancy parameter with wavelength, is obtained.

(2) Upper and lower boundary conditions are added, and the analysis for a sinusoidal temperature anomaly is repeated. Additional information about the effect of boundaries, phase change depth, and phase change width, is obtained.

(3) More realistic upwellings and downwelling are considered, assuming a Gaussian horizontal temperature profile. The effect of the important lengthscales, namely width of feature, spacing of features, depth of phase transition, and width of phase transition, are obtained. Convective features which have just reached the phase boundary, as well as those which extend throughout the mantle depth, are considered.

Infinite domain, sinusoidal anomaly

The flow solution for a sinusoidal (horizontally) temperature anomaly in an infinite domain with a phase transition can be straightforwardly obtained by deriving the solution for the periodic anomaly with no phase change, deriving the solution for a sinusoidal sheet mass anomaly, and exploiting the linearity of the problem, by simply adding these to obtain the total solution.

Firstly, equation (4.1) is transformed into Fourier space:

$$(k^2 + l^2)^2 \, \tilde{\psi} = -ik\tilde{\rho} \tag{4.6}$$

$$\tilde{\psi} = -\frac{ik\tilde{\rho}}{(k^2 + l^2)^2} \tag{4.7}$$

where k and l are the horizontal and vertical wave numbers respectively, and ρ is density. Thus, the different flow solutions can be obtained by inserting appropriate density anomalies into the above equation.

Periodic T

Consider a periodic temperature distribution with wavenumber k_0. For algebraic simplicity we will use the form exp(ikx), bearing in mind that the physically observable component (sine) corresponds to the imaginary part of this.

$$T = T_0 \exp(ik_0 x) \tag{4.8}$$

$$\rho = \rho_0 + Ra.T = \rho_0 + Ra.T_0 \exp(ik_0 x) \tag{4.9}$$

where ρ_0 is the background density and the Rayleigh number (Ra) is defined in terms of previously defined parameters plus dynamic viscosity η and thermal diffusivity κ, as:

$$Ra = \frac{\rho_0 g \alpha \Delta T h^3}{\eta \kappa} \tag{4.10}$$

Transforming into Fourier space (where the $1/2\pi$ normalization is applied entirely on the reverse transform):

$$\tilde{\rho} = Ra.\delta(k - K_0)\delta(l) \tag{4.11}$$

and substituting into (4.1)

$$\tilde{\psi} = -\frac{iRa}{k_0^3}\delta(k - k_0)\delta(l) \tag{4.12}$$

yields a spatial solution:

$$\psi = -\frac{iRa}{k_0^3}\exp(ik_0 x) \tag{4.13}$$

giving velocities:

$$v_x = 0 \quad ; \quad v_z = \psi_{,x} = \frac{Ra}{k_0^2}\exp(ik_0 x) \tag{4.14}$$

Sheet mass anomaly

Consider a periodic sheet mass anomaly at z=0 with surface density σ

$$\rho = \sigma\delta(z)\exp(ik_0 x) \tag{4.15}$$

Transforming, we obtain

$$\tilde{\rho} = \frac{1}{2\pi}\sigma\delta(k - k_0) \tag{4.16}$$

Yielding a flow solution

$$\tilde{\psi} = -\frac{ik_0}{2\pi(k_0^2 + l^2)^2}\sigma\delta(k - k_0) \tag{4.17}$$

Noting that:

$$IFT\left(\frac{k_0}{(k_0^2 + l^2)^2}\right) = \frac{\pi}{2k_0^2}[1 + k_0|z|]\exp(-k_0 z) \tag{4.18}$$

where IFT denotes inverse Fourier transform, we obtain

$$\psi = \frac{i\sigma}{4k_0^2}(1 + k_0|z|)\exp(-k_0|z| + ik_0x) \tag{4.19}$$

hence the vertical velocity

$$v_z = -\frac{\sigma}{4k_0}(1 + k_0|z|)\exp(-k_0|z| + ik_0x) \tag{4.20}$$

Total solution

To obtain the total vertical velocity at the position of the phase change, z=0, the vertical velocity solutions for thermally and phase-change driven flow are summed. The sheet mass anomaly resulting from phase change deflection is given by:

$$\sigma = -P.Ra.T \tag{4.21}$$

giving a total vertical velocity of:

$$v_{z,tot}(x,0) = Ra.T_0\left[\frac{1}{k_0^2} + \frac{P}{4k_0}\right]\exp(ik_0x) \tag{4.22}$$

Thus, by requiring v_z=0, the critical phase buoyancy parameter for inhibition of flow of wavelength λ across the phase transition is obtained.

$$P_{crit} = -(2/\pi)\lambda \tag{4.23}$$

So there is a straightforward proportionality between P_{crit} and λ. This is easy to understand since in this case there is only one lengthscale, the horizontal wavelength, and thus a self-similar solution is expected, dependent on the single parameter λ/P. This relationship provides a first-order explanation of the observation made in *Tackley et al.* [1994], that flow at long wavelengths tends to penetrate the phase transitions whereas flow at short wavelengths tends to be inhibited from penetrating.

Note that shorter wavelengths, or stronger P, would imply a total vertical velocity (at z=0) in the opposite direction to thermally-driven flow. However, a real, thermally-driven convective system would be unable to reach a point at which local phase-change driven flow exceeded local thermally-driven flow, since it would first have to pass through a point at which the two were equal, implying zero vertical velocity. The system would adjust itself so that $v_z(x,0)=0$ for wavelengths less than the critical.

For P=-0.1, the representative value from Table 4.1, the critical nondimensional wavelength is 0.157, corresponding to a dimensional wavelength of 454 km.

Bounded domain, periodic T

It is desirable to determine the effect of boundaries on the above solution, and for this purpose, impermeable, free-slip boundaries are imposed at z=0 (lower boundary) and z=1 (upper boundary), with the phase change occurring at a distance d_{ph} from the upper boundary, i.e., at $z=1-d_{ph}$. A sinusoidal temperature anomaly, independent of z, is imposed, as before. Note that this is not the temperature field of thermal convection, which normally has constant temperature boundary conditions, but it can be thought of as a realisitic Fourier decomposition of the temperature field everywhere except in the boundary layers. At this point the effect of finite width phase boundary (as opposed to discontinuous) is also investigated, leading to four parameters: the horizontal wavelength λ, the phase

buoyancy parameter P, the depth of the phase change d_{ph}, and the half-width of the phase change w_{ph}.

The velocity solution is obtained numerically using the spectral technique described in Appendix C. A complex Fourier expansion is used in the x-direction and a sine expansion in the z-direction. Enough harmonics are taken (typically 128 spectral modes in each direction) to ensure that the values of P_{crit} are accurate to 10^{-4}, and convergence tests are also given in Appendix C. As with the infinite domain case, solutions for thermally-driven flow and phase-change-driven flow are calculated separately. Using the linearity of the instantaneous velocity solution, the phase buoyancy parameter required for zero flow across the phase boundary is derived. In cases with a finite-width phase transition, a tanh profile describes the transition from one phase to the other, leading to a phase-change effective thermal expansivity [*Christensen and Yuen*, 1985] as given below:

$$\alpha_{phase}(d) = \frac{P}{2w_{ph}}\left(1 - \tanh^2\left[\frac{d - d_{ph}}{w_{ph}}\right]\right) \tag{4.24}$$

Figures 4.2 and 4.3 show flow solutions for short and long horizontal wavelengths respectively. In each case the critical phase bouyancy parameter has been chosen for the total solution. For the shorter wavelength, the phase-change driven flow (Fig. 4.2b) is localized around the phase boundary, and away from the phase boundary, the total solution (Fig. 4.2c) resembles the thermally-driven solution (Fig. 4.2a). For the long wavelength, however, both thermally-driven flow and phase-change driven flow fill the domain. This indicates that the vertical extent of flow caused by a sheet mass anomaly is comparable to the horizontal wavelength of the sheet mass anomaly, as is evident from Equation (4.17).

The dependence of P_{crit} on the three important lengthscales is given in Fig. 4.4. For each graph, the other lengthscales are set to the default values given in Table 4.2. Figure 4.4a gives the dependence of P_{crit} on the horizontal wavelength, nondimensionalized to the

depth of the box. At short wavelengths, the slope of the graph is approximately $(2/\pi)$, consistent with the analytical solution derived earlier. At these wavelengths, the effects of boundaries is negligible and it is reasonable to assume an infinite domain when calculating flow close to the phase boundary. However, as the wavelength is increased, the boundaries become increasingly important and the gradient of the curve decreases greatly, thereby reducing P_{crit} from the infinite domain solution. The boundary conditions reduce the strength of phase transition required to prevent flow from penetrating, particularly at long wavelengths.

The effect of phase transition depth is illustrated in Fig. 4.4b, for two wavelengths, 0.25 and 2.0. Over a depth range of approximately 0.2 to 0.8, the depth of the phase change has very little influence on P_{crit}. However, when the phase transition is very close to the boundary, the required phase change strength can change greatly.

The width of the phase transition is varied in Fig. 4.4c, for the same two wavelengths. At the longer wavelength of 2.0, the required value of $|P_{crit}|$ increases slightly as the width of phase transition in increased to 0.1. However, for the shorter wavelength of 0.25, there is a large increase in $|P_{crit}|$, approximately doubling from around 0.13 to 0.26. Thus, a wider phase transition region decreases the ability of a phase transition to stop flow, particularly when the wavelength is comparable to the width of the phase transition, implying that the short wavelengths which are most likely to be inhibited are also the most sensitive to the width of the phase transition. This is in accordance with the two-dimensional axisymmetric numerical simulations of *Peltier and Solheim* [1992], and illustrates the importance of trying to obtain a phase transition width as narrow as possible. The phase transition width for the Earth is expected, from laboratory experiments [*Ito and Takahashi*, 1989] and seismological observations [*Benz and Vidale*, 1993] to be a few kilometers at the most.

Given that P_{670} for the Earth is of order -0.1, as shown earlier, only the shortest wavelengths are likely to be completely inhibited from crossing the phase transition,

Figure 4.2. Flow fields (streamfunction) for a short-wavelength sinusoidal temperature field (wavelength=0.25). Thermally driven flow (top), phase-change driven flow (center) and total flow for critical phase buoyancy parameter (bottom). Note how the phase-change driven flow is localized around the phase transition for this wavelength.

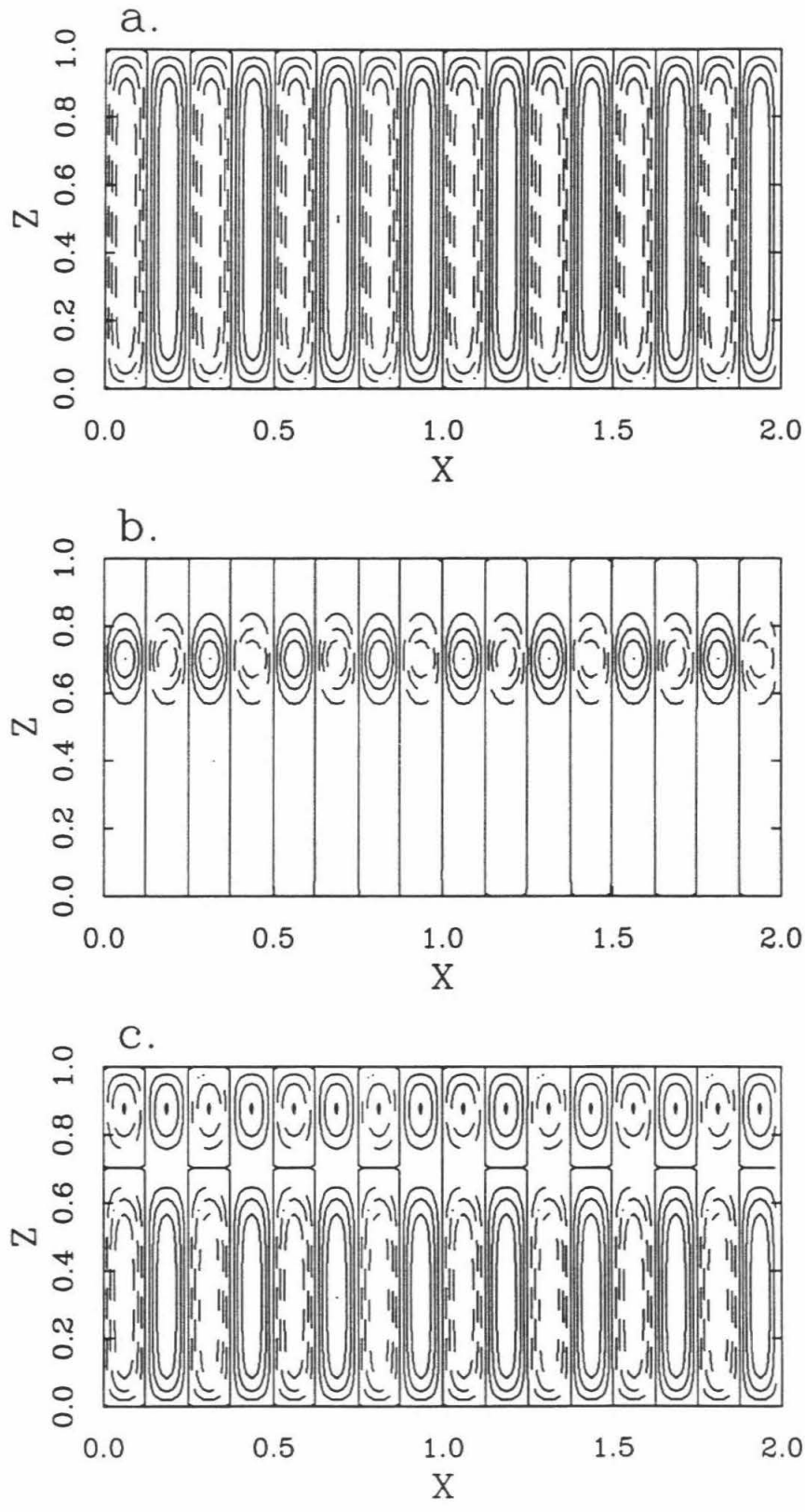
a.
Z
0.0 0.2 0.4 0.6 0.8 1.0
0.0 0.5 1.0 1.5 2.0
X
b.
Z
0.0 0.2 0.4 0.6 0.8 1.0
0.0 0.5 1.0 1.5 2.0
X
c.
Z
0.0 0.2 0.4 0.6 0.8 1.0
0.0 0.5 1.0 1.5 2.0
X

Figure 4.3. Flow fields (streamfunction) for a long-wavelength sinusoidal temperature field (wavelength=2.0). Thermally driven flow (top), phase-change driven flow (center) and total flow for critical phase buoyancy parameter (bottom). Note how the phase-change driven flow extends throughout the domain for this wavelength.

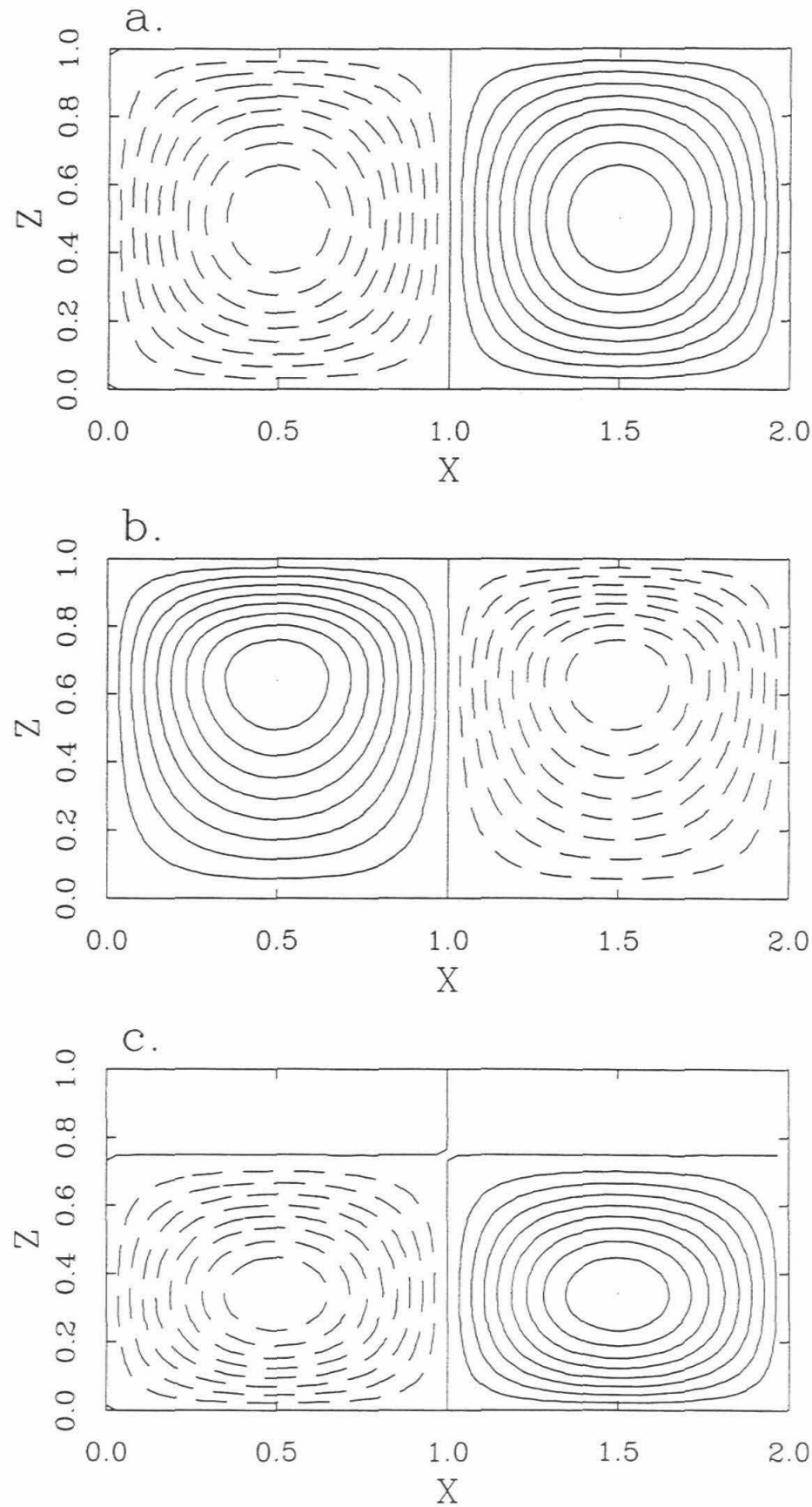
a.
b.
c.
Z
X
0.0
0.2
0.4
0.6
0.8
1.0
0.0
0.5
1.0
1.5
2.0

Figure 4.4. Critical phase buoyancy parameter (P_{crit}) plotted against the three important lengthscales, for a sinusoidal temperature field in a bounded domain. The two curves in b) and c) refer to short (0.2, dashed line) and long (2.0, solid line) wavelengths.

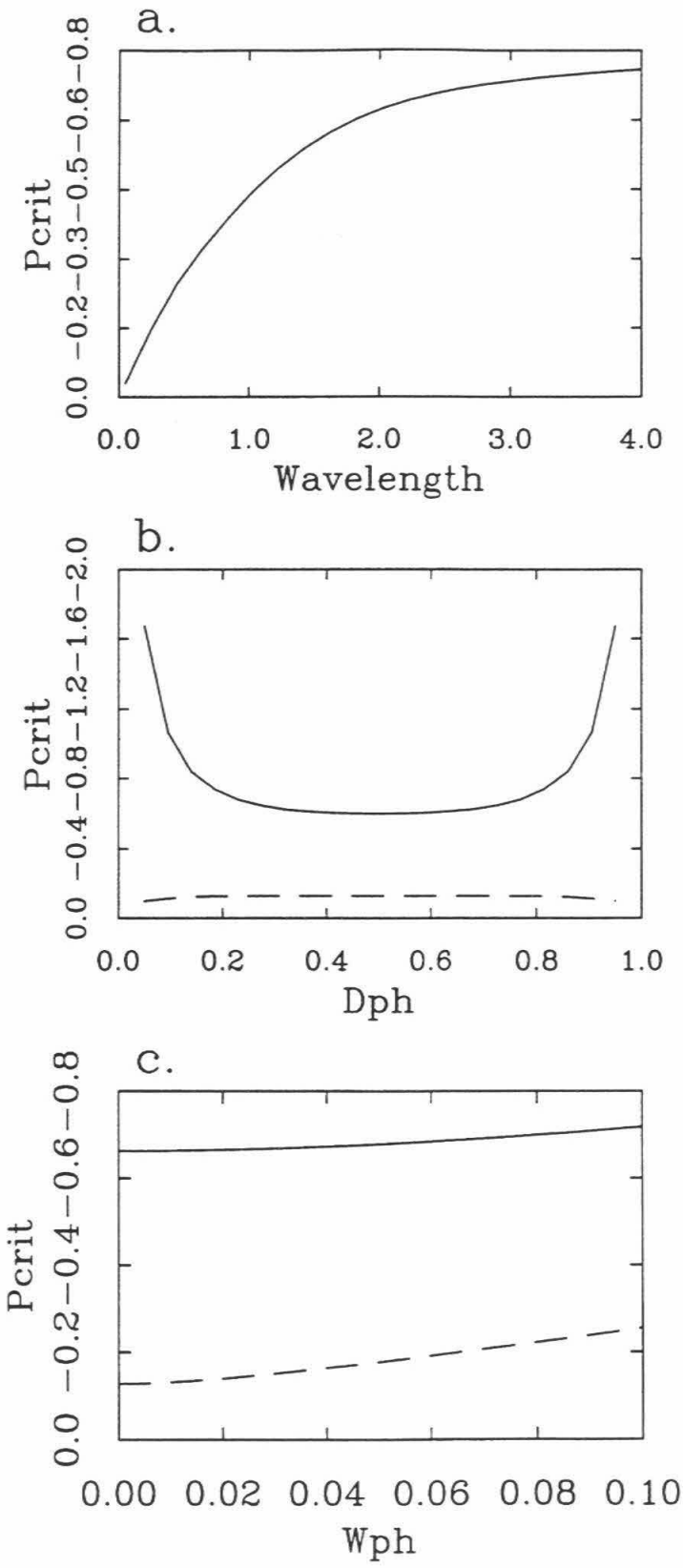
a.
Pcrit
0.0 −0.2−0.3−0.5−0.6−0.8
0.0
1.0
2.0
3.0
4.0
Wavelength
b.
Pcrit
0.0 −0.4−0.8−1.2−1.6−2.0
0.0
0.2
0.4
0.6
0.8
1.0
Dph
c.
Pcrit
0.0 −0.2−0.4−0.6−0.8
0.00
0.02
0.04
0.06
0.08
0.10
Wph

assuming a constant amplitude with depth. However, if long-wavelength temperature anomalies have a peak near 660 km depth, as indicated in the numerical solutions, then these modes will be more inhibited than predicted here.

Symbol	Meaning	Default value
λ or L_x	wavelength	2.0
d_{ph}	phase transition depth	0.25
w_{ph}	phase transition half-width	0.0
w_x	half-width of up/downwelling	0.01

Table 4.2. Default values of lengthscales

Gaussian up/downwellings

Convective features in real systems do not in general resemble sine waves, and thus it is desirable to consider the interaction of more realistic up/downwellings with phase transitions. In constant-viscosity simulations, the up/downwellings have an approximately Gaussian temperature profile, the profile that is chosen here. Four idealized scenarios are considered, as illustrated in Fig. 4.5. These span the extremes of complete basal heating, represented by an upwelling and a downwelling of equal strength and width, and internal heating, in which only downwellings are present. Of course, these are only crude approximations of real convective systems, which may have long wavelength anomalies in addition to concentrated features, but are useful for establishing some first-order trends. Initially, we consider up/downwellings which extend the depth of the box, as in *Yuen and Olson* [1982]. Since we are, however, interested in determining whether an

up/downwelling that has just reached the phase change will penetrate, we then progress to cases in which the up/downwellings have just reached the phase transition.

An additional lengthscale, the width of convective feature, is introduced, leading to a total of four lengthscales: the horizontal periodicity (L_x), depth of phase transition (d_{ph}), width of phase loop (w_{ph}) and width of convective feature (w_x). Default values of these are listed in Table 4.2. The numerical technique is that used in the previous section and described in Appendix A. In these results, w_x is defined as the Gaussian half-width of the temperature anomly, i.e., the temperature profile through an up/downwelling is given by:

$$\Delta T \propto \exp\left[-\left(\frac{x-x_0}{w_x}\right)^2\right] \tag{4.25}$$

A typical flow pattern for the case of basal heating and up/downwellings extending the full height of the box (as illustrated in Fig. 4.5a) is given in Fig. 4.6. The total solution has $P=P_{crit}$, which is here defined as the value required for zero velocity in the center of the up/downwelling. However, away from the up/downwelling, flow penetrates the phase transition, a phenomena which can be seen in the numerical results of *Weinstein* [1993]. It is only in regions where temperature anomalies exist at 660 km that flow is inhibited from crossing the phase transition.

Figure 4.7 shows the results for the case of basal heating with Gaussian up/downwellings extending the full height of the box (as illustrated in Fig. 4.5a). The trends of P_{crit} with w_{ph} (Fig. 4.7a) and d_{ph} (Fig. 4.7b) are similar to those observed with the sinusoidal anomaly: increased phase loop thickness increases P_{crit}, and phase change depth does not have much effect except when the phase transition is near one of the boundaries. The trends of P_{crit} with w_x and L_x are new. P_{crit} increases as the width of up/downwelling increases, so that for a fixed P, narrow features are deflected whereas broad features will penetrate. The horizontal spacing of features (L_x) does not have much

Figure 4.5. Idealized up/downwellings for the four cases analyzed. Black features are cold downwellings, and white features are hot upwellings. On the top row are basally-heated cases, on the bottom row are internally-heated cases. Left column shows up/downwellings extending through the full depth of the box, right column shows up/downwellings just reaching the phase transition.

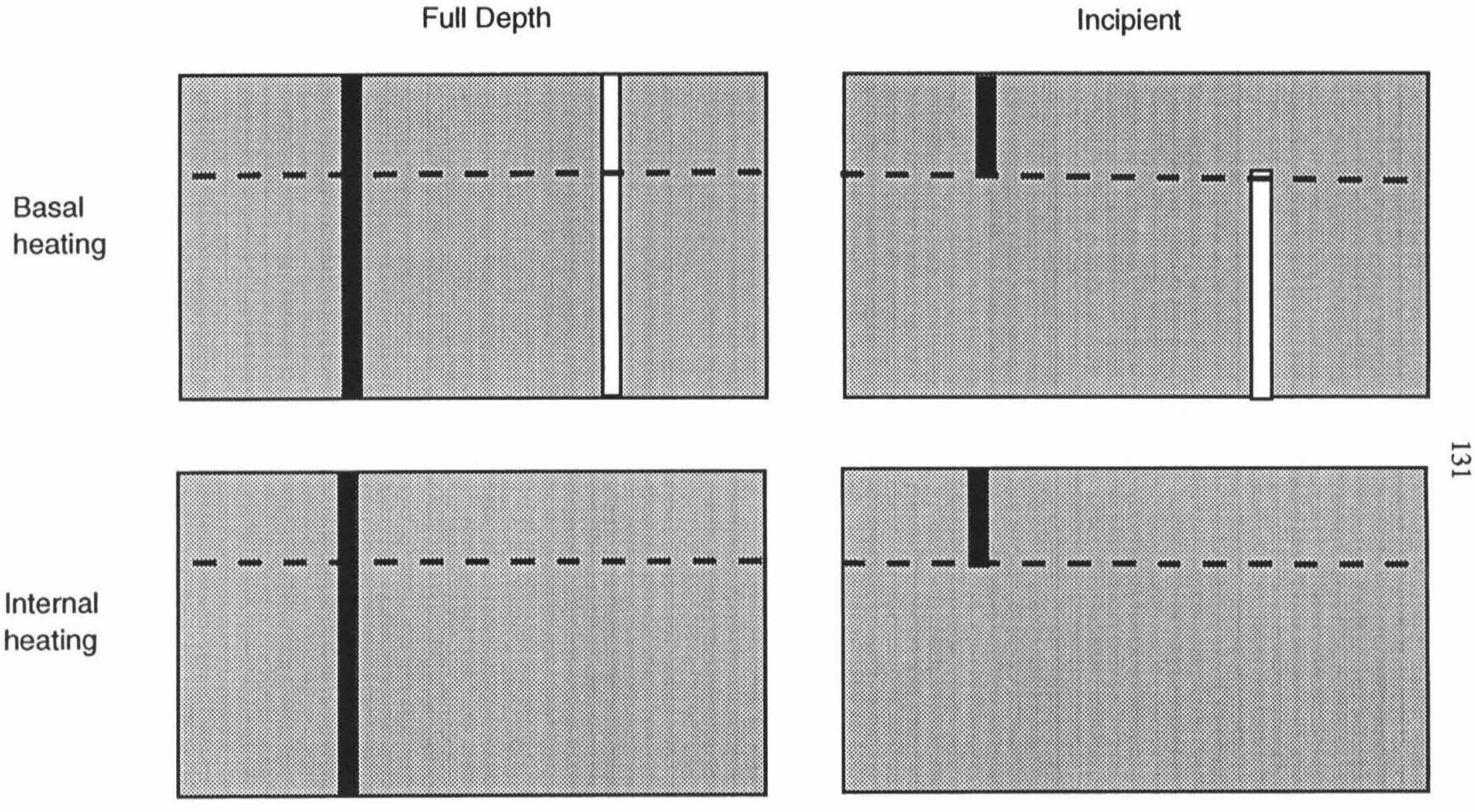
Full Depth
Incipient
Basal heating
Internal heating

Figure 4.6. Flow field for full-depth, basally-heated case. Upwelling at x=0, x=2 and downwelling at x=1.0. Note that away from the up/downwellings, flow penetrates the phase transition.

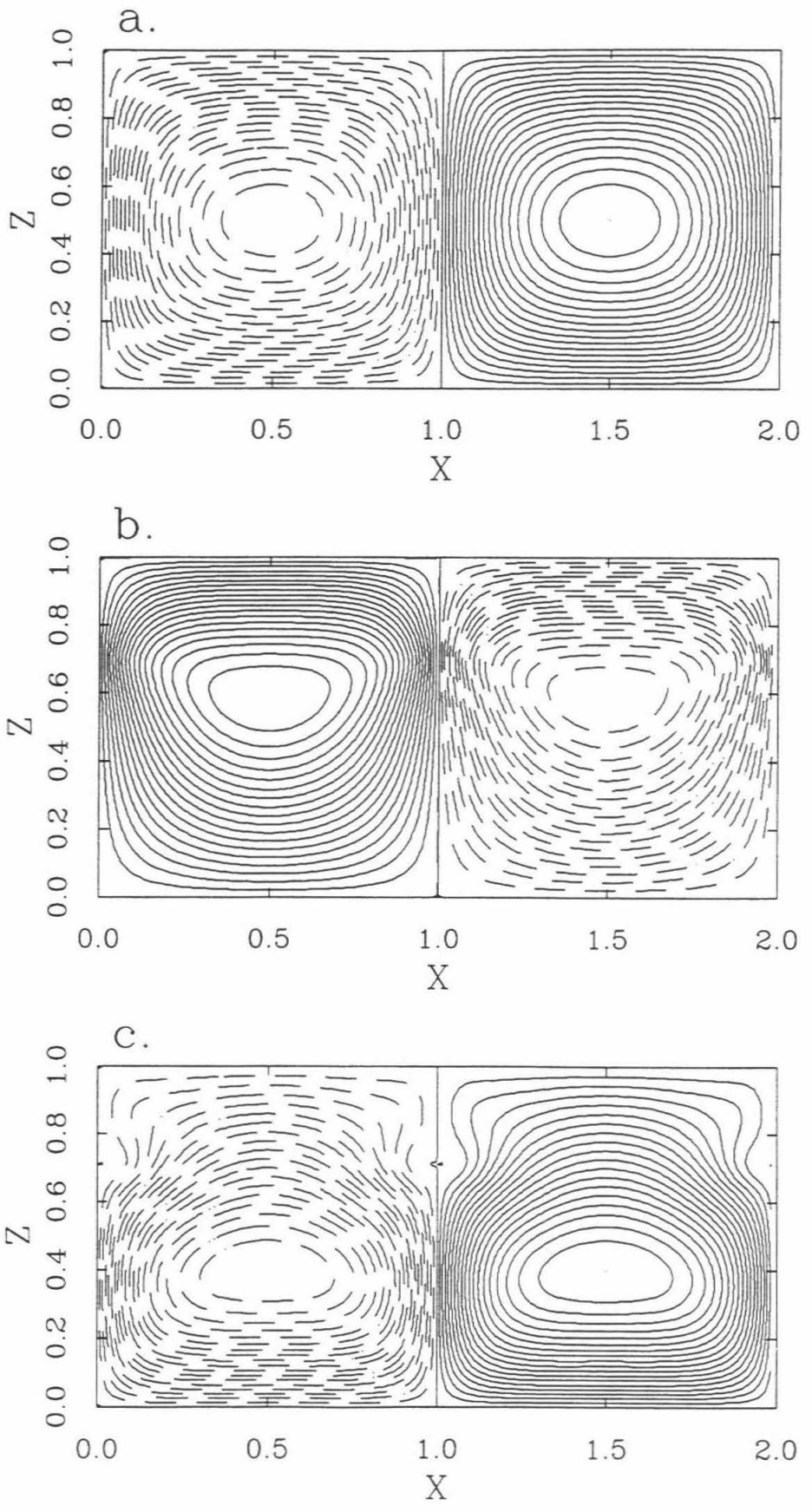
a.
b.
c.
Z
X
0.0
0.2
0.4
0.6
0.8
1.0
0.5
1.5
2.0

Figure 4.7. Critical phase buoyancy parameter P_{crit}, plotted against the four important lengthscales, for basally heated convection with up/downwellings extending throughout the entire domain (Fig. 4.5a).

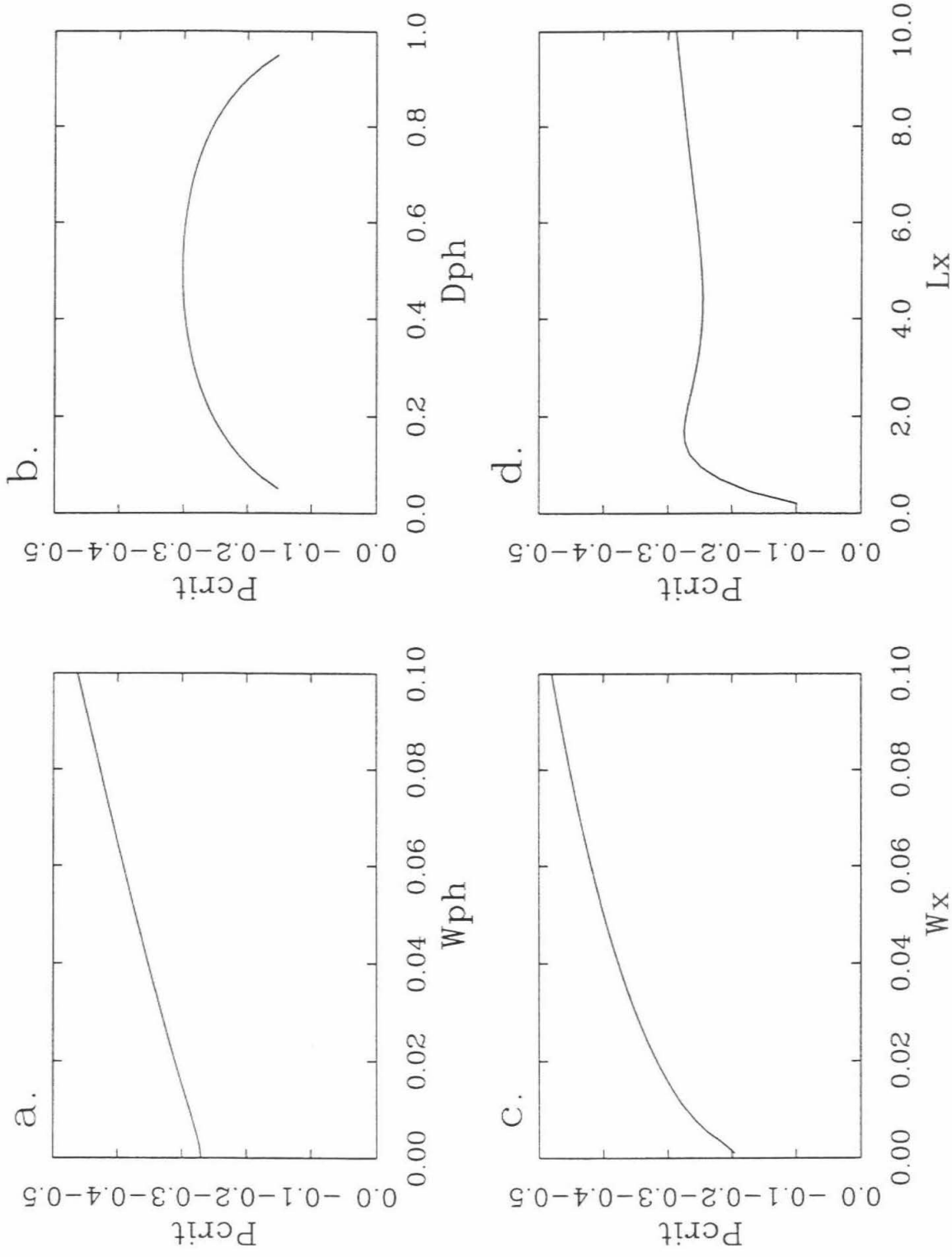
a.
b.
c.
d.
Pcrit
0.0
−0.1
−0.2
−0.3
−0.4
−0.5
Wph
Dph
Wx
Lx
0.00
0.02
0.04
0.06
0.08
0.10
0.0
0.2
0.4
0.6
0.8
1.0
2.0
4.0
6.0
8.0
10.0

Figure 4.8. Critical phase buoyancy parameter P_{crit}, plotted against the four important lengthscales, for internally heated convection with downwellings extending throughout the entire domain (Fig. 4.5c).

a.
b.
c.
d.
Pcrit
0.0
−0.1
−0.2
−0.3
−0.4
−0.5
Wph
0.00
0.02
0.04
0.06
0.08
0.10
Dph
0.0
0.2
0.4
0.6
0.8
1.0
Wx
Lx
2.0
4.0
6.0
8.0
10.0

Figure 4.9. Critical phase buoyancy parameter P_{crit}, plotted against the four important lengthscales, for basally heated convection with up/downwellings just reaching the phase transition (Fig. 4.5b). Solid lines are for upwellings, dashed lines for downwellings.

a.
b.
c.
d.
Pcrit
0.0 −0.1 −0.2 −0.3 −0.4 −0.5
Wph
0.00 0.02 0.04 0.06 0.08 0.10
Dph
0.0 0.2 0.4 0.6 0.8 1.0
Wx
Lx
0.0 2.0 4.0 6.0 8.0 10.0

Figure 4.10. Critical phase buoyancy parameter P_{crit}, plotted against the four important lengthscales, for internally heated convection with downwellings just reaching the phase transition (Fig. 4.5d).

a.
b.
c.
d.
Pcrit
0.0
-0.1
-0.2
-0.3
-0.4
-0.5
Wph
Dph
Wx
Lx
0.00
0.02
0.04
0.06
0.08
0.10
0.0
0.2
0.4
0.6
0.8
1.0
2.0
4.0
6.0
8.0
10.0

effect, except for very small spacing, at which deflection of up/downwellings becomes easier.

With internal heating (graphs in Fig. 4.8, illustration in Fig. 4.5c), similar trends are observed, except that values of P_{crit} are lower, implying that internal heating increases the propensity to layering.

When up/downwellings that have just reached the phase transition are considered (graphs in Fig.4.9, illustrated in Fig. 4.5b), the trends are similar to the case with full-length up/downwellings, but a number of differences arise. Firstly, when the phase transition is not at mid-depth, a different strength is required to stop the upwelling than to stop the downwelling, as indicated by the two curves in each part of Fig. 4.9. When the phase change is at shallow depth, the upwelling can penetrate more easily than the downwelling, as observed in the numerical simulations of *Tackley et al.* [1993b,1994]. Secondly, the values of P_{crit} are significantly lower. This is due to the fact that the phase-change deflection and hence buoyancy is the same, but depth-integrated thermal buoyancy is reduced since the features do not extend through the whole depth of the box.

For internal heating and up/downwellings that have just reached the phase change (graphs in Fig. 4.10, illustrated in Fig. 4.5d), similar trends are observed but the following differences arise. Firstly, the depth of the phase transition becomes very important, with deflection becoming easier for shallower phase changes, and more difficult for deeper phase changes. Secondly, the value of P_{crit} is much lower for internal heating than that for basal heating, a result which has been observed in numerical simulations, e.g., *Solheim and Peltier* [1994].

Discussion and conclusions

In the interaction of upwellings and downwellings with an endothermic phase transition, there are two important lengthscales of the flow: (1) The wavelength associated

with the spacing of up/downwellings and (2) the wavelength associated with the width of convective features. In general, the long wavelengths associated with the spacing of up/downwellings pass through the phase transition, even when a concentrated feature is deflected at the boundary. This is shown in Fig. 4.6, which shows up- and downwellings being deflected even though the broad-scale flow penetrates the phase transition. Deflection of an up/downwelling by the phase transition is a short-wavelength mode of flow, and the results here indicate that shortwavelengths are more easily deflected than long wavelengths.

From the results presented here, most of the trends observed in numerical simulations of convection with phase transitions (summarized in the introduction) can be explained as a consequence of geometry. These are (1) wavelength-dependence of flow penetration, and increased layering due to (2) higher Rayleigh number, (3) internal heating and (4) narrower phase loops. These points will now be discussed in detail, together with (5) the effect of phase transition depth and (6) the effect of horizontal wavelength.

(1) *Tackley et al.* [1993b, 1994] observe in three-dimensional spherical simulations of phase-transition modulated convection that flow penetration through the 670 km phase transition is strongly wavelength-dependent, with the longest wavelengths penetrating the phase change easily, but shorter wavelengths becoming increasingly inhibited. The results here with a sinusoidal temperature field provide a direct explanation of this observation. At short wavelengths, only features in the direct vicinity of the '660' influence flow penetration, and there is a proportionality between the phase change strength required to stop flow (P_{crit}), and the wavelength of the flow. Indeed, this proportionality implies that only buoyancy forces that are within a distance to the phase change comparable to the horizontal wavelength matter when considering flow penetration. Thus, a more suitable choice of lengthscale to use in the definition of phase buoyancy parameter (equation 5) would be horizontal wavelength of the feature in question--with this choice, the critical P would always be of order 1. At longer wavelengths, however, features in the entire

domain, including boundary conditions, influence the flow, reducing P_{crit} from the value predicted from a proportionally with wavelength.

(2) These results show that narrower convective features are more easily deflected and thus result in a greater propensity to layering. This is related to the wavelength-dependence of flow penetration observed with sinusoidal anomalies: narrower features have more short-wavelength power than broad features. Since higher Rayleigh numbers lead to narrower features, this implies that higher Rayleigh numbers lead to greater layering, a trend which is well established from numerical simulations [*Christensen and Yuen*, 1985; *Solheim and Peltier*, 1994; *Yuen et al.*, 1994].

Solheim and Peltier [1994] attribute the increase in layering with Rayleigh number to greater temperature anomalies and thus greater phase change deflections. However, it is not clear how this would cause the observed trend, since the important criterion for penetration is the ratio of buoyancy due to phase change deflection to thermal buoyancy, as discussed earlier, and both of these buoyancies increase in proportion to temperature. Thus, if phase change deflections and hence temperature anomalies are higher, thermal buoyancy will be higher by the same proportion, and the ratio of the two buoyancy forces is not changed. The results presented here show that greater layering at higher Ra is a natural consequence of geometry, with narrow features being more easily deflected, and does not require any arguments based on temperatures or any other factor. Note, however, that this study does not address the suitability of a local Rayleigh number criterion in determining the breakdown of layered convection [*Solheim and Peltier,* 1994], since this is a different aspect of the system's behavior (compare Fig. 4.1 parts a. and c.).

(5) For basally-heated convection, the depth of the phase transition does not have a large effect on the propensity to layering. This is consistent with the numerical simulations of *Christensen and Yuen* [1985] who note that phase transition depth does not have a strong influence on the critical phase buoyancy parameter. However, when the phase transition is shallower than mid-depth, upwellings penetrate more easily than

downwellings, consistent with the numerical simulations of *Tackley et al.* [1993b, 1994]. Thus, for an internally-heated mantle, phase transition depth has a large effect on the ability of downwellings to penetrate, such that a shallower phase transition increases the propensity to layering. Since the mantle is thought to be largely internally heated [*Schubert*, 1979; *Davies and Richards*, 1992], it is important to have the phase transition at the correct depth in numerical models, if the results are to be quantitatively correct.

(3) These results indicate that increased internal heating strongly favors greater layering, particularly when the phase change is at a realistic shallow depth. This is consistent with the numerical results of *Solheim and Peltier* [1994].

(4) *Peltier and Solheim* [1992] demonstrate how layering is enhanced by narrower phase loops, a trends that is also indicated by the results presented here. The present results also show that the influence of phase loop width is dependent on the horizontal wavelengths, such that short wavelengths are more affected by phase loop width. This suggests that phase loop width is important when it becomes comparable to the width of convective features. Provided the phase loop width is much smaller than convective features, the exact value is not important. However, in most of the numerical simulations currently being performed, phase loop width is comparable to the width of convective features and thus the degree of layering is probably underpredicted.

(6) *Zhong and Gurnis* [1994] demonstrate using two-dimensional models that with an imposed constant surface velocity (representing a plate), the degree of layering is strongly affected by the imposed plate length, such that longer lengths favor easier penetration. This may at first appear to contradict the present results, in which horizontal wavelength (L_x) does not significantly affect the dynamics. However, the surface velocity that these authors use is the same for all plate lengths, so that longer plates are thicker. Hence, up/downwellings are broader, and penetrate the endothermic phase transition more easily. Thus, the present analysis suggests that the greater penetration observed for longer

plates is due to the thicker downwellings, rather than any inherent effect of the horizontal wavelength.

These results have shown that a simple criterion for flow penetration leads to an explanation for all the trends observed in numerical experiments. In the future, it would be useful to apply this model to determine the effects of additional complications. These include three-dimensionality, i.e., does a cylindrical feature penetrate more or less easily than a linear feature?; the effect of the 400 km phase transition, which acts in the opposite sense to the 660 km phase transition, enhancing the flow of material through itself; the effect of depth-dependent properties associated with compressibility; and the effect of temperature-dependent viscosity, which leads to stronger downwellings and weaker upwellings, thereby influencing flow penetration.

Chapter 5

Effects of strongly temperature-dependent viscosity on time-dependent, three-dimensional models of mantle convection

Numerical simulations of thermal convection in a wide (8x8x1) Cartesian box heated from below with temperature-dependent viscosity contrasts of 1000, and a Rayleigh number 10^5 show that boundary conditions and aspect ratio have an enormous effect on the preferred flow pattern. With rigid upper and lower boundaries, spoke-pattern flow with small (diameter ~ 1.5) cells is obtained, consistent with laboratory experiments and previous numerical results. However, with the arguably more realistic stress-free boundaries, the flow chooses the largest possible wavelength, forming a single square cell of aspect ratio 8, with one huge cylindrical downwelling surrounded by upwelling sheets. The addition of stress-dependence to the rheology weakens the stiff upper boundary layer, resulting in smaller cells, though still with upwelling sheets and downwelling plumes.

Introduction

Increasingly realistic numerical models of three-dimensional (3-D) thermal convection in planetary mantles have been published in recent years, with Rayleigh numbers approaching that of the Earth, and various other complexities such as spherical geometry, depth-dependent properties, and mineralogical phase changes [*Bercovici et al.*, 1989b, *Balachandar et al.*, 1992, *Tackley et al.*, 1993b]. However, by far the largest approximation in these calculations is the assumption of viscosity which is constant, or only depth-dependent. The viscosity of the Earth's mantle is known to be very strongly temperature dependent, resulting in the formation of rigid surface plates, and strongly modulating the characteristics of other proposed features, such as plumes from the core-mantle boundary. Thus, it is essential to incorporate such rheology into numerical models.

Laboratory experiments have given some insights into variable viscosity convection, but are limited in their applicability to the Earth by the use of rigid boundary conditions, since the mobility of plates on the Earth suggests that stress-free boundary conditions are appropriate. *White* [1988] determined that the spoke-pattern is preferred for rigid boundary conditions, Rayleigh numbers above about 25000 and large viscosity variations.

Numerical work has mainly focussed on steady-state solutions in small boxes. *Ogawa et al.* [1992] modeled viscosity contrasts of up to 10^5, identifying the stagnant lid regime, characterized by upwelling plumes and downwelling sheets beneath a stagnant lid, and the whole-mantle regime, characterized by up- and down-welling plumes with sheet-like extensions. *Christensen and Harder* [1991] determined that in small boxes (aspect ratio up to 1.5) temperature-dependent viscosity favors upwelling plumes and downwelling sheets. They also obtained a spoke-pattern solution for rigid boundary conditions in a 4x4x1 box with viscosity contrasts of 30. Perhaps the most prophetic result was obtained by *Weinstein and Christensen* [1991], who, in the same 4x4x1 box, found that simply

changing the upper boundary condition to stress-free resulted in a much longer wavelength pattern consisting of upwelling sheets and a downwelling plume.

In order to understand the Earth's mantle, it is important to determine the flow patterns with stress-free boundaries at both top and bottom, with large viscosity contrasts, and in a box whose aspect ratio is similar to the effective aspect ratio of the Earth's mantle. Here, solutions with these characteristics are presented.

Model

In order to isolate the effect of variable viscosity, the Boussinesq approximation is assumed, with all coefficients constant except viscosity. The infinte Prandtl number equations, non-dimensionalized to thermal diffusion timescale (D^2/κ), mantle depth (D), and superadiabatic temperature drop (ΔT), are as follows:

$$\nabla \bullet \underline{v} = 0 \tag{5.1}$$

$$\nabla \bullet \underline{\underline{\tau}} - \nabla p = Ra_{1/2} T \hat{\underline{z}} \tag{5.2}$$

$$\tau_{ij} = \eta(v_{i,j} + v_{j,i}) \tag{5.3}$$

$$\frac{\partial T}{\partial t} = \nabla^2 T - \nabla \bullet (\underline{v} T) \tag{5.4}$$

where $\underline{v}$, p, T, $\underline{\underline{\tau}}$, and η are velocity, dynamic pressure, temperature (varying from 0 at the top boundary to 1 at the base), deviatoric stress and dynamic viscosity, respectively, $\underline{z}$ is a unit vector in the vertical direction, and the Rayleigh number $Ra_{1/2}$ is defined using the viscosity at T=0.5 as follows:

$$Ra_{1/2} = \frac{\rho g \alpha \Delta T D^3}{\eta_{1/2} \kappa} \tag{5.5}$$

where ρ=density, g=gravitational acceleration, α=thermal expansivity and κ=thermal diffusivity. Viscosity is described by an Arrhenius law:

$$\eta_{New}(T) = \exp\left[13.8155\left(\frac{1}{T+1} - \frac{1}{1.5}\right)\right] \tag{5.6}$$

giving a variation between 100 and 0.1, with $\eta(0.5) = 1.0$

For the stress-dependence case:

$$\eta_{non-New} = \eta_{New}^{1/n} \dot{e}^{1/n-1} \sigma_0^{1-1/n} \tag{5.7}$$

$$\eta_{eff} = 2(\eta_{New}^{-1} + \eta_{non-New}^{-1})^{-1} \tag{5.8}$$

where n is the power-law index, $\dot{e}$ is the strain rate and σ_0 is a reference stress. This gives Newtonian creep at low stresses, and non-Newtonian creep at high stresses.

The side boundaries are periodic, with top and bottom boundaries being isothermal (T=0 and 1 respectively) and impermeable, and either stress-free or rigid.

Numerical method

The instantaneous velocity and pressure fields given by (5.1)-(5.3) are calculated by a finite difference (control volume) multigrid technique, using primitive variables ($\underline{v}$ and p) on a staggered grid [e.g., *Patankar*, 1980]. The iterative scheme is extremely robust, converging for almost any viscosity contrast. This scheme is incorporated into a standard multigrid V-cycle [*Brandt*, 1982, *Press et al.*, 1992], giving convergence in order (number

of points) operations. When stress-dependent viscosity is included, the viscosity field is re-calculated after every V-cycle. Explicit timestepping (equation (5.4)) is performed using the MPDATA algorithm [*Smolarkiewicz*, 1984] for advection, and second order finite-differences for diffusion. Steps of one half the Courant condition are used. The method is well suited to parallel computers, and the presented results were obtained on the Intel Touchstone Delta at the California Institute of Technology.

Extensive benchmarking has been performed, in two dimensions against the standard benchmarks for constant [*Travis et al.*, 1990a] and temperature-dependent [*Blankenbach et al.*, 1989] viscosity, and in three dimensions againt the results of *Travis et al.* [1990b] for constant viscosity, and *Ogawa et al.* [1991] for viscosity contrasts of up to 3.2×10^4. For cases with Rayleigh number of order 10^5, agreement of the Nusselt number to 2% was found with 32 vertical grid cells.

Parameters

Case	Viscosity	Boundaries	Time (steps)	Nu	Tmean
1	constant	stress-free	0.437 (19600)	9.05	0.488
2	1000,n=1	rigid	0.353(14200)	4.15	0.674
3	1000,n=1	stress-free	0.188(10500)	6.22	0.629
4	1000,n=3	stress-free	0.231(15200)	8.91	0.602

Table 5.1. Simulation Characteristics

The four cases presented are listed in Table 5.1: one has constant viscosity, two have temperature-dependent viscosity and different boundary conditions, and one has stress-dependence added. All cases are entirely heated from below, with an aspect ratio of 8 in both horizontal directions, slightly less than the effective aspect ratio of the Earth's mantle

(~10 at mid-depth), and 128x128x32 grid cells in the two horizontal and vertical directions respectively. $Ra_{1/2}$ is 10^5, two orders of magnitude lower than that of the Earth's mantle, but similar to that used in previous numerical and laboratory studies.

Cases were started from an identical initial state consisting of an isothermal interior (T=0.5), error-function boundary layers at top and bottom, and small random (white noise) perturbations of amplitude 0.05. After initial transients, the flow patterns were found to evolve very slowly but steadily, requiring large integration times (time≈0.2-0.4, 10000-19000 steps) to ensure solutions had overcome their transient nature and basal and surface Nusselt numbers were in good agreement.

In case 4, the nondimensional reference stress σ_0 was set to 500, approximately the mean stress from case 3, in order to weaken the upper boundary layer without getting the extreme viscosity variations obtained with non-Newtonian creep at all stress levels [*Malevsky and Yuen*, 1992].

Results

Temperature-dependent viscosity reduces the Nusselt number (Nu) and increases the mean temperature (Tmean), as listed in Table 5.1. The remainder of the discussion will focus on convective pattern.

The constant viscosity case (case 1) is illustrated in Fig. 5.1a. There is a rough symmetry between up- and downwellings, which both start off as sheets, decaying into plumes as they ascend or descend respectively. The downwellings exhibit greater connectivity in this very weakly time-dependent pattern, reflected in T_{mean} being slightly lower than 0.5; however, this is just by chance, since the equations are symmetric with respect to the vertical coordinate in this case. In small aspect-ratio boxes, stable patterns at this Rayleigh number include 2-D rolls, bimodal flow, and square or hexagonal cells, depending on the box dimensions and initial conditions [*Travis et al.*, 1990b]. The weakly

time-dependent pattern obtained here lies somewhere between these idealized cases, also displaying some characteristics of the spoke pattern.

Case 2 (Fig. 5.1b) has temperature-dependent viscosity and rigid boundary conditions. The spoke pattern is observed, as in laboratory experiments [*White*, 1988]. There is an asymmetry between up- and downwellings, also noted by *Christensen and Harder* [1991]: downwelling sheets persist beyond mid-depth, whereas upwelling sheets have broken up into plumes by mid-depth.

A completely different pattern is obtained with stress-free boundary conditions (case 3, Fig. 5.1c). Initially, many small cells formed, but over a nondimensional time of ~0.05, the downwellings merged to form one huge quasi-cylindrical downwelling, resulting in a single square cell filling the entire computational domain. Upwelling sheets extend all the way from the base to the surface. Although the overall pattern remained very stable throughout the remainder of the calculation, the exact details of upwellings and downwellings were highly time-dependent. In order to test the robustness of this solution to initial conditions, an additional calculation was done, starting from the final state of the rigid boundary case 2. After a nondimensional time of ~0.1, a single square cell was again formed. Stable long-wavelength flows resulting from temperature-dependent viscosity and stress-free boundaries have previously been found in two-dimensional simulations, also in an aspect ratio 8 box [*Daly*, 1980].

In case 4 (Fig. 5.1d), the stress-dependent viscosity has resulted in softening of the stiff upper boundary layer, making it easier for it to enter the interior and hence resulting in smaller circulation cells. Again, upwelling sheets and downwelling plumes are obtained.

Discussion

The upwelling sheets and downwelling plumes found in the stress-free cases are compatible with the result obtained by *Weinstein and Christensen* [1991] in a 4x4x1 box

Fig. 5.1. Isocontours of residual temperature, showing where the temperature is higher (red) or lower (blue) than the horizontally-averaged value, by ±0.15 except where stated: a) (top left) Case 1, b) (top right) Case 2, c) (bottom left) Case 3, red contour is +0.1, d) (bottom right) Case 4, contours are ±0.1

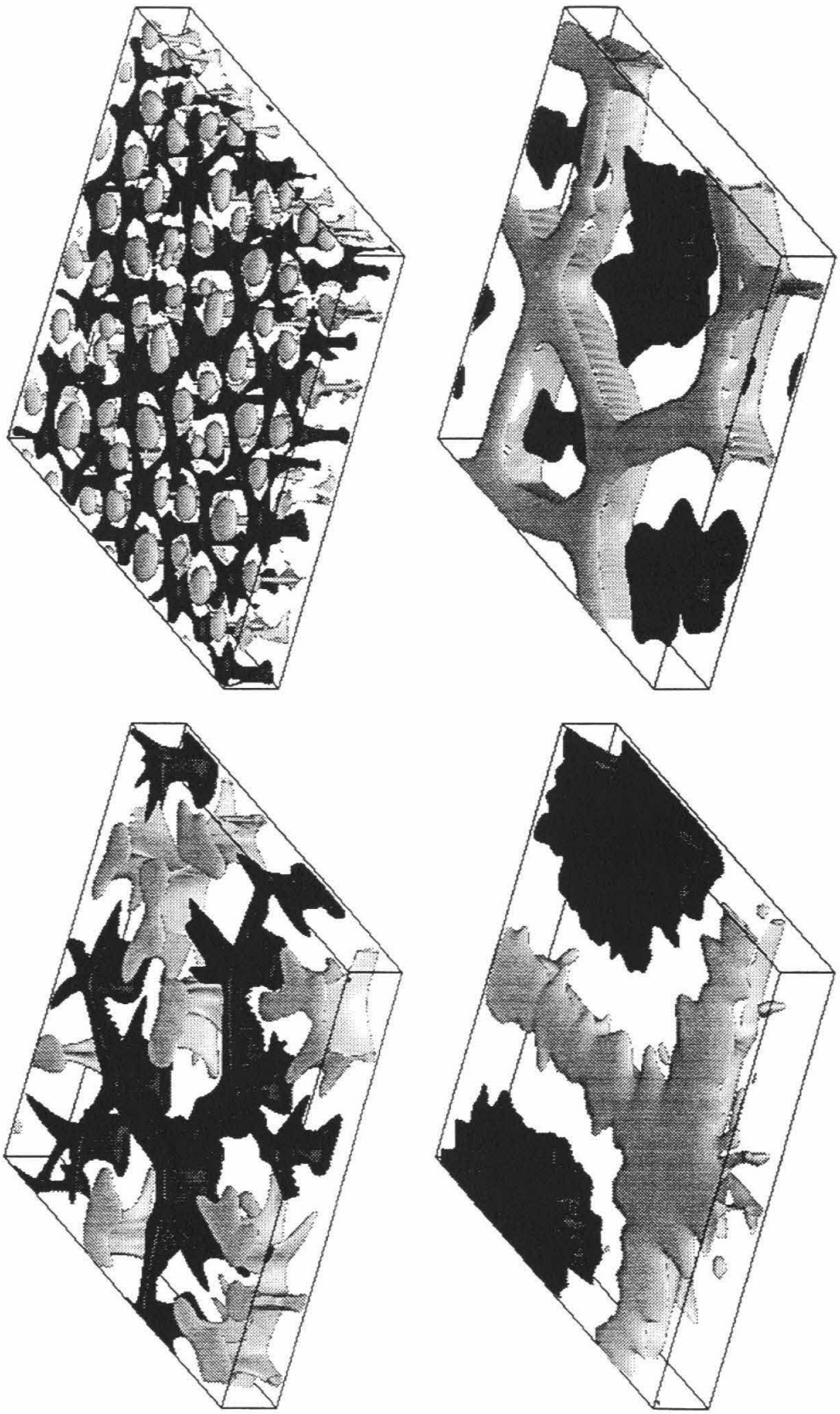

with isothermal, rigid lower and stress-free upper boundaries, and a viscosity contrast of 50. The pattern can be understood in the following terms: Depth-dependent properties cause the local Rayleigh number to decrease with depth, resulting in large cells with downwelling sheets and upwelling plumes [*Balachandar et al.*, 1992]. In these simulations, the local Rayleigh number increases by three orders of magnitude with depth. Thus, the inverse flow pattern is obtained: upwelling sheets and downwelling plumes, with the viscous upper boundary layer imposing a long wavelength to the flow. Future calculations must establish the flow pattern when both depth-dependent properties and temperature-dependent viscosity are included, as well as the effects of spherical geometry, which favors upwelling plumes and downwelling sheets [*Bercovici et al.*, 1989b], and strong internal heating, which favors disconnected cold plumes [*Houseman*, 1988]. If taken literally, the upwelling sheets would suggest active deep upwelling below mid-ocean ridges. However, this would seem to contradict various geophysical observables [*Davies*, 1988a]; thus the robustness of these features to the above mentioned effects must be tested.

Although linear slab-like downwellings are not obtained, on the Earth these generally occur at continental margins, suggesting that continents are necessary to obtain slabs. On Venus, the huge quasi-cylindrical downwellings may correspond to plateau-shaped highlands found in, for example, Ishtar Terra or Aphrodite Terra [*Bindschadler et al.*, 1992]

In these simulations, the upper boundary layer participates in the flow. If the viscosity contrast were increased sufficiently, a 'stagnant lid' would develop [*Ogawa et al.*, 1991], and the convective pattern might resemble the rigid boundary case, with small cells. However, the mobility of plates on the Earth suggest that this regime is not relevant to Earth dynamics, even though the viscosity contrast over the lithosphere may be extremely large. On Venus, the high surface temperature also raises doubts about the relevance of this regime.

Conclusions

These results show clearly the importance of stress-free boundary conditions and wide domains in understanding mantle convection with temperature-dependent viscosity. Very large cells are formed, with upwelling sheets and downwelling plumes, in contrast to the small-wavelength spoke pattern obtained with rigid boundary conditions. Although deep upwelling below mid-ocean ridges is suggested, the robustness of these patterns to internal heating, depth-dependent properties, spherical geometry and higher Rayleigh number needs to be established.

Chapter 6

Effects of strongly variable viscosity on three-dimensional compressible convection in planetary mantles

A systematic investigation into the effects of temperature-dependent viscosity on three-dimensional compressible mantle convection has been performed by means of numerical simulations in Cartesian geometry using a finite-volume multigrid code, with a factor of 1000-2500 viscosity variation, Rayleigh numbers ranging from 10^5-10^7, and stress-free upper and lower boundaries. Enormous differences in model behavior are found depending on the details of rheology, heating mode, compressibility and boundary conditions. Parameter choices were guided by realistic Earth models.

In Boussinesq, basally-heated cases with viscosity solely dependent on temperature and stress-free, isothermal boundaries, very long-wavelength flows (~25000 km, assuming the depth corresponds to mantle thickness) with cold plumes and hot upwelling sheets result, in contrast to the upwelling plumes and downwelling sheets found in small domains, illustrating the importance of simulating wide domains. The addition of depth-dependence results in small cells, and reverses the

planform, causing hot plumes and cold sheets. Compressibility, with associated depth-dependent properties, results in a tendency for broad upwelling plumes and narrow downwelling sheets, with large aspect-ratio cells.

Perhaps the greatest modulation effect occurs in internally-heated compressible cases, in which the short-wavelength pattern of time-dependent cold plumes commonly observed in constant-viscosity calculations completely changes into a very long-wavelength pattern of downwelling sheets (spaced up to 24000 km apart) with time-dependent plume-like instabilities. These results are particularly interesting since the basal heat flow in the Earth's mantle is usually thought to be very low, e.g., 5-20% of total.

The effects of viscous dissipation and adiabatic heating play only a minor role in the heat budget for constant-viscosity cases, an observation which is not much affected by the Rayleigh number. However, viscous dissipation becomes very important in the stiff upper boundary layer when viscosity is temperature-dependent, an effect which is caused by the very high stresses occurring in this stiff lid, typically two orders of magnitude higher than the stresses in the interior of the domain, for the viscosity contrast modeled here. The temperature in the interior of convective cells is highly sensitive to the material properties, with temperature-dependent viscosity and depth-dependent thermal conductivity strongly increasing the internal temperature, and depth-dependent viscosity strongly decreasing it.

The sensitivity of the observed flow pattern to these various complexities clearly illustrates the importance of performing compressible, variable-viscosity mantle convection calculations with rheological and thermodynamic properties matching as closely as possible those of the Earth.

Introduction

Arguably the most important varying material property of mantle minerals is the extreme temperature-dependence of the viscosity as well as its dependence on pressure and stress [*Weertman*,1970; *Weertman and Weertman*, 1975; *Stocker and Ashby*, 1973; *Durham et al.*, 1979]. Viscosity is likely to vary by many orders of magnitude over the range of conditions encountered in the mantles of Earth or Venus, and thus, if we are to obtain a complete understanding of this process, viscosity variations are an essential component in numerical models. In order to simultaneously obtain the range of features observed in planetary mantle convection, for example, linear slabs, cylindrical plumes, and toroidal motion, three-dimensionality (3-D) is also an essential ingredient. Indeed, two-dimensional (2-D) rolls become unstable to 3-D disturbances at a fairly low Rayleigh number, both with rigid [*Busse*, 1967; *Richter,* 1978; *Frick et al.*, 1983] and stress-free [*Travis et al.*, 1990b; *Christensen and Harder*, 1991] upper and lower boundaries. Although there has been much progress in 3-D modeling of mantle convection over the past decade, it has only recently become possible to include large viscosity variations in time-dependent, 3-D models with wide domains [*Tackley*, 1993]. The purpose of this present study is to further analyze and greatly extend the Boussinesq, basally-heated results of *Tackley* [1993], focusing on the effects that compressibility, internal heating, depth-dependence of the viscosity, and Rayleigh number, on mantle circulation with temperature-dependent viscosity.

It is instructive to review our current understanding of 3-D mantle convection as it relates to this present study, starting with constant-viscosity fluids and moving on to variable-viscosity fluids. Both laboratory and numerical studies have been performed. Although laboratory experiments have played a useful role, they are limited in their applicability to the Earth by the common use of rigid boundary conditions, since the

mobility of plates on the Earth suggests that stress-free boundary conditions are appropriate.

Constant-viscosity studies

Boussinesq. The Boussinesq approximation [*Boussinesq*, 1903; *Rayleigh*, 1916], in which density is assumed constant except for weak variations with temperature which appear in the bouyancy term of the momentum equation, and (usually) material properties are assumed constant, has commonly been used in studies of mantle convection. Numerical simulations and laboratory experiments on Boussinesq fluids with constant material properties at moderate Rayleigh numbers (Ra) in rectangular Cartesian boxes have indicated that many different convective patterns are possible at a particular Ra, depending on the initial conditions, size of box and heating mode. For basally-heated convection, *Whitehead and Parsons* [1978] performed laboratory experiments with rigid upper and lower boundaries at Rayleigh numbers (Ra) between $5x10^4$ and $7.6x10^5$ and found that spoke patterns (i.e., up- and downwelling plumes interconnected at the boundaries by an irregular polygonal network of linear spokes) or bimodal patterns (i.e., orthogonal superimposed rolls) were possible over this range, with square patterns being possible at the highest Ra. The stability of squares and bimodal patterns were investigated numerically by *Frick et al.* [1983], who computed steady solutions in periodic boxes with rigid upper and lower boundaries for Ra up to $2.6x10^4$, finding that squares were unstable over this parameter range, decaying into rolls or bimodal flow. *Travis et al.* [1990b] modeled the more realistic case of free-slip upper and lower boundaries over Ra ranging from $2x10^4$ to $5x10^5$, and studied the stability of the various patterns as a function of aspect ratio, Ra and initial conditions. At $Ra=10^5$, they found that stable solutions include rolls, bimodal flow, up-squares (i.e., upwelling hot plumes surrounded by square patterns of downwelling cold sheets), down-squares (i.e., downwelling cold plumes surrounded by square patterns of

upwelling hot sheets), and hexagons. *Malevsky and Yuen* [1993] reported time-dependent solutions at very high Ra of up to 10^8, and found that at Ra higher than about 10^7, these simple patterns break down into a complex time-dependent flow characterized by disconnected up- and downwelling plumes emanating from irregular cellular ridge patterns at the upper and lower boundaries.

In these simple cases with constant material properties, identical upper and lower mechanical and thermal boundary conditions and no internal heating, patterns are symmetric with respect to upwellings and downwellings, with, for example, downwelling plumes (as found in down-squares or hexagons, for example) being equally as likely as upwelling plumes (as in up-squares or hexagons). This symmetry is, however, broken by (1) internal heating, (2) compressibility (with associated depth-dependent properties), (3) spherical geometry, and (4) temperature-dependent viscosity. These effects will now be discussed.

Internal heating. It is thought that the mantle resembles to first order an internally-heated fluid [*Schubert*, 1979], with core heat flow accounting for only 6-20% of the surface heat flow [*Davies*, 1988a; *Sleep*, 1990; *Davies and Richards*, 1992; *Stacey*, 1992], secular cooling accounting for up to 30% [*Sharpe and Peltier*, 1978; *Schubert et al.*, 1980; *Stacey*, 1992; *Breuer and Spohn*, 1993] and the remainder due to the radioactive decay of elements ^{238}U, ^{232}Th and ^{40}K in the mantle [*Turcotte and Schubert*, 1982; *Stacey*, 1992]. Laboratory experiments on internally-heated plane layers with rigid boundary conditions [e.g., *Carrigani*, 1985 and references therein] have generally focused on the stability of hexagonal patterns, finding that up-hexagons (i.e., upwelling hot plumes surrounded by haxagonal cold sheets) are preferred at higher Ra. With free-slip boundaries, however, internally-heated convection is characterized by isolated cold downwelling plumes amidst a diffuse hot upwelling flow. *Schubert et al.* [1993] obtained steady-state, internally-heated Boussinesq solutions at a Ra of 1.4×10^4 in both Cartesian and spherical geometries, finding that several solutions were possible. However, internally-heated convection

becomes time-dependent at lower Ra than basally heated convection [*Schubert and Anderson*, 1985] and the resulting patterns are characterized by relatively closely-spaced, transient cold plumes, with sheet-like interconnections at the upper boundary layer, and little or no long-lived coherent structure, as illustrated by *Houseman* [1988] at $Ra=5.9x10^5$ and *Parmentier et al.* [1994] at Ra up to $3x10^7$. Convection heated partly from within and partly from below has been investigated by *Houseman* [1988], *Weinstein and Olson* [1990] and *Travis et al.* [1990c], who find that as the fraction of internal heating is decreased, downwellings become more sheet-like and interconnected.

Compressibility. The studies discussed above all use the Boussinesq limit. Compressibility, which implies depth-dependence of material properties as well as additional terms in the equations, has been included in the Cartesian, basally-heated calculations of *Balachandar et al.* [1992,1993]. They find that compressibility breaks the symmetry between upwellings and downwellings, resulting in very broad, strong hot upwelling plumes surrounded by interconnected narrow cold downwelling sheets.

Spherical geometry. Spherical geometry also breaks the symmetry between up- and downwellings, resulting in a strong preference for plume-like upwellings and sheet-like downwellings. Early results [*Young*, 1974; *Machetel et al.*, 1986] were at only mildly supercritical Ra. Strongly supercritical Boussinesq, steady-state solutions with tetrahedral and cubic arrangements of plumes were obtained at Ra up to $7x10^4$ by *Bercovici et al.* [1989a]. Compressible solutions at relatively high Rayleigh numbers [*Baumgardner*, 1985,1988; *Glatzmaier*, 1988; *Bercovici et al.*, 1989b&c; *Glatzmaier et al.*, 1990; *Schubert*, 1992] confirm that the preferred form of convection is upwelling plumes and downwelling sheets, with the downwelling sheets becoming disconnected and plume-like as the degree of internal heating increases, as in the Cartesian models discussed earlier.

Other complexities that have been considered in 3-D constant-viscosity mantle convection include layering [*Olson*, 1984; *Cserepes et al.*, 1988; *Glatzmaier and Schubert*,

1993], plates [*Cserepes and Christensen*, 1990; *Gable et al.*,1991] and phase transitions [*Tackley et al.*, 1993b, 1994; *Honda et al.*, 1993].

Variable viscosity

By far the largest approximation in all the above calculations is the assumption of viscosity which is constant, or only depth-dependent. The viscosity of the Earth's mantle is known to be very strongly temperature dependent, which is certain to affect the pattern of convection. Thus, it is essential to include such rheology in laboratory or numerical studies.

Booker [1976] performed laboratory experiments at Ra~10^5 and viscosity contrasts of up to 300 and found that if the Ra is defined using the viscosity for the average of top and bottom boundary temperatures, the dependence of Nusselt number (Nu) on Ra was not greatly affected by viscosity contrast, a finding that was corroborated by *Richter et al.* [1983] and *Giannandrea and Christensen* [1993]. *White* [1988] studied convection with rigid boundaries at a range of Rayleigh numbers up to 6.3×10^4 and viscosity contrasts up to 1000, mapping the stability diagram of rolls, bimodal, hexagons, squares and spokes as a function of Ra and viscosity contrast. He determined that increasing temperature-dependence of viscosity lowers the Ra at which patterns become unstable to spoke-pattern flow, to about 2.5×10^4 for a viscosity variation of 1000. Squares and hexagons are stable at lower Ra and rolls or bimodal flow at lower viscosity contrasts. At high viscosity contrasts the cold upper boundary layer became stagnant, with convection occurring below this rigid lid. The effect of a stress-free upper boundary was investigated by *Weinstein and Christensen* [1991] at Ra~10^5 and moderate viscosity contrasts (~50) and they found a long-wavelength pattern with upwelling sheets and downwelling plumes. *Giannandrea and Christensen* [1993] confirmed this result but found that at much higher viscosity contrasts

(above ~1000) a stagnant lid develops and the pattern becomes similar to that obtained with a rigid lid.

Numerical work has focused mainly on steady-state solutions in small boxes, and much of it has concentrated on reproducing laboratory experiments rather than modeling the Earth. *Busse and Frick* [1985] obtained solutions for convection in a square box with linear dependence of viscosity on temperature and rigid upper and lower boundaries, and verified the experimental observation of *Booker* [1976] that rolls are stable at low viscosity contrasts, with squares at high viscosity contrasts. *Ogawa et al.* [1991] modeled the more realistic free-slip boundaries, obtaining steady-state solutions at low Ra and viscosity contrasts of up to 10^5 in a highly restrictive 0.5x1.7x1 box. The stagnant lid regime, characterized by upwelling plumes and downwelling sheets beneath a stagnant lid, was obtained at high viscosity contrasts, whereas the whole-mantle regime, in which the surface boundary layer participates in the flow, was obtained at lower contrasts. The latter regime is characterized by up- and downwelling plumes with sheet-like extensions. *Christensen and Harder* [1991] obtained steady-state solutions in small boxes (aspect ratio up to 1.5) with various boundary conditions, Ra up to 10^5 and viscosity contrasts of up to 1000, mapping the domains of stability for squares (which are unstable at low viscosity contrasts) and rolls (which are unstable at high viscosity contrasts and low Ra). For their experimental conditions, temperature-dependent viscosity favors upwelling plumes and downwelling sheets. For larger domains and rigid boundaries, additional patterns were obtained, including up-hexagons and triangles, and, in a 4x4x1 box with a viscosity contrast of 30, they obtained spoke-pattern flow. However, *Weinstein and Christensen* [1991], found that in the same 4x4x1 box, simply changing the upper boundary condition to stress-free resulted in a much longer wavelength pattern consisting of upwelling sheets and a downwelling plume. The huge effect of boundary conditions and box size was further demonstrated by *Tackley* [1993], who presented solutions in an 8x8x1 periodic box with Ra=10^5 and viscosity contrast of 1000. With rigid boundaries, small aspect-ratio

spoke-pattern flow was obtained, but with stress-free boundaries, large aspect-ratio down-square pattern (i.e., with a downwelling cold plume and upwelling sheets) was found.

However, all of the above solutions are basally-heated and in the Boussinesq limit, whereas it is well established that the Earth's mantle is substantially internally-heated, and that the effects of compressibility play a significant role. Clearly, it is necessary to establish how these results are affected by such complications, as well as depth-dependence of viscosity and higher Ra. In this paper we start from the results of *Tackley* [1993], and systematically investigate the effect of these additional complexities.

Model, method and parameters

Equations

As is standard in studies of mantle convection, we make the infinite-Prandtl number approximation, neglecting inertial terms in the momentum equation, which is valid since the Prandtl number for the mantle is of order (10^{24}), and the anelastic approximation, valid since the sound velocity is much faster than convective velocities. For computational convenience we make the anelastic-liquid approximation, discussed by *Jarvis and McKenzie* [1980], in which the influence of dynamic pressure on temperature is neglected. Since this term is of order (10^{-2}), this approximation is not expected to have much impact on the results. The equations are nondimensionalized to the depth of the mantle (D), thermal diffusion timescale (D^2/κ, where κ=thermal diffusivity) and superadiabatic temperature drop, ΔT_{sa}. Other nondimensionalizations, for example velocity (κ/D) and stress ($\eta\kappa/D^2$), follow from these.

The equations are those of continuity:

$$\nabla \bullet (\overline{\rho}\,\underline{v}) = 0 \qquad (6.1)$$

conservation of momentum:

$$\nabla \bullet \underline{\underline{\tau}} - \nabla p = Ra.\overline{\alpha\rho} T \, \hat{\underline{z}} \quad ; \quad \tau_{ij} = \eta(v_{i,j} + v_{j,i} - \tfrac{2}{3} v_{k,k} \delta_{ij}) \qquad (6.2)$$

and conservation of energy:

$$\overline{\rho}\overline{C}p \frac{DT}{Dt} = -Di_s \overline{\alpha\rho} T v_z + \nabla \bullet (\overline{k} \nabla T) + \overline{\rho}\overline{H} + \frac{Di_s}{Ra} \tau_{ij} v_{i,j} \qquad (6.3)$$

where the surface dissipation number Di_s is given by:

$$Di_s = \frac{\alpha_s g D}{Cp_s} \qquad (6.4)$$

v, p, T, τ, and η and D are velocity, dynamic pressure, absolute temperature, deviatoric stress, dynamic viscosity, and depth of mantle, respectively, $\underline{z}$ is a unit vector in the vertical direction, and the barred quantities ρ, α, C_p, κ, and k ($=\rho C_p \kappa$) are depth-dependent reference state parameters density, thermal expansivity, heat capacity, thermal diffusivity and thermal conductivity, respectively. The subscript 's' indicates the surface value, and the vertical coordinate z runs from 0 at the base to 1 at the surface. The Boussinesq approximation is recovered by setting Di=0 and all depth-dependent properties to 1.

The definition of Rayleigh number for a system with variable coefficients, in particular viscosity, is somewhat arbitrary. We choose a definition based on the surface values of reference state variables, and the viscosity for the value of the reference adiabat at the surface. For Boussinesq cases this is T=0.5, and with viscosity dependent solely on temperature, the Rayleigh number thus defined is identical to $Ra_{1/2}$ used by many authors [e.g., *Booker*, 1976]. The Ra based on the viscosity at the surface boundary condition

rather than adiabat [e.g., *Ogawa et al.*, 1991; *Hansen et al.*, 1993] would be approximately 2 orders of magnitude lower. In cases with depth-dependent viscosity, an alternative choice would be to use the viscosity on the reference adiabat at mid-depth: this Ra is approximately an order of magnitude higher than the stated values. A volume-averaged Ra [e.g., *Glatzmaier*, 1988] is awkward to use since $<\eta>$ is an output parameter, and it is desirable to use a definition of Ra that allows it to be an input parameter.

Thus:

$$Ra = \frac{\rho_s g \alpha_s \Delta T_{sa} D^3}{\eta(T_{s,a}, 0)\kappa_s} \tag{6.5}$$

where g=gravitational acceleration and the other quantities have already been defined.

Viscosity

As is in keeping with the Earth's mantle, we use an Arrhenius law [*Weertman*, 1970] to describe the variation of viscosity with temperature, which gives more rapid viscosity variations at low temperatures than at high temperatures. The exp(-aT) law that has commonly been used in numerical studies has been used for numerical convenience and has little basis in physical reality.

Unfortunately, the viscosity variations that can be modeled are limited by the convergence of the numerical method, and thus the viscosity law that is used is a compromise between the ideal law and that which is numerically tractible. The following compromises are made: (1) We use a nondimensional activation energy of 13.8155 (nondimensionalized to $R.\Delta T_{sa}$) that is lower than measured values. For example, the value of 540 kJ mol^{-1} for dry olivine measured by *Karato and Wu* [1993] corresponds to 26.0 nondimensional units. (2) The temperature that appears in the denominator of the Arrhenius law is offset from the absolute nondimensional model temperature, in order to

avoid the extremely large viscosities that would otherwise occur in the upper thermal boundary layer. (3) The depth-dependence of viscosity, when included, is specified as an exponential dependence on depth, rather than an activation volume. If an activation volume were used, it would have a similar effect to having a large activation energy in the deep mantle, resulting in very large viscosity variations [*van Keken et al.*, 1994], which would cause numerical difficulties.

The resulting viscosity law is as follows:

$$\eta(T,z) = A_0 \exp[-z \ln \Delta\eta_z] \exp\left[\frac{13.8155}{T + T_{off}}\right] \qquad (6.6)$$

where A_0 is calculated such that $\eta(\mathrm{Tas},1) = 1.0$. $\Delta\eta_z$ is the fractional variation of viscosity between the upper and lower boundaries due to pressure-dependence, and is taken to be 1 or 100. T_{off} is the temperature offset added to the nondimensional temperature to reduce the viscosity variation across the upper boundary, and is taken to be 1.0 for Boussinesq cases (in which the surface temperature boundary condition is 0) and 0.88 for compressible cases (in which the surface temperature boundary condition is 0.12).

The resulting viscosity variation due to temperature is a factor of 1000 for Boussinesq cases, independent of depth. For compressible cases, the variation is a factor of ~500 near the surface, ~2000 near the CMB, and ~2500 between the upper boundary condition and lower boundary condition.

Reference state

Over the depth (pressure) range of the mantle, density and thermodynamic quantities vary significantly. Here we use a simple thermodynamic model to calculate $\rho(z)$ and $\alpha(z)$. Heat capacity Cp is assumed constant, as may be approximately true in the

Earth's mantle, and thermal conductivity k(z) is assumed to vary with the fourth power of density, giving an increase consistent with experiments [*Osako and Ito*, 1991] and theory [*Anderson*, 1987].

The magnitude of temperature and density stratification is controlled by dissipation and compressibility numbers respectively:

$$Di = \frac{\alpha g D}{c_p} \quad ; \quad K = \frac{\alpha g D}{\gamma c_p} = \frac{Di}{\gamma} \tag{6.7}$$

$$\frac{\partial \overline{T}}{\partial z} = -Di.\overline{T} = -Di_s \frac{\overline{\alpha}}{\overline{c}_p} \overline{T} \quad ; \quad \frac{\partial \overline{\rho}}{\partial z} = -K\overline{\rho} = K_0 \frac{\overline{\alpha}}{\overline{c}_p} \left(\frac{\gamma_0}{\gamma} \right) \overline{\rho} \tag{6.8}$$

where γ is the Gruneisen parameter and the other symbols were defined earlier. To complete the equations, variations of γ and α must be specified. As is often assumed, we take $\gamma\rho = \text{constant}$ [*Duffy and Ahrens*, 1993] and relate α to compression using the derivation of *Anderson et al.* [1992], which gives a very similar result to *Chopelas & Boehler* [1992]:

$$\left(\frac{\partial \ln \alpha}{\partial \ln \rho} \right)_T = \delta_T = \delta_{T0} \left(\frac{\rho_0}{\rho} \right)^n \tag{6.9}$$

$$\text{giving } \alpha = \alpha_0 \exp\left[-\frac{\delta_{T0}}{n} \left(1 - \left(\frac{\rho_0}{\rho} \right)^n \right) \right] \tag{6.10}$$

where δ_{T0} = 6.0, n=1.4. For the Boussinesq cases, Di=K=0, giving constant coefficients.

Thus, in order to construct the nondimensional reference state, the following surface quantities must be specified: Di_s, T_{as}, Co_s and γ_s. This leads to depth variations of ρ, α, and k, which are all assumed to be 1.0 at the surface. The resulting volume-averaged

value of Di is 0.44, comparable to that thought to be appropriate for the Earth. The adiabatic temperature increase for a reference adiabat is also calculated, although this is not used during the calculation, since absolute nondimensional temperatures are used.

Parameter	Symbol	Value	Units	Non-D value
		Input surface parameters		
Dissipation number	Di_S	-	-	1.2
Compressibility number	Co_S	-	-	1.1
Gruneisen parameter	γ_S			1.091
Reference adiabat	T_{as}	1600	K	0.64
Boundary temperature	T_S	300	K	0.12
		Non-dimensionalization		
Superadiabatic temperature	ΔT_{sa}	2500	K	1.0
Density: surface	ρ_S	4000	kg m^{-3}	1.0
Expansivity: surface	α_S	5.0×10^{-5}	K^{-1}	1.0
Conductivity: surface	k_S	3.0	W m^{-1} K^{-1}	1.0
Heat capacity	Cp	1200	J kg^{-1} K^{-1}	1.0
Depth of mantle	D	2890	km	1.0
		Derived quantities		
Mean dissipation #	<Di>	-	-	0.441
Gruneisen parameter: CMB	γ_C	-	-	0.775
Adiabatic T rise	ΔT_a	900	K	0.36
Temperature: CMB	T_C	3700	K	1.48
Density: CMB	ρ_C	5600	kg m^{-3}	1.4
Expansivity: CMB	α_C	1.0×10^{-5}	K^{-1}	0.20
Conductivity: CMB	k_C	11.8	W m^{-1} K^{-1}	3.92
Velocity	v	1	cm yr^{-1}	1465
Time	t	423	Gyr	1.0
Heat flux	F	2.5	mW m^{-2}	1.0
Conductive heat flux	F_{cond}	7.5	mW m^{-2}	3.02
Internal heating rate	H	2.245×10^{-13}	W kg^{-1}	1.0

Table 6.1: Thermodynamic Parameters

These input parameters were chosen to give good fits to recent thermodynamic analyses of the lower mantle [*Chopelas and Boehler*, 1992; *Anderson et al.*, 1992; *Duffy and Ahrens*, 1993] and are listed in Table 6.1. Since density jumps associated with phase transitions are not included, the density increase over the entire mantle is not as large as in Earth models such as PREM [*Dziewonski and Anderson*, 1981]. Table 6.1 also lists typical dimensional values. These dimensional values are not used during the calculation, but are given to allow quantitative comparison of the results with observations. The resulting depth variation of density, temperature, thermal expansivity, thermal conductivity and thermal diffusivity is illustrated in Fig. 6.1, and Table 6.1 lists basal values of these and other quantities.

Since the definition of Rayleigh number is extremely ambiguous when coefficients are varying with temperature and depth, as discussed earlier, a better guide to how close convection is to the Earth-like regime can be obtained by considering observational measures such as heat flux and convective velocity, and Table 6.1 lists typical conversions between nondimensional and dimensional values for these quantities. The Earth's total heat flux of 87 mW m^{-2} [*Pollack et al.*, 1993] corresponds to a nondimensional flux of 35 units; however, this includes heat loss from radioactive elements in the crust; more appropriate is the mantle heat flux of 60-70 mW m^{-2} [*Stacey*, 1992; *Pollack et al.*, 1993] which corresponds to 24-28 nondimensional units. A velocity of 1 cm/year corresponds to 1500 non-dimensional units.

Due to the increase of thermal conductivity and density with depth, the heat flux that would be conducted across the mantle in the absence of convection has a nondimensional value of 2.5, when the nondimensionalization is based on surface values. Thus, the nondimensional heat flux is 2.5 times higher than the Nusselt number, when the latter is defined as the actual heat flux divided by the conductive heat flux. Indeed, if the increase of thermal conductivity given by *Osako and Ito* [1991] is correct, the Nusselt number of the Earth is in the range 10-13, much lower than commonly quoted values. For Boussinesq cases, Nusselt number is identical to heat flux.

Fig. 6.1. Variation of nondimensional reference-state thermodynamic parameters with depth. a) density, b) temperature, c) thermal expansivity, d) thermal conductivity, e) thermal diffusivity. For reference dimensional values see Table 6.1.

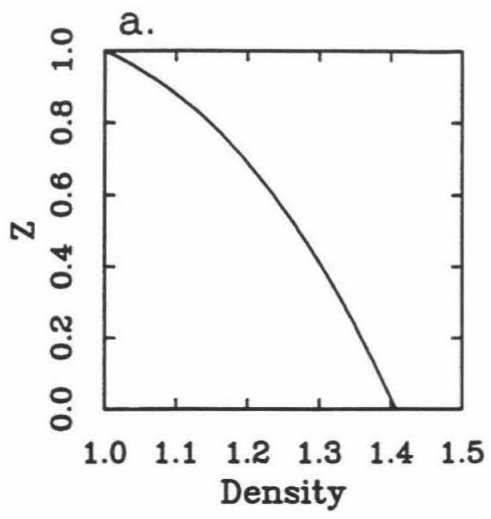
a.
z
0.0 0.2 0.4 0.6 0.8 1.0
1.0 1.1 1.2 1.3 1.4 1.5
Density

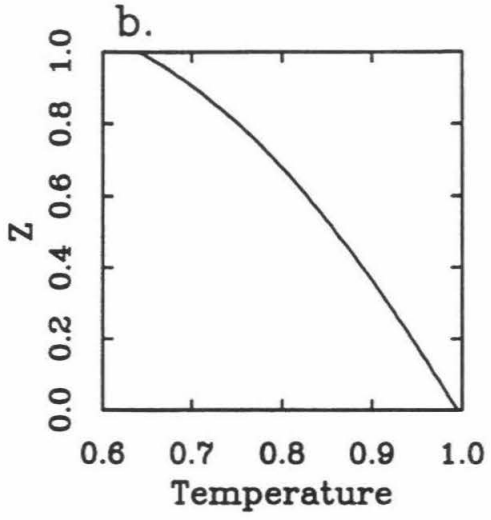
b.
z
0.0 0.2 0.4 0.6 0.8 1.0
0.6 0.7 0.8 0.9 1.0
Temperature

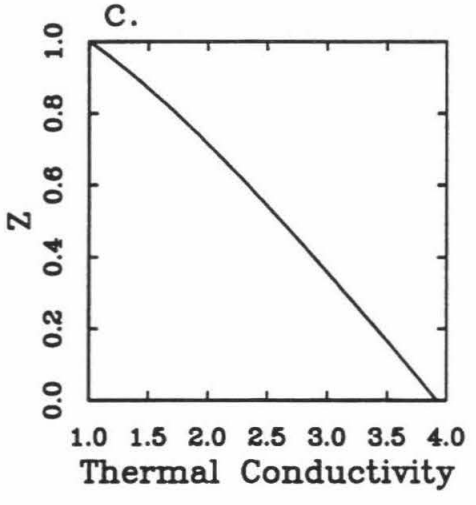
c.
z
0.0 0.2 0.4 0.6 0.8 1.0
1.0 1.5 2.0 2.5 3.0 3.5 4.0
Thermal Conductivity

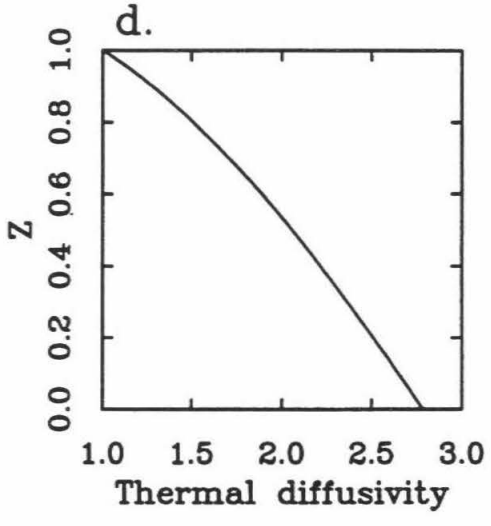
d.
z
0.0 0.2 0.4 0.6 0.8 1.0
1.0 1.5 2.0 2.5 3.0
Thermal diffusivity

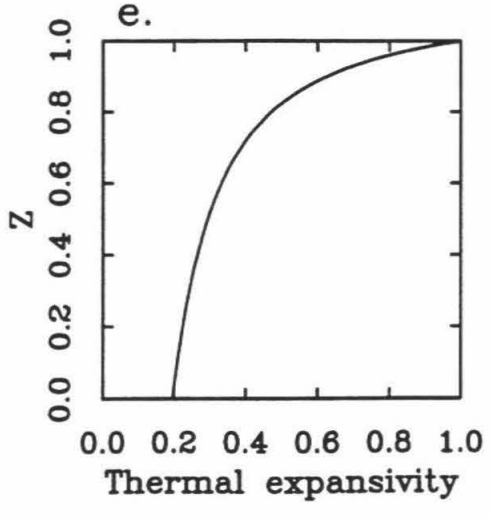
e.
z
0.0 0.2 0.4 0.6 0.8 1.0
0.0 0.2 0.4 0.6 0.8 1.0
Thermal expansivity

Numerical Method

The exact details of the numerical method and its benchmarking are described in Appendix B and are only briefly summarized here. The instantaneous velocity and pressure fields given by (6.1)-(6.3) are calculated by a finite difference (control volume) multigrid technique. Primitive variables (three components of velocity, and pressure) are defined on a staggered three-dimensional Cartesian grid, with vertical grid refinement in the upper and lower boundary layers. Use of a staggered grid apparently gives similar accuracy to a non-staggered grid with twice the number of points in each direction [*Brandt*, 1982]. An iterative sweep consists of relaxing each equation in turn over the entire domain, similar to the SIMPLER method of *Patankar* [1980]. This iteration scheme is extremely robust, converging for almost any viscosity contrast. In addition, because the finite-volume scheme is based on balancing surface stresses on the sides of volume elements with body forces within them, volume-integrated quantities are preserved to machine accuracy. The scheme is incorporated into a standard multigrid V-cycle [*Brandt*, 1982, *Press et al.*, 1992], giving an execution time which scales in proportion to the total number of grid points. Timestepping (equation (6.4)) is performed explicitly, using the Multidimensional Positive-Definite Advection Transport Algorithm of *Smolarkiewicz* [1984] for advection, and second order finite-differences for diffusion, viscous dissipation and adiabatic heating/cooling. Steps of typically 0.5-0.9 the Courant condition are used. The method is well suited to parallel computers, and the presented results were obtained on the Intel Touchstone Delta at the California Institute of Technology and the Intel Paragon at San Diego Supercomputer Center. Benchmarks and accuracy are described in Appendix B.

Results

Overview

The cases presented constitute a systematic progression from the simplest case (Boussinesq, constant-viscosity, basal heating) to the most complex case (compressible, with pressure- and temperature-dependent viscosity and internal heating), allowing the influence of each individual complexity to be clearly identified and understood.

Case	Ra	visc	a bc	nh,nz	start	time	Nu	Vrms	<T>
B1	10^5	const	8 P	128,32	rand	0.437	9.05	196	0.486
B2	10^5	T	8 P	128,32	rand	0.629	6.22	192	0.629
B3	10^5	T	8 R	128,16r	rand	0.422	5.87	197	0.643
B4	10^5	T	4 R	64,16r	rand	0.898	5.95	187	0.636
B5	10^5	Z	4 R	64,16r	rand	2.164	3.58	40.1	0.338
B6	10^5	T+Z	4 R	64,16r	rand	1.86	3.30	28.8	0.434
B7	10^6	T	4 R	128,32r	B4	0.0484	12.6	791	0.685
B8	10^6	T+Z	4 R	128,32r	rand	0.166	6.75	99.7	0.408

Table 6.2. Simulation characteristics for Boussinesq, basally-heated cases. For viscosity, 'T' indicates temperature-dependence and 'Z' indicates Z-dependence, with parameters as dicussed in the text. 'a' refers to aspect ratio and side boundary conditions are 'P' periodic or 'R' reflecting. 'nh' and 'nz' are the number or horizontal and vertical grid cells respectivelty, with an 'r' indicating vertical grid refinement in the boundary layers. 'rand' indicates random start conditions.

The 24 cases presented are listed in Tables 2, 3 and 4, and are divided into 3 groups: Boussinesq with basal heating (Table 6.2, cases B1-B8), compressible with basal heating (Table 6.3, cases C1-C8), and compressible with internal heating (Table 6.4, cases I1-I8). Although the degree of basal heating for the Earth is probably in the range 6-20%, as discussed earlier, it is instructive to consider the limiting cases of completely basal and completely internal heating, in order to obtain a thorough understanding of the underlying fluid dynamics. Each group contains cases in which viscosity is constant, depth-dependent, temperature-dependent and temperature- and depth-dependent, as well as cases with different Rayleigh numbers.

Case	Ra	visc	nh,nz	start	time	F	Vrms	<T>
C1	10^6	const	64,32r	rand	1.1375	21.4	482	1.047
C2	10^6	Z	64,32r	rand	0.7022	12.1	149	0.808
C3	10^6	T	128,32r	C1	0.0450	13.7	662	1.148
C4	10^6	T+Z	128,32r	rand	0.0906	12.7	241	1.000
C5	10^5	T+Z	64,16r	rand	1.4576	6.55	45.7	1.001
C6	10^7	T+Z	128,64r	rand	0.041	25.5	1003	0.962
C7	10^7	Z	128,32r	C2	0.0529	22.2	587	0.771
C8	10^5	const	64,16r	rand	0.6503	10.7	122	1.056

TABLE 6.3: Simulation characteristics for compressible, basally-heated cases. All cases are in a 4x4x1 box with reflecting side boundaries. Columns have the same meaning as in Table 6.2, except that heat flux F replaces Nu.

Case	Ra	H	visc	nh,nz	start	time	F	Vrms	<T>
I1	10^6	16	const	128,32r	rand	0.0631	20.2	181	1.05
I2	10^6	10	Z	128,32r	I1	0.253	12.6	106	0.852
I3	10^6	10	T	128,32r	I1	0.0386	12.5	379	1.204
I4	10^6	10	T+Z	128,32r	I1	0.3350	12.3	211	1.132
I5	10^5	8	const	64,16r	rand	0.2774	9.94	70.1	1.060
I6	10^5	5	T+Z	64,16r	I5	1.082	6.29	35.1	0.964
I7	10^7	32	const	256,64r	rand	0.0181	40.2	651	1.119
I8	10^7	20	T+Z	128,64r	rand	0.028	25.7	595	1.145

TABLE 6.4: Simulation characteristics for internally-heated, compressible cases. All cases are in a 4x4x1 box with reflecting side boundaries. Columns have same meaning as in Table 6.2.

In all cases the upper boundary is impermeable, stress-free and isothermal. The lower boundary is impermeable and stress-free, and either isothermal (basally-heated cases B1-8 and C1-8) or insulating (internally-heated cases I1-8). Side boundaries are reflecting, except for cases B1 and B2, in which they are periodic, as in *Tackley* [1993]. The computational domain consists of a 4x4x1 Cartesian box (i.e., four times wider than it is deep) except for cases B1-B3, which use an 8x8x1 box. The number of grid cells in the horizontal directions (nh) and vertical directions (nz) are listed in Table 6.2, where an 'r' denotes (smoothly varying) vertical grid refinement in the boundary layers, by a factor of approximately 3. For example, a grid of nh=128, nz=32r in an aspect ratio 4 box gives a horizontal resolution of 90 km and a vertical resolution ranging from 36 km near to boundaries to 103 km near mid-depth. Vertical grid refinement results in greatly improved

accuracy compared to results with constant grid spacing, as shown by the benchmark tests in Appendix B.

Starting conditions and run durations (1 nondimensional time unit ≈ 423 Gyr) are also listed in Tables 2-4. Cases were started either from the final frame of a previous case, or from a random initial state consisting of an isothermal interior (T=0.5 for Boussinesq or the reference adiabat for compressible cases), error-function boundary layers at top and bottom, and small random (white noise) perturbations of amplitude 0.05. After initial transients, the flow patterns were generally found to evolve very slowly but steadily, requiring large integration times (up to nondimensional 2.1, or 10000-19000 time steps) to ensure solutions had overcome their transient nature and basal and surface heat fluxes were in good agreement. Mean temperature <T>, surface heat flux (equal to Nusselt number in the Boussinesq cases) and average (r.m.s.) velocity are also listed. Many cases are time-dependent and thus these values fluctuate somewhat; however, the fluctuations are not large and the given values are representative of the system.

Studies of internally-heated convection have typically used a temperature nondimensionalization based on the conductive heat flux, i.e., $\Delta T_{ref}=(HD^2)/k$, where H=internal heating rate [e.g., *Parmentier et al.*, 1994]. This results in very low nondimensional temperatures when convection is strongly supercritical. However, when temperature-dependent viscosity is included, it is important for nondimensional temperatures to be similar to those obtained in the basally-heated results, so that similar viscosities are obtained. Thus, the approach taken here is to use the same temperature scale in the internally-heated cases as in the basally-heated cases, and to choose the internal heating rate for a particular Ra_T in order to obtain the same surface heat flux, and thus similar nondimensional temperature differences, as in an equivalent basally-heated case. This is simple since in equilibrium the surface heat flux F is related to internal heating rate H by:

$$F=H\langle\rho\rangle \qquad (6.11)$$

where $\langle\rho\rangle$ is the volume-averaged nondimensional density. For example, the internal heating rates for I1-I4 have been chosen to give similar surface heat flows to cases C1-C4 respectively. As is shown later, the resulting temperature drops and hence viscosity contrasts over the upper boundary layer are similar.

Boussinesq cases

The eight Boussinesq cases presented are listed in Table 6.2 and illustrated in Fig. 6.2. All cases are entirely heated from below and have different viscosity laws, different aspect ratios (8 or 4) and horizontal boundary conditions. Cases B1 and B2 are the same as cases 1 and 3 respectively of *Tackley* [1993], and are included here for comparison with the new results. Case B1 has constant viscosity, B2-4 have temperature-dependent viscosity and different boundary conditions and aspect ratios, and B7-B8 are as B4 and B6 except at a higher Ra of 10^6. The $Ra_{1/2}$ of 10^5 is two orders of magnitude lower than that thought to be appropriate for the Earth's mantle, but similar to that used in previous numerical and laboratory studies, thereby allowing direct comparions to be made.

The constant viscosity case (case B1) is illustrated in Fig. 6.2a. There is a rough symmetry between up- and downwellings, which both start off as sheets, decaying into plumes as they ascend or descend respectively. The downwellings exhibit greater connectivity, reflected in $\langle T\rangle$ (see Table 6.2) being slightly lower than 0.5; however, this is just by chance, since the equations are symmetric with respect to the vertical coordinate in this case. In small aspect-ratio boxes, stable patterns at this Rayleigh number include 2-D rolls, bimodal flow, and square or hexagonal cells, depending on the box dimensions and initial conditions [*Travis et al.*, 1990b]. The weakly time-dependent pattern obtained lies somewhere between these extremes, also containing characteristics of the spoke pattern.

Fig. 6.2. Convective patterns for Boussinesq, basally-heated cases. Plotted are isosurfaces of residual temperature (i.e., temperature relative to horizontally-averaged value). Light contours indicate upwellings, showing where the temperature is 0.1 hotter than the horizontal average; dark contours indicate downwellings, showing where the temperature is 0.1 colder than the horizontal average. a. (top left) case B1, constant viscosity, b. (top right) case B2, $\eta(T)$, periodic sides, c. (2nd row left) case B3, $\eta(T)$, reflecting sides, d. (2nd row right) case B4, $\eta(T)$, aspect ratio 4, with the same solution as B2, e. (3rd row left) case B5, $\eta(Z)$, f. (3rd row right) $\eta(T,Z)$, g. (bottom left) case B7, $\eta(T)$, $Ra=10^6$, h. (bottom right) case B8, $\eta(T,Z)$, $Ra=10^6$. For further details see Table 6.2.

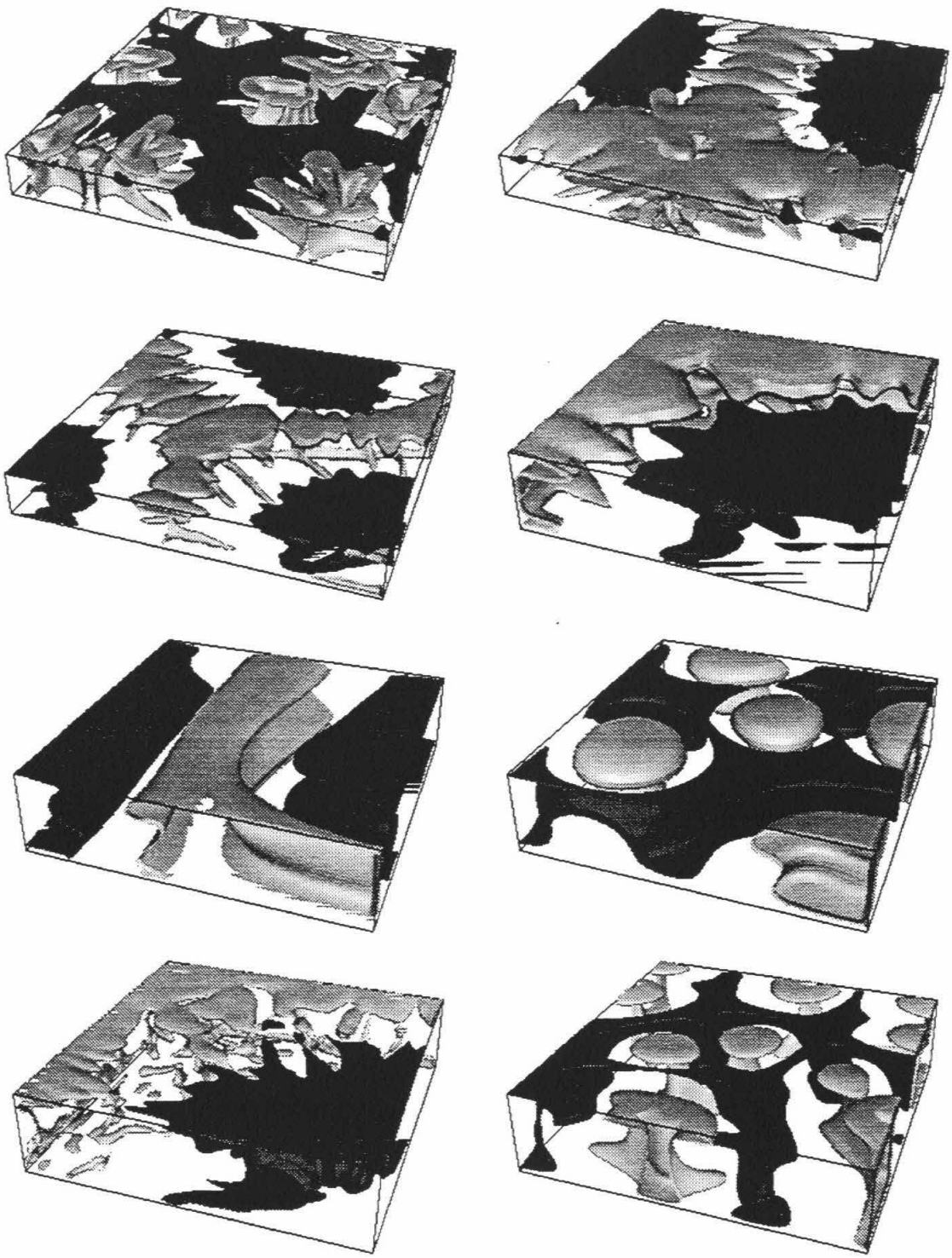

Temperature-dependent viscosity: When temperature-dependent viscosity is added, the downwellings merge to form one huge quasi-cylindrical downwelling, resulting in a single square cell filling the entire computational domain. Upwelling sheets extend all the way from the base to the surface. Although the overall pattern remained very stable throughout the remainder of the calculation, the exact details of upwellings and downwellings were highly time-dependent. Thus, two scales of flow are exhibited: the broad-scale flow which is very stable, and small-scale flow which is highly time-dependent. In order to test the robustness of this solution to initial conditions, an additional calculation was performed, starting from the final state of a case with a rigid boundary (case 2 of *Tackley* [1993]). After a nondimensional time of ~0.1, a single square cell was again formed.

Boundary conditions and aspect ratio: In order to test the effect of horizontal boundary conditions, two additional simulations were performed using reflecting rather than periodic sides. In case B3, which has the same aspect ratio as B2, upwelling sheets are also obtained, with a similar aspect ratio to case B2, except with hexagonal rather than square cells. The pattern obtained in case B4, which has half the aspect ratio of case B2, is (once symmetry has been considered) identical to that of case B2, i.e., a square cell with periodicity of 8. In a periodic domain, the maximum possible wavelength of the flow pattern is equal to the width of the domain, but with reflecting sidewalls, the maximum possible wavelength is double the width of the domain. Thus, the same flow pattern can be obtained in a 4x4x1 reflecting box (case B4) as in an 8x8x1 periodic box (case B2). Since it is computationally much more efficient to use a 4x4x1 box, the remainder of the reported simulations use the 4x4x1 reflecting box. It is interesting to note that case B3 could have formed a square cell with a periodicity of 16, but instead chose a pattern with similar aspect ratio to case B2, thus indicating that the preferred periodicity is closer to 8 than 16.

Depth-dependent viscosity: Case B5 has a viscosity which increases exponentially with depth by 2 orders of magnitude. The Nusselt number is extremely low, and the

resulting pattern is almost one of two-dimensional rolls. This case has an extremely long integration time (2.16), but is still evolving very slowly. When the viscosity is dependent on temperature as well as depth (case B6), a short-wavelength, cellular pattern is observed, with upwelling plumes surrounded by interconnected downwelling sheets. Thus, the addition of depth-dependence has reversed to tendency to form large cells observed in cases where the viscosity is purely temperature-dependent (e.g., case B4).

Rayleigh number: Cases B7 and B8 are identical to B4 and B6 but with Rayleigh numbers an order of magnitude higher, with a $Ra_{1/2}$ of 10^6 rather than 10^5. The overall patterns are very similar to the lower Ra cases, with B7 displaying narrower features and greater time-dependence, and B8 displaying an even shorter-wavelength pattern than B6. Thus, for these examples, Ra is not important in determining the basic pattern; it simply has a modulating effect on the detailed structure.

In these results, adding temperature-dependent viscosity at a constant $Ra_{1/2}$ has reduced the Nusselt number by around 31%, from 9.05 (case B1) to 6.22 (case B2). This appears to contradict the observation of *Booker* [1977], *Richter et al.* [1983] and *Giannandrea and Christensen* [1993], who find that Nusselt number does not change greatly with viscosity contrast. A resolution of this apparent contradiction probably lies in the differences between these laboratory experiments and the results presented here. Firstly, the upper and lower boundaries are stress-free in this present study, whereas they were rigid or mixed in the laboratory experiments. Secondly, the viscosity law used here gives much greater viscosity variation for cold temperatures than for hot temperatures (a factor of 100 between T=0.0 and T=0.5, but only a factor of 10 between T=1.0 and T=0.5), whereas the viscosity law of the laboratory fluids gave a more equal distribution. Thus, the experimental rule may need modification when a more realistic (for the Earth) viscosity law is used.

The volume-averaged r.m.s. velocity is not significantly affected by temperature-dependent viscosity. Depth-dependence, however, greatly reduces this r.m.s. velocity.

Fig. 6.3. Convective patterns for compressible, basally-heated cases. Isocontours show the same T values as for Fig. 6.2. a. (top left) C1 - constant viscosity; b. (top right) C2 - $\eta(Z)$; c. (mid left) C3 - $\eta(T)$, d. (mid right) C4, $\eta(T,Z)$, e. (bottom left) C5, $\eta(T,Z)$, $Ra=10^5$, f. (bottom right) C6, $\eta(T,Z)$, $Ra=10^7$.

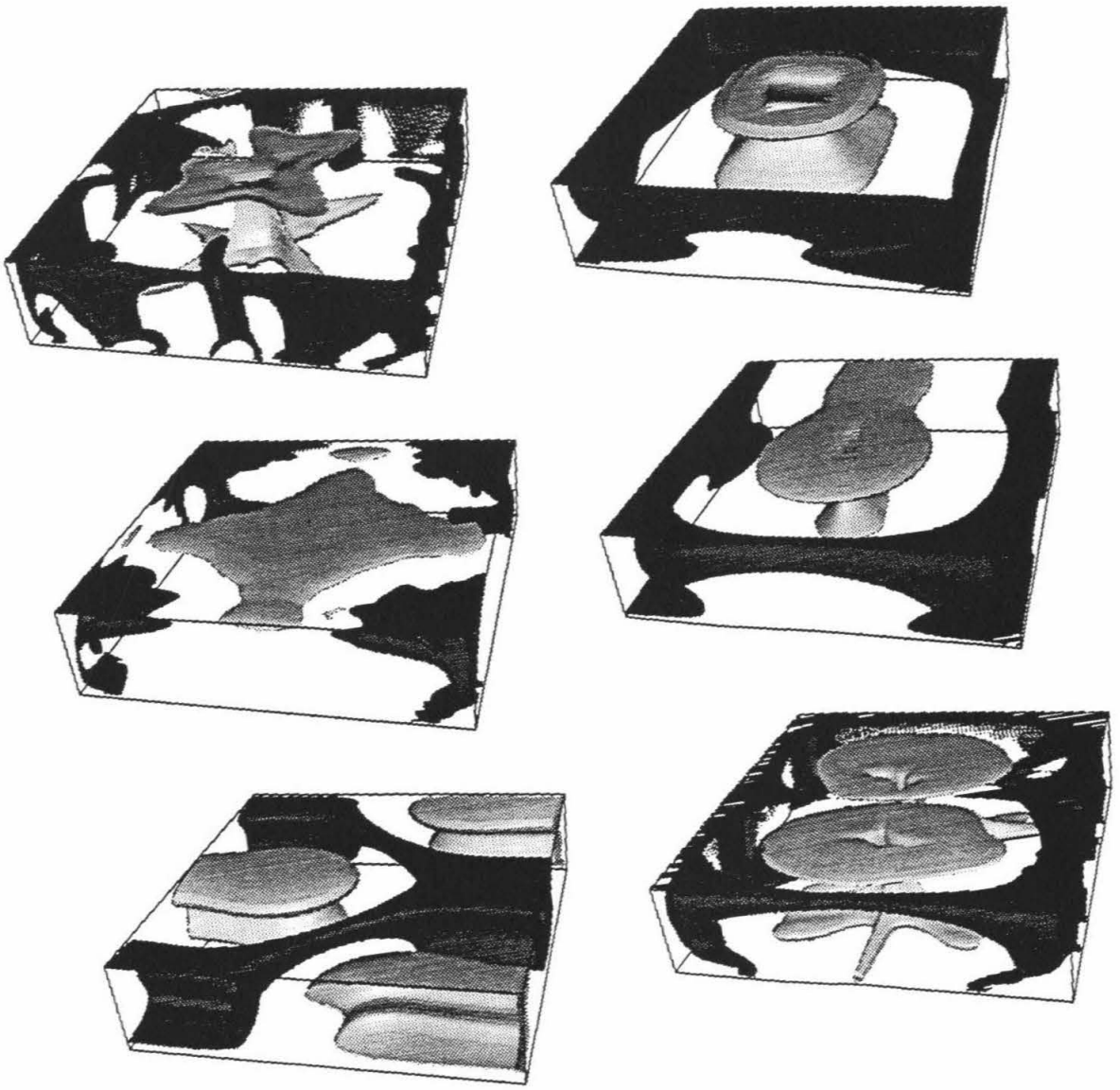

Compressibility

Six compressible, basally-heated cases are presented, listed in Table 6.3 and illustrated in Fig. 6.3. As discussed earlier, compressibility implies the depth-dependence of thermal expansivity, thermal conductivity and density, as well as the addition of viscous dissipation and adiabatic heating to the energy equation.

With constant-viscosity (case C1), a single, square cell with a broad upwelling plume surrounded by time-dependent, downwelling sheets is observed. This result is similar to that obtained by *Balachandar et al.* [1992] in a 5x5x1 periodic box using a completely different numerical technique (a spectral method). When compared to case B1, in which both upwellings and downwellings start as sheets and decay into plumes, the effect of compressibility in breaking the symmetry between up- and downwellings becomes clear. When the viscosity is dependent on depth only (case C2), the central plume becomes much broader at its base, decreasing in thickness as it ascends. Both the upwelling plume and downwelling sheets are stabilized, resulting in a steady-state solution at this Ra.

When the viscosity is dependent on temperature only (case C3), four cylindrical downwellings occur at the corners of the box. The interior of the convective cell has heated up greatly, so that the temperature contrast between the upwellings and downwellings is very small. However, the upwellings are indeed sheet-like, as with the equivalent Boussinesq case (B2). Thus, the sheet-like nature of the upwellings with temperature-dependent viscosity is not affected by compressibility.

The addition of depth-dependence (case C4) to the temperature-dependence, however, again results in a strong central plume. Although still broader at its base (as with C2), the temperature-dependence has reduced the amount of broadening. Downwellings are linear in the shallow mantle, decaying into more cylindrical forms before they reach the

base of the box. The elongation of the central plume, resulting in the formation of a 4x8 rectangular pattern, indicates a preference for larger cell size.

The effect of varying the Rayleigh number is examined in cases C5 and C6, which have the same parameters as C4 but Rayleigh numbers an order of magnitude higher and lower, at 10^5 and 10^7 respectively. At the lower Ra (C5) the local Ra at the base of the box is sub-critical, and penetrative convection occurs, with somewhat smaller cells. It would be interesting to investigate the effect of starting condition on this case, in order to determine whether longer-wavelength patterns, for example, the pattern of case C4, are stable. At the higher Ra (case C6) an up-square is again formed, but the flow is highly time-dependent. A preference for smaller cell size than case C4 is exhibited, suggesting that cell size may diminish at higher Ra for a fixed viscosity contrast.

Internal heating

The eight internally-heated, compressible cases are listed in Table 6.4 and plotted in Figure 6.4. With constant viscosity (case I1), a time-dependent network of downwelling plumes interconnected at the surface by sheets is formed, similar to previous Boussinesq calculations [e.g., *Houseman*, 1988]. When depth-dependence is added, however, these merge to form downwelling sheets, with a single square cell filling the box, although the small-scale structure suggests that a slightly shorter-wavelength pattern would be preferred. Interestingly, a broad hot upwelling plume is observed in the center, even though there is no heat entering the base. This broad hot region is a passive feature.

When temperature-dependent viscosity is added, the pattern changes enormously. A large-scale flow is set up, with a complex, highly time-dependent region of downwelling near one edge of the box. Time-dependent, transient ridges emanate radially from the region of downwelling. The contrast between this solution and case C1 provides a very clear demonstration of the ability of temperature-dependent viscosity to produce long-

Fig. 6.4. Convective patterns for compressible, internally-heated cases. Isocontours show the same T values as for Fig. 6.2. Cases are I1-I8, running from left to right and down the page.

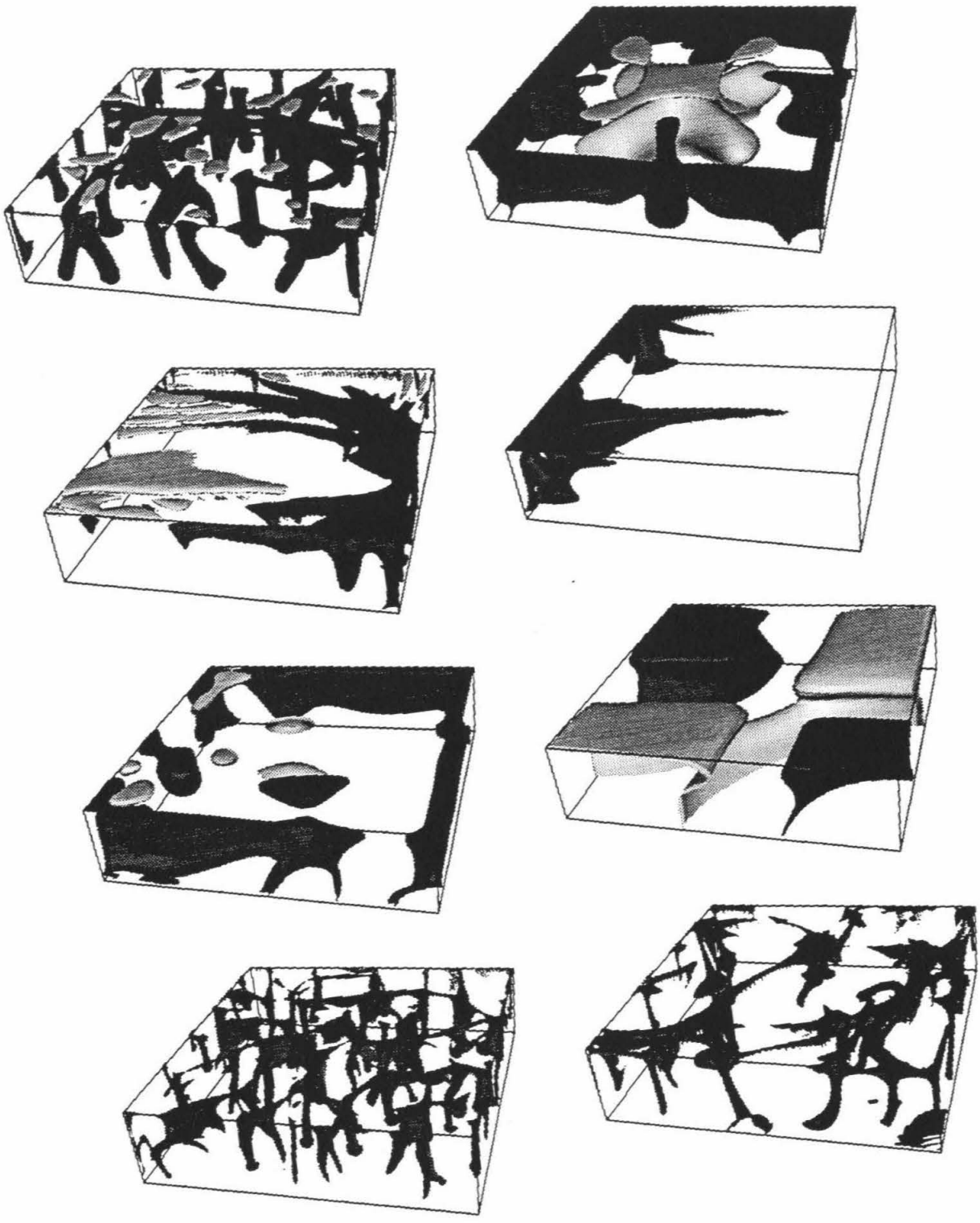

wavelength flows. The pattern has a similar wavelength to that obtained in the Boussinesq, basally-heated cases B2 and B4.

With both temperature- and depth-dependent viscosity, downwelling is again restricted to one side of the box, where a downwelling sheet with time-dependent plume-like instabilities is observed. This corresponds to an infinite series of sheet-like downwellings with horizontal spacing 8 (equivalent to ~23,000 km). Time-dependent, linear extensions appear from these plumes into the hot upwelling region.

Constant-viscosity cases for two other Rayleigh numbers are presented (I5 and I7). At the lower Rayleigh number, a much more stable pattern with fragmented downwelling sheets is formed. This appears to differ from low Rayleigh-number Boussinesq solutions, in which downwelling plumes are still obtained [*Schubert et al.*, 1993]. At the higher Ra, the basic characteristics are the same as for case C1, but the downwellings are narrower and more closely-spaced.

Cases with temperature- and depth-dependent viscosity are also presented for two other Rayleigh numbers (case I6 at $Ra_T=10^5$ and case I8 at $Ra_T=10^7$), and can be compared to case I4. At the lower Ra, two steady-state downwelling plumes have formed at opposing corners of the box, with the hot material filling in the gaps between these. At the higher Ra, however, a highly time-dependent network of narrow plume-like downwellings is observed, connected by linear sheets. The spacing associated with these downwellings is much smaller than with the case at $Ra=10^6$ (I4), although larger than the constant-viscosity case I. This provides further evidence that the characteristic horizontal wavelength decreases with increasing Ra, although this solution is only marginally resolved horizonally and needs to be verified using a denser numerical mesh.

Horizontally-averaged profiles

Figures 6.5 to 6.7 shows vertical profiles of horizontally-averaged temperature <T>, viscosity <η>, r.m.s. velocity (v_{rms}) and stress (i.e., $\sqrt{(\tau_{ij}\tau_{ij})}$), for the three groups of cases. In each group the solid line represents the constant-viscosity case.

Boussinesq (Fig. 6.5). The constant-viscosity case displays an approximately isothermal interior with T≈0.5, and upper and lower boundary layers have an approximately equal temperature drop and thickness of around 0.1, which is roughly $(Ra_c/Ra)^{1/3}$, where Ra_c is the critical Rayleigh number for the onset of convection. Since there is no adiabatic increase of temperature with depth in the Boussinesq approximation, this isotherm is equivalent to an adiabat. Regions of subadiabaticity are observed near the upper and lower boundary layers; these are due to the horizontal spreading of up- and downwellings at these depths. These regions are expected to become smaller as the Rayleigh number increases, and the interior temperature profile would become closer to an isotherm, as with 2-D calculations [*Jarvis and Peltier*, 1989].

When depth-dependence of viscosity is added (B5, dashed line), the interior temperature drops greatly to around 0.3, resulting in a lower thermal boundary layer with much greater temperature drop and vertical extent of around 0.25. The effect of depth-dependent viscosity in decreasing the interior temperature has previously been observed in two-dimensional simulations [*Torrance and Turcotte*, 1971; *Gurnis and Davies*, 1986a; *Yuen and Zhang*, 1989; *Hansen et al.*, 1993]. The effect can be understood by noting that convection tends to be more vigorous where viscosity is lower. The lower viscosity towards the top of the layer results in more vigorous convection, and hence higher heat transport, near the top than near the base, thus cooling the interior until the temperature drops over upper and lower thermal boundary layers adjust to equalize the heat transport. Essentially, it is easier to transport heat through the surface than through the base. A rough scaling relationship can be obtained by applying a local Rayleigh number criterion

Fig. 6.5. Profiles of a) horizontally-averaged temperature <T>, b) dynamic viscosity <η>, c) rms velocity V_{rms} and d) stress, for Boussinesq, basally-heated cases.

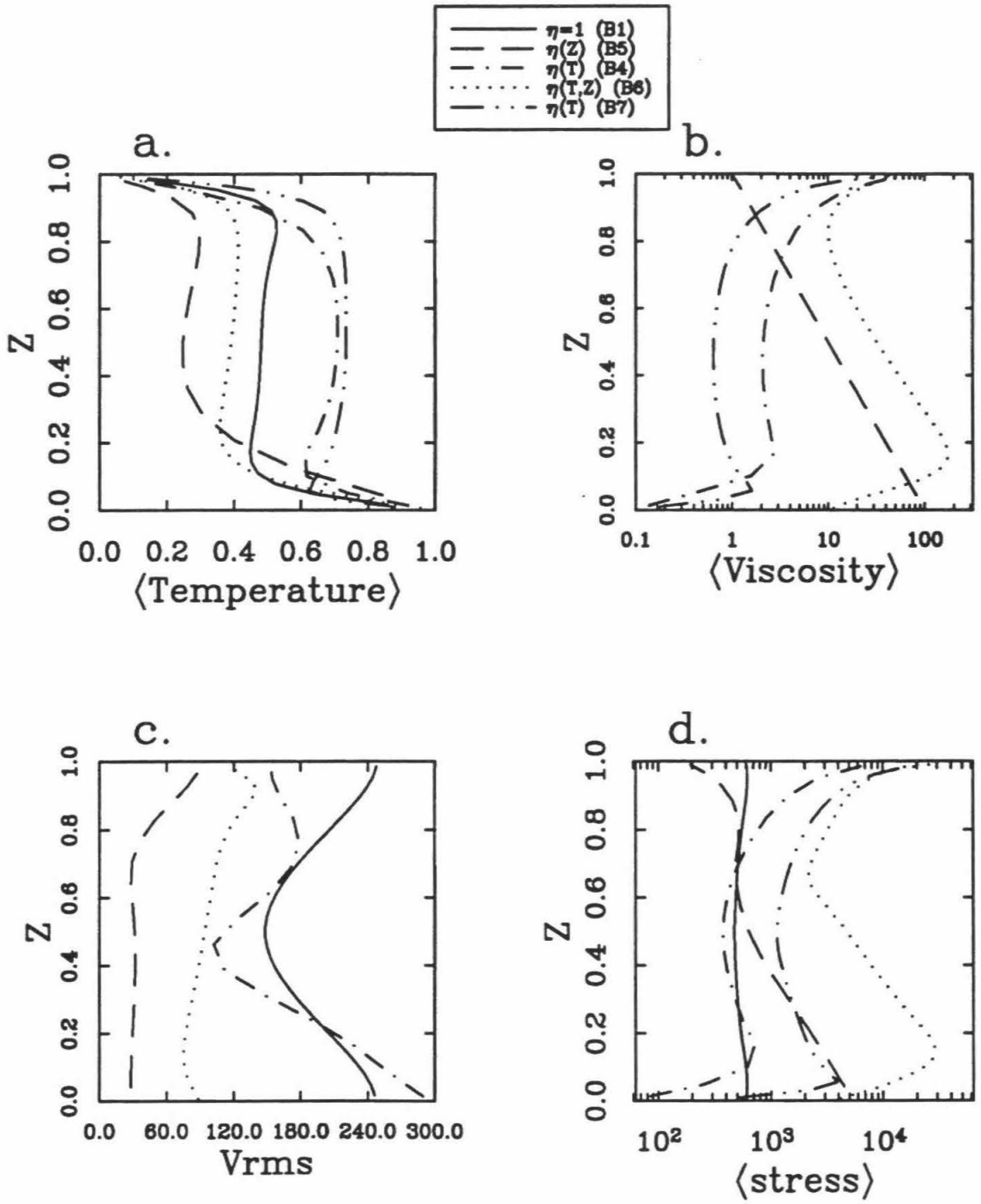
η=1 (B1)
η(Z) (B5)
η(T) (B4)
η(T,Z) (B6)
η(T) (B7)
a.
b.
c.
d.
Z
⟨Temperature⟩
⟨Viscosity⟩
Vrms
⟨stress⟩
0.0 0.2 0.4 0.6 0.8 1.0
0.1 1 10 100
0.0 60.0 120.0 180.0 240.0 300.0
10² 10³ 10⁴

Fig. 6.6. Profiles of a) horizontally-averaged temperature <T>, b) dynamic viscosity <η>, c) rms velocity V_{rms} and d) stress, for Compressible, basally-heated cases.

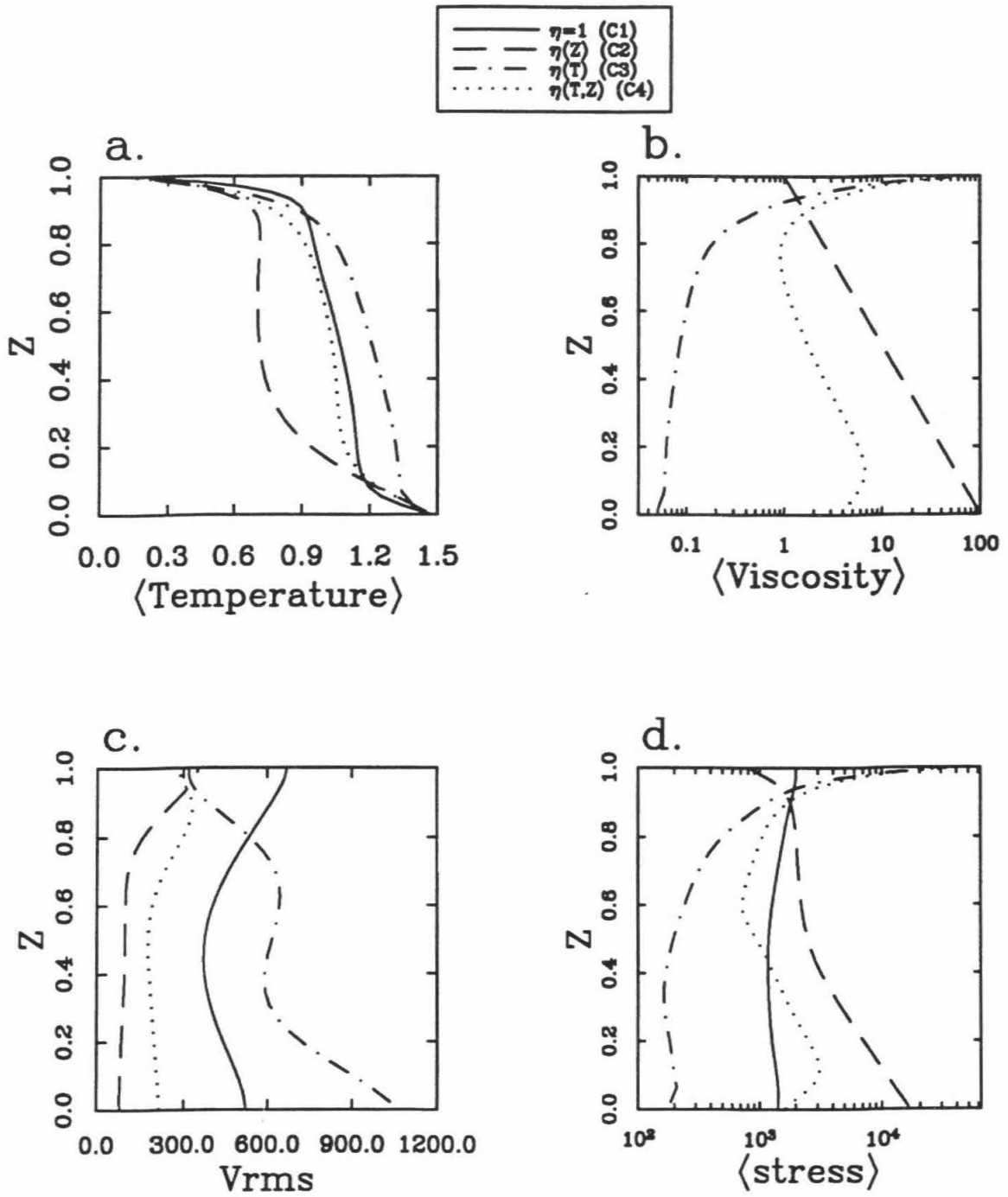
η=1 (C1)
η(Z) (C2)
η(T) (C3)
η(T,Z) (C4)
a.
Z
0.0 0.2 0.4 0.6 0.8 1.0
0.0 0.3 0.6 0.9 1.2 1.5
⟨Temperature⟩
b.
Z
0.0 0.2 0.4 0.6 0.8 1.0
0.1 1 10 100
⟨Viscosity⟩
c.
Z
0.0 0.2 0.4 0.6 0.8 1.0
0.0 300.0 600.0 900.0 1200.0
Vrms
d.
Z
0.0 0.2 0.4 0.6 0.8 1.0
10² 10³ 10⁴
⟨stress⟩

Fig. 6.7. Profiles of a) horizontally-averaged temperature <T>, b) dynamic viscosity <η>, c) rms velocity V_{rms} and d) stress, for Compressible, internally-heated cases.

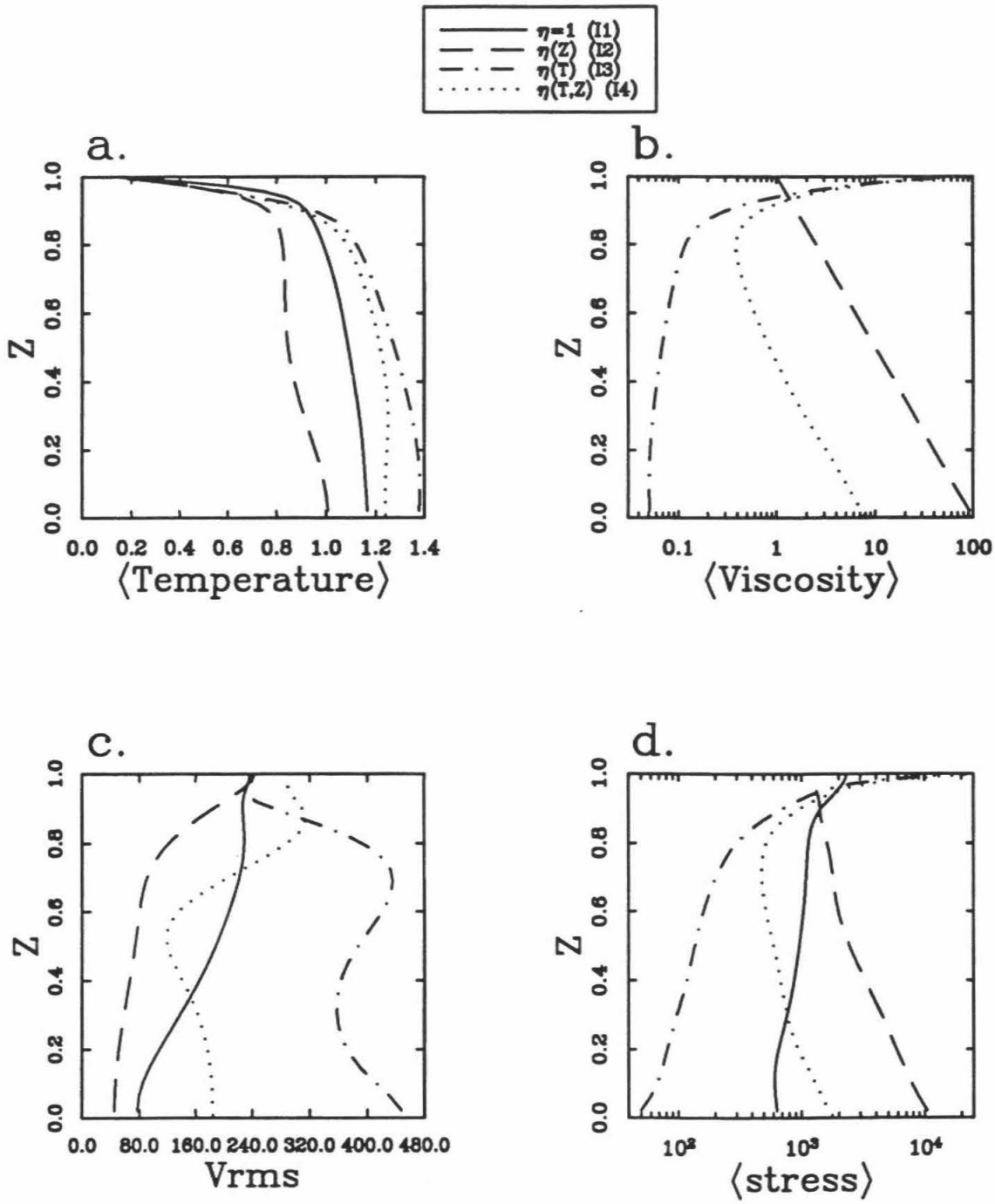
η=1 (I1)
η(Z) (I2)
η(T) (I3)
η(T,Z) (I4)
a.
b.
c.
d.
Z
⟨Temperature⟩
⟨Viscosity⟩
Vrms
⟨stress⟩
0.0 0.2 0.4 0.6 0.8 1.0
0.0 0.2 0.4 0.6 0.8 1.0 1.2 1.4
0.1 1 10 100
0.0 80.0 160.0 240.0 320.0 400.0 480.0
10² 10³ 10⁴

[*Howard*, 1966] to each boundary layer. The boundary layer Ra numbers must be equal to the critical Rayleigh number for convective instability:

$$\frac{\Delta T_u \delta_u^3}{\eta_u} \approx \frac{\Delta T_l \delta_l^3}{\eta_l} \tag{6.12}$$

where δ is the boundary-layer thickness, subscripts u and l denote upper and lower boundaries respectively, and the other symbols were defined earlier. In addition, heat flow through top and bottom must be equal:

$$\frac{\Delta T_u}{\delta_u} = \frac{\Delta T_l}{\delta_l} \tag{6.13}$$

Thus,

$$\frac{\Delta T_l}{\Delta T_u} = \frac{\delta_l}{\delta_u} \approx \left(\frac{\eta_l}{\eta_u} \right)^{1/4} \tag{6.14}$$

giving a ratio of approximately 3 for the 100-fold viscosity increase used here, approximately what is observed.

When the viscosity is dependent only on temperature (cases B4 and B7), the upper boundary layer becomes stiff, heat transport is impeded, and the interior temperature rises to around 0.7 for the cases reported here. This increase of interior temperature due to temperature-dependent viscosity has been noted in most of the previous laboratory and numerical studies discussed earlier. The interior of the cell is again approximately isothermal, with a marked cold region just above the lower thermal boundary layer, which is due to the horizontal spreading of the large cylindrical downwelling plumes. As the Rayleigh number is increased from 10^5 to 10^6 (case B2 to B7), the boundary layers and this cold region become smaller in vertical extent, and the interior is more nearly

isothermal. A local boundary layer Ra analysis is difficult due to the rapidly varying viscosity in the boundary layers.

The viscosity profiles for these cases display the same features. The interior mean viscosity for case B4 is greater than 1 even though the interior mean temperature is greater than 0.5, and $\eta(T=0.5)=1$. This is due to the fact that the exponential of the mean of some values is not the same as the mean of the exponential of the values, and the highly-viscous cold downwelling plumes raise the horizontally-averaged viscosity more above 1. If the geometric rather than arithmetic mean of the viscosity was used (equivalent to taking the mean in logarithmic space) as in *Christensen* [1985a], this effect would be less pronounced, and the viscosity profile could be calculated directly from the mean temperature profile. In case B7, the narrower cold plumes associated with the higher Ra have a smaller effect on horizontally-averaged viscosity, and thus $\langle\eta\rangle$ is significantly lower than case B4, more so than would be predicted simply from the change in $\langle T\rangle$.

Nataf [1991] observed that in laboratory experiments, the internal temperature adjusts so that the viscosity contrast over the lower boundary layer never exceeds a factor of about 8, regardless of the total viscosity contrast across the layer. In these 3-D simulations, a somewhat larger viscosity contrast of about 20 is obtained across the lower boundary layer. This difference could be due to the stress-free boundary conditions, as opposed to the rigid boundaries of laboratory experiments, or to differences in the viscosity law, which in these current simulations, gives much larger viscosity variations for cold regions than for hot regions. It would be interesting to progress to higher total viscosity contrasts, in order to establish whether the lower viscosity contrast would remain constant. Limitations in the numerical technique prevent this test for the moment, however.

Adding depth-dependence to the temperature-dependence of viscosity (case B6) reduces the interior temperature to about 0.4, resulting in a slightly subadiabatic internal temperature profile, and a systematic increase in viscosity with depth, except within the boundary layers. Thus, it seems that the interior temperature of the mantle is quite sensitive

to the exact details of the rheological law, and is a delicate balance between temperature-dependence increasing the temperature and depth-dependence decreasing the temperature.

The r.m.s. velocity profiles give an indication of convective vigor. When depth-dependent viscosity is included (cases B5 and B6), there is a systematic decrease in velocity with depth, as would be expected. Constancy of heat transport is obtained by the larger temperature drop over the lower boundary layer, resulting in larger horizontal temperature differences in the deep mantle, where circulation is sluggish. Temperature-dependent viscosity (cases B4 and B6) causes a local decrease in velocity in the upper boundary layer and a local increase in velocity in the lower boundary layer. Flow is not greatly inhibited at the top, however, and the stiff upper boundary layer still participates in the flow, corresponding to the whole-mantle regime described by *Ogawa et al.* [1991].

Stress profiles appear closely related to the viscosity profiles, displaying the same features. The constant viscosity case (B1) has approximately constant stress. Cases with temperature-dependent viscosity display stress minima in the hot lower boundary layer and strong stress maxima at the surface. Indeed, the stress level at the surface is typically around 1.5-2 orders of magnitude larger than the the stress in the interior of the cell. With depth-dependent viscosity included, there is an additional stress maximum in the lower mantle.

Compressible (Fig. 6.6). The profiles for the constant-viscosity compressible case C1 display some marked differences from the Boussinesq case B1. As expected, the interior temperature now exhibits a gradient due to adiabatic compression. The interior temperature is also higher, with a much larger temperature drop over the upper boundary layer, although the boundary layers are of similar thickness. These points can again be analyzed using a local boundary layer analysis, assuming the criteria of equal heat flow (noting that heat capacity is held constant):

$$\frac{\rho_u \kappa_u \Delta T_u}{\delta_u} \approx \frac{\rho_l \kappa_l \Delta T_l}{\delta_l} \tag{6.15}$$

and critical local Ra:

$$\frac{\rho_u \alpha_u \Delta T_u \delta_u^3}{\eta_u \kappa_u} \approx \frac{\rho_l \alpha_l \Delta T_l \delta_l^3}{\eta_l \kappa_l} \tag{6.16}$$

leading to:

$$\frac{\Delta T_u}{\Delta T_l} \approx \frac{\rho_l}{\rho_u}\left(\frac{\kappa_l}{\kappa_u}\right)^{1/2}\left(\frac{\alpha_l \eta_u}{\alpha_u \eta_l}\right)^{1/4} \tag{6.17}$$

and

$$\frac{\delta_u}{\delta_l} \approx \left(\frac{\kappa_u}{\kappa_l}\right)^{1/2}\left(\frac{\alpha_l \eta_u}{\alpha_u \eta_l}\right)^{1/4} \tag{6.18}$$

These scaling laws explain all the trends that have been observed in these and previous 2-D numerical simulations with depth-dependent parameters. Decreasing α or increasing η with depth reduces the interior temperature [*Gurnis and Davies*, 1986a; *Yuen and Zhang*, 1989; *Hansen et al.*, 1993], and increasing k with depth increases the interior temperature [*Yuen and Zhang*, 1989; *Leitch et al.*, 1991]. Quantitatively, the formulae are less successful: for the reference state values listed in Table 6.1 and constant dynamic viscosity (case C1), we expect $\Delta T_u/\Delta T_l \approx 1.5$ and $\delta_u/\delta_l \approx 0.4$, both somewhat lower than observed.

For the cases with viscosity variations (C2-C4), the same trends as for the Boussinesq cases can be observed, i.e., temperature-dependence of viscosity increases interior temperature, and depth-dependence decreases the interior temperature. For case C3, which has temperature-dependent viscosity, the interior temperature is so high that the

temperature contrasts associated with upwellings are difficult to detect in images of the T field. In case C3, the adiabatic increase of temperature with depth results in a decrease of viscosity with depth, an effect which reduces the amount of viscosity increase with depth in case C4.

Velocities and stress also display the same trends as for the constant viscosity cases. For the constant-viscosity case C1, circulation is somewhat more sluggish in the deep mantle than in the shallow mantle, presumably due to the decrease of local Ra caused by depth-dependent properties.

Internal heating (Fig. 6.7). Cases I1-I4 are all characterized by a slightly subadiabatic internal temperature profile, a strong upper boundary layer and no basal boundary layer. Since the internal heating rates were chosen to give similar surface heat flows to cases C1-C4, as discussed earlier, nondimensional internal temperatures are similar to these cases and display the same trends with temperature-dependence and depth-dependence of viscosity. The velocities and stress levels in the deep mantle are somewhat lower than for the basally-heated cases, due to the lack of upwellings from the lower thermal boundary layer.

Thermal budget

Figure 6.8 shows the horizontally-averaged heating (positive) or cooling (negative) rates due to the various terms in the energy equation (Equation (6.3)), namely advection, diffusion (second term on the right hand side), and the compressible terms adiabatic heating (AH - first term on the right hand side) and viscous dissipation (VD - last term on the right hand side), for various cases. Similar information for spherical geometry is plotted in Fig. 2 of *Glatzmaier* [1988]. The term 'adiabatic heating' is somewhat misleading, since no entropy production is involved; the term arises simply from material moving up and down adiabats. Conservation of mass necessitates that the upward mass flux through a particular

depth is equal to the downward mass flow through that depth. However, 'hot' adiabats are steeper than 'cold' adiabats, hence hot upwelling material will be adiabatically cooling as it rises more rapidly than cold downwelling material will be adiabatically warming as it descends. Thus, the horizontally-averaged adiabatic heating is negative. The term disappears when the thermal equation is written in terms of entropy rather than temperature [e.g., *Glatzmaier*, 1988].

Constant viscosity. For the constant-viscosity cases, the dominant terms are observed to be advection and diffusion, which have large peaks in the boundary layers. The additional terms associated with compressibility (VD and AH) play only a minor role in the heat budget for these cases. All of the contributions to heat budget increase with Rayleigh number. Advection and diffusion also become more localized towards the boundaries, due to the narrower boundary layers. *Balachandar et al.* [1993] state that VD and AH become more important at higher Ra, and the results presented here confirm that these terms increase with Ra. However, the peak values for advection and diffusion increase equally or more rapidly with Ra than the peak values for VD and AH. Thus, in terms of the overall heat budget, AH and VD do not become more important as Ra increases. These authors also state that the maximum in the temperature profile close to the upper boundary (Fig. 3 in *Balachandar et al.* [1993]) is due to viscosity dissipation. However, this maximum is also observed in Boussinesq cases, where viscous dissipation is not present (see Fig. 7.4, *Jarvis and Peltier* [1989], p502). Temperature profiles for equivalent Boussinesq and compressible cases are compared in *Jarvis and Peltier* [1989], p527. These show that the Boussinesq cases display a similar overshoot in the temperature profile to the compressible cases. This overshoot is due to the spreading of hot upwellings below the upper thermal boundary layer, not to viscous dissipation.

A simple scaling analysis, based on the idealized scaling of Nusselt number ($Ra^{1/3}$), velocity ($Ra^{2/3}$), and boundary layer thickness ($Ra^{-1/3}$) [*Turcotte and Schubert,*

Fig. 6.8. Heat balance for various cases. Plotted are depth profiles of the horizontally-averaged values of the various terms in the temperature equation: advection (dotted lines), diffusion (dot-dash lines), viscous dissipation (solid lines), adiabatic heating (dashed line). Top row: constant-viscosity compressible cases C8 ($Ra=10^5$) and C1 ($Ra=10^6$); middle row: temperature- and depth-dependent viscosity compressible cases C4 ($Ra=10^6$) and C6 ($Ra=10^7$); bottom row: internally-heated cases I1 (constant viscosity, $Ra=10^6$) and I4 (temperature- and depth-dependent viscosity, $Ra=10^6$).

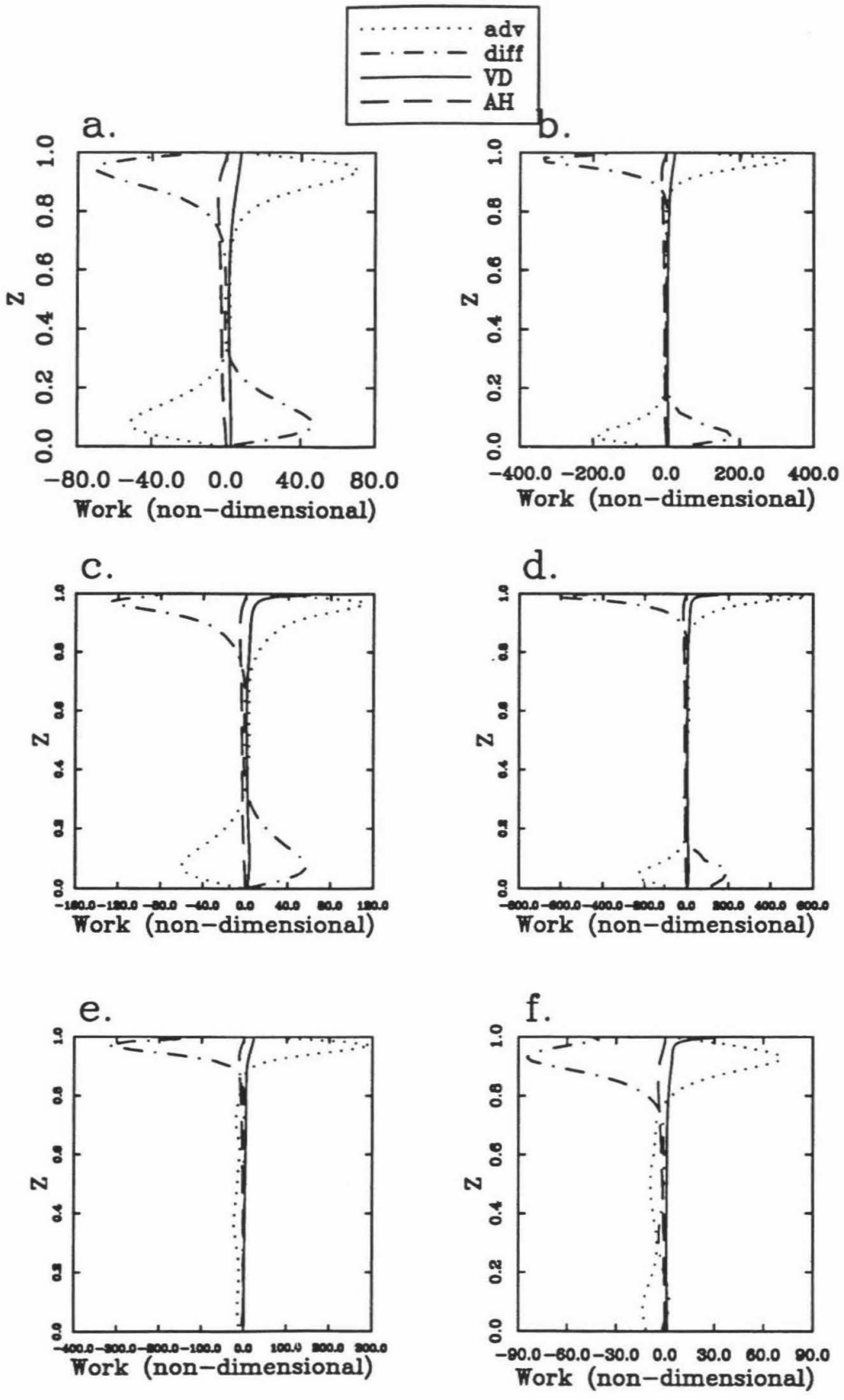
adv
diff
VD
AH
a.
b.
c.
d.
e.
f.
z
Work (non−dimensional)
−80.0 −40.0 0.0 40.0 80.0
−400.0 −200.0 0.0 200.0 400.0
0.0 0.2 0.4 0.6 0.8 1.0

1982] supports these observations. Advection and diffusion terms scale as the Nusselt number, i.e., $Ra^{1/3}$. Adiabatic heating scales as the velocity ($Ra^{2/3}$) times the width of convective features ($Ra^{-1/3}$) resulting in a $Ra^{1/3}$ scaling. It seems reasonable to assume that strain rate and thus non-dimensional stress (because $\eta \equiv 1$) scale in proportion to velocity, i.e., $Ra^{2/3}$. Nondimensional viscous dissipation is the product of these divided by Ra (see Equation (6.3)), resulting in an overall $Ra^{1/3}$ scaling for this term. Thus, all terms are expected to increase by similar amounts with increasing Ra, as observed in the presented simulations. If flow were highly localized, which is not the case in the presented results, the magnitude of the viscous dissipation term would increase as $(1/\text{lengthscale})^2$, and thus may become important.

T-dep viscosity. The addition of temperature-dependent viscosity results in a large increase in horizontally-averaged viscous dissipation towards the upper surface. The magnitude of VD is now comparable to that of the advection and diffusion terms, and thus viscous dissipation is a significant contributor to the surface heat flux when temperature-dependent viscosity is included. The increase of VD with temperature-dependent viscosity was previously noted in the 3-D calculations of *Balachandar and Yuen* [1993]. The peak in viscous dissipation arises from the stress peak in the upper boundary layer noted in the discussion of radial profiles.

Discussion

Hot sheets and coldspots?

The upwelling sheets and downwelling plumes found in the basally-heated cases with purely temperature-dependent viscosity (B2, B3, B4 and C3) are compatible with the result obtained by *Weinstein and Christensen* [1991] in a 4x4x1 box with rigid lower and stress-free (isothermal) upper boundaries, and a viscosity contrast of 50. The pattern can be

understood in the following terms: Depth-dependent properties cause the local Rayleigh number to decrease with depth, resulting in large cells with downwelling sheets and upwelling plumes (case C1 and *Balachandar et al.* [1992]). In the present cases listed above, the local Rayleigh number increases by 3 orders of magnitude with depth. Thus, the inverse flow pattern is obtained: upwelling sheets and downwelling plumes, with the viscous upper boundary layer imposing a long wavelength to the flow. It may be tempting to interpret these upwelling sheets as possible active deep upwelling below mid-ocean ridges. However, this would contradict various geophysical observables [*Davies*, 1988a]. Other results presented here show that adding greater realism in the form of depth-dependent viscosity and/or internal heating and/or compressibility, push the system towards a preference for upwelling plumes. Spherical geometry is likely to work in the same direction. Thus, it seems likely that for realistic material properties, heating mode and geometry, upwelling plumes, rather than narrow upwelling sheets, will be the preferred mode of upwelling.

On Earth, downwellings seem to occur exclusively as linear slabs: cylindrical 'coldspots' are not observed. This may be a natural consequence of plate tectonics and the associated complete subduction of rigid lithosphere by means faults in the crust and lithosphere. It is difficult to imagine a fault system that would allow rigid plate to converge radially from all directions into a common coldspot, without it being extremely dissipative. On Venus, however, plate tectonics is not currently operative and quasi-cylindrical downwellings may well occur below a rigid lid. Indeed, plateau-shaped highlands found in regions such as Aphrodite Terra or Ishtar Terra have been associated with cold cylindrical downwellings by some researchers [*Kiefer and Hager*, 1991; *Bindschadler et al.*, 1992].

Horizontal wavelengths

A huge variation in characteristic horizontal wavelengths is observed, depending on the material properties and heating mode. Temperature-dependent viscosity with no depth-dependence favors huge cells. However, adding depth-dependence results in very small cells. Compressibility acts in the opposite direction, increasing the cell size.

These effects may be understood in terms of a competition between boundary layers. When one boundary layer is much more sluggish than the other, which could be the upper boundary layer in a Boussinesq case with temperature-dependent viscosity, or the lower boundary layer in a case with constant viscosity but depth-dependent compressible parameters, long-wavelength cells result. However, when both boundary layers are of similar stiffness, as in the Boussinesq case with depth- and temperature-dependent viscosity (B6), short-wavelength cells result. These effects can again be examined using simple scaling relationships and local Rayleigh numbers to determine the ratio of the preferred lengthscales for upper and lower boundaries.

Firstly, assume that material with the interior temperature is emplaced in the boundary layer and moves horizontally with velocity v. The thermal boundary layer will thicken by thermal diffusion, eventually becoming thick enough that the local Ra exceeds the critical Ra, and an up- or downwelling will result. The characteristic lengthscale is thus given by:

$$L = v t_{diff} \tag{6.19}$$

where

$$t_{diff} \approx \delta_{crit}^2 / \kappa \tag{6.20}$$

and

$$\delta_{crit}^3 \approx \frac{\eta \kappa}{\rho g \alpha \Delta T} Ra_{crit} \tag{6.21}$$

thus

$$L \approx \frac{\nu}{\kappa^{1/3}} \left(\frac{\eta}{\rho \alpha \Delta T} \right)^{2/3} \tag{6.22}$$

$$\frac{L_u}{L_l} \approx \frac{\nu_u}{\nu_l} \left(\frac{\kappa_l}{\kappa_u} \right)^{1/3} \left(\frac{\eta_u \rho_l \alpha_l \Delta T_l}{\eta_l \rho_u \alpha_u \Delta T_u} \right)^{2/3} \tag{6.23}$$

and substituting the expression found earlier for temperature drops, we obtain:

$$\frac{L_u}{L_l} \approx \frac{\nu_u}{\nu_l} \left(\frac{\eta_u \alpha_l}{\eta_l \alpha_u} \right)^{1/2} \tag{6.24}$$

Thus, the ratio of prefered lengthscales is strongly affected by contrasts in viscosity and thermal expansivity. In the future, it is desirable to obtain a scaling for velocity.

Rayleigh number also appears to play a role in determining horizontal lengthscales, particularly when one or more depth-dependent properties are present. A decrease in cell size with an order-of-magnitude increase in Ra was noted when viscosity was dependent on temperature and pressure for Boussinesq cases (B6 to B8), compressible, basally-heated cases (B4 to B6) and for compressible, internally-heated cases (I4 to I8). A decrease was also noted for constant-viscosity, compressible, internally-heated cases (I5 to I1 to I7). More tests are needed to establish whether this trend holds true for all combinations of parameters. *Hansen et al.* [1993] found using steady-state 2-D calculations that temperature-dependent viscosity has less influence on the convection as Rayleigh number is increased with a fixed viscosity contrast. The results presented here indicate that temperature-dependent viscosity tends to result in large cells, compared to constant-viscosity cases. If the viscosity variations had less effect at higher Ra, the cell size might decrease towards the size observed in constant-viscosity cases. This mechanism may be

particularly appropriate for explaining the difference between case I1 and case I7. Since the viscosity contrast in the mantles of Earth or Venus is likely to be much higher than that modeled here, however, this trend may not be relevant to planetary mantles.

Plume character

Temperature-dependent viscosity results in a low-viscosity layer immediately above the CMB, strongly affecting the formation and dynamics of upwelling plumes [*Sleep*, 1987; *Olson et al.*, 1987, 1993]. Popular models for plumes in the Earth (for summaries see *Loper* [1991], and *Duncan and Griffiths* [1991]) assume that plume conduits are uniformly narrow throughout the depth of the mantle. In global seismic tomographic models [*Su et al.*, 1992b; *Fukao*, 1992], very broad hot regions, resembling huge upwelling plumes, are observed in the lower mantle, although since narrow plumes cannot be detected in such models, it is not clear whether these regions should be interpreted as single plumes, or simply as hot regions through which concentrated narrow plumes are rising.

In the compressible cases presented here, upwelling plumes are very broad, even when temperature-dependent viscosity is included, more closely resembling those of seismic tomography than the idealized models. However, temperature-dependent viscosity is observed to narrow the plumes (compare cases C2 and C4) and the viscosity contrast associated with plumes in these results is much smaller than that likely to be appropriate for the Earth, because (1) numerical considerations limit the total viscosity contrast that can be modeled, (2) the Arrhenius law used results in larger viscosity variations in cold features than in hot features, and (3) when no mechanism for producing surface plates is included, the viscosity contrast over the lower thermal boundary layer remains low even when the total viscosity contrast across the layer is increased [*Nataf*, 1991]. Thus, the hot plumes in

these models would be expected to become much narrower if a more realistic rheology were included.

However, even with a more realistic viscosity contrast, plumes would still be broader at their base, narrowing as they ascend. This is due to the depth-dependence of material properties, particularly thermal expansivity and thermal conductivity, which result in a decrease of the local Rayleigh number by at least an order of magnitude over the depth of the mantle. The likely increase in horizontally-averaged viscosity with depth by 1-3 orders of magnitude would further reduce the local Ra by the same factor, resulting in an overall 2-4 order of magnitude decrease in local Ra over the depth of the mantle. Despite the large, first-order effect on plume dynamics that this decrease would have, our current understanding of plumes is based on laboratory experiments [e.g., *Griffiths and Campbell,* 1990] and numerical and analytical models of plume formation, growth and propagation though mantle [e.g., *Olson et al.,* 1993; *Sleep*, 1990] which assume constant-properties (excluding temperature-dependent viscosity). The true picture of mantle plumes may be significantly different from the simple models on which our current understanding is based.

Internal heating

The Earth's mantle is thought to be mainly internally-heated [*Schubert*, 1979; *Davies and Richards*, 1992] and indeed, first-order evidence for this can be obtained by looking at surface observables: oceanic plates have a temperature anomaly of ~1300 K [*Turcotte and Schubert*, 1982] and account for ~75% of the heat loss from the interior [*Sclater et al.*, 1980] whereas hotspots, which are generally thought to be associated with hot upwelling plumes, have a much smaller thermal anomaly of only ~300 K in the upper mantle (although this temperature contrast may not be a good guide to the temperature drop over the lower thermal boundary layer) and account for only ~5-20% of the total heat loss [*Davies*, 1988a; *Sleep*, 1990; *Davies and Richards*, 1992]. However, it has long been a

problem that mantle convection simulations with large amounts of internal heating display a short-wavelength pattern of closely-spaced, time-dependent downwelling plumes, therefore resembling the Earth less than the downwelling sheets obtained in basally-heated simulations (cases I1,I7 and [*Houseman*, 1988; *Travis et al.*, 1990b; *Schubert*, 1992; *Parmentier et al.*, 1994]). These results show that variable viscosity provides a way of reconciling the observation of long-wavelength flow with internal heating. Long-wavelength flows are obtained even with internal heating, and there is a greater propensity for the downwellings to be linear, similar to slabs. In one result (case I2) with depth-dependent viscosity, when residual temperature (i.e., relative to geotherm) was plotted, a very broad hot upwelling 'plume', somewhat reminiscent of those observed under the Pacific and Africa in global seismic tomographic models [e.g., *Su et al.*, 1992b; *Fukao*, 1992], was visible, even though there was no heat being conducted through the core-mantle boundary. This indicates that the large plumes apparently observed in tomographic models are not necessarily indicative of high basal heat flux.

Stagnant lid

In these simulations, the upper boundary layer participates in the flow. If the viscosity contrast were increased sufficiently, a 'stagnant lid' would develop [*Ogawa et al.*, 1991], and the convective pattern might resemble the rigid boundary case, with small cells [*Giannandrea and Christensen*, 1993]. However, the mobility of plates on the Earth suggest that this regime is not relevant to Earth dynamics, even though the viscosity contrast over the lithosphere may be extremely large. On Venus, the high surface temperature and widespread tectonic deformation [*Saunders et al.*, 1991] also raise doubts about the relevance of this regime.

Conclusions

These results show that an enormous range of convective styles and characteristic horizontal wavelengths are possible, depending on the exact details of rheology, compressibility, heating mode and Rayleigh number. All of these have a significant effect on the flow, indicating the importance of including them into numerical models, and matching the Earth's parameter space as closely as possible.

Results obtained under the Boussinesq approximation show clearly the importance of modeling wide domains. With rheology dependency solely on temperature and stress-free boundaries, very wide cells are formed (periodicity 8) with upwelling sheets and downwelling plumes, in contrast to the small-wavelength spoke pattern obtained with rigid boundaries [*White*, 1988; *Tackley*, 1993]. *Christensen and Harder* [1990] previously concluded that upwelling sheets are unlikely to occur in temperature-dependent viscosity convection. However, these results indicate that at sufficiently large aspect-ratio and with stress-free boundaries, they are the preferred solution. Adding depth-dependence completely reverses these characteristics, resulting in small cells with upwelling plumes and downwelling sheets. Increasing the Rayleigh number by an order of magnitude does not appear to fundamentally change the convective pattern, resulting in narrower features and greater time-dependence, and in some cases, smaller cell sizes.

Compressibility, with the associated depth-dependent material properties, results in fairly large cells for basally-heated models, and a preference for large upwelling plumes and narrow downwelling sheets. However, when the viscosity is dependent solely on temperature, downwelling plumes and linear upwellings are observed, in accordance with the equivalent Boussinesq solutions.

Perhaps the greatest modulation effect of viscosity variations occurs in internally-heated, compressible cases. It is thought that the Earth and Venus are dominantly internally heated; however, constant-viscosity internally-heated convection models display short-

wavelength, highly time-dependent cold plumes, which look less like the Earth than the downwelling sheets and upwelling plumes obtained in basally-heated models. However, when the viscosity is dependent on temperature and/or depth, the planform is substantially changed to a long wavelength pattern consisting of downwelling sheets at the surface with plume-like instabilities as they descend. Thus, internally-heated models are compatible with the Earth observations, provided an appropriate rheological law is used.

The temperature in the interior of convection cells, and the associated temperature drops over upper and lower boundary conditions, are strongly affected by the exact values of rheological and thermodynamic parameters. The interior temperature is strongly increased by temperature-dependent viscosity and depth-dependent thermal conductivity, but strongly decreased by depth-dependent viscosity. This further illustrates the importance of trying to match the Earth's parameters as closely as possible. However, the temperature-dependence of viscosity in the Earth is much stronger than in these simulations, which acts to buffer the interior temperature through a self-regulation mechanism first described by *Tozer* [1972], and thus, the effect of various parameters on the internal mantle temperature may be lower than that predicted by these simulations. The interior temperature profile (away from boundary layers) is always close to adiabatic, and usually somewhat subadiabatic.

The convective vigor, as measured by r.m.s. velocity, is diminished in regions of high viscosity. However, in these calculations, the stiff upper boundary layer still participates in the flow; a larger viscosity contrast would be necessary to cause a rigid lid. The stress distribution resembles the viscosity distribution, with very high stress levels in the upper boundary layer.

Examination of the energy balance reveals that viscous dissipation and adiabatic heating are only minor contributors to the heat budget for constant-viscosity compressible mantle convection, with advection and diffusion playing the dominant role. Although the magnitude of viscous dissipation and adiabatic heating terms increases with Rayleigh

number, advection and diffusion terms increase by a similar or larger factor, and thus viscous dissipation and adiabatic heating are still relatively unimportant. However, when temperature-dependent viscosity is included, viscous dissipation becomes very important in the stiff upper boundary layer due to the high stresses, and is an important contributor to the surface heat flow.

In these results, realistic plates and subduction is not obtained. Temperature-dependent viscosity by itself does not result in plate-like behavior. The downwellings are two-sided, and a concentration of stress occurs where they leave the upper boundary layer. In order for plates to occur, an additional mechanism is needed to create weak zones in the stiff lid, such as nonlinear power-law rheology [*Cserepes*, 1982; *Christensen*, 1984b; *Weinstein and Olson*, 1992], or a 'stick-slip' rheology [*Bercovici,* 1993]. A priority in future work must be to examine the influences of these rheologies in self-consistent three-dimensional models. Other priorities include the effects of phase transitions, spherical geometry, compositional variations and continents. Other possible rheological complexities not considered here include power law, non-Newtonian creep in the upper and possibly lower mantle [*Kirby and Kronenberg*, 1987; *Karato and Wu*, 1993], a viscosity jump at or around the 670 km discontinuity [*Hager and Richards*, 1989; *King et al.*, 1992; *Forte et al.*, 1993; *Mitrovica and Peltier*, 1993], a hard garnet layer leading to higher viscosities in the transition zone [*Meade and Jeanloz*, 1990], and transformational superplasticity [*Karato and Li*, 1992].

Bibliography

Akaogi, M. and E. Ito, Refinement of enthalpy measurement of MgSiO3 perovskite and negative pressure-temperature slopes for perovskite-forming reactions, *Geophys. Res. Lett., 20*, 1839-1842, 1993.

Akaogi, M., E. Ito and A. Navrotsky, Olivine-modified spinel-spinel transitions in the system Mg2SiO4-Fe2SiO4: Calorimetric measurements, thermochemical calculation, and geophysical application, *J. Geophys. Res., 94*, 15671-15685, 1989.

Allègre, C.J. and E. Lewin, Chemical structure and history of the Earth: evidence from global non-linear inversion of isotopic data in a three-box model, *Earth Planet. Sci. Lett., 96*, 61-88, 1989.

Allègre, C.J. and D.L. Turcotte, Implications of a two-component marble-cake mantle, *Nature, 323*, 123-127, 1986.

Anderson, D.L., Phase changes in the upper mantle, *Science 157*, 1165-1173, 1967.

Anderson, D.L., Petrology of the mantle, *Mineralog. Soc. America Spc. Paper, 3*, 85-93, 1970.

Anderson, D.L., The upper mantle transition zone: Eclogite?, *Geophys. Res. Lett., 6*, 433-435, 1979.

Anderson, D.L., The chemical composition and evolution of the mantle: Advances in Earth and planetary sciences, in *High Pressure Research in Geophysics, ed., S. Akimoto and M.H. Manghani,* pp301-318, D. Reidel, Hingham, Mass., 1982a.

Anderson, D.L., Hotspots, polar wander, mesozoic convection, and the geoid, *Nature, 297*, 391-393, 1982b.

Anderson, D.L., A seismic equation of state II. Shear properties and thermodynamics of the lower mantle, *Phys. Earth Plan. Int.*, 45, 307-323 , 1987.

Anderson, D.L., *Theory of the Earth*, 366pp, Blackwell, Boston, 1989.

Anderson, D.L., Chemical boundaries in the mantle, in *Glacial Isostacy, Sea-level and mantle rheology, ed. R. Sabadini et al.*, Kluwer, 1991.

Anderson, D.L. and J.D. Bass, Mineralogy and composition of the upper mantle, *Geophys. Res. Lett., 11*, 637-640, 1984.

Anderson, D.L. and J.D. Bass, The transition region of the Earth's upper mantle, *Nature, 320*, 321-328, 1986.

Anderson, D.L. and M.N. Toksöz, Surface waves on a spherical Earth 1. Upper mantle structure from Love waves, *J. Geophys. Res., 68*, 3483-3500, 1963.

Anderson, O.L., H. Oda and D. Isaak, A model for the computation of thermal expansivity at high compression and high temperatures: MgO as an example, *Geophys. Res. Lett.*, 19, 1987-1990, 1992.

Ashby, M.F. and R.A. Verall, Micromechanisms of flow and fracture, and their relevance to the rheology of the upper mantle, *Phil. Trans. R. Soc. London A., 288*, 59-95, 1977.

Balachandar, S. and D.A. Yuen, Time-dependent three-dimensional compressible convection with depth-dependent properties, *Geophys. Res. Lett.,* 19, 2247-2250, 1992.

Balachandar, S. and D.A. Yuen, Fully spectral methods for 3-D time-dependent compressible convection with temperature-dependent viscosity, *EOS Trans Amer. Geophys. Union, 74*, p598, 1993.

Balachandar, S., D.A. Yuen and D. Reuteler, Viscous and adiabatic heating effects in 3-dimensional compressible convection at infinite Prandtl number, *Phys. Fluid. A., 5*, 2938-2945, 1993.

Balmino, G., K. Lambeck and W.M. Kaula, A spherical harmonic analysis of the Earth's topography, *J. Geophys. Res., 78*, 478-481, 1973.

Baskett, F. and J.L. Hennessy, Microprocessors: From desktops to supercomputers, *Science 261, 864-871*, 1993.

Baumgardner, J.R., Three-dimensional treatment of convective flow in the Earth's mantle, *J. Stat. Phys., 39*, 501-511, 1985.

Baumgardner, J.R., Application of supercomputers to 3-D mantle convection, in *The Physics of the Planets, ed. S.K. Runcorn*, 199-231, Wiley, New York, 1988.

Baumgardner, J.R., 3-D numerical investigation of the mantle dynamics associated with the breakup of Pangea, in *Flow and Creep in the Solar System: Observations, Modeling and Theory, ed. D.B. Stone and S.K. Runcorn*, pp207-224, Kluwer, 1993.

Bénard, Les tourbillons cellulaires dans une nappe liquide transportant de la chaleur par convection en régime permanent, *Annales de Chimie at de Physique, 7e serie, Tome XXIII*, 62-144, 1901.

Benioff, H., Orogenesis and deep crustal structure: Additional evidence from seismology, *Bull. Geol. Soc. Am., 65*, 385-400, 1954.

Benz, H.M. and J.E. Vidale, Sharpness of upper-mantle discontinuities determined from high-frequency reflections, *Nature, 365*, 147-150, 1993.

Bercovici, D., A simple model of plate generation from mantle flow, *Geophys. J. Int., 114*, 635-650, 1993.

Bercovici, D., G. Schubert and G.A. Glatzmaier, Influence of heating mode on three-dimensional mantle convection, *Geophys. Res. Lett., 16*, 617-620, 1989a.

Bercovici, D., G. Schubert and G.A. Glatzmaier, Three-dimensional spherical models of convection in the Earth's mantle, *Science, 244*, 893-1016, 1989b.

Bercovici, D., G. Schubert and G.A. Glatzmaier, Model growth and coupling in three-dimensional spherical convection, *Geophys. Astrophys. Fluid Dyn., 61*, 149-159, 1991.

Bercovici, D., G. Schubert and G.A. Glatzmaier, Three-dimensional convection of an infinite-Prandtl-number compressible fluid in a basally heated spherical shell, *J. Fluid Mech, 239*, 683-719, 1992.

Bercovici, D., G. Schubert, G.A. Glatzmaier and A. Zebib, Three-dimensional convection in a spherical shell, *J. Fluid Mech., 206*, 75-204, 1989c.

Bercovici, D., G. Schubert and P.J. Tackley, On the penetration of the 660 km phase change by mantle downflows, *Geophys. Res. Lett, 20,* 2599-2602, 1993.

Bina, C.R. and B.J. Wood, Olivine-spinel transitions, *J. Geophys. Res., 92,* 4853-4866, 1987.

Bindschadler, D.L., G. Schubert and P.G. Ford, Venus's center of figure - center of mass offset, *Icarus, submitted*, 1994.

Bindschadler, D.L., G. Schubert and W.M. Kaula, Coldspots and hotspots: Global tectonics and mantle dynamics of Venus, *J. Geophys. Res., 97*, 13495-13532, 1992.

Birch, F., Elasticity and composition of the Earth's interior, *J. Geophys. Res.*, 57, 227-286, 1952.

Blankenbach, B., F. Busse, U. Christensen, L. Cserepes, D. Gunkel, U. Hansen, H. Harder, G. Jarvis, M. Koch, G. Marquart, D. Moore, P. Olson, H. Schmeleing and T. Scnaubelt, A benchmark comparison for mantle convection codes, *Geophys. J. Int., 98,* 23-28, 1989.

Booker, J.R., Thermal convection with strongly temperature-dependent viscosity, *J. Fluid Mech., 76*, 741-754, 1976.

Boussinesq, J., *Théorie analytique de la Chaleur mise en Harmonie avec la Thermodynamique et avec la Théorie mécanique de la Lumière*, Tome II, Gauthier-Villars, Paris, 157-176, 1903.

Brandt, A., Guide to multigrid development, in *Multigrid Methods: Proceedings Koln-Porz, 1981, Lecture Notes in Mathematics, ed Hackbusch W and Trottenberg U.*, Springer-Verlag, Berlin, 220-312, 1982.

Brandt, A., Multigrid techniques: 1984 guide, with applications to fluid dynamics, lecture notes for *Computational Fluid Dynamics Series, von-Karmen Institute for Fluid Dynamics,* Rhode-Saint-Genese, Belgium, 1984.

Breuer, D. and T. Spohn, Cooling of the Earth, Urey ratios, and the problem of Potassium in the core, *Geophys. Res. Lett., 20*, 1655-1658, 1993.

Bullard, E.C., J.E. Everett and A.G. Smith, The fit of the continents around the Atlantic, *Phil. Trans. R. Soc. London A., 258*, 41-51, 1965.

Burdick, L.J and D.L. Anderson, Interpretation of velocity profiles of the mantle, *J. Geophys. Res., 80*, 1070-1074, 1975.

Busse, F.H., Fundamentals of thermal convection, *Mantle Convection:Plate Tectonics and Global Dynamics, ed. W.R. Peltier,* 23-95, Gordon and Breach, New York, 1989.

Busse, F.H., U. Christensen, R. Clever, L. Cserepes, C. Gable, E. Giannandrea, L. Guillou, G. Houseman, H.-C. Nataf, M. Ogawa, M. Parmentier, C. Sotin and B. Travis, 3D convection at infinite Prandtl number in Cartesian geometry - A benchmark comparison, submitted to *Geophys. Astrophys. Fluid Dyn.*, 1993.

Busse, F.H. and H. Frick, Square-pattern convection in fluids with strongly temperature-dependent viscosity, *J. Fluid Mech., 150*, 451-465, 1985.

Buttles, J., L. Gillou and P. Olson, laboratory experiments on the deep structure of subducted slabs, *EOS Trans. Amer. Geophys. Union*, 74, 300-300, 1993.

Buzbee, B., Workstation clusters rise and shine, *Science 261, 852-853*, 1993.

Cadek, O., Z. Martinec and C. Matyska, Spectral variational approach to the non-Newtonian stokes problem in a spherical shell, *Comput. Phys., 71,* 56-70, 1992.

Cadek, O. and Y. Ricard, Toroidal poloidal energy partitioning and global lithospheric rotation during the Cenozoic, *Earth Plan. Sci. Lett., 109*, 621-632, 1992.

Cadek, O., D.A. Yuen, V. Steinbach, A. Chopelas and C. Matyska, Lower mantle thermal structure deduced from seismic tomography, mineral physics and numerical modeling, *Earth Plan. Sci. Lett., 121*, 385-402, 1994.

Carlson, R.W., Geophysical evolution of the crust and mantle, *Rev. Geophys., 25,* 1011-1020, 1987.

Carrigan, C.R., Convection in an internally heated, high Prandtl number fluid: a laboratory study, *Geophys. Astrophys. Fluid Dyn., 32*, 1-21, 1985.

Cassen, P. and Young, R.E., On the cooling of the Moon by solid convection, *The Moon, 12*, 361-368, 1975.

Chopelas, A. and R. Boehler, Thermal expansivity in the lower mantle, *Geophys. Res. Lett., 19*, 1983-1986, 1992.

Chopra, P.N. and M.S. Paterson, The experimental deformation of dunite, *Tectonophysics, 78,* 453-473, 1981.

Christensen, U.R., Convection in a variable viscosity fluid: Newtonian versus non-Newtonian rheology, *Earth Plan. Sci. Lett., 64*, 153-162, 1983.

Christensen, U.R., Heat transport by variable viscosity convection and implications for the Earth's thermal evolution, *Phys. Earth Planet. Inter., 35*, 264-282, 1984a.

Christensen, U.R., Convection with pressure- and temperature-dependent non-Newtonian rheology, *Geophys. J. R. Astr. Soc., 77,* 343-384, 1984b.

Christensen, U.R., Heat transport by variable viscosity convection II: pressure influence, non-Newtonian rheology and decaying heat sources, *Phys. Earth Planet. Inter., 37*, 183-205, 1985a.

Christensen, U.R., Viscosity-velocity correlation in convection cells with non-uniform viscosity, *J. Geophys., 57,* 72-75, 1985b.

Christensen, U.R., Time-dependent convection in elongated Rayleigh-Bénard cells, *Geophys. Res. Lett., 14*, 220-223, 1987a.

Christensen, U.R., Some geodynamical effects of anisotropic viscosity, *Geophys. J. R. Astr. Soc., 91,* 711-736, 1987b.

Christensen, U.R., The heat transport by convection rolls with free boundaries at high Rayleigh number, *Geophys. Astrophys. Fluid Dyn., 46*, 93-103, 1989a.

Christensen, U., Mixing by time-dependent convection, *Earth Plan. Sci. Lett., 95,* 382-394, 1989b.

Christensen, U.R., Models of mantle convection: one or several layers, *Phil. Trans. R. Soc. Lond. A, 328*, 417-424, 1989c.

Christensen, U.R., Mantle rheology, constitution, and convection, in *Mantle Convection: Plate Tectonics and Global Dynamics ed. W.R. Peltier,* Gordan and Breach, New York, 595-656, 1989d.

Christensen, U. and H. Harder, 3-D convection with variable viscosity, *Geophys. J. Int., 104,* 213-226, 1991.

Christensen, U.R. and D.A. Yuen, The interaction of a subducting lithospheric slab with a chemical or phase boundary, *J. Geophys. Res., 89*, 4389-4402, 1984.

Christensen, U.R. and D.A. Yuen, Layered convection induced by phase transitions, *J. Geophys. Res., 90*, 10291-10300, 1985.

Christensen, U. and D. Yuen, On the aspect ratio of Rayleigh-Benard convection cells, *Geophys. Res. Lett., 15*, 597-600 , 1988.

Christensen, U.R. and D.A. Yuen, Time-dependent convection with non-Newtonian viscosity, *J. Geophys. Res., 94*, 814-820, 1989.

Creager, K.C. and T.H. Jordan, Slab penetration into the lower mantle, *J. Geophys. Res., 89*, 3031-3049, 1984.

Creager, K.C. and T.H. Jordan, Slab penetration into the lower mantle beneath the Mariana and other island arcs of the northwest Pacific, *J. Geophys. Res., 91*, 3573-3589, 1986.

Cserepes, L., Numerical studies of non-Newtonian mantle convection, *Phys. Earth Plan. Inter., 30*, 49-61, 1982.

Cserepes, L., Effect of depth-dependent viscosity on the pattern of mantle convection, *Geophys. Res. Lett.*, 20, 2091-2094, 1993.

Cserepes, L. and U. Christensen, Three-dimensional convection under drifting plates, *Geophys. Res. Lett., 17*, 1497-1500, 1990.

Cserepes, L., M. Rabinowicz and C. Rosemberg-Borot, Thre-dimensional infinite Prandtl number convection in one and two layers with implications for the Earth's gravity field, *J. Geophys. Res.*, 93, 12009-12025, 1988.

Daly, S., The vagaries of variable viscosity convection, *Geophys. Res. Lett., 7*, 841-844, 1980.

Davies, G.F., Mantle convection under simulated plates: Effects of heating modes and ridge and trench migration, and implications for the core-mantle boundary, bathymetry, the geoid and Benioff zones, *Geophys. J. R. Astron. Soc., 84*, 153-183, 1986.

Davies, G.F., Ocean bathymetry and mantle convection 1. Large-scale flow and hotspots, *J. Geophys. Res., 93*, 1-467-10480, 1988a.

Davies, G.F., Role of the lithosphere in mantle convection, *J. Geophys. Res., 93*, 10451-10466, 1988b.

Davies, G.F., Mantle convection with a dynamic plate: topography, heat flow and gravity anomalies, *Geophys. J. Int.*, *98*, 461-464, 1989a.

Davies, G.F., Effect of a low viscosity layer on long-wavelength topography, upper mantle case, *Geophys. Res. Lett., 16*, 625-628, 1989b.

Davies, G.F. and M. Gurnis, Interaction of mantle dregs with convection: lateral heterogeneity at the core-mantle boundary, *Geophys. Res. Lett., 13*, 1517-1520, 1986.

Davies, G.F. and M.A. Richards, Mantle convection, *J. Geology, 100,* 151-206, 1992.

Davies, J.H., O. Gudmundsson and R.W. Clayton, Spectra of mantle shear velocity structure, *Geophys. J. Int., 108*, 865-882, 1992.

DePaulo, D.J. and G.J. Wasserburg, Inferences about mantle sources and mantle structure from variations of $^{143}Nd/^{144}Nd$, *Geophys. Res. Lett., 3*, 743-746, 1976.

DePaulo, D.J. and G.J. Wasserburg, Petrogenic mixing models and Nd-Sr isotopic patterns, *Geochim. Cosmochim. Acta, 43*, 615-627, 1979.

Dietz, R.S., Continent and ocean basin evolution by spreading of the sea floor, *Nature, 190,* 854-857, 1961.

Dongarra, J.J., Performance of various computers using standard linear equations software, *Computer Science Department, University of Tennesee, Knoxville, TN 37996,* 1993.

Duffy, T.S. and T.J. Ahrens, Thermal expansion of mantle and core materials at very high pressures, *Geophys. Res. Lett., 20*, 1103-1106, 1993.

Duffy, T.S. and D.L. Anderson, Seismic velocities in mantle minerals and the mineralogy of the upper mantle, *J. Geophys. Res., 94*, 1895-1912, 1989.

Duncan, R.A. and M.A. Richards, Hotspots, mantle plumes, flood basalts, and true polar wander, *Rev. of Geophys., 29*, 31-50, 1991.

Durham, W.B., C. Froidevaux and O. Jaoul, Transient and steady-state creep of pure forsterite at low stress, *Phys. Earth Planet. Inter., 19*, 263-274, 1979.

Dziewonski, A.M., Mapping the lower mantle: Determination of lateral heterogeneity in P-velocity up to degree and order 6, *J. Geophys. Res., 89*, 5929-5952, 1984.

Dziewonski, A.M. and D.L. Anderson, Preliminary reference Earth model, *Phys. Earth Plant. Inter., 25*, 297-356, 1981.

Ellsworth, K. and G. Schubert, Numerical models of thermally and mechanically coupled two-layer convection of highly viscous fluids, *Geophys. J., 93,* 347-363, 1988.

Fisher, O., *Physics of the Earth's Crust,* Murray, London, 1881.

Forte, A.M., A.M. Dziewonski and R.L. Woodward, Aspherical structure of the mantle, tectonic plate motions, nonhydrostatic geoid, and topography of the core-mantle-boundary, in *Dynamics of the Earth's Deep Interior and Earth Rotation*, edited by J.L. LeMouel, D.E. Smylie and T. Herring, AGU Geophysical monograph 72, 1993.

Forte, A.M. and W.R. Peltier, Plate-tectonics and aspherical Earth structure - the importance of poloidal-toroidal coupling, *J. Geophys. Res., 92*, 3645-3679, 1987.

Forte, A.M., W.R. Peltier and A.M. Dziewonski, Inferences of mantle viscosity from tectonic plate velocities, *Geophys. Res. Lett., 18*, 1747-1750, 1991.

Foster, I., W. Gropp and R. Stevens, The parallel scalability of the spectral transform method, Mathematics and Computer Science Division, Argonne National Laboratory, Argonne, IL60439, 1991.

Frick, H., F.H. Busse and R.M. Clever, Steady three-dimensional convection at high Prandtl numbers, *J. Fluid. Mech., 127*, 141-153, 1983.

Fukao, Y., Seismic tomogram of the Earth's mantle: Geodynamic implications, *Science, 258,* 625-630, 1992.

Fukao, Y., M. Obayashi, H. Inoue and M. Nenbau, Subducting slabs stagnant in the mantle transition zone, *J. Geophys. Res., 97,* 4809-4822, 1992.

Gable, C.W., R.J. O'Connell and B.J. Travis, Convection in three dimensions with surface plates: generation of toroidal flow, *J. Geophys. Res., 96*, 8391-8405, 1991.

Garfunkel, Z., C.A. Anderson and G. Schubert, Mantle circulation and the lateral migration of subducted slabs, *J. Geophys. Res.*, 91, 7205-7223, 1986.

Garnero, E.J., D.V. Helmberger and S.P. Grand, Preliminary evidence for a lower mantle shear-wave velocity discontinuity beneath the central Pacific, *Phys. E. Plan. Inter., 79,* 335-347, 1993.

Giannandrea, E. and U. Christensen, Variable viscosity convection experiments with a stress-free upper boundary and implications for the heat transport in the Earth's mantle, *Phys. Earth Planet. Int., 78*, 139-152, 1993.

Glatzmaier, G.A., Numerical simulations of mantle convection: time-dependent, three-dimensional, compressible, spherical shell, *Geophys. Astrophys. Fluid Dyn., 43*, 223-264, 1988.

Glatzmaier, G.A. and G. Schubert, 3D spherical models of layered and whole mantle convection, *J. Geophys. Res., 98*, 21969-21976, 1993.

Glatzmaier, G.A., G. Schubert and D. Bercovici, Chaotic, subduction-like downflows in a spherical model of convection in the Earth's mantle, *Nature 347*, 274-277, 1990.

Goldreich, P. and A. Toomre, Some remarks on polar wandering, *J. Geophys. Res., 74*, 2555-2569, 1969.

Grand, S.P., Tomographic inversion for shear velocity structure beneath the north-American plate, *J. Geophys. Res., 92,* 14065-14090, 1987.

Griffiths, R.W. and I.H. Campbell, Stirring and structure in mantle plumes, *Earth Planet. Sci. Lett., 99,* 66-78, 1990.

Gudmundsson, O., J.H. Davies and R.W. Clayton, Stochastic analysis of global traveltime data: Mantle heterogeneity and random errors in the ISC data, *Geophys. J. Int, 102*, 25-43, 1990.

Gurnis, M., Stirring and Mixing in the mantle by plate-scale flow: Large persistent blobs and long tendrils coexist, *Geophys. Res. Lett., 13*, 1474-1477, 1986.

Gurnis, M., Large-scale mantle convection and the aggregation and dispersal of supercontinents, *Nature, 332*, 695-699, 1988.

Gurnis, M., A reassessment of the heat transport by variable viscosity convection with plates and lids, *Geophys. Res. Lett., 16*, 179-182, 1989.

Gurnis, M., Bounds on global dynamic topography from Phanerozoic flooding of continental platforms, *Nature, 344*, 754-756, 1990a.

Gurnis, M., Plate-mantle coupling and continental flooding, *Geophys. Res. Lett., 17*, 623-626, 1990b.

Gurnis, M., Rapid continental subsidence following the initiation and evolution of subduction, *Science 255*, 1556-1558, 1992.

Gurnis, M., Phanerozoic marine inundation of continents driven by dynamic topography above subducting slabs, *Nature 364,* 589-593, 1993.

Gurnis, M. and G.F. Davies, Numerical study of high Rayleigh number convection in a medium with depth-dependent viscosity, *Geophys. J. R. Astron. Soc., 85*, 523-541, 1986a.

Gurnis, M. and G.F. Davies, Mixing in numerical models of mantle convection incorporating plate kinematics, *J. Geophys. Res., 91*, 6375-6395, 1986b.

Gurnis, M. and G.F. Davies, The effect of depth-dependent viscosity on convective mixing in the mantle and the possible survival of primitive mantle, *Geophys. Res. Lett., 13*, 541-544, 1986c.

Gurnis, M. and B.H. Hager, Controls on the structure of subducted slabs, *Nature, 335*, 317-321, 1988.

Gurnis, M. and S. Zhong, Generation of long wavelength heterogeneity in the mantle by the dynamic interaction between plates and convection, *Geophys. Res. Lett., 18*, 581-584 , 1991.

Gutenberg, B., H. Benioff, J.M. Burgers and D. Griggs, Colloquium on plastic flow and deformation within the Earth, *Trans. AGU, 32*, 497-543, 1951.

Hager, B.H. and R.W. Clayton, Constraints on the structure of mantle convection using seismic observations, flow models, and the geoid, in *Mantle convection: Plate tectonics and global dynamics*, edited by W.R. Peltier, 657-764, Gordon and Breach, New York, 1989.

Hager, B.H., R.W. Clayton, M.A. Richards, R.P. Comer and A.M. Dziewonski, Lower mantle heterogeneity, dynamic topography and the geoid, *Nature, 313*, 541-546, 1985.

Hager, B.H., and M. Gurnis, Mantle convection and the state of the Earth's mantle, *Rev. Geophys., 25*, 1277-1285, 1987.

Hager, B.H. and M.A. Richards, Long-wavelength variations in Earth's geoid: Physical models and dynamical implications, *Phil. Trans. R. Soc. Lond.*, 328, 309-327, 1989.

Hansen, U., High Rayleigh number regime of temperature-dependent viscosity convection and the Earth's early thermal history, *Geophys. Res. Lett., 20*, 2191-2194, 1993.

Hansen, U. and A. Ebel, Time-dependent thermal convection - a possible explanation for a multiscale flow in the Earth's mantle, *Geophys. J., 94,* 181-191, 1988.

Hansen, U., D.A. Yuen and S.E. Kroening, Transition to hard turbulence in thermal convection at infinite Prandtl number, *Phys. Fluids A, 2*, 2157-2163, 1990.

Hansen, U., D.A. Yuen and S.E. Kroening, Mass and heat transport in strongly time-dependent thermal convection at infinite Prandtl number, *Geophys. Astrophys. Fluid Dyn., 63*, 67-89, 1992.

Hansen, U., D.A. Yuen, S.E. Kroening and T.B. Larsen, Dynamical consequences of depth-dependent thermal expansivity and viscosity on mantle circulations and thermal structure, *Phys. Earth Plan. Inter., 77*, 205-223, 1993.

Harder, H., Numerical simulation of thermal convection with Maxwellian viscoelasticity, *J. Non-New. Fluid Mech., 39*, 67-88, 1991.

Hess, H.H., History of ocean basins, in *Petrologic Studies: A volume in honor of A.F. Buddington, ed., A.E.J. Engel, H.L. James, and B.F. Leonard,* Geol. Soc. Amer., New York, 559-620, 1962.

Hillis, W.D. and B.M. Boghosian, Parallel scientific computation, *Science 261*, 856-863, 1993.

Hoffman, N.R.A. and D.P. McKenzie, the destruction of geochemical heterogeneities by differential fluid motions during mantle convection, *Geophys. J. Roy. Astron. Soc. 82*, 163-206, 1985.

Hofmann, A.W. and W.M. White, Mantle plumes from ancient oceanic crust, *Earth Planet. Sci. Lett., 57*, 421-436, 1982.

Holmes, A., Radioactivity and Earth movements, *Trans. Geol. Soc. Glasgow, 18 (Part 3)*, 559-606, 1931.

Honda, S., D.A. Yuen, S. Balachandar and D. Reuteler, Three-dimensional instabilities of mantle convection with multiple phase transitions, *Science 259*, 1308-1311, 1993.

Houseman, G., The dependence of convection planform on mode of heating, Nature, 332, 346-349, 1988.

Howard, L.N., Convection at high Rayleigh number, in *Proceedings of the Eleventh International Congress of Applied Mechanics,* ed. H. Gortler, pp. 1109-1115, Springer-Verlag, New York, 1966.

Hsui, A.T., D.L. Turcotte and K.E. Torrance, Finite amplitude thermal convection within a self-gravitating fluid sphere, *Geophys. Fluid Dyn., 3*, 35-44, 1972.

Inoue, H., Fukao, Y., Tanabe, K. and Ogata, Y., Whole mantle P-wave travel time tomography, *Phys. Earth Plan. Int., 59*, 294-328 , 1990.

Irving, E., Paleomagnetic and paleoclimatological aspects of polar wandering, *Pure Appl. Geophys., 33,* 23-41, 1956.

Isaaks, B. and P. Molnar, Distribution of stresses in the descending lithosphere from a global survey of focal-mechanism solutions of mantle earthquakes, *Rev. Geophys. Space Phys., 9*, 103-174, 1971.

Isaaks, B., J. Oliver and L.R. Sykes, Seismology and the new global tectonics, *J. Geophys. Res., 73*, 5855-5899, 1968.

Ita, J. and S. King, The sensitivity of convection with an endothermic phase change to the form of governing equations, initial conditions, aspect ratio, and equation of state, *J. Geophys. Res.*, in press, 1994.

Ita, J. and L. Stixrude, Petrology, elasticity, and composition of the mantle transition zone, *J. Geophys. Res., 97,* 6849-6866, 1992.

Ito, E., M. Akaogi., L. Topor and A. Navrotsky, Negative pressure-temperature slopes for reactions forming MgSiO3 perovskite from calorimetry, *Science, 249*, 1275-1278, 1990.

Ito, E. and E. Takahashi, Postspinel transformations in the system Mg2SiO4-Fe2SiO4 and some geophysical implications, *J. Geophys. Res., 94*, 10637-10646, 1989.

Ito, E. amd H. Yamada, Stability relations of silicate spinels, ilmenites, and perovskites, in *High Pressure Research In Geophysics, ed. S. Akimoto, M.H. Manghini*, pp405-419, Center of Academic Publishing, Tokyo, 1982.

Jackson, I., Some geophysical constraints on the chemical composition of the lower mantle, *Earth Plan. Sci. Lett., 62*, 91-103, 1983.

Jacobsen, S.B. and G.J. Wasserburg, Transport models for crust and mantle evolution, *Tectonophysics, 75,* 163-179, 1981.

Jacoby, W.R., Paraffin model experiment of plate tectonics, *Tectonophysics, 35,* 103-113, 1976.

Jacoby, W.R. and H. Schmeling, On the effects of the lithosphere on mantle convection and evolution, *Phys. Earth Planet. Inter., 29*, 305-319, 1982.

Jarvis, G.T. and J.X. Mitrovica, On Nusselt numbers and the relative resolution of plumes and boundary layers in mantle convection, *Geophys. J. Int., 99*, 497-509, 1989.

Jarvis, G.T. and W.R. Pelter, Mantle convection as a boundary layer phenomenon, *Geophys. J. R. Astron. Soc., 68*, 389-427, 1982.

Jarvis, G.T. and W.R. Peltier, Lateral heterogeneity in the convecting mantle, *J. Geophys. Res. 91*, 435-451, 1986.

Jarvis, G.T. and W.R. Peltier, Convection models and geophysical observations, in *Mantle Convection: Plate Tectonics and Global Dynamics ed. W.R. Peltier, Gordan and Breach, New York*, 479-594, 1989.

Jeanloz, R., Effects of phase transitions and possible compositional changes on the seismological structure near 650 km depth, *Geophys. Res. Lett., 18*, 1743-1746, 1991.

Jeanloz, R. and E. Knittle, Density and composition of the lower mantle, *Phil. Trans. R. Soc. A, 328*, 377-389, 1989.

Jeanloz, R. and A.B. Thompson, Phase transitions and mantle discontinuities, *Rev. Geophys. Space Phys., 21*, 51-74, 1983.

Johnson, S., G. Masters, P.J. Tackley and G.A. Glatzmaier, How well can we resolve a convecting earth with seismic data? (abstract), *EOS Trans AGU 74,* p80, 1993.

Jordan, T.H., P. Puster, G.A. Glatzmaier, and P.J. Tackley, Comparisons of seismic Earth models and mantle flow models using radial correlation functions, *Science, 261,* 1427-1431, 1993.

Karato, S., Importance of anelasticity in the interpretation of seismic tomography, *Geophys. Res. Lett., 20*, 1623-1626, 1993.

Karato, S. and P. Li, Diffusion creep in perovskite - implications for the rheology of the lower mantle, *Science, 255*, 1238-1240, 1992.

Karato, S. and P. Wu., Rheology of the upper mantle: a synthesis, *Science, 260*, 771-778, 1993.

Katsura, T. and E. Ito, The system Mg2SiO4-Fe2SiO4 at high pressures and temperatures: Precise determination of stabilities of olivine, modified spinel, and spinel, *J. Geophys. Res.*, 94, 15663-15670, 1989.

Kaula, W.M., Gravity fields: Implications for planetary interiors, in *Encyclopedia of Geophysics,* edited by D.E. James, Van Nostrand Reinhold, Princeton, pp. 622-627, 1989.

Kellogg, L.H., Interaction of plumes with a compositional boundary at 670 km, *Geophys. Res. Lett., 18*, 865-868, 1991.

Kellogg, L.H., Mixing in the mantle, *Ann. Rev. Earth Planet. Sci., 20*, 365-388, 1992.

Kellogg, L.H. and C.A. Stewart, Mixing by chaotic convection in an infinite Prandtl number fluid with implications for mantle convection, *Phys. Fluids A, 3,* 1374-1378, 1991.

Kellogg, L.H. and D.L. Turcotte, Homogenization of the mantle by convective mixing and diffusion, *Earth Plan. Sci. Lett., 81,* 371-378, 1987.

Kellogg, L.H. and D.L. Turcotte, Mixing and distribution of heterogeneities in a chaotically convecting mantle, *J. Geophys. Res., 95*, 421-432, 1990.

Kiefer, W.S. and B.H. Hager, Mantle downwelling and crustal convergence - a model for Ishtar Terra, Venus, *J. Geophys. Res., 96*, 967-980, 1991.

Kiefer, W.S., M.A. Richards, B.H. Hager and B.G. Bills, A dynamic model of Venus gravity field, *Geophys. Res. Lett., 13*, 14-17, 1986.

Kincaid, C. and P. Olson, An experimental study of subduction and slab migration, *J. Geophys. Res.*, *92*, 13832-13840, 1987.

King, S.D., Radial models of mantle viscosity: results from a genetic algorithm, submitted to *Geophys. J. Int.,* 1994.

King, S.D. and B.H. Hager, Subducted slabs and the geoid: 1) numerical calculations with temperature-dependent viscosity, submitted to *J. Geophys. Res.*, 1994.

King, S.D. and G. Masters, An inversion for radial viscosity structure using seismic tomography, *Geophys. Res. Lett., 19*, 1551-1554, 1992.

Kirby, S.H. and Kronenberg, A.K., Rheology of the Lithosphere: selected topics, in *US National Report to international Union of Geodesy and Geophysics 1983-1986, Contributions in Tectonophysics*, 1219-1244, American Geophysical Union, Washington, DC, 1987.

Kumazawa, M., H. Sawamoto, E. Ohtani and K. Masaki, Postspinel phase of forsterite and evolution of the mantle, *Nature, 247*, 356-358, 1974.

Larsen, T.B., A.V. Malevsky, D.A. Yuen and J.L. Smedsmo, Temperature-dependent Newtonian and non-Newtonian convection - implications for lithospheric processes, *Geophys. Res. Lett., 20*, 2595-2598, 1993a.

Larsen, T.B., D.A. Yuen, A.V. Malevsky and J.L. Smedsmo, Dynamics of thermal convection with Newtonian temperature-dependent viscosity at high Rayleigh number, submitted to *Phys. Earth Planet. Inter.*, 1993b.

Lay, T., The fate of descending slabs, *Ann. Rev. Earth Plan. Sci., 22,* 33-62, 1994.

Lay, T. and D.V. Helmberger, A shear velocity discontinuity in the lower mantle, *Geophys. Res. Lett., 10*, 63-66, 1983a.

Lay, T. an D.V. Helmberger, A lower mantle S-wave triplication and the shear velocity structure of D", *Geophys. J. R. Astron. Soc., 75*, 799-837, 1983b.

Lees, A., M.S.T. Bukowinski and R. Jeanloz, Reflection properties of phase transition and compositional change models of the 670 km discontinuity, *J. Geophys. Res., 88*, 8145-8159, 1983.

Le Pichon, X., Sea floor spreading and continental drift, *J. Geophys. Res., 73,* 3661-3697, 1968.

Leitch, A. and D. Yuen, Internal heating and thermal constraints on the mantle, *Geophys. Res. Lett., 16*, 1407-1410, 1989.

Leitch, A.M., D.A. Yuen, and G. Sewell, Mantle convection with internal heating and pressure-dependent thermal expansivity, *Earth Plan. Science Lett., 102*, 213-232, 1991.

Li, X.-D. and B. Romanowicz, Comparison of global waveform inversions with and without considering cross-branch modal coupling, submitted to *Geophys. J. Int.,* 1994.

Lithgow-Bertelloni, C., M.A. Richards, Y. Ricard, R.J. O'Connell and D.C. Engebretson, Toroidal-Poloidal partitioning of plate motions since 120 ma, *Geophys. Res. Lett., 20*, 375-378, 1993.

Liu, L.G., On the 670 km discontinuity, *Earth Planet. Sci. Lett., 42*, 202-208, 1979.

Liu, M., D.A. Yuen, W. Zhao and S. Honda, Development of diapiric structures in the upper mantle due to phase transitions, *Science, 252*, 1836-1839, 1991.

Loper, D.E., Mantle plumes, *Tectonophysics, 187,* 373-384, 1991.

Loper, D.E. and F.D. Stacey, The dynamical and thermal structure of deep mantle plumes, *Phys. Earth Planet. Inter., 33,* 304-317, 1983.

Lowman, J.P. and G.T. Jarvis, Mantle convection flow reversals due to continental collisions, *Geophys. Res. Lett., 20,* 2087-2090, 1993.

Machetel, P., Constraints on mantle structure from seimological and convection results, in *Dynamics of Earth's deep interior and Earth rotation, Geophysical Monograph 72, ed. J.-L. le Mouel, D.E. Smylie and T. Herring,* pp167-180, AGU and IUGG, 1993.

Machetel, P., M. Rabinowicz and P. Bernardet, Three-dimensional convection in spherical shells, *Geophys. Astrophys. Fluid. Dyn., 37,* 57-84, 1986.

Machetel, P. and P. Weber, Intermittent layered convection in a model mantle with an endothermic phase change at 670 km, *Nature, 350,* 55-57, 1991.

Machetel, P. and D.A. Yuen, Chaotic axisymmetric spherical convection and large-scale mantle convection, *Earth Plan. Sci. Lett., 86,* 93-104, 1987.

Machetel, P. and D.A. Yuen, Penetrative convective flows induced by internal heating and mantle compressibilitiy, *J. Geophys. Res., 94,* 10609-10626, 1989.

Malevsky, A.V. and D.A. Yuen, Strongly chaotic non-Newtonian mantle convection, *Geophys. Astrophys. Fluid. Dyn., 65,* 149-171, 1992.

Malevsky, A.V. and D.A. Yuen, Plume structures in the hard-turbulent regime of three-dimensional infinite Prandtl number convection, *Geophys. Res. Lett., 20,* 383-386, 1993.

Martinec, Z., C. Matyska, O. Cadek and P. Hrdina, The Stokes problem with 3D Newtonian viscosity in a spherical shell, *J. Comput. Phys., 76,* 63-79, 1993.

Masters, T.G., H. Bolton and P. Shearer, Large-scale 3-dimensional structure of the mantle, *EOS Trans. Amer. Geophys. Union, 73,* 201, 1992.

McKenzie, D.P., The relation between fault plane solutions for earthquakes and the directions of principal stresses, *Seismol. Soc. Amer. Bull., 59,* 591-601, 1969a.

McKenzie, D.P., Spaculations on the consequences and causes of plate motions, *Geophys. J. R. Astr. Soc., 18*, 1-32, 1969b.

McKenzie, D.P., and R.L. Parker, The North Pacific: An example of tectonics on a sphere, *Nature, 216*, 1276-1280, 1967.

McKenzie, D.P., J.M. Roberts and N.O. Weiss, Convection in the Earth's mantle: Towards a numerical solution, *J. Fluid Mech., 62*, 465-538, 1974.

McKenzie, D.P. and J.G. Sclater, Heat flow inside the island arcs of the northwestern Pacific, *J. Geophys. Res., 73*, 3173-3179, 1968.

Meade, C. and R. Jeanloz, The strength of mantle silicates at high pressures and room temperature: implications for the viscosity of the mantle, *Nature, 348*, 533-535, 1990.

Minear, J.W. and M.N. Toksöz, Thermal regime of a downgoing slab and new global tectonics, *J. Geophys. Res., 75*, 1397-1419, 1970.

Mitrovica, J.X. and W.R. Peltier, The inference of mantle viscosity from an inversion of the Fennoscandian relaxation data, *Geophys. J. Int*, 114, 45-62, 1993.

Morgan, W.J., Rises, trenches, great faults and crustal blocks, *J. Geophys. Res., 73*, 1959-1982, 1968.

Moser, J., D.A. Yuen and T.B. Larsen, Influences of depth-dependent properties on large-scale upwellings in planetary convection and temporal changes in the moment of inertia, submitted to *Phys. Earth Plan. Inter.*, 1993.

Mueller, S. and R.J. Phillips, On the initiation of subduction, *J. Geophys. Res., 96*, 651-665, 1991.

Müller, R., The performance of classical versus modern finite-difference advection schemes for atmospheric modeling in a one-dimensional test-bed, *Monthly Weather Review, 120*, 1407-1415, 1992.

Nakanishi, I., and D.L. Anderson, Measurements of mantle wave velocities and inversion for lateral heterogeneity and anisotropy 1. Analysis of great-circle phase velocities, *J. Geophys. Res., 88,* 10267-10283, 1983.

Nataf, H.-C., Mantle convection, plates, and hotspots, *Tectonophysics, 187*, 361-371, 1991.

Nataf, H.-C., C. Froidevaux and J.L. Levrat, Laboratory convection experiments: Effect of lateral cooling and generation of instabilities in the horizontal boundary layers, *J. Geophys. Res., 86*, 6143-6154, 1981.

Nataf, H.-C. and S. Houard, Seismic discontinuity at the top of D" - a worldwide feature, *Geophys. Res. Lett., 20*, 2371-2374, 1993.

Nataf, H.-C., S. Moreno and P. Cardin, What is responsible for thermal coupling in layered convection?, *J. Phys. France, 49*, 1707-1714, 1988.

Nataf, H.-C., I. Nakanishi and D.L. Anderson, Measurements of mantle wave velocities and inversion for lateral heterogeneities and anisotropy 3. inversion, *J. Geophys. Res., 91*, 7261-7307, 1986.

Nataf, H.-C. and J. VanDecar, Seismological detection of a mantle plume?, *Nature, 364*, 115-120, 1993.

Navrotsky, A., Lower mantle phase transitions may generally have negative pressure-temperature slopes, *Geophys. Res. Lett., 7*, 709-711, 1980.

Ogawa, M., G. Schubert and A. Zebib, Numerical simulations of three-dimensional thermal convection in a fluid with strongly temperature-dependent viscosity, *J. Fluid Mech., 233*, 299-328, 1991.

Olson, P., An experimental approach to thermal convection in a two-layered mantle, *J. Geophys. Res., 89*, 11293-11301, 1984.

Olson, P. and D. Bercovici, On the equipartition of kinetic energy in plate tectonics, *Geophys. Res. Lett., 18*, 1751-1754, 1991.

Olson, P. and C. Kincaid, Experiments on the interaction of thermal convection and compositional layering at the base of the mantle, *J. Geophys. Res., 96,* 4347-4354, 1991.

Olson, P., G. Schubert and C. Anderson, plumes formation in the D" layer and the roughness of the core-mantle boundary, *Nature, 327*, 409-413, 1987.

Olson, P., G. Schubert and C. Anderson, Structure of axisymmetric mantle plumes, *J. Geophys. Res., 98*, 6829-6844, 1993.

Olson, P., G. Schubert, C. Anderson and P. Goldman, Plume formation and lithosphere erosion: A comparison of laboratory and numerical experiments, *J. Geophys. Res., 93,* 15065-15084, 1988.

Olson P., D.A. Yuen and D. Balsiger, Mixing of passive heterogeneities by mantle convection, *J. Geophys. Res., 89*, 425-436, 1984.

Osako, M. and E. Ito, Thermal diffusivity of MgSiO3 perovskite, *Geophys. Res. Lett., 18*, 239-242, 1991.

Parmentier, E.M. and J. Morgan III, Thermal convection in non-Newtonian fluids: volumetric heating and boundary layer scaling, *J. Geophys. Res., 87*, 7757-7762, 1982.

Parmentier, E.M., C. Sotin and B.J. Travis, Turbulent 3D thermal convection in an infinite Prandtl number, volumetrically heated fluid: implications for mantle dynamics, *Geophys. J. Int.*, in press, 1994.

Parmentier, E.M. and D.L. Turcotte, Two-dimensional mantle flow beneath a rigid accreting lithosphere, *Phys. Earth Planet. Inter., 17*, 281-289, 1978.

Parmentier, E.M., D.L. Turcotte and K.E. Torrance, Studies of finite amplitude non-Newtonian thermal convection with application to convection in the Earth's mantle, *J. Geophys. Res., 81*, 1839-1846, 1976.

Parsons, B. and J.G. Sclater, An analysis of the variation of ocean floor bathymetry and heat flow with age, *J. Geophys. Res., 82*, 803-827, 1977.

Patankar, S.V., Numerical Heat Transfer and Fluid Flow, *Hemisphere Pulishing Corporation, New York,* 1980.

Pekeris, C.L., Thermal convection in the interior of the Earth, *Mon. Not. R. Astron. Soc. Geophys. Suppl., 3,* 343-367, 1935.

Peltier, W.R., Mantle convection and viscoelasticity, *Ann. Rev. Fluid Mech. 17*, 561-608, 1985.

Peltier, W.R. and L.P. Solheim, Mantle phase transitions and layered chaotic convection, *Geophys. Res. Lett., 19,* 321-324, 1992.

Peltier, W.R. and L.P Solheim, The supercontinent cycle and phase transition modulated mantle mixing (abstract), *EOS Trans. AGU*, 74, 47, 1993.

Phipps Morgan, J. and P.M. Shearer, Seismic constraints on flow and discontinuity topography near 660 km - new evidence for whole mantle convection, *Nature, 365,* 506-511, 1993.

Plafker, G., Tectonic deformation associated with the 1964 Alaskan earthquake, *Science, 148,* 1675-1687, 1965.

Pollack, H.N., S.J. Hurter and J.R. Johnson, Heat flow from the Earth's interior - analysis of the global data set, *Reviews of Geophys., 31,* 267-280, 1993.

Press, W.H., S.A. Teulolsky, W.T. Vetterling, B.P. Flannery, Numerical Recipes (Second Edition), Cambridge University Press, Cambridge UK, 1992.

Pulliam, R.J., D.W. Vasco and L.R. Johnson, Tomographic inversions for mantle P wave velocity structure based on the minimization of L2 and L1 norms of international seismological center travel time residuals, *J. Geophys. Res., 98*, 699-734, 1991.

Puster, P., and T.H. Jordan, Stochastic analysis of mantle convection experiments using two-point correlation functions, *Geophys. Res. Lett.,* 21, 305-308, 1994.

Rapp, R.H. and N.K. Pavlis, The development and analysis of geopotential coefficient models to spherical harmonic degree 360, *J. Geophys. Res.*, 95, 21885-21911, 1990.

Ray, T.W. and D.L. Anderson, Spherical disharmonics in the Earth sciences and the spatial solution: Ridges, hotspots, slabs, geochemistry and tomography correlations, submitted to *J. Geophys. Res.*, 1993.

Rayleigh, Lord, On convective convective currents in a horizontal layer of fluid, when the higher temperature is on the under side, *Philosophical Magazine, Series VI, 32*, 529-546, 1916.

Ricard, Y., L. Fleitout and C. Froidevaux, Geoid heights and lithospheric stresses for a dynamic Earth, *Annales Geophysicae, 2*, 267-286, 1984.

Ricard, Y., M. Richards, C. Lithgow-Bertelloni and Y. Lestunff, A geodynamic model of mantle density heterogeneity, *J. Geophys. Res., 98*, 21895-21909, 1993.

Ricard, Y. and B. Wuming, Inferring the viscosity and 3-D density structure of the mantle from geoid, topography and plate velocities, *Geophys. J. Int., 105*, 561-571, 1991.

Richards, M.A. and D.C. Engebretson, Large scale mantle convection and the history of subduction, *Nature, 355*, 437-440, 1992.

Richards, M.A. and B.H. Hager, Geoid anomalies in a dynamic Earth, *J. Geophys. Res., 89*, 5987-6002, 1984.

Richter, F.M., Dynamical models for seafloor spreading, *Rev. Geophys. Space Phys. 11*, 223-287, 1973.

Richter, F.M., Mantle convection models, *Ann. Rev. Earth Planet. Sci., 6,* 9-19, 1978a.

Richter, F.M., Experiments on the stability of convection rolls in fluids whose viscosity depends on temperature, *J. Fluid Mech., 89*, 553-560, 1978b.

Richter, F.M., Convection and the large-scale circulation of the mantle, *J. Geophys. Res., 78*, 8735-8745, 1982.

Richter, F.M. and C.E. Johnson, Stability of a chemically layered mantle, *J. Geophys. Res., 79,* 1635-1639, 1974.

Richter, F.M. and D.P. McKenzie, On some consequences and possible causes of layered mantle convection, *J. Geophys. Res., 86,* 6133-6142, 1981.

Richter, F.M., H.C. Nataf and S.F. Daly, Heat transfer and horizontally-averaged temperature of convection with large viscosity variations, *J. Fluid Mech., 129*, 173-192, 1983.

Richter, F.M. and B. Parsons, On the interaction of two scales of convection in the mantle, *J. Geophys. Res., 80*, 2529-2541, 1975.

Ringwood, A.E., Phase transitions and mantle dynamics, *Earth Planet. Sci. Lett., 14*, 233-241, 1972.

Ringwood, A.E., Phase transformations and differentiation in subducted lithosphere: Implications for mantle dynamics, basalt petrogenesis, and crustal evolution, *J. Geology*, 90, 611-643, 1982.

Ringwood, A.E., Phase transformations and their bearing on the constitution and dynamics of the mantle, *Geochim. Cosmochim. Acta*, 55, 2083-2110, 1991.

Ringwood, A.E. and T. Irifune, Nature of the 650-km seismic discontinuity: implications for mantle dynamics and differentiation, *Nature, 331*, 131-136, 1988.

Romanowicz, B., Anelastic tomography: A new perspective on upper mantle thermal structure, *submitted to Nature*, 1994.

Runcorn, S.K., Paleomagnetic comparisons between Europe and north America, *Proc. Geol. Soc. Can., 8*, 77-85, 1956.

Saunders, R.S., R.E. Arvidsen, J.W. Head, G.G. Schaber, E.R. Stofan ad S.C. Soloman, An overview of Venus geology, *Science, 252,* 249-260, 1991.

Schmeling, H., Compressible convection with constant and variable viscosity: The effect on slab formation, geoid and topography, *J. Geophys. Res., 94,* 12463-12481, 1989.

Schmeling, H. and G. Marquart, The influence of second-scale convection on the thickness of continental crust and lithosphere, *Tectonophysics, 189,* 281-306, 1991.

Schubert, G., Subsolidus convection in the mantles of terrestrial planets, *Ann. Rev. Earth. Planet. Sci., 7,* 289-342, 1979.

Schubert, G., Numerical models of mantle convection, *Ann. Rev. Fluid. Mech., 24*, 359-394, 1992.

Schubert, G. and C.A. Anderson, Finite element calculations of very high Rayleigh number thermal convection, *Geophys. J. R. Astron. Soc., 80*, 575-601, 1985.

Schubert, G., D. Bercovici and G.A. Glatzmaier, Mantle dynamics in Mars and Venus: Influence of an immobile lithosphere on 3-dimensional mantle convection, *J. Geophys. Res., 95*, 14105-14129, 1990.

Schubert, G., G.A. Glatzmaier and B. Travis, Steady, three-dimensional, internally heated convection, *Phys. Fluids A, 5*, 1928-1932, 1993.

Schubert, G., D.J. Stevenson and P. Cassen, Whole mantle cooling and the radiogenic heat source contents of the Earth and Moon, *J. Geophys. Res., 85*, 2531-2538, 1980.

Schubert, G. and D.L. Turcotte, Phase transitions and mantle convection, *J. Geophys. Res., 76*, 1424-1432, 1971.

Schubert, G., D.L. Turcotte and E.R. Oxburgh, Stability of planetary interiors, *Geophys. J. R. Astron. Soc., 18*, 441-460, 1969.

Schubert, G. and R.E. Young, Cooling of the Earth by whole mantle subsolidus convection: A constraint on the viscosity of the lower mantle, *Tectonophysics, 35*, 201-214, 1976.

Schubert, G., R.E. Young and P. Cassen, Solid state convection models of the lunar internal temperature, *Philos. Trans. R. Soc. London Ser. A, 285*, 523-536, 1977.

Schubert, G., D.A. Yuen and D.L. Turcotte, Role of phase transitions in a dynamic mantle, *Geophys. J. R. astr. Soc., 42*, 705-735, 1975.

Sclater, J.G., C. Jaupart and D. Galson, The heat flow through oceanic and continental crust and the heat loss of the Earth, *Rev. Geophys., 18*, 269-311, 1980.

Scrivner, C. and D.L. Anderson, The effect of post Pangea subduction on global mantle tomography and convection, *Geophys. Res. Lett., 19,* 1053-1056, 1992.

Sharpe, H.N. and W.R. Peltier, Parameterized mantle convection and the Earth's thermal history, *Geophys. Res. Lett., 5*, 737-740, 1978.

Shearer, P.M. and T.G. Masters, Global mapping of topography on the 660-km discontinuity, *Nature, 355*, 791-796, 1992.

Sleep, N.H., An analytic model for a mantle plume fed by a thermal boundary layer, *Geophys. J. R. astr. Soc., 90*, 119-128, 1987.

Sleep, N.H., Hotspots and mantle plumes: Some phenomenology, *J. Geophys. Res.*, 95, 6715-6736, 1990.

Smolarkiewicz, P.K., A fully multidimensional positive definite advection transport algorithm with small implicit diffusion, *J. Comput. Phys., 54*, 325-362, 1984.

Solheim, L.P. and W.R. Peltier, Heat transfer and the onset of chaos in a spherical, axisymetric, anelastic model of whole mantle convection, *Geophys. Astrophys. Fluid Dyn., 53,* 205-255, 1990.

Solheim, L.P. and W.R. Peltier, Avalanche effects in phase transition modulated thermal convection: A model of the Earth's mantle, *J. Geophys. Res., 91*, 6997-7018, 1994.

Solheim, L.P. and W.R. Peltier, 660 km phase boundary deflections and episodically layered isochemical convection, *J. Geophys. Res., in press*, 1994.

Solomatov, V.S., Scaling of temperature- and stress-dependent viscosity convection, submitted to *Phys. Fluids*, 1994.

Stacey, F.D., *Physics of the Earth (Third Edition)*, 513pp, Brookfield, Kenmore, Queensland, Australia, 1992.

Stauder, W. and G.A. Bollinger, The S-wave project for focal mechanism studies - earthquakes of 1963, *Air Force Off. Sci. Res., Grant AF-AFOSR62-458, Rep.*, 1965.

Steinbach, V., U. Hansen and A. Ebel, Compressible convection in the Earth's mantle - a comparison of different approaches, *Geophys. Res. Lett., 16*, 633-636, 1989.

Steinbach, V. and D.A. Yuen, The effects of multiple phase transitions on Venusian mantle convection, *Geophys. Res. Lett., 19,* 2243-2246, 1992.

Steinbach, V. and D.A. Yuen, Convection with phase transitions and temperature-dependent viscosity, *EOS Trans Amer. Geophys. Union.*, 74, 300-300, 1993.

Steinbach, V., D.A. Yuen and W.L. Zhao, Instabilities from phase-transitions and the timescales of mantle thermal evolution, *Geophys. Res. Lett., 20,* 1119-1122, 1993.

Stixrude, L., R.J. Hemley, Y. Fei and H.K. Mao, Thermoelasticity of silicate perovskite and magnesiowustite and stratification of the Earth's mantle, *Science 257,* 1099-1101, 1992.

Stocker, R.L. and M.F. Ashby, On the rheology of the upper mantle, *Rev. Geophys. Space Phys., 11*, 391-426, 1973.

Su, W.-J. and A.M. Dziewonski, Predominance of long-wavelength heterogeneity in the mantle, *Nature, 352*, 121-126 , 1991.

Su, W.-J. and A.M. Dziewonski, On the scale of mantle heterogeneity, *Phys. Earth. Planet. Inter., 74*, 29-54 , 1992.

Su,W.-J., R.L. Woodward and A.M. Dziewonski, Deep origin of mid-ocean-ridge seismic velocity anomalies, *Nature, 360,* 149-152 , 1992a.

Su, W.-J., R.L. Woodward and A.M. Dziewonski, Joint inversions of travel-time and waveform data for 3-D models of the Earth up to degree 12 (abstract), *Eos Trans. Amer. Geophys. Union, 73*, 201-202, 1992b.

Sykes, L.R., Mechanism of earthquakes and nature of faulting on the mid-ocean ridges, *J. Geophys. Res., 72*, 2131-2153, 1967.

Tackley, P.J., Effects of strongly temperature-dependent viscosity on time-dependent, three-dimensional models of mantle convection, *Geophys. Res. Lett., 20*, 2187-2190, 1993a.

Tackley, P.J. and D.J. Stevenson, A mechanism for spontaneous self-perpetuating volcanism on the terrestrial planets, in *Flow and Creep in the Solar System: Observations, Modeling and Theory, ed. D.B. Stone and S.K. Runcorn*, Kluwer, 307-322, 1993b.

Tackley, P.J. and D.J. Stevenson, Volcanism without plumes: melt-driven instabilities, buoyant residuum and global implications, *EOS Trans Amer. Geophys. Union, 74*, p188, 1993.

Tackley, P.J., D.J. Stevenson and G.A. Glatzmaier, 3D simulations of mantle convection and the Earth's true polar wander, *Concurrent Supercomputing Consortium Annual Report 1991-1992*, 8-10, 1993a.

Tackley, P.J., D.J. Stevenson, G.A. Glatzmaier and G. Schubert, Effects of an endothermic phase transition at 670 km depth in a spherical model of convection in the Earth's mantle, *Nature, 361*, 699-704, 1993b.

Tackley, P.J., D.J. Stevenson, G.A. Glatzmaier and G. Schubert, Effects of multiple phase transitions in a 3-D spherical model of convection in the Earth's mantle, *J. Geophys. Res., in press*, 1994.

Talwani, M., A review of marine geophysics, *Mar. Geol., 2*, 29-80, 1961.

Tanimoto, T., Predominance of large-scale heterogeneity and the shift of velocity anomalies between the upper and lower mantle, *J. Phys. Earth, 38*, 493-509, 1990a.

Tanimoto, T., Long-wavelength S-wave velocity structure throughout the mantle, *Geophys. J. Int., 100,* 327-336 , 1990b.

Todesco, M. and F.J. Spera, Stability of a chemically layered upper mantle, *Phys. Earth Planet. Inter., 71*, 85-99, 1992.

Torrance, K.E. and D.L. Turcotte, Thermal convection with large viscosity variations, *J. Fluid Mech., 47*, 113-125, 1971.

Tozer, D.C., Towards a theory of thermal convection in the mantle, in *The Earth's Mantle, ed. T.F. Gaskell, Academic, London*, 325-353, 1967.

Tozer, D.C., The present thermal state of the terrestrial planets, *Phys. Earth Planet. Inter., 6*, 182-197, 1972.

Travis, B.J., C. Anderson, J. Baumgardner, C.W. Gable, B.H. Hager, R.J. O'Connell, P. Olson, A. Raefsky and G. Schubert, A benchmark comparison of numerical methods for infinite Prandtl number thermal convection in two-dimensional Cartesian geometry, *Geophys. Astrophys. Fluid Dynamics, 55,* 137-160, 1990a.

Travis, B.J., P. Olson and G. Schubert, The transition from two-dimensional to three-dimensional planforms in infinite-Prandtl-number thermal convection, *J. Fluid Mech., 216*, 71-91, 1990b.

Travis, B., S. Weinstein and P. Olson, Three-dimensional convection planforms with internal heat generation, *Geophys. Res. Lett., 17*, 243-246, 1990c.

Turcotte, D.L., A.T. Hsui, K.E. Torrance and G. Schubert, Influence of viscous dissipation on Bénard convection, *J. Fluid Mech., 64*, 369-374, 1974.

Turcotte, D.L. and E.R. Oxburgh, Finite amplitude convection cells and continental drift, *J. Fluid Mech., 28,* 29-42, 1967.

Turcotte, D.L. and E.R. Oxburgh, Mantle convection and the new global tectonics, *Ann. Rev. Fluid Mech., 4,* 33-68, 1972.

Turcotte, D.L. and G. Schubert, *Geodynamics: Applications of Continuum Physics to Geological Problems,* Wiley, New York, 1982.

van der Hilst, R., R. Engdahl, W. Spakman, and G. Nolet, Tomographic imaging of subducted lithosphere below northwest Pacific island arcs, *Nature, 353*, 37-43, 1991.

van Keken, P.E., D.A. Yuen and A.P. van den Berg, Pulsating diapiric flows: Consequences of vertical variations in mantle creep laws, *Earth Plan. Sci. Lett., 112*, 179-194, 1992.

van Keken, P.E., D.A. Yuen and A.P. van den Berg, Implications for mantle dynamics from the high melting point of perovskite, *Science, in press,* 1994.

Vasco, D.W., R.J. Pulliam and L.R. Johnson, Formal inversion of ISC arrival times for mantle P-velocity structure, *Geophys. J. Int., 113*, 586-606, 1993.

Vidale, J.E. and D. Garcia-Gonzales, Seismic observation of a high-velocity slab 1200-1600 km in depth, *Geophys. Res. Lett., 15*, 369-372, 1988.

Vine, F.J. and D.H. Mathews, Magnetic anomalies over oceanic ridges, *Nature, 199*, 947-949, 1963.

Walker, D.W., P.H. Worley and J.B. Drake, Parallelizing the spectral transform method - Part II, *Engineering Physics and Mathematics Division, Oak Ridge National Laboratory, Oak Ridge, Tennessee 37831*, 1991.

Weertman, J., The creep strength of the Earth's mantle, *Rev. Geophys. Space Phys., 8*, 146-168, 1970.

Weertman, J. and J.R. Weertman, High temperature creep of rock and mantle viscosity, *Ann. Rev. Earth Planet. Sci.*, 293-315, 1975.

Wegener, A., Die Enstehung der Kontinente and Ozeane. *Vieweg, Brauschweig. 4th Ed.* Transl. as The Origin of Continents and Oceans. *Methuen, London,* 1929, Reprinted *Dover*, 1966.

Weidner, D.J., Mantle model based on measured physical properties of minerals, in *Chemistry and Physics of the Terrestrial Planets, ed. S.K. Saxena*, pp 251-274, Springer-Verlag, NY, 1986.

Weinstein, S.A., Induced compositional layering in a convecting fluid layer by an endothermic phase-transition, *Earth. Planet. Sci. Lett., 113*, 23-39, 1992.

Weinstein, S.A., Catastrophic overturn of the Earth's mantle driven by multiple phase changes and internal heat generation, *Geophys. Res. Lett., 20*, 101-104, 1993.

Weinstein, S.A. and Christensen, U., Convection planforms in a fluid with a temperature-dependent viscosity beneath a stress-free upper boundary, *Geophys. Res. Lett., 18,* 2035-2038, 1991.

Weinstein, S.A., P. Olson and D.A. Yuen, Time-dependent large aspect-ratio convection in the Earth's mantle, *Geophys. Astrophys. Fluid Dyn., 47*, 157-197, 1989.

Weinstein, S.A. and P. Olson, Planforms in thermal convection with internal heat sources at large Rayeigh and Prandtl numbers, *Geophys. Res. Lett., 17*, 239-242, 1990.

Weinstein, S.A. and P.L. Olson, Thermal convection with non-Newtonian plates, *Geophys. J. Int., 111*, 515-530, 1992.

White, D.B., The planforms and onset of convection with a temperature-dependent viscosity, *J. Fluid Mech., 191,* 247-286, 1988.

Whitehead, J.E., Convection models: Laboratory vs. mantle, *Tectonophysics, 35*, 215-229, 1976.

Whitehead, J.A. and B. Parsons, Observations of convection at Rayleigh numbers up to 760,000 in a fluid with large Prandtl number, *Geophys. Astrophys. Fluid Dyn., 9*, 201-217, 1978.

Wilson, J.T., Evidence from islands on the spreading of the ocean floor, *Nature, 197*, 536-538, 1963.

Wilson, J.T., A new class of faults and their bearing on continental drift, *Nature, 207*, 343-347, 1965.

Woodhouse, J.H. and A.M. Dziewonski, Global images of the Earth's interior, *Science 236*, 37-48, 1987.

Woodhouse, J.H. and A.M. Dziewonski, Seismic modeling of the Earth's large-scale 3-dimensional structure, *Phil. Trans. R. Soc. Lond. A., 328*, 291-, 1989.

Worley, P.H. and J.B. Drake, Parallelizing the spectral transform method - Part I, *Engineering Physics and Mathematics Division, Oak Ridge National Laboratory, Oak Ridge, Tennessee 37831*, 1991.

Wyllie, P.J., Magma genesis, plate tectonics, and chemical differentiation of the Earth, *Reviews of Geophysics, 26*, 370-404, 1988.

Young, C.J. and T. Lay, Multiple phase analysis of the shear velocity structure in the D" region beneath Alaska, *J. Geophys. Res., 95*, 17385-17402, 1990.

Young, R.E., Finite-amplitude thermal convection in a spherical shell, *J. Fluid Mech, 63,* 695-721, 1974.

Young, R.E. and G. Schubert, Temperatures inside Mars: is the core liquid or solid?, *Geophys. Res. Lett., 1*, 157-160, 1974.

Yuen, D.A., O. Cadek, A. Chopelas and C. Matyska, Geophysical inferences of thermal-chemical structures in the lower mantle, *Geophys. Res. Lett., 20*, 899-902, 1993a.

Yuen, D.A., U. Hansen, W. Zhao, A.P. Vincent and A.V. Malevsky, Hard turbulent thermal convection and thermal evolution of the mantle, *J. Geophys. Res., 98*, 5355-5373, 1993b.

Yuen, D.A. and P. Olson, Thermochemical plumes and mantle phase transitions, *J. Geophys. Res., 87*, 3993-4002, 1982.

Yuen, D.A., D.M. Reuteler, S. Balachandar, V. Steinbach, A.V. Malevsky and J.L. Smedsmo, Various influences on three-dimensional mantle convection with phase transitions, *Phys. E. Plan. Inter., in press*, 1994.

Yuen, D.A., R. Sabadini and E. Boschi, Mantle rheology from a geodynamical standpoint, *Riv. Nuovo Cim., 5,* 1-35, 1983.

Yuen, D.A. and S. Zhang, Equation of state and rheology in deep mantle convection, in *Geophysical Monograph 45, Perovskite: A structure of great interest to geophysics and materials science, Ed. A. Navrotsky and D.J. Weidner, AGU, Washington DC*, 1989.

Zalesak, Fully multidimensional flux corrected transport algorithms for fluids, *J. Comput. Phys., 31*, 335-362, 1979.

Zhang, S. and U. Christensen, Some effects of lateral viscosity variations of geoid and surface velocities induced by density anomalies in he mantle, *Geophys. J. Int., 114*, 531-547, 1993.

Zhang, Y.-S. and T. Tanimoto, Global Love wave phase velocity variation and its significance to plate tectonics, *Phys. Earth Planet. Inter. 66*, 160-202, 1991.

Zhang, Y.-S. and T. Tanimoto, Ridges, hotspots and their interaction as observed in seismic velocity maps, *Nature, 355*, 45-49, 1992.

Zhang, Y.-S. and T. Tanimoto, High-resolution global upper mantle structure and plate tectonics, *J. Geophys. Res., 98,* 9793-9823, 1993.

Zhao, W., D.A. Yuen, and S. Honda, Multiple phase transitions and the style of mantle convection, *Phys. Earth Plan. Int., 72*, 185-210, 1992.

Zhong, S. and M. Gurnis, Viscous flow model of a subduction zone with a faulted lithosphere: long and short wavelength topography, gravity and geoid, *Geophys. Res. Lett., 19*, 1891-1894, 1992.

Zhong, S. and M. Gurnis, Dynamic feedback between a continentlike raft and thermal convection, *J. Geophys. Res., 98,* 12219-12232, 1993.

Zhong, S. and M. Gurnis, Role of plates and temperature-dependent viscosity in phase change dynamics, *J. Geophys. Res., in press*, 1994.

Zhou, H.W. and D.L. Anderson, Search for deep slabs in the northwest Pacific mantle, *Proc. Natl. Acad. Sci. USA, 86,* 8602-8606, 1989.

Zhou, H.W. and R.W. Clayton, P and S wave travel time inversions for subducting slab under the island arcs of the northwest Pacific, *J. Geophys. Res., 95*, 6829-6851, 1990.

Appendix A

Parallelization of the spherical-shell, spectral transform mantle convection code

Introduction

This Appendix describes the functioning and parallelization of the three-dimensional spherical-shell mantle convection code that was used to produce the results in Chapters 2 and 3 of this thesis. This code was originally written by Gary Glatzmaier, and has previously been used in many numerical studies of planetary mantle convection [*Glatzmaier*, 1988; *Bercovici et al.*, 1989a,b,c, 1991, 1992; *Schubert et al.*, 1990; *Glatzmaier et al.*, 1990; *Glatzmaier and Schubert,* 1992], running on Cray vector supercomputers. In 1992 I converted this vector code into a parallel code, porting it to the Intel iPSC/860 and Delta supercomputers at the California Institute of Technology. This parallelization is a major operation, requiring fundamental changes in the code. An overview of these changes, together with some quantitative performance measures, is given. The code was further modified to include the phase transitions at 400 and 670 km depth. Details of this modification are not given here, but in Chapters 2 and 3, as well as *Tackley et al.* [1993a&b,1994].

Overview of numerical method

A detailed description of the equations, parameterization and method is given in *Glatzmaier* [1988]. The anelastic approximation and infinite-Prandtl number approximation are used. Variables are expressed relative to a reference state based on an adiabatic polytrope. Velocity is expanded in terms of a poloidal mass flux potential, automatically satisfying mass conservation and continuity at all points and times. Variables pressure (p), entropy (s), gravitational potential (g) and poloidal mass flux potential (w) are expanded horizontally in surface spherical harmonics up to degree and order L. Because the coefficients are constant horizontally, the equations decouple for each spherical harmonic degree, leading to (L+1)(L+2)/2 sets of equations in radius and time for the spherical harmonic coefficients. To solve these, variables are expanded radially in Chebyshev polynomials, and a collocation method is used, forcing the equations to be satisfied at each radial level except at the boundaries, where boundary conditions are satisfied. In order to advance the system in time, various nonlinear products are required. The essence of the spectral transform method is to calculate these nonlinear terms in grid space, by calculating the relevant derivatives in spectral space, transforming them to grid space where the products are formed, and transforming the products back to spectral space in order to advance the energy equation in time. These stages in a timestep are summarized in the flow diagram in Fig A.1.

Parallel processing

It is useful to review some of the basic principles of parallel computing as they relate

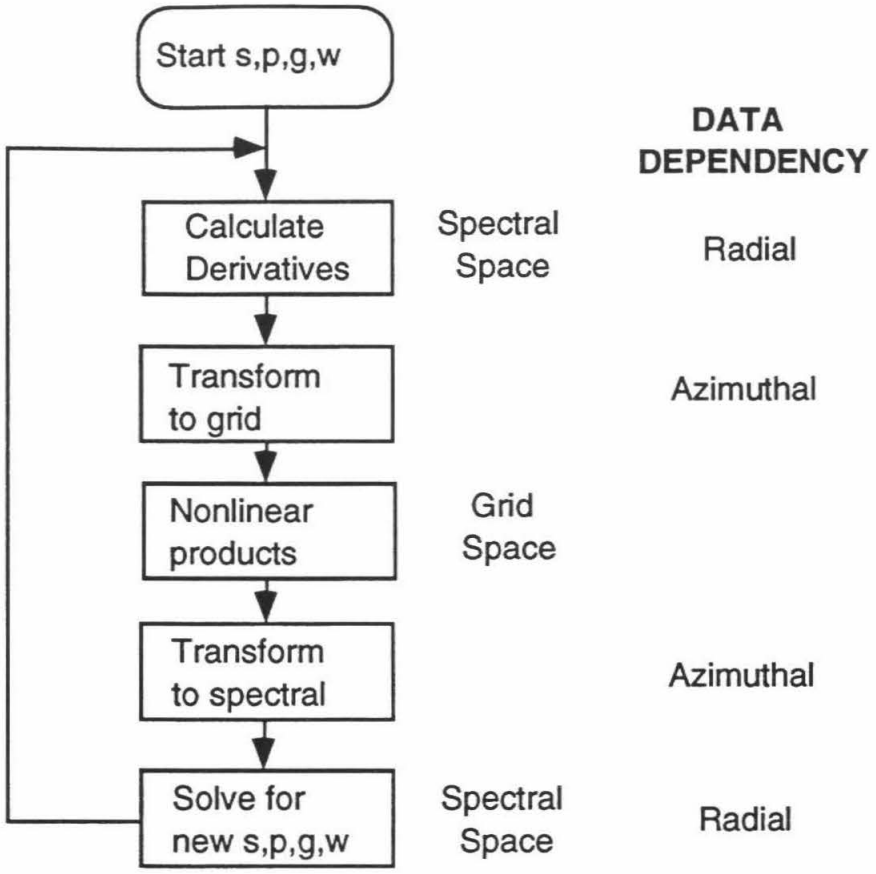

Fig. A.1. Flow diagram showing the various operations involved in one time step.

to the parallelization of this code and the multigrid code (in Appendix B). *Hillis and Boghosian* [1993], provide additional background discussion.

Nodes and topology

The Intel parallel supercomputers used for this work belong to a class of computers known as MIMD (multiple instruction multiple data), indicating that each node (of which there are up to several hundred) is self-contained, with its own processor(s) and memory, and hence each node has its own executable and its own data and can operate totally

independently of the other nodes. However, the power of these computers comes from large numbers of nodes working on the same problem simultaneously, and for this purpose, inter-node communication is necessary. Thus, the nodes are networked together by a network of communication channels, the topology of which is different for different MIMD computers. The Intel iPSC/860 has a hypercube topology, in which the nodes are connected together in an n-dimensional cube (for example a six-dimensional cube for 64 nodes, the size of machine that has been used here), a type of topology which has commonly been used in the past, e.g., in the nCUBE/2 and Thinking Machines CM-2 (note that the latter is not a MIMD machine). On the Intel Touchstone Delta, however, the nodes are connected together as a two-dimensional mesh, with the 512 compute nodes arranged as 16 rows by 32 columns. The Intel Paragon range shares a similar topology. Other topologies include a three-dimensional toroidal mesh (the Cray T3D) and a spanning tree (the Thinking machines CM-5).

Programming

Although more advanced compilers are appearing, the programming paradigm for most MIMD machines is that of explicit parallelization, using standard C or FORTRAN with additional message-passing instructions. This means that the parallel computer appears as though it were a number of workstations networked together, each running the same code at the same time. If no changes are made to a scalar code, each processor would perform exactly the same calculation, and there would be a duplication of effort. Parallelization is achieved by inserting statements into the code so that each node determines which part of the problem to work on. When data that is stored on another node is required, it must be transferred between nodes using explicit message-passing calls inserted into the code. Although this style of programming may appear tedious and is prone to obscure bugs, it has the advantages of (1) large segments of the original scalar code can

be retained unaltered - the parallelization consists mainly of changing the loop limits and inserting additional instructions to communicate data, (2) the programmer has full control of the decomposition and communication, allowing fine tuning to maximize performance, and (3) the programmer is forced to confront the issue of parallelization directly, possibly resulting in a more efficient code than if the compiler attempted to extract parallelization itself.

Although a MIMD computer has the capacity for different processors to be performing completely different instructions at a particular time, the type of problem investigated in this thesis lends itself to a regular domain decomposition, in which the computational domain is split into equally-sized blocks which are distributed amongst the nodes, in which case all processors are typically performing the same operations, except on different data, a style of parallel programming that is referred to as SIMD (single instruction multiple data).

Communication and efficiency

On a parallel computer, the total execution time is the sum of computation time and communication time:

$$t_{total} = t_{compute} + t_{comm} \tag{A.1}$$

with the parallel efficiency being defined as:

$$E = \frac{t_{1-node}}{N t_{total}} \tag{A.2}$$

where N=number of nodes and $t_{1\text{-node}}$ is the execution time on a single node. If the computational component scales perfectly, this becomes:

$$E = \frac{t_{compute}}{t_{total}} \tag{A.3}$$

Communication on current parallel supercomputers is slow relative to memory access or computation speed, and thus communication time is usually a significant fraction of the overall execution time. Furthermore, the communication overhead generally increases with number of processors, whereas computation time decreases with number of processors, making a problem of a given size less efficient as the number of nodes is increased, and limiting the overall scalability of an application. Thus, care must be taken in the design of a parallel algorithm to minimize this communication time, by (1) minimizing the total amount of communication, and (2) following strategies to minimize the time taken for the communication that is absolutely necessary.

The time taken to pass a message ($t_{message}$) between nodes can be approximated as:

$$t_{message} = t_l + n_b t_b + dt_h \tag{A.4}$$

where t_l is the latency, which is the (fixed) time required to start a message, n_b is the number of bytes being communicated, t_b is the time required to transmit each byte of data, d is the distance (the number of 'hops' between the nodes) that the message must pass, and t_h is the per-hop time. For the Intel iPSC/860, the times are approximately $t_l \approx 130$ μs, $t_b = 0.36$ μs, $t_h = 2.0$ μs, and for Intel Touchstone Delta, $t_l \approx 75$ μs, $t_b \approx 0.2$ μs, t_h is negligible. A commonly quoted figure is the "two-way" communication bandwidth, i.e., the number of bytes per second for simultaneously sending and receiving; this is approximately 10 MByte/second for the Delta.

Thus, in order to minimize the communication time, the following strategies must be adopted in the design of a parallel program:

(1) Minimize the total number of bytes communicated.

(2) Minimize the total number of messages, to reduce the total latency time. Thus, for a given amount of data, a few long messages are more efficient than many short messages.

(3) Localize the communication as much as possible. The reason for this is obvious on the iPSC/860, where per-hop time is significant. On the Delta, per-hop time is negligible, but it is important to localize communication in order to avoid different messages interfering with each other on the mesh. The links between processors have a limited bandwidth, so that only two messages can be passed simultaneously at full speed. If more than two messages pass along a particular link, the speed of each one is degraded. If all nodes were simultaneously engaged in distant communication, many messages would be passing along each link, greatly reducing performance.

Other important strategies, which are not obvious from the preceding discussion, are:

(4) Load balancing. It is important that the computation is divided evenly amongst the processors, otherwise the processor with the most work to do will slow down the entire program.

(5) Use asynchronous communication where possible. Asynchronous communication is where communication and computation take place simultaneously, and contrasts which synchronous communication, where the program execution must stop while communication takes place.

(6) There are often additional tuning techniques which are specific to particular computers or message-passing implementations.

Decomposition and differing topologies

From the discussion above, it is clear that care must in taken both in (1) how the computation is decomposed into parallel parts, and (2) how these parts are mapped onto the actual nodes. The latter operation is made more complicated by the differing topologies of parallel computers, e.g., hypercube or mesh. A strategy for simplifying this is to treat the

program decomposition in terms of an idealized virtual or logical node grid, which might for example be a two-dimensional grid (as is used for this code) or a three-dimensional grid (as in Appendix B). A second step is to map this logical grid onto the actual nodes in a manner which localizes communication as much as possible. This approach enables the decomposition to be independent of the specific topology, so that the same program can be used on parallel computers with different topologies, simply by changing the way the logical node grid is mapped onto the actual physical nodes.

Parallelization

The method of parallelization used follows from research performed at Argonne and Oak Ridge National Laboratories for modeling the shallow water equations and atmosphere in spherical geometry [*Foster et al.*, 1991; *Worley et al.*, 1991; *Walker et al.*, 1991]. The model space is decomposed using a two-dimensional horizontal domain decomposition in both spectral and grid space. In grid space, decomposition is by longitude and latitude and in spectral space, by spherical harmonic degree and order. Thus, parallel FFT and Legendre transforms are necessary, with matrix solution and Chebyshev transforms in radius being contained on-node.

The parallel transforms and data dependencies are illustrated in Fig. A.2. In going from spectral to grid space, the first step is to perform the Legendre transform, resulting an intermediate, semi-spectral (θ,m) space. The second step is to perform a parallel Fast Fourier Transform (FFT), leading to grid space. The parallelization of these transforms is now discussed in detail.

Parallel FFT

The standard FFT algorithm is described in *Press et al.* [1992]. Methods for parallelization of this method are well established [*Hillis and Boghosian*, 1993]. The FFT

PARALLEL TRANSFORMS

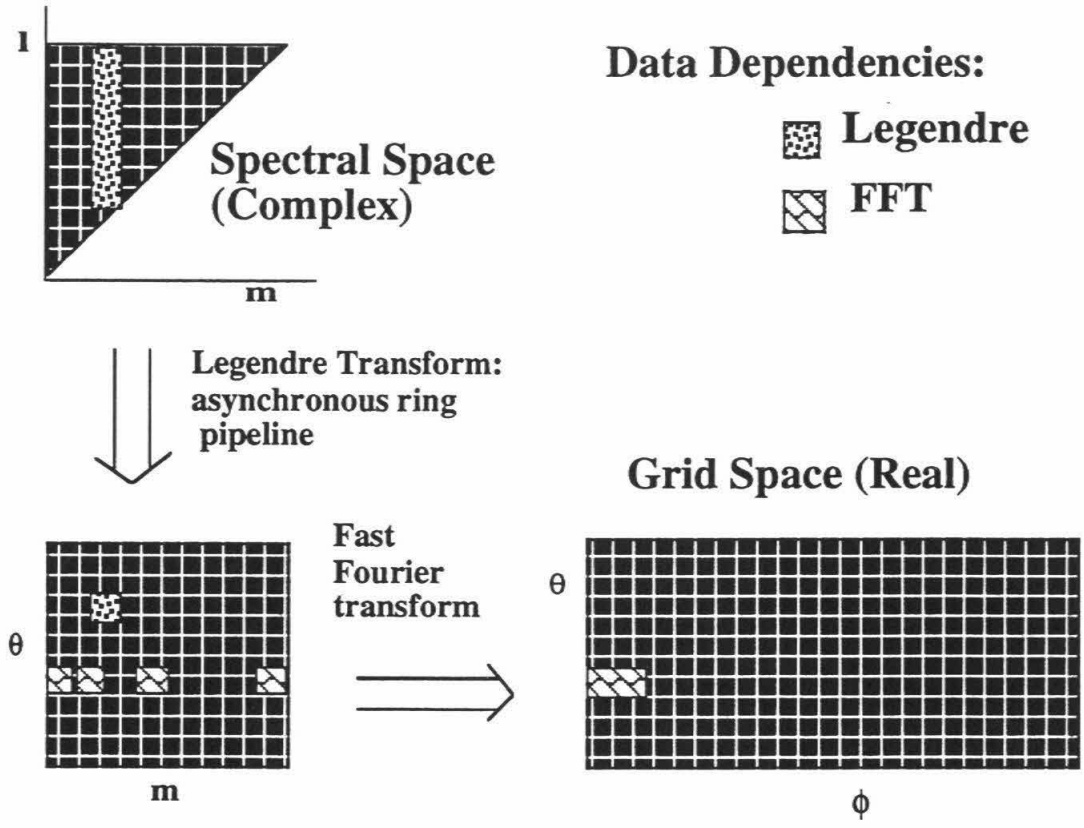

Fig. A.2. Parallel transforms and data dependencies. Data is first Legendre transformed from spectral (l,m) space to an intermediate (θ,m) space using an asynchronous ring pipeline. One value in this intermediate space is dependent on all spectral values with the same spherical harmonic order (m). The data is then Fast Fourier Transformed into grid space, with more complex communication requirements as discussed in the text.

consists of taking $\log_2(n)$ 'doubling' steps, where n is the number of points. When the data is distributed over p processors, $\log_2(p)$ of these steps will involve communication, and $\log_2(n/p)$ will be contained on-node. The communication steps are such that each pair of

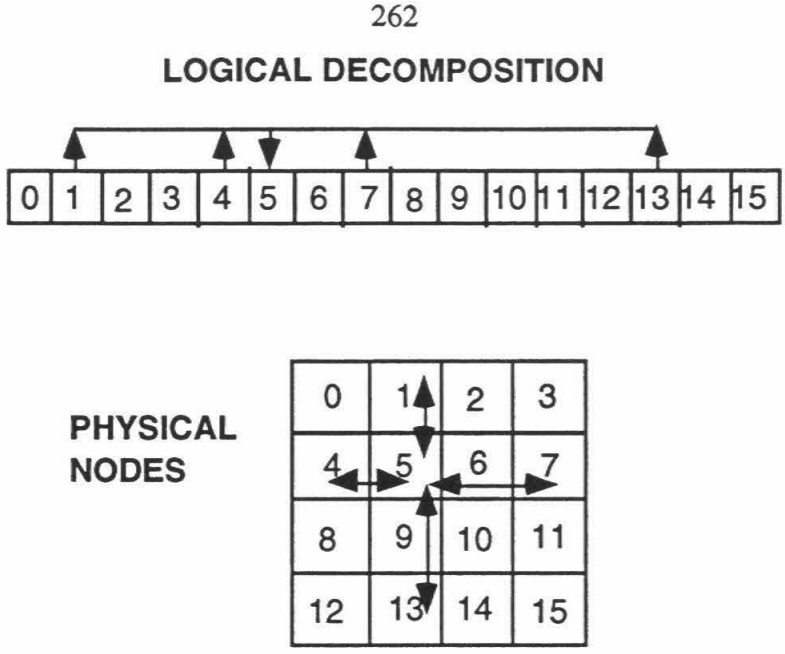

Figure A.3. Decomposition of the Fast Fourier Transform onto 16 nodes of a mesh topology. The upper part shown the logical decomposition, with communication requirements for processor 5 indicated. The lower part shows how this is mapped onto the physical nodes, with the same communication requirements indicated.

nodes needs to know all of the data values on the other node. However, this can be accomplished by swapping half of the data values on each node rather than all of them, which leads to permuted data.

If the FFT is distributed onto logical nodes with consecutive node numbers, as shown in Fig. A.3, the communication requirements are such that a particular node must communicate with other nodes whose numbers are different by 1,2,4,8,16, etc. The nodes on a hypercube are numbered such that these nodes are all nearest-neighbors, allowing the logical nodes to be easily mapped onto physical nodes in a way that minimizes communication. On a mesh, the physical decomposition is more complicated, and the best method is to map the logical nodes onto a square of physical nodes, as shown in Fig. A.3.

The maximum communication distance is then $\sqrt{(p/2)}$ where p is number of processors. For example, for 16 nodes, the maximum communication distance is 2.

There are various complications to the FFT which must be considered:

(1) 'bit reversal' [*Press et al.*, 1992]. This is a step necessary to get the data in the correct order for doubling. The communication requirements are very messy and require each node to communicate with several others. Thus, this step is avoided by storing the data in bit-reversed order in spectral space, using a Cooley-Tukey FFT (bit-reversal first) algorithm to transform to grid space and a Sande-Tukey algorithm (bit-reversal last) to transform from grid to spectral space. This introduces another permutation to the spectral data.

(2) Since the grid variables are real, the spectral data is complex conjugate, i.e., $A_{l,-m}=(A_{l,m})^*$ (in fact only positive m-values are stored), and a real to complex-conjugate FFT algorithm is required. This is straightforward, consisting of the conventional FFT algorithm with an additional step [*Press et al.*, 1992]. The communication for this extra step is well-ordered and does not present any serious problems. An additional permutation is introduced into the spectral data.

(3) Since a triangular truncation is used in spectral space, it may appear that load imbalance (a different number of frequencies on each node) would occur if the data were straightforwardly divided up by spherical harmonic order m. However, due to all of the permutations introduced into the spectral data (due to bit reversal, exchanging half the values during doubling, and the real to complex-conjugate step), the m values are ordered such that no load imbalance occurs, and each processor has an identical number of frequency components.

Legendre transform

Unfortunately, there is no fast algorithm for performing the Legendre transforms; they must proceed via straightforward matrix multiplication, resulting in a number of operations that scales as L^3, where L is the maximum spherical harmonic degree (the scaling of FFT is $L^2 \log_2 L$. Looking at Fig. A.2, the data dependency and hence communication requirements can be deduced. To calculate a particular value in grid space, all l values for a particular m must be known. The communication can be arranged using a logical ring pipeline, as shown in Fig. A.4. The spectral data is passed around the ring pipeline, and at each step the processor calculates the contribution of the current block of spectral coefficients to the local patch of grid space (which is retained on the node throughout). At each step, all the spectral coefficients on a node are passed one step around the pipeline. If q processors are used, q-1 steps are required. A characteristic of the data dependencies is that the spectral data is not changed as it is passed around the ring, so that the data that is needed for the next step is not dependent on completing the previous step. This can be exploited to reduce the communication overhead, by using asynchronous communication, in which communication takes place in the background while computation continues. This asynchronous communication reduces the communication overhead significantly. Unfortunately, in the FFT, each computation step must be completed before communication, requiring synchronous communication, in which processing came to a halt until communication is complete.

The logical decomposition (a ring pipeline) can be straightforwardly mapped onto the physical nodes with all communication nearest-neighbor, both on a hypercube and a mesh. In order to achieve load balancing despite the triangular truncation, the spectral data is split into 2q rows, and each processor is allocated complementary rows such that all processors get the same number of spectral coefficients.

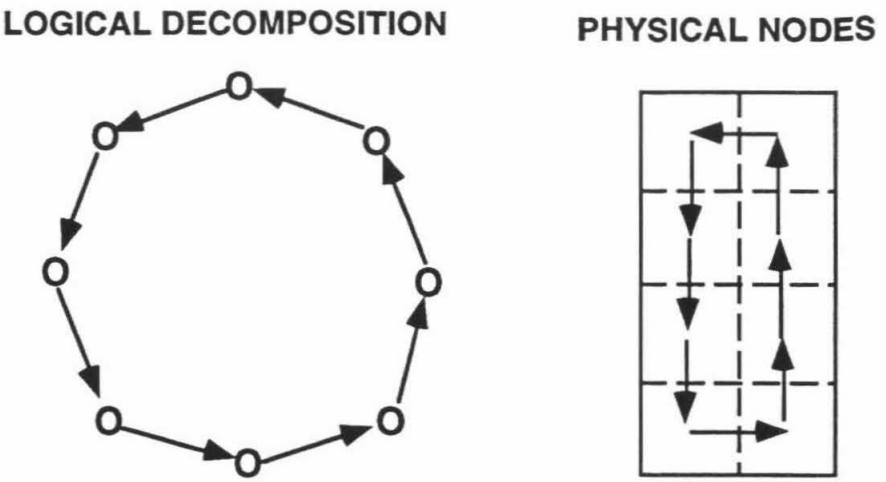

Fig. A.4. Decomposition of the Legendre transform into a ring pipeline, showing (left) the logical decomposition and (right) the mapping onto physical nodes for a mesh topology.

Combined transforms

In general, the program will be decomposed onto N nodes in both the Fourier (p ways) and Legendre directions (q ways, where q=N/p), such that one must consider the physical node mapping that occurs when both decompositions are used simultaneously. On a hypercube, both decompositions can be used while still retaining nearest-neighbor communication. On a 2-D mesh, however, this is not possible, and a compromise must be made. Two main alternatives can be identified: keeping the FFT squares close together, in which case the ring pipeline links in the Legendre transform involve communicating a distance of $\sqrt{p}$ nodes, and the FFT a maximum distance of $(\sqrt{p})/2$ nodes; and keeping the Legendre transform close together in a square, in which case the Legendre transform involves nearest-neighbor communication and the FFT involves a maximum

communication distance of $(\sqrt{N})/2$ nodes. Tests indicate that the former method results in better performance, and thus it has been adopted.

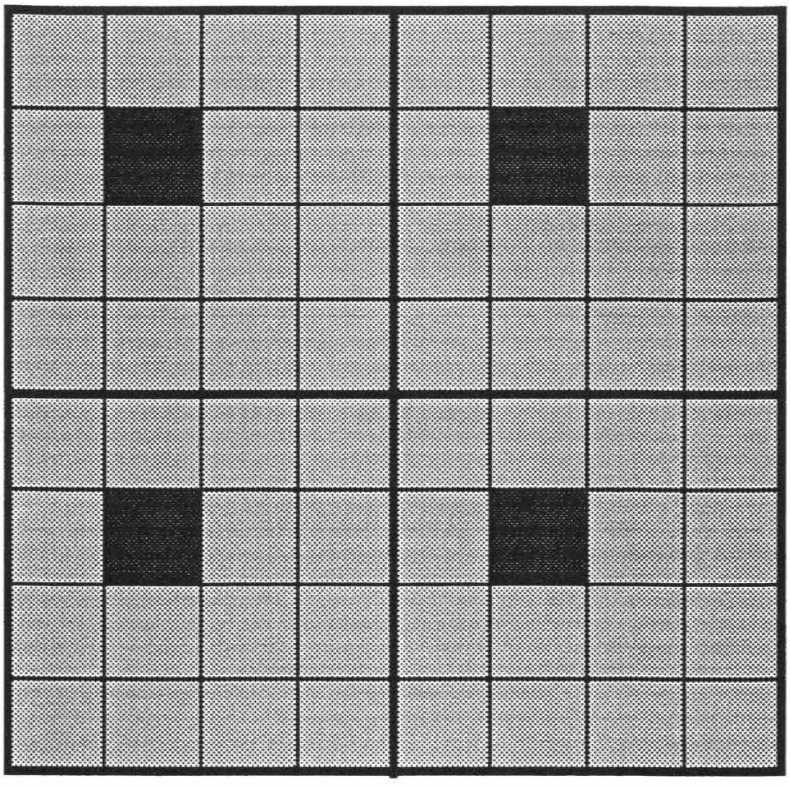

Fig. A.5. Simultaneous decomposition of the FFT and Legendre transforms onto a mesh topology, on 64 nodes. In this case the FFT is decomposed 16 ways, and the Legendre transform 4 ways. FFTs proceed independently in the four 4x4 squares of nodes. Legendre transforms proceed using ring pipelines, with the dark squares indicating one such pipeline.

Performance

Figure A.6 shows the performance of the parallel code for various horizontal resolutions and numbers of nodes, on the 512-node Intel Touchstone Delta. The vertical

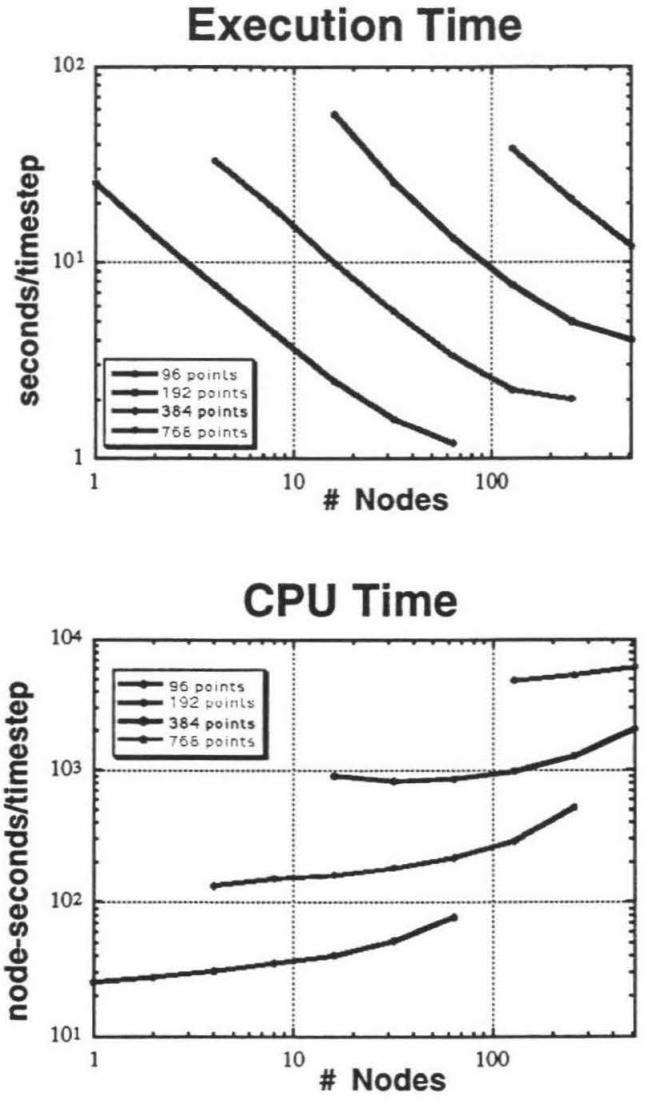

Fig. A.6. Execution time (top) and CPU time (bottom) for one timestep, on 1 to 512 nodes of the Intel Touchstone Delta. The vertical resolution is 33 radial levels, with horizontal resolution ranging from 96 points around the equator, corresponding to a spectral truncation at spherical harmonic degree 31, to 768 points around the equator, corresponding to a spectral truncation at spherical harmonic degree 255.

resolution is kept constant at 33 radial levels, and the horizontal resolution is varied in steps of two from 96 points around the equator (48 from pole to pole), corresponding to maximum spherical harmonic degree and order 31, as used in *Bercovici et al.* [1989abc, 1991, 1992] and *Schubert et al.* [1990], to 768 points around the equator, corresponding to maximum spherical harmonic degree and order 255. The intermediate resolution of 192 points around the equator (maximum spherical harmonic degree 63) was used by *Glatzmaier* [1988] and *Glatzmaier et al.* [1990], whereas 384 points around the equator (maximum spherical harmonic degree 127) are used in this thesis and in *Tackley et al.* [1993b, 1994]. For simulations, the vertical resolution would also be increased as the horizontal resolution is increased, but since we are most interested in the performance of the horizontal (parallel) transforms, the vertical resolution is kept constant for this test.

The upper part of Fig. A.6 shows the execution time, in number of seconds per time step. Increasing the number of nodes decreases the execution time, as expected, but the non-constant slope of the curves indicates that each doubling of number of nodes does not result in a doubling of the speed. This is shown more clearly in the lower plot, which shows the total CPU time, in node-seconds, per time step, for the same cases. If the speed scaled perfectly with number of nodes, the lines on this graph would be horizontal. In fact, the total CPU time increases as the number of nodes is increased, even though the actual execution time (top plot) decreases. This is normal for parallel programs, and is due to two effects: (1) The communication overhead increases as the number of nodes is increased, resulting in a lower efficiency, as explained earlier. (2) As the number of nodes is increased for a fixed size of problem, each node has less data, and the size of loops in the code decreases, leading to lower pipelining performance on the processors.

The relative time taken in different parts of the code is illustrated in Fig. A.7 for the 4 resolutions, running on the lowest number of processors possible for each resolution (which is determined by memory requirements) so that communication is minimized. The

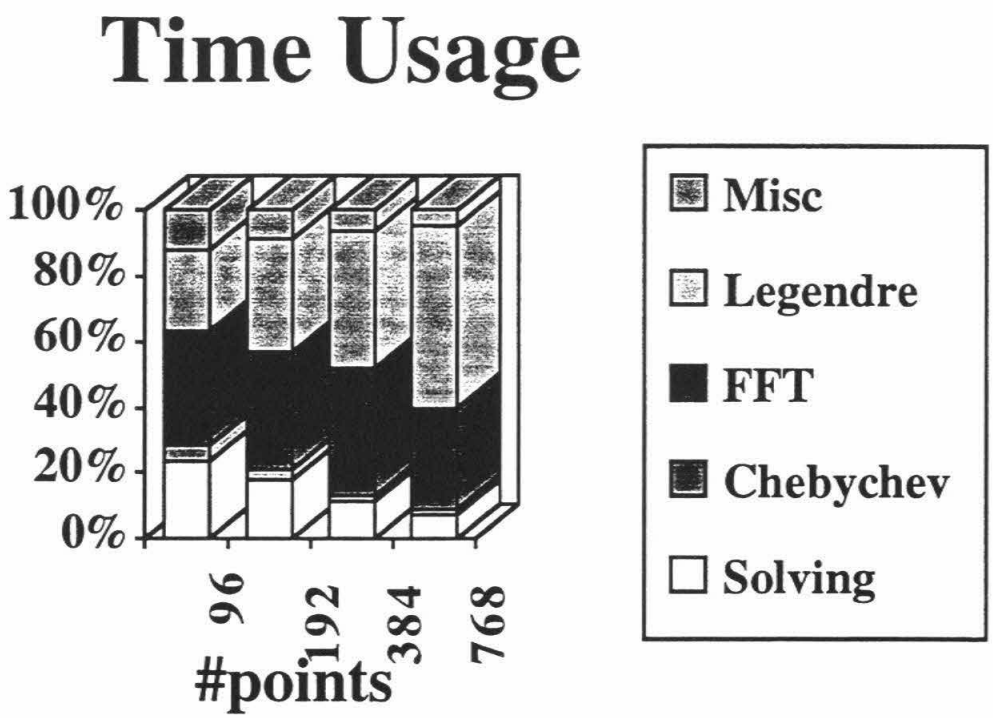

Fig. A.7. The fraction of time used in various parts of the code on the Intel Touchstone Delta, for four different horizontal resolutions and 33 radial levels. Note the large increase in time required for transforms, particularly Legendre transforms, as resolution is increased.

main trend is that as the horizontal resolution is increased, the transforms take up a larger fraction of the total execution time, dominating the execution time. In particular, the time taken for the Legendre transform grows faster than any of the other components. This is to be expected, since if L=maximum spherical harmonic degree and N=number of radial levels, the time taken for the various parts of the program scale as follows: Legendre transforms - NL^3; FFT - $NL^2\log_2 L$; Chebyshev transforms - $N\log_2 NL^2$; Matrix solution -

N^2L^2. Thus, all parts of the method scale faster than the total number of grid points (NL^2), a characteristic that limits the usefulness of the spectral method for very large problems.

Since this code has previously been run on a Cray Y-MP, it is instructive to compare the execution times, to see whether the use of a parallel computer is justified. The Cray version of the code has assembly-language modules for the major parts, resulting in a substantial increase in performance compared to all FORTRAN coding. The standard problem with 192x96 horizontal points (L=63) and 33 radial levels uses 5.74 CPU seconds per timestep on a single Cray Y-MP processor, corresponding to a speed of 125 Mflops (million floating point operations per second). The parallel version is written entirely in FORTRAN, and 32 nodes of the Intel Delta give a similar performance to the Cray, at 5.63s per step. Both of these tests are in double precision. The cases reported in Chapters 2 and 3 were run on 128 or 256 nodes, giving a performance equivalent to 4 or 8 Cray Y-MP processors. Another advantage of using the Intel Delta is the large amount of memory available. The resolution of 768x384x33 would apparently be difficult to fit on a Cray Y-MP .

Conclusions

These results demonstrate that the spectral transform method in spherical geometry is feasible on a massively-parallel supercomputer, and can give a performance equivalent to many Cray Y-MP processors. Communication is a significant concern; however, the next generation of parallel supercomputers, such as the Intel Paragon and Cray T3D, have much faster communication, relative to the speed of processors, and thus greater efficiencies should be obtained. A long-term problem is the basic scaling characteristics of the spectral transform method with number of grid points: for all parts of the code, execution time and memory usage increase faster than the number of grid points. As computers and numerical

simulations get larger, this will lead to a preference for numerical methods in which execution time scales in proportion to number of grid points, such as the multigrid method.

Appendix B

A finite-volume multigrid method for modeling mantle convection with large viscosity variations on massively-parallel supercomputers

Introduction

This Appendix describes the code that was used in Chapters 5 and 6 of this thesis. This code solves the equations of infinite Prandtl number, compressible anelastic flow with large viscosity variations, and is implemented on Intel parallel supercomputers. The method uses a finite-volume discretization of the equations in combination with a multigrid solver. The motivation for developing a completely new code, rather than simply modifying the existing, spherical code [*Glatzmaier*, 1988 and Appendix A], is that the spectral technique used by the latter code is not well suited to the study of convection with large viscosity variations. Various authors have developed spectral solvers for variable-viscosity flow [*Christensen and Harder*, 1991; *Cadek et al.*, 1992; *Martinec et al.*, 1993; *Zhang and Christensen*, 1993; *Balachandar and Yuen*, 1993]; however, these require large execution times due to the iterative treatment of coupling between modes, and are generally limited to fairly low viscosity contrasts. In contrast, using a grid-based method, viscosity variations

can be naturally incorporated into the formulation, and for large problems, an iterative multigrid solver is the natural choice of method. Indeed, *Baumgardner* [1985, 1988] and *Parmentier et al.* [1994] have demonstrated the feasibility of this method for modeling mantle convection. This appendix gives details of discretization, multigrid implementation, timestepping, parallelization, code verification and benchmarking.

Equations and nondimensionalization

In order to study the slow, highly viscous creeping flow in planetary mantles, the infinite-Prandtl number approximation is assumed (the Prandtl number for the Earth is of order 10^{23}), which involves neglecting inertial terms in the momentum equation. Compressibility is included using the anelastic-liquid approximation [*Jarvis and McKenzie,* 1980]. The equations are nondimensionalized to the depth of the mantle (D), thermal diffusion timescale (D^2/κ, where κ=thermal diffusivity) and superadiabatic temperature drop, ΔT_{sa}. Other nondimensionalizations, for example velocity (κ/D) and stress ($\eta\kappa/D^2$), follow from these.

These assumptions lead to the following set of equations, describing conservation of mass, momentum and energy respectively:

$$\nabla \bullet (\rho \underline{v}) = 0 \tag{B.1}$$

$$\nabla \bullet \underline{\underline{\tau}} - \nabla p = Ra.\tilde{\alpha}\tilde{\rho}T\,\hat{\underline{z}} \quad ; \quad \tau_{ij} = \eta(v_{i,j} + v_{j,i} - \tfrac{2}{3}v_{k,k}\delta_{ij}) \tag{B.2}$$

$$\overline{\rho}\,\overline{C}p\frac{\partial T}{\partial t} = \nabla \bullet (\overline{k}\nabla T) - \overline{\rho}\,\overline{C}p\underline{v} \bullet \nabla T - Di_s\overline{\alpha}\overline{\rho}Tv_z + \overline{\rho}\overline{H} + \frac{Di_s}{Ra_s}\tau_{ij}v_{i,j} \tag{B.3}$$

The surface dissipation number and Rayleigh number are given by:

$$Di_s = \frac{\alpha_s g D}{Cp_s} \tag{B.4}$$

$$Ra_s = \frac{\rho_s g \alpha_s \Delta T_{sa} D^3}{\eta_{s,a} \kappa_s} \tag{B.5}$$

where the subscript 's' denotes surface values, v=velocity, p=dynamic pressure, T=absolute temperature, τ=deviatoric stress, η=dynamic viscosity, $\underline{z}$ is a unit vector in the vertical direction, and the barred quantities ρ, α, Cp, κ, and k (=ρCpκ) are depth-dependent reference state parameters density, thermal expansivity, heat capacity, thermal diffusivity and thermal conductivity respectively. The vertical coordinate z runs from 0 at the base to 1 at the surface. The Boussinesq approximation is recovered by setting Di=0 and all depth-dependent properties to 1. Viscosity can be an arbitrary function of variables such as temperature, depth, stress, and composition:

$$\eta = \eta(T, z, \tau, C, \ldots) \tag{B.6}$$

Various forms of viscosity law have been used in numerical studies; however, an Arrhenius law [*Weertman*, 1970] is most appropriate for planetary mantles, as discussed in Chapter 6.

There are various ways of deriving the depth-dependent reference state parameters, but the exact form of these is not important for the numerical implementation discussed in this Appendix. The choice of reference state used in this thesis is described in Chapter 6.

When viscosity is constant and equal to one, the momentum equation may be written in a simpler form as:

$$\nabla^2 \underline{v} - \nabla p = Ra.\tilde{\alpha}\tilde{\rho}T\hat{\underline{z}} \tag{B.7}$$

which results in significantly fewer terms in the discretized equations.

Discretization

Primitive variables, namely three components of velocity, and scalar variables such as pressure and temperature, are defined on a staggered, three-dimensional Cartesian grid. A two-dimensional version of this grid is illustrated in Figure B.1.

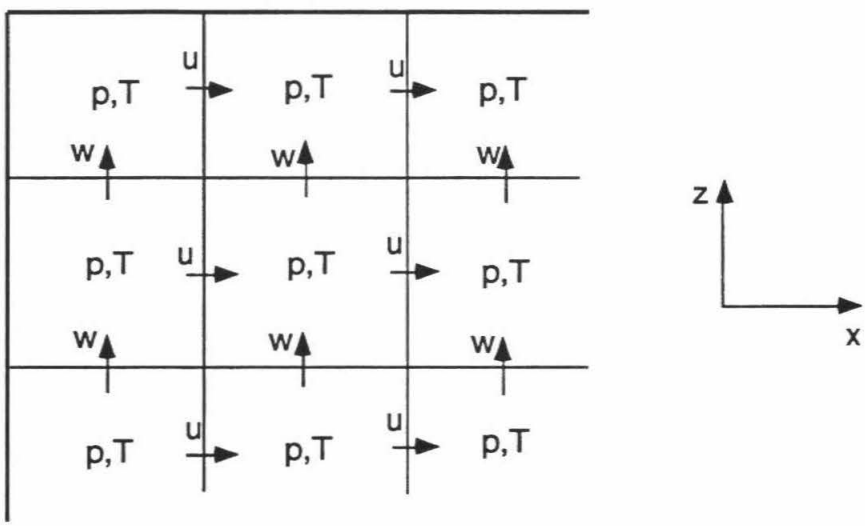

Fig. B.1. A two-dimensional version of the staggered grid. Pressure (p) and temperature (T) are defined at the cell centers, horizontal velocity (u) at the center of the cell walls perpendicular to the x-direction, and vertical velocity (w) at the center of the cell walls perpendicular to the z-direction. Vertical and side boundaries (at top and left) coincide with cell walls, allowing easy implementation of boundary conditions.

The domain is divided into cells. Scalar variables (pressure and temperature) are defined at the center of the cells, and velocity components are defined at the center of the

cell faces which are perpendicular to the particular velocity component. Domain boundaries are taken to coincide with the faces, allowing easy implementation of boundary conditions.

There are various advantages to using a staggered grid, which are discussed following the description of iterations. The problem of solving equations (B.1)-(B.6) must be split into two parts: solving the momentum equation (B.2) and continuity (B.1) at each instant in time, for which a multigrid solver is used; and stepping the energy equation (B.3) forward in time, for which a standard finite-volume method is used. The most challenging part is to solve the momentum equation, and the following discussion is mainly concerned with this.

Iteration scheme

The iterative technique used to simultaneously solve equations B.1 and B.2 was developed independently by the author, but is quite similar to the SIMPLER algorithm of *Patankar* [1980], so the reader is referred to his book for further information on various points. Each equation (the three momentum equations and continuity) is relaxed in turn over the entire domain, as listed in Table 1.

Equation	Centered on	Variable(s) adjusted
x-momentum	x-face	u
y-momentum	y-face	v
z-momentum	z-face	w
continuity	center	p,u,v,w

Table B.1. Relaxation procedure. One equation is corrected at a time by sweeping through the entire domain and adjusting the listed variable(s). p=pressure, and u,v,w are the velocities in the x,y and z directions respectively.

In terms of finite-volume theory, one can think of the domain as being divided into discrete volume cells or control volumes centered on the relevant points, and relaxation consists of balancing the stresses on the sides of a control volume with body forces within them. Note that the cell boundaries are different for each of the momentum equations, such that the velocity component being adjusted lies in the center of the cells [*Patankar*, 1980]. For the continuity equation, the cell boundaries are the same as those in Fig. 1, and these cell boundaries are also used for the energy equation. An alternative way of envisioning the relaxation process is in terms of finite-differences, in which case the equations are forced to be satisfied at the grid points in question rather than for volume cells. For the second-order approximation used here and a Cartesian grid, these approaches yield identical discretized equations, although this would not be the case for higher order approximations.

As an example of a discretized derivative, the expression for $\tau_{xx,x}$ for incompressible flow is given below:

$$\tau_{xx,x} = 2\frac{\eta_{\delta x/2}(u_{\delta x} - u_0) - \eta_{-\delta x/2}(u_0 - u_{-\delta x})}{(\delta x)^2} \tag{B.8}$$

where u is x velocity, subscripts denote the position of the variable relative to the central point (denoted by 0) and δx is the cell size in the x direction. This derivative is calculated at the same locations as x-velocity. Due to the staggered grid, viscosity variations are naturally incorporated into the expression without the need to calculate derivatives of viscosity. However, in order to calculate all of the required stress components, viscosity must be known at 4 locations in a unit cell. Viscosity is first calculated at the cell centers, where temperature is defined, and from these values, viscosity at the other three locations is derived.

Thus, a relaxation sweep for a particular variable, e.g., u, involves going through all of the u values the entire domain, calculating corrections which would reduce the residual (error) in the equations to zero. These corrections, or some fraction of them (in the case of

under-relaxation) are then applied. In the current implementation, Jacobi iterations (in which all of the corrections are calculated before any are applied) are used rather than Gauss-Seidel (in which corrections are applied at each point as soon as they are calculated). This is because the latter approach is fundamentally serial, requiring all of the points in the domain to be stepped through in order, which is not compatible with parallel processing. It would, however, be possible to use red-black Gauss-Seidel iterations (in which two sweeps are made, adjusting alternate grid points), and experiments with this approach are in progress.

When correcting the continuity equation (equation B.1), which is centered on the pressure points, velocity corrections are applied to the six neighboring velocity values in order to eliminate any divergence of mass flux. Pressure is then adjusted, to prevent the divergence from happening again; for example, if there was a net convergence of mass flux into a cell, pressure would have to be increased. The equation for the pressure correction is:

$$\Delta p = -\frac{\eta \nabla.(\rho \underline{v})}{\rho} \tag{B.9}$$

Since the pressure corrections are based solely on neighboring velocity values, boundary conditions for pressure do not need to be specified, but arise naturally as a consequence of velocity boundary conditions [*Patankar*, 1980].

There are several advantages to using a staggered grid, finite-volume technique, as opposed to a non-staggered grid finite-difference technique (in which all variables are defined at the same points):

(1) With non-staggered grids, checkerboard pressure solutions may result due to decoupling of alternate grid points. An arbitrary checkerboard pressure pattern can be added to the solution, and it will still satisfy the discretized equations [*Patankar*, 1980]. In addition, oscillating velocity fields will satisfy the discretized continuity equation. These problems are avoided with a staggered grid.

(2) Iterations are convergent even for large viscosity contrasts. This is because relaxation of the momentum equations can be considered as diffusing momentum flux across cell walls. Thus, provided the stresses are defined in such a way that the calculated value of stress on a particular face is identical for cells that share that face, as is the case with finite-volume iterations, convergent behavior is guaranteed. Associated with this is the fact that it is not necessary to calculate derivatives of viscosity, as mentioned earlier (Equation B.8).

(3) The staggered finite-volume grid gives greater accuracy than a non-staggered grid. This is because (i) first derivatives, for example ∇P, involve adjacent points in the staggered grid but points which are separated by two times the grid spacing in a non-staggered grid. Thus, approximately twice as many non-staggered points in each direction are necessary to get the same accuracy as the staggered grid. A non-staggered grid can often be shown to be equivalent to interlaced staggered grids with twice the grid spacing, so that many times the computational effort is expended for obtaining a solution of similar accuracy [*Brandt*, 1984]. (ii) The finite-volume approach involves balancing stresses on the cell boundaries with volume-integrated body forces inside the cells, thus conserving integrated quantities to machine accuracy, as with the finite-element method.

(4) Timestepping involves calculating fluxes across cell boundaries, and thus results in conservation of energy to machine accuracy. Additionally, finite volume advection is widely used in the fluid dynamical community and there are many accurate advection schemes that can be used, as discussed later.

Multigrid solver

A multigrid algorithm [e.g., *Brandt*, 1982,1984; *Press et al.*, 1992] is used to accelerate the convergence of the finite-volume iterations. Jacobi or Gauss-Seidel iterations on their own resemble a diffusive process (i.e., one can imagine the solution diffusing

through the numerical grid), and thus the number of iterations required to achieve a specified convergence is proportional to the square of the number of grid points along the longest axis. Thus, the computational effort scales approximately as $N^{5/3}$, where N is the total number of grid points. A multigrid algorithm relaxes all wavelengths simultaneously, thereby achieving convergence in a number of iterations which is independent of the number of grid points, resulting in a computational effort which scales in proportion to the number of grid points N.

Standard multigrid V-cycles are used. These involve relaxation steps on a hierarchy of nested grids, starting from the finest grid, and progressing through increasingly coarse grids to a grid with only a few points in each direction. On each grid, a solution to the residual (error) from the next finest grid is sought. At the coarsest level, an exact solution to the remaining residual is obtained. Then, by stepping through the grids in the reverse direction, from the coarsest to finest levels, these solutions are applied as corrections to the solution on the next finest grid, with additional relaxation steps being taken. The reader is referred to references for exact details [*Brandt*, 1982; *Press et al.*, 1992]. For constant viscosity cases, two relaxation steps are taken at each level ((2,2) cycles) whereas for variable viscosity, (3,3) cycles are typically used. As is usual, each stage of coarsening reduces the number of cells by a factor of 2 in each direction. Coarse-to-fine and fine-to-coarse operators are made more complicated by the staggered grid, since coarse grid points do not in general lie exactly on fine grid points. Local averaging or injection is used for the fine-to-coarse operator, with linear interpolation for the coarse-to-fine operators. A more complex restriction is necessary for the viscosity field; the geometric mean of local values was found to give the best convergence out of the simple methods tried.

On the coarsest grid, which is usually taken to have 2 cells in the vertical direction, it is necessary to calculate an 'exact' solution to the remaining residual. The major alternatives for doing this are to use a direct matrix solver, or repeated iterations of the Jacobi scheme. Experimentation revealed that for the grid geometry typically used in this thesis, the matrix

solver was the slower method, because, due to there being 4 variables per cell, the matrix can be quite large. For example, the 8x8x2 cell coarsest grid typically used for cases in this thesis would lead to a 512x512 matrix. Unfortunately, even using repeated iterations, the time taken for obtaining the coarsest solution is significant, and more work is needed to reduce this overhead.

When large viscosity contrasts are modeled, small-scale variations in viscosity and hence in the velocity solution are not adequately represented on coarser grids, and the coarse grid corrections do not necessarily improve the fine grid solution. Thus, the maximum viscosity contrast that can be modeled using the multigrid is limited by the ability of coarse grid corrections to improve the finest grid solution, even though iterations on a particular grid converge for any viscosity contrast. It is found that with large viscosity contrasts, damping of the coarse grid corrections is helpful in achieving overall convergence, with a damping factor of typically 0.7-0.8, meaning that only this fraction of the calculated correction on a particular coarse grid is applied to the next finest level.

The use of an iterative solver allows the user to set the accuracy of the velocity/pressure solution, by specifying a maximum residual (error). Iterations continue until the actual residual drops below this specified value. Greater accuracy requires more iterations and more CPU time, and thus, in order to make best use of available resources, it is important to determine the minimum level of accuracy that is required. If the solution accuracy is set too low, significant errors may arise, but if too high an accuracy is demanded, an unnecessarily large amount of CPU time will be used, less cases can be run, and less scientific progress is made.

Two other sources of inaccuracy arise, and a general rule is that the convergence criterion for the flow solver must be set to be less than these. These sources are (1) the discretization error, i.e., the error associated with representing the solution on the chosen discrete grid rather than a perfect, continuous domain with infinite resolution, and (2) the timestep error, i.e., the amount by which the velocity/pressure solution changes over a

timestep due to the time evolution of buoyancy forces and viscosity. Both of these errors are generally of the order 10^{-2}, and thus, a reasonable convergence criterion would seem to be that the r.m.s. error in the velocity/pressure solution be of order 10^{-3} of the r.m.s. solution.

Timestepping

The terms on the right-hand side of the energy equation (equation B.3) correspond to advection, diffusion, adiabatic heating/cooling and viscous dissipation, respectively. Out of these, advection and diffusion are dominant, as shown in Chapter 6, and thus they are the most critical for the overall accuracy of the code. The accuracy of these terms is related to the fraction of the Courant timestep (i.e., Courant number) that is used, with many small steps being more accurate than few large steps. At high Rayleigh number, the overall timestep is limited by the Courant step for advection, and the Courant number for diffusion is low. This implies that the accuracy with which the advection term is treated is much more critical for overall accuracy than the accuracy of the diffusion term.

There are many finite-volume advection techniques described in the literature, which are designed to give accurate advection of small features with low numerical dissipation. Examples are Flux Corrected Transport (FCT) [*Zalesak*, 1979] and the schemes compared in *Müller* [1992]. For this current code, the Multidimensional Positive Definite Advection Transport Algorithm (MPDATA) of *Smolarkiewicz* [1984] is chosen, due to its simplicity and computational economy. The method is based on the simple upwind scheme, with accuracy improved iteratively by taking corrective advection steps with 'anti-diffusive' velocities. The iterative nature of this scheme allows arbitrary spatial accuracy to be specified as an input parameter.

Simple second-order explicit finite-differences are used for the diffusive term. As explained earlier, the Courant number of this term is low and thus the mathematical

accuracy is not critical to overall code accuracy. To calculate the viscous dissipation term, products of stress and strain are calculated for each component at the relevant staggered grid points, and summed to the cell centers where scalar variables are defined. Adiabatic heating is straightforwardly calculated from the vertical velocity interpolated to cell center.

Parallelization

For background information on parallel computers and programming, see Appendix A. The numerical method described here has been implemented in FORTRAN on the Intel iPSC/860, Delta and Paragon parallel supercomputers using a MIMD, message-passing paradigm with Intel's NX message-passing calls. The code is portable to scalar computers such as workstations by the use of dummy NX calls which simulate running on one node. The computational domain is decomposed into three-dimensional blocks, which are distributed amongst the processors. This is illustrated in Fig. B.2. These blocks are approximately cubic, in order to minimize the ratio of surface area to volume, which is closely related to the ratio of communication to computation. Blocks overlap sides with their neighbors, and communication involves exchanging these overlapping values each time a variable is updated, requiring six messages, one for each direction. Thus, many small messages are required and the communication performance is most sensitive to latency rather than bandwidth.

When the computational nodes are arranged in a hypercube topology, as with the Intel iPSC/860, the three-dimensional array of blocks can be assigned to the nodes in such a way that nearest neighbors in physical space are also nearest neighbor nodes. On a two-dimensional mesh architecture such as the Intel Delta, however, this is not possible, and one dimension must be 'collapsed' onto adjacent nodes. Since the domain is typically much wider than it is deep, the z-dimension is chosen for this, and the mesh coordinates reflect the x and y coordinates in the physical domain, as illustrated in Fig. B.2.

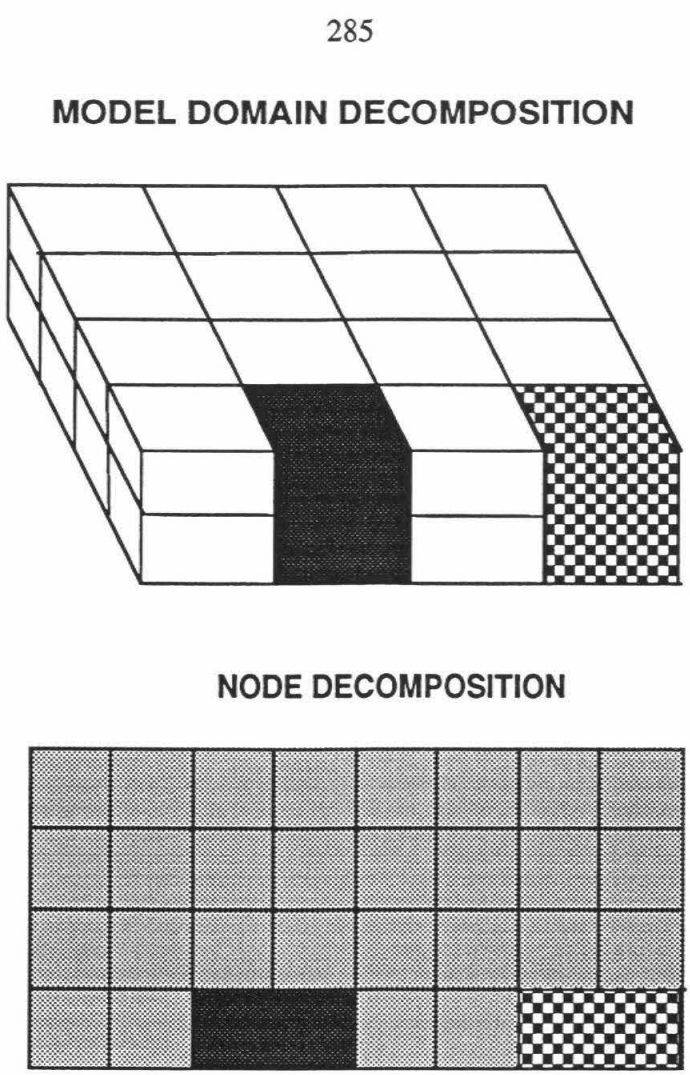

Fig. B.2. The computational domain is divided up using a three-dimensional block decomposition (top). This is mapped in a straightforward manner onto a two-dimensional mesh of 32 nodes (bottom), in which the mesh coordinates reflect x and y coordinates of the domain. Vertical columns of blocks are collapsed onto nearby nodes, minimizing communication distance.

Iterations on the coarser grids, where there are very few points per node, can be very inefficient, with the execution time dominated by message latency time. However, iterations on coarse grids involve much fewer operations, making them so much faster than the finest grid iterations, that this inefficiency does not matter very much. The exception to

this is on the coarsest grid, where it is necessary to iterate to convergence, requiring 50-100 iterations, rather than the 2-3 required on the finest and intermediate grids. The communication overhead for the coarsest grid can become a significant part of the overall V-cycle time. In order to reduce this overhead, the coarsest grid iterations are performed on a single node, with no communication. A single communication step is necessary to bring the solution from being distributed across all nodes onto a single node.

Benchmarking

The code has been verified by performing many of the standard benchmark tests that exist in the mantle convection community, both in two dimensions [*Blankenbach et al.*, 1989; *Travis et al.*, 1990a] and three dimensions [*Busse et al.*, 1993]. These cover cases with constant viscosity or temperature-dependent viscosity, and with basal heating or internal heating.

The first test is constant-viscosity two-dimensional convection with basal heating, at a Rayleigh number of 10^5, corresponding to case 1b of *Blankenbach et al.* [1989]. The results are given in Table B.2. This test was performed using a grid with either constant spacing, or with smoothly-varying vertical grid refinement in the upper and lower boundary layers, by a factor of around 3, and with either first-order or second-order advection. The results indicate quite clearly that both grid refinement and second-order advection (rather than first order) significantly improve the accuracy of the solution, with only one exception. When both are used, the accuracy is with 2% for 16x16 grid points, and within 0.05% for 64x64 points, compared with 5.5% and 0.83% respectively for constant grid spacing and first-order advection. Thus, both enhancements are used in the other benchmarks.

Similar results at a Rayleigh number of 10^4 are given in Table B.3. Due to the lower Rayleigh number, features are broader, and can be more accurately resolved.

nx,nz	refine	IORD	Nusselt number		RMS velocity	
			value	% error	value	% error
	'correct' result		10.534	-	193.21	-
16,16	-	1	9.959	-5.46	190.24	-1.54
32,32	-	1	10.628	0.89	195.33	1.1
64,64	-	1	10.621	0.83	194.69	0.77
16,16	3	1	10.416	-1.12	195.22	1.04
32,32	3	1	10.429	-1.0	193.98	0.40
64,64	3	1	10.463	-0.67	193.50	0.15
16,16	-	2	9.794	-7.02	185.00	-4.25
32,32	-	2	10.475	-0.56	192.19	-0.53
64,64	-	2	10.540	0.06	193.13	-0.04
16,16	3	2	10.350	-1.75	190.57	-1.37
32,32	3	2	10.509	-0.24	192.75	-0.24
64,64	3	2	10.531	-0.03	193.11	-0.05

Table B.2. Benchmark results for steady-state, basally heated, constant-viscosity convection with Rayleigh number 10^5 (case 1b of *Blankenbach et al.* [1989]). The Boussinesq approximation is assumed in a unit aspect ratio box. Table columns show number of grid cells in the x and z directions (nx,nz), approximate fractional grid refinement in the top and bottom boundary layers (refine), order of MPDATA advection scheme (IORD - see *Smolarkiewicz* [1984]), Nusselt number and rms velocity, and the percentage deviation of these quantities from the 'correct' values.

nx,nz	refine	IORD	Nusselt number		RMS velocity	
			value	% error	value	% error
	'correct' result		4.884	-	42.865	-
16,16	3	2	4.857	-0.55	42.50	-0.85
32,32	3	2	4.878	-0.12	42.775	-0.21

Table B.3. Benchmark comparison for steady-state, basally heated, constant viscosity convection at a Rayleigh number of 10^4 (case 1a of *Blankenbach et al.* [1989]). Other details and symbols are as in Table B.2.

nx,nz	refine	IORD	Nusselt number		RMS velocity	
			value	% error	value	% error
	'correct' result		21.972	-	833.99	-
16,16	3	2	20.087	-8.58	789.56	-5.33
32,32	3	2	21.881	-0.41	829.71	-0.51
64,64	3	2	21.998	0.12	833.55	-0.05

Table B.4. Benchmark comparison for steady-state, basally heated, constant viscosity convection at a Rayleigh number of 10^6 (case 1a of *Blankenbach et al.* [1989]). Other details and symbols are as in Table B.2.

Results for a Rayleigh number of 10^6 are given in Table B.4. In this case, the 16x16 solution is quite inaccurate, but the 32x32 solution is within ~0.5% of the correct result.

The two-dimensional constant-viscosity tests were completed by computing an internally heated result corresponding to case B2 of *Travis et al.* [1990a]. For this case

(Table B.5) the heat flux is set by the internal heating rate, so kinetic energy and velocities are listed. Again, 32x32 gives a reasonable accuracy of around ~0.5 %.

nx,nz	K.E.		w_{peak}		u_{peak}	
	value	% error	value	% error	value	% error
'correct'	324.30	-	-51.436	-	40.602	-
16,16	321.46	-0.88	-50.507	-1.8	40.115	-1.2
32,32	323.39	-0.28	-51.162	-0.53	40.432	-0.42

Table B.5. Benchmark comparison for internally heated, constant viscosity convection with a Rayleigh number of 38880 (case B2 of *Travis et al.* [1990a]). Vertical grid refinement by a factor of 3 in the boundary layers, and IORD=2 are used. Other details and symbols are as in Table B.2.

nx,nz	refine	IORD	Nusselt number		RMS velocity	
	top,bot		value	% error	value	% error
	'correct'		10.066	-	480.4	-
16,16	9,4.5	2	9.927	-1.38	408.5	-14.9 ?
32,32	9,4.5	2	10.217	1.50	465.7	-3.06
64,64	9,4.5	2	10.072	0.06	466.174	-2.96

Table B.6. Benchmark comparison for basally heated, temperature-dependent viscosity convection (case 2a of *Blankenbach et al.* [1989]). Viscosity varies by factor of 1000, $Ra_{1/2}=3.162 \times 10^5$. Other details and symbols are as in Table B.2.

Results for the variable viscosity benchmark 2a of *Blankenbach et al.* [1990] are listed in Table B.6. With temperature-dependent viscosity, the resolution requirements are more critical.

Finally, results for two of the three-dimensional benchmark cases in *Busse et al.* [1993] are listed in Table B.7. Accuracy of better than 1% is obtained with a 16x16x16 grid in both cases.

nx,ny,nz	Nusselt number		rms velocity	
	value	% error	value	% error
Case 1a: Constant viscosity, bimodal, rigid boundaries, $Ra=3x10^4$				
'best estimate'	3.5374	-	40.999	-
8,8,8	3.607	1.9	41.114	0.28
16,16,16	3.574	1.0	41.138	0.33
32,32,32	3.542	0.13	41.025	0.06
Case 2: Temperature-dependent viscosity, ratio=20, $Ra=2x10^4$				
'best estimate'	3.0393	-	35.13	-
8,8,8	3.117	2.6	34.77	-1.02
16,16,16	3.047	0.25	35.01	-0.34
32,32,32	3.043	0.12	35.14	0.03

Table B.7. Three-dimensional benchmark comparison of *Busse et al.* [1993].

Performance

The most time-consuming part of the code is the multigrid velocity/pressure solution, and thus this section concentrates on the time taken for multigrid V-cycles. When calculating a velocity/pressure solution from scratch, several V-cycles are required.

However, in a time-dependent calculation, the solution from the previous timestep is used as an initial condition, and 1-2 V-cycles are typically required to update this solution. Several tests have been performed to determine how the time required for a V-cycle is dependent on the size of problem and number of nodes.

In the first test, the size of problem is increased in proportion to the number of nodes. Table B.8 gives the time required to perform a multigrid V-cycle on 1, 256 or 512 nodes of the Intel Touchstone Delta. The number of grid cells per node is kept constant at 32x32x32 or 64x32x32, and thus the total number of cells increases in proportion to the number of nodes. The maximum number of cells that can fit in the memory of one Delta node with 16 MByte memory is 64x32x32, so the maximum possible grid size (on all 512 nodes) is 512x256x256. The viscosity is constant in this test, and the compiler options used were -O4 -Mvect=recog -Knoieee.

The results show that the time per V-cycle is fairly constant, regardless of the number of nodes. The communication overhead when using more than one node is 14-19% of the total execution time, a quite acceptable figure. Thus, the scalability of the algorithm is demonstrated: provided the computing power is increased in proportion to size of problem, execution time stays constant. This is not the case for the spectral method, where the total number of operations increases more rapidly than the size of problem (see Appendix A). Table B.8 also shows the CPU time per cell per V-cycle. This also stays fairly constant, although it is slightly higher for 32x32x32 cells per node than for 64x32x32 cells per node, as would be expected since the ratio of communication to computation is lower. This ratio scales roughly in proportion to surface area / volume of a cell, i.e., as $n^2/n^3=1/n$, where n is the number of cells along each edge of a node.

It is interesting to compare this performance with that obtained on a Sun Sparcstation 2 workstation. A constant viscosity problem with 128x128x32 cells takes 221.4 s/V, corresponding to 422 μs/cell/V, approximately twice as long per cell as the Intel Delta. A 32x32 problem, however, takes 1.12 s/V, corresponding to 1096 μs/cell/V. This difference

is because large problems are more able to take advantage of scalar pipelining in microprocessors, resulting in a higher computation speed.

Grid	Nodes	Cells/node	s/V	node-μs/cell/V	Efficiency
$64x32^2$	1	$64x32^2$	11.7	179	100%
256^3	256	$64x32^2$	14.0	213	84%
$512x256^2$	512	$64x32^2$	14.4	220	81%
32^3	1	32^3	6.4	195	100%
256^2x128	256	32^3	7.4	226	86%
256^3	512	32^3	7.7	235	83%

Table B.8. Execution time per multigrid V-cycle (V) on the Intel Touchstone Delta for various grid sizes and numbers of nodes, and constant viscosity. Grid sizes were chosen to give the same number of cells per node, to examine the scalability. CPU time (in node-microseconds) per cell for one V-cycle are also given, together with parallel efficiency.

Cells	Nodes	Cells/node	t/V-cycle	node-μs/cell/V
128^2x32	8	$64x32^2$	20.5	313
""	16	32^3	11.3	345
""	32	32^2x16	6.8	415
""	64	$32x16^2$	4.8	586

Table B.9. Time per multigrid (2,2) V-cycle for a 128x128x32 grid with various numbers of nodes, and variable viscosity. The CPU time per cell per V-cycle (in node-microseconds) is also derived.

In the second test, reported in Table B.9, the size of grid is kept constant as the number of nodes is increased. The number of cells is the same as that used in Chapter 5 and *Tackley* [1993], and the variable viscosity solver is used, requiring approximately 50% more operations than the constant viscosity solver, due to the additional terms in the discretized equations.

The CPU time per cell for one V-cycle gives an indication of the efficiency, and would be the same for any number of nodes if the program were perfectly efficient. Reasonable efficiency is obtained on 8 or 16 nodes, but there is a considerable loss of efficiency as the number of nodes is increased beyond 32 for this size of problem.

Viscosity Contrast	Multigrid V(2,2) cycles
1	3
10	4
10^2	5
10^3	6
10^4	13
10^5	16

Table B.10. Convergence characteristics, in terms of number of multigrid V-cycles to obtain convergence to 1% accuracy, for a two-dimensional 32x32 test problem and various viscosity contrasts.

Another aspect of performance is the number of multigrid V-cycles required to obtain a certain level of convergence. Table B.10 lists the number of V-cycles required to reduce the r.m.s. residual to 1% of the r.m.s. right-hand side, as a function of the viscosity contrast, for a two-dimensional problem where viscosity varies exponentially with

temperature. The temperature field is taken from a steady-state two-dimensional constant viscosity solution at $Ra=10^5$, and the instantaneous flow is calculated, with a grid resolution of 32x32 cells.

It can be seen that the number of V-cycles required increases with viscosity contrast, so that for a viscosity contrast of 1000, around twice as many V-cycles are required than for constant viscosity. This is also true during a time-dependent simulation, when the velocity solution from the previous timestep is used as an initial estimate rather than starting from scratch. The number of V-cycles required per step for variable viscosity simulations is typically 2, whereas for constant viscosity it is typically 1.

Conclusions

These results show that the multigrid finite volume method is an efficient tool for modeling mantle convection with large viscosity variations, and is well suited to implementation on massively-parallel supercomputers. In the future, the most important priority is to improve the convergence of the multigrid when very large viscosity contrasts are being used. The basic finite volume iterations converge for any viscosity contrast; however, this ability is lost when multigrid is used, because coarse-grid corrections do not necessarily improve the fine-grid solution when strong local variations in viscosity and velocity are present. It should be possible to improve this, with two possible directions being (1) the use of better coarse-to-fine operators, which take account of viscosity variations on the fine grid and (2) better restriction of viscosity to coarse grids, so that the calculated correction more accurately reflects the actual error in the solution.

Another enticing possibility is to improve the accuracy of the velocity/pressure solution by using a higher order approximation of the underlying equations. This is likely to be a more efficient way of improving overall accuracy than using more grid points in

each direction. It is also possible that this would improve the convergence of the multigrid for large viscosity contrasts [*J.R. Baumgardner*, personal communication, 1993].

Appendix C

Solution method used in Chapter 4

This Appendix describes the numerical technique used to obtain velocity solutions in Chapter 4. In order to calculate the velocity field associated with a given distribution of buoyancy forces, a spectral technique is used. Variables are expanded using complex Fourier components horizontally (assuming a periodic domain) and a sine or cosine expansion vertically. A vertical sine expansion is used for the stream function ψ and vertical velocity and a cosine expansion for horizontal velocity; for example:

$$\psi(x,z) = \sum_{l,n} \tilde{\psi}_{\ln} \exp(-i2\pi lx / A_x)\sin(n\pi z) \qquad \text{(C.1)}$$

where A_x is the aspect ratio.

Fourier transforming equation (C.1) both horizontally and vertically, we obtain:

$$\tilde{\psi} = -\frac{2il}{\pi^3(4l^2+n^2)^2}\tilde{\rho} \qquad \text{(C.2)}$$

and hence the velocity components:

$$\tilde{v}_x = \frac{2inl}{\pi^2(4l^2+n^2)^2}\tilde{\rho} \tag{C.3}$$

$$\tilde{v}_z = -2\pi il\tilde{\psi} = -\frac{4l^2}{\pi^2(4l^2+n^2)^2}\tilde{\rho} \tag{C.4}$$

Thus, the numerical technique is very straightforward, consisting of (1) transforming the density distribution into (l,n) space using Fast Fourier Transforms, (2) multiplying the density coefficients by the above factors to get velocity coefficients, then (3) transforming velocities back into grid space. This method is very efficient computationally and can be accomplished on a Sun Sparcstation 2 workstation, even with hundreds of points in each direction.

Accuracy and convergence. Some of the density distributions considered, such as the sheet mass anomaly (a delta-function in z), do not have a convergent spectral representation. However, we are interested in the velocity field and, as can be seen above, the spectral coefficients for velocity drop off asymptotically as n^{-3} or n^{-4} for a delta-function density anomaly, and thus the velocity field can be well resolved with relatively few harmonic coefficients, even if the density field cannot.

To test the number of vertical and horizontal components required, convergence tests have been performed for the standard case of stopped Gaussian anomalies of half-width 0.01 in a periodic (in x) domain of period 2, sheet-mass anomaly phase change at 0.25 depth. The calculated value of P_{crit} is tabulated below for various resolutions:

Resolution		Spectral drop-off		P_{crit}
nx	nz	x	z	
1024	1025	21.7	12.6	-0.165803
512	513	19.6	10.8	-0.166254
256	257	8.35	9.01	-0.165460
128	129	4.83	7.23	-0.166257
64	65	3.60	6.10	-0.181275

Table C.1. Convergence test for standard problem.

In the cases reported, a resolution of 128x129 is typically used, giving an accuracy of better than one part in 10^3.